SIMULATION OF OBSERVED TOPOGRAPHY USING A PHYSICALLY-BASED BASIN EVOLUTION MODEL

by

GLENN E. MOGLEN

RAFAEL L. BRAS

RALPH M. PARSONS LABORATORY
HYDROLOGY AND WATER RESOURCES

Report Number 340

Prepared under the support of
U.S. Army Research Office
Agreement DAAL03-92-G-0182

OCTOBER 1994

MIT

DEPARTMENT
OF
CIVIL
ENGINEERING

SCHOOL OF ENGINEERING
MASSACHUSETTS INSTITUTE OF TECHNOLOGY
Cambridge, Massachusetts 02139

R94-07

Simulation of Observed Topography Using a Physically-Based Basin Evolution Model

by

Glenn E. Moglen

Rafael L. Bras

RALPH M. PARSONS LABORATORY
HYDROLOGY AND WATER RESOURCES

Report Number 340

Prepared under the support of
U.S. Army Research Office
Agreement DAAL03-92-G-0182

OCTOBER 1994

Simulation of Observed Topography Using a Physically-Based Basin Evolution Model

Abstract

This work presents a model for basin evolution and a procedure for estimating the parameters of this model to reproduce a given topography. The model is calibrated based on three measures: the slope-area relationship, the cumulative area distribution, and the hypsometric curve. We find that these measures quantify fundamentally different characteristics of the drainage basin.

We show that spatial variability and structure are inherently necessary to sufficiently reproduce observed statistics of a basin. The presence of uncorrelated spatial variability introduces scatter to the slope-area relationship which is consistent to the scatter observed for an observed system. Uncorrelated spatial variability also influences the cumulative area distribution by causing the drainage aggregation pattern to encompass a greater spread of cumulative drainage areas around the representative hillslope scale. In contrast, a system with no spatial variability exhibits an almost single-valued distribution for the representative hillslope scale.

We illustrate how the channel selectively chooses pixels of greater susceptibility to erosion in which to grow. Based on a knowledge of the underlying distribution of spatial heterogeneities, we show that channel extension is limited to effectively three potential growth sites at any location. These results were confirmed for two different distributions: normal and uniform. This channel selectivity has the consequence of reducing the mean channel slope by an analytically determined amount based on the fluvial sediment transport parameters and the distribution of heterogeneities.

We analyze the effect of spatially correlated soil heterogeneities on simulated basins. Such correlations cause a shift in the slope-area relationship power-law exponent, θ. Correlated heterogeneities also have a profound influence on the hypsometric curve. We show how correlated erosivity in the horizontal direction leads to smaller mean basin elevations compared to the control or prototypical case. Meanwhile, stratification in heterogeneities may lead to larger or smaller mean basin elevations depending on the stratification pattern.

The process for calibrating the basin evolution model to statistically reproduce a given topography is presented. The process entails making initial estimates of model parameters from the observed slope-area relationship and using a numerical optimization package to determine the remaining parameter values. The numerical optimization process employs an off-line version of the evolution model which predicts the cumulative area distribution that would result from a given set of parameter values. The optimization selects the model parameters that will best reproduce the observed cumulative area distribution. The resulting simulation may be subsequently improved to reflect stratification or any other peculiarities that are present in the observed system.

Finally, we illustrate how the hydrologic response of a simulated basin is a function of the basin evolution model parameters that created it. Most notably, we show

that the distribution of saturated areas is significantly affected by the presence of spatial heterogeneities in erosivity. Results indicate that as heterogeneities increase within a basin, there is a greater spread in saturation indices. Thus, as the degree of heterogeneity in erosivity increases within a basin, the predicted runoff response from the basin becomes decreasingly sensitive to errors in estimation of the degree of saturation.

Acknowledgements

This report essentially constitutes the Doctor of Philosophy thesis of Glenn E. Moglen.

We gratefully acknowledge the support of the U.S. Army Research Office (agreement DAAL03-92-G-0182). The views, opinions and/or findings contained in this report are those of the authors and should not be construed as an official Department of the Army position, policy or decision unless so designated by other documentation.

Contents

List of Figures

List of Tables

Chapter 1

Introduction

The processes which shape the land leave their signature on the topography. Channel networks, hillslopes, floodplains, and basin divides are some of the topographic features which are formed by these erosive processes. Whether the topography can be characterized as smooth, jagged, rolling, dissected, flat, or hilly depends on the relative strength of these processes. This work is based on the assumption that analysis of the form of the landscape can be used to determine the forces that shaped it.

Anyone who's ever contemplated the shape of the land from a mountaintop or airplane has fashioned some mental picture of what constitutes a "reasonable looking landscape". Our first goal is to quantify the characteristics of landscapes from varied locations which are naturally subjected to differing geologic and climatic forces. This information will be used to achieve our second goal: to estimate the parameters of a physically-based basin evolution model. Attaining these two goals will lead to our ultimate objective of reproducing observed topography.

This work is motivated largely by recent work done in this field at MIT. That work has been along two lines of research. The first line of research involves the use of Digital Elevation Models (DEMs) which characterize observed topography in terms of a regular grid of elevation values generally at a 30m x 30m resolution. From this information it is possible to determine the channel network and measure many other properties of the actual drainage basin. The second line of research involves numerical simulations of physically-based equations of erosion which describe the evolution of a synthetic landscape in space and time. The work presented here represents the union of these two research lines. In essence, the goal is to use the numerical model to reproduce *by some measure* what is observed in the DEMs.

Several natural problems arise and will be addressed in this work. The phrase "*by some measure*" is italicized for two reasons. First, the deterministic reproduction of an existing topography is an impossibility since the basin evolution process is extremely sensitive to initial conditions and the initial state of an arbitrary basin is generally not known. And second, it will be shown that it is not a trivial matter to determine which measure, or group of measures, of a basin are significant. Basic assumptions about the consequences of the nature of elevation and flow discretization algorithms will be questioned and analyzed. Even the mathematical implications of the form of the idealized sediment yield equations will be shown to affect the simulated topography

under some conditions. All of these issues must be considered and understood before the basic task of calibrating the numerical model can be undertaken.

This work may be logically broken down into four sections. The first section contains introductory material. This includes Chapter 2 which presents a literature review detailing previous efforts in geomorphology. Previous studies which measured and quantified observed or simulated topography will be identified. These measures will play an important role in the later chapters. Past efforts to model the formation and structure of the landscape will also be emphasized. Chapter 3 will then present the model used in the work presented here, and illustrate its use with several simple sample simulations. This model is, in spirit, similar to that proposed by Willgoose *et al.* (1991a, b, c) so we will also discuss differences, modifications, and enhancements that have been implemented since this work.

The second section addresses the issue of appropriate measures and modeling assumptions. Chapter 4 illustrates the application of many geomorphic measures to actual and simulated drainage basins. Chapter 5 addresses the selection of appropriate parameter values and algorithmic choice to be used within the model. This second section will form the basis for those measures and algorithms to be applied in the remainder of this work.

The third section, Chapters 6 through 9 (and Appendices A, B, and C), constitute the primary contributions of this work to the field of geomorphic modeling. Chapters 6 and 7 consider the effect of uncorrelated and correlated erosivity, respectively, on simulated topography. Based on these findings, Chapter 8 presents a method to calibrate the model to observed topography and illustrates this procedure in a series of case studies. Chapter 9 addresses the ultimate question of implications on hydrologic response due to geomorphic expression, as a function of the calibrated parameters.

The final section, Chapter 10, summarizes findings and discusses possible avenues for additional research. Three appendices follow which illustrate some more rudimentary aspects of using the model. Appendix A demonstrates the effects of normally distributed versus uniformly distributed white noise in the model. Appendix B presents a case study of the parameter estimation and adjustment process for the basin evolution model. Finally, Appendix C addresses the issue of resolution and the modeling of topography at different grid scales.

Chapter 2

Literature Review

The body of literature concerning geomorphology is quite large, and owing primarily to high-speed computers and high resolution digital elevation data, the field of geomorphology is enjoying renewed interest. It would be a monumental task to summarize all the work that has been done in this field. Rather than attempt this endeavor, this chapter will discuss the fundamentals and history of geomorphology and summarize the work that is most immediately applicable to the work presented in later chapters.

2.1 Early Influences

There are two fundamentally differing hypotheses concerning drainage basins and their condition relative the forces that have shaped them. These hypotheses are personified by the two individuals who set them forth: William Morris Davis and Grove Karl Gilbert. Let us start by examining their ideas.

2.1.1 W.M. Davis

Davis' primary contribution to geomorphology was his model for landscape development he called the "geographical cycle" (1909). This cycle was actually a series of three interwoven cycles: a cycle of landscape development, a cycle of river (and network) development, and a cycle of slope development. Davis saw each of these elements a evolving through a series of stages from an early youth to old age. The youth stages of the cycle begin with a period of rapid uplift followed by a terrain characterized by high relief, rough terrain, waterfalls and rapids. Mature landscapes continued to decline in overall relief, developed river meanders, and rounded drainage divides. Old age manifests itself with very wide valley floors, low relief, and ultimately a flat, featureless peneplain.

2.1.2 G.K. Gilbert

In contrast to Davis, Gilbert's model of landscape organization was not cyclical, but rather independent of time. All of Gilbert's hypotheses are based on a landscape

which is in a state of dynamic equilibrium. The following is a quote from his *Report on the Henry Mountains,* (1877):

> *Of the main conditions which determine the rate of erosion, namely, quantity of running water, vegetation, texture of rock, and declivity, only the last is reciprocally determined by rate of erosion. Declivity originates in upheaval, or in the displacements of the earth's crust by which mountains and continents are formed; but it receives its distribution in detail in accordance with the laws of erosion. Wherever by reason of change in any of the conditions the erosive agents come to have locally exceptional power, that power is steadily diminished by the reaction of rate of erosion upon declivity. Every slope is a member of a series, receiving the water and the waste of the slope above it, and discharging its own water and waste upon the slope below. ... And as any member of the system may influence all the others, so each member is influenced by every other. There is an interdependence throughout the system.*

Thus Gilbert saw the landscape as a stable feature in which all parts of the drainage basin communicated any changes in a local condition. Any such change would impart a negative feedback tending to push the system back to a stable condition.

2.1.3 Contrasting Davis and Gilbert

An appreciation of the ideas expressed by both individuals is well-merited. One should not view either concept as either correct or incorrect, but rather that both views lie at opposite ends of a spectrum of possibilities. The beauty of Davis' ideas is how they encompass the notion of time dependency and how they accommodate varied landscapes. On the other hand, Gilbert's time-independent model appeals to our common experience with stable, undisturbed topography.

In the next chapter we will introduce our model for landscape evolution. Behavior reminiscent of both these individual's ideas can be observed. The early part of any evolution is most consistent with Davis' ideas since the topography is far from equilibrium. Since we are interested in producing non-trivial topography (not a peneplain) we impose a constant uplift component to our evolution. This mandates that the topography inevitably reach a stable dynamic equilibrium form, consistent with Gilbert's ideas. Ultimately, the determining factor in any landscape evolution is the nature and presence of external forcings such as tectonic uplift.

2.2 Theoretical Geomorphology

One of the key questions in geomorphology is: *Where do channels begin?* The "blue lines" of one map scale may place channel heads at one location. A different map scale may place the channel heads in a different location. Field surveys would likely provide yet a third source of channel head locations. It is a labor intensive and often

intractable option to perform a field survey of a basin to determine the location of all channel heads. The determination of channel heads by some remote means using an objective procedure would be very useful, since the knowledge of channel head location translates directly to knowing the drainage density of a basin. Drainage density, the total length of streams per unit area of a basin, is a key quantity in characterizing the response of a basin to a rainfall event. The greater the drainage density, the quicker we can expect the basin to produce runoff.

In a paper aptly titled, "*Where do channels begin?*" Montgomery and Dietrich (1988) survey a number of sites and seek to characterize the elements necessary for channelization to occur. They note that smaller source areas are needed to produce channelization in steeper terrain and that larger source areas are required to produce channels in drier regions. Decisive conclusions were hampered by different channelization processes: landsliding versus overland flow.

Smith and Bretherton (1972) performed a stability analysis which illustrated how the transition from an unchannelized, convex, hillslope to channelized, concave, hillslope corresponded to a shift in dominance of diffusive to advective processes of sediment transport. Additionally, they predicted that the fastest growing instabilities (the ones to be observed first) would have the shortest wavelengths. By this argument, a concave hillslope profile with the slightest perturbation would be subject to instabilities that would grow to form channels. Because the shortest wavelength would be most dominant, the concave profile would be **infinitely** rilled. But concave profiles do not necessarily produce channels and are certainly not infinitely rilled.

Loewenherz (1991) incorporated other physical mechanisms omitted by Smith and Bretherton and thus produced a theory which yielded a small, but finite, dominant wavelength (or rill separation distance) that could be expected by considering hydrodynamic implications of overland flow. In essence, by considering these other hydrodynamic issues, she introduced a threshold that needed to be exceeded before channel incision could occur. Her analysis also had the effect of moving the channel head downslope from the point of inflection of the convex-concave hillslope profile.

Similar to Loewenherz, Izumi and Parker (1993) presented a more hydraulically based perspective on the issue of channelization and network formation. They found that flow is most apt to cause channelization when the wavelength of a perturbations in elevation is comparable to the sheet flow depth divided by the slope of the surface. They also examined channel bifurcation and determined that the tendency to bifurcate increases as the radius of the sink (approximating a bifurcation site) divided by the flow depth increases.

Tarboton (1989) used this shift from convex to concave hillslope profiles as his key to determining the location of the channel head given DEM data. His procedure was to determine the break in scaling between slope and area using a two-phase regression. The hypothesis was that this break in scaling was the result of a transition from one dominant process to another, presumably diffusive to advective sediment transport. The area at which the break in scaling was observed corresponded to the mean source area required for channelization. For some data sets, however, the break in scaling was observed to be from one negative exponent to another, suggesting a break between one concave profile and another. This is not consistent with the stability theories

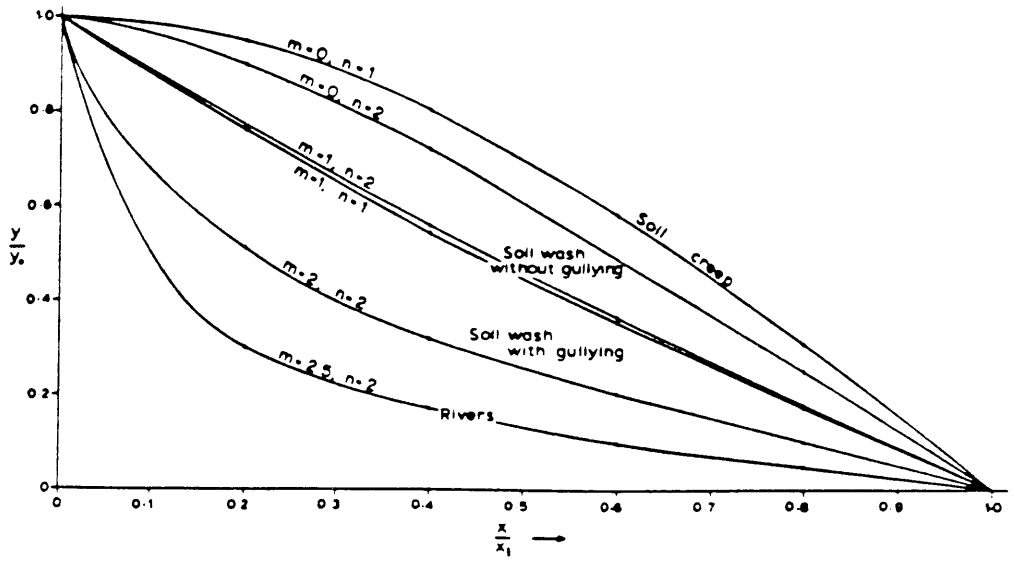

Figure 2-1: Characteristic slope profiles. (from Carson and Kirkby, 1972)

argued by Smith and Bretherton (1972) or Loewenherz (1991). That no break from positive to negative scaling was observed in some cases suggests that the data may have been too coarse in resolution and that the break in scaling actually occurred at a scale s maller than a single pixel.

Kirkby (1971) and Carson and Kirkby (1972) characterized sediment flux, F as:

$$F \propto a^m S^n \tag{2.1}$$

where a is cumulative area and S is slope. They illustrate how different combinations of m and n produce profiles of different shapes as shown in Figure 2-1. In general, larger m and n reflect fluvial transport processes dominant at larger scales. Likewise, m small or zero corresponds to the smallest scale diffusive processes which are only a function of slope and are dominant on hillslopes.

2.3 Geomorphological Measures and Relationships

A basin is a three-dimensional object which transports water and sediment from within its boundaries to its outlet. The characteristics which a given measure will quantify will naturally be based on elevation, area, and the drainage path. As each measure is discussed we will identify which characteristics are quantified by each measure.

2.3.1 Horton Ratios

In his classic work, Horton (1945) developed a scheme for organizing the pattern of the drainage network. The drainage network is discretized into a series of nodes which represents sources and drainage confluences. These nodes are connected following

the drainage path by line segments called links. A link which begins at a source is called an *exterior* link. Links which begin at confluences are called *interior* links. If we denote the number of interior links by n, then the total number of links in the system, N, must be:

$$N = 2n - 1$$

This value, N, is referred to as the *magnitude* of the system and can be used as a surrogate for drainage area or discharge. Another hydrologic term that will be used throughout this document is the *drainage density*, D_d. The drainage density quantifies how well-drained an area is and is defined as,

$$D_d = \frac{\sum L}{A_T} \tag{2.2}$$

where $\sum L$ is the sum of the length of all links in the basin and A_T is the total area of the drainage basin. Notice that drainage density has units of L^{-1} so it is a units-dependent measure. Horton (1945) suggested that the drainage density was related to the average overland flow distance by:

$$\bar{L_H} = \frac{1}{2D_d} \tag{2.3}$$

where $\bar{L_H}$ is the average overland flow length. In Shreve (1967), the approximation is made that the mean area draining to a link is proportional to the mean link length, l:

$$A_l = \kappa l^2 \tag{2.4}$$

where κ is a constant. Combining equations 2.2 and 2.3 the drainage density is related to the mean link length by:

$$D_d = \frac{Nl}{N\kappa l^2} = \frac{1}{\kappa l} \tag{2.5}$$

The Horton/Strahler ordering scheme works as follows: all exterior links have a Horton order of 1. When two links of the same order, ω, meet at a confluence, the resulting downstream link has order, $\omega + 1$. When two links of differing orders meet, the downstream link has the same order as the greater of the two contributing links. Horton streams are created by connecting sets of contiguous links which have the same order. This ordering scheme as originally proposed by Horton was refined by Strahler (1952) to remove the need for the subjective choice of parent streams as Horton originally defined them. Strahler's scheme is a purely topological method.

Several quantities: the number of streams, stream lengths, and the area drained by a stream can be grouped according to the order associated with the streams. Horton noted that ratios of these quantities were fairly constant within a basin and across many basins. These ratios have since become known as "Horton Ratios".

Three Horton ratios will be examined: bifurcation, stream length, and stream area. These ratios result from Horton's Laws:

- **Law of Stream Numbers:**

$$R_B = \frac{N_{\omega-1}}{N_\omega} \tag{2.6}$$

- **Law of Stream Length:**

$$R_L = \frac{\bar{L}_\omega}{\bar{L}_{\omega-1}} \tag{2.7}$$

- **Law of Stream Area:**

$$R_A = \frac{\bar{A}_\omega}{\bar{A}_{\omega-1}} \tag{2.8}$$

where R_B, R_L, and R_A are Horton's bifurcation, length, and area ratios, respectively, ω is the stream order, N_ω is the number of streams of order ω, $\bar{L}_\omega$ is the average stream length with order ω, and $\bar{A}_\omega$ is the average area drained by a stream of order ω. Typical values for these ratios are 3 to 5 for R_B, 1.5 to 3.5 for R_L, and 3 to 6 for R_A. Researchers (Shreve, 1966 and Kirchner, 1993) have argued that for statistical reasons, these ratios are constrained to these fairly narrow limits for any dendritic system. Thus, although Horton's laws are valid, their universality renders them of little value in discriminating between different dendritic systems.

2.3.2 The Slope-Area Relationship

Flint (1974) illustrated how slope could be shown to be a declining function of increasing order, magnitude, and discharge. In particular we are interested in the relationship between slope and discharge since order and magnitude are both discrete quantities while discharge is continuous. Since the measurement of discharge in a continuous fashion throughout a network is intractable, we use drainage area as a surrogate for discharge.

The slope-area relationship is a measure which quantifies the local topographic gradient as a function of drainage area. This measure unites both planar and vertical properties. Figure 2-2 shows an example slope-area plot for the Schoharie drainage basin in New York. The plot shows average local slope on the vertical axis plotted against cumulative area on the horizontal axis. There are two distinctly different regions to this relationship. For relatively small area (Region A) the trend in the data is for slope to increase with cumulative area. This is the area that is dominated by diffusive, smoothing processes such as wind erosion, soil creep, rainsplash, local landsliding, and even transport due to small animals. As the cumulative area increases the trend becomes negative (Region B) implying that local slope decreases with increasing area. These areas are typically hollows and channels in which the predominant sediment transport mechanism is due to flowing water or fluvial transport. If slope is a power law function of area such that:

$$S = cA^\theta$$

then Figure 2-2 shows a line consistent with a power law scaling exponent of $\theta = -0.4$ which roughly approximates the slope of the fluvially dominated region of the slope-

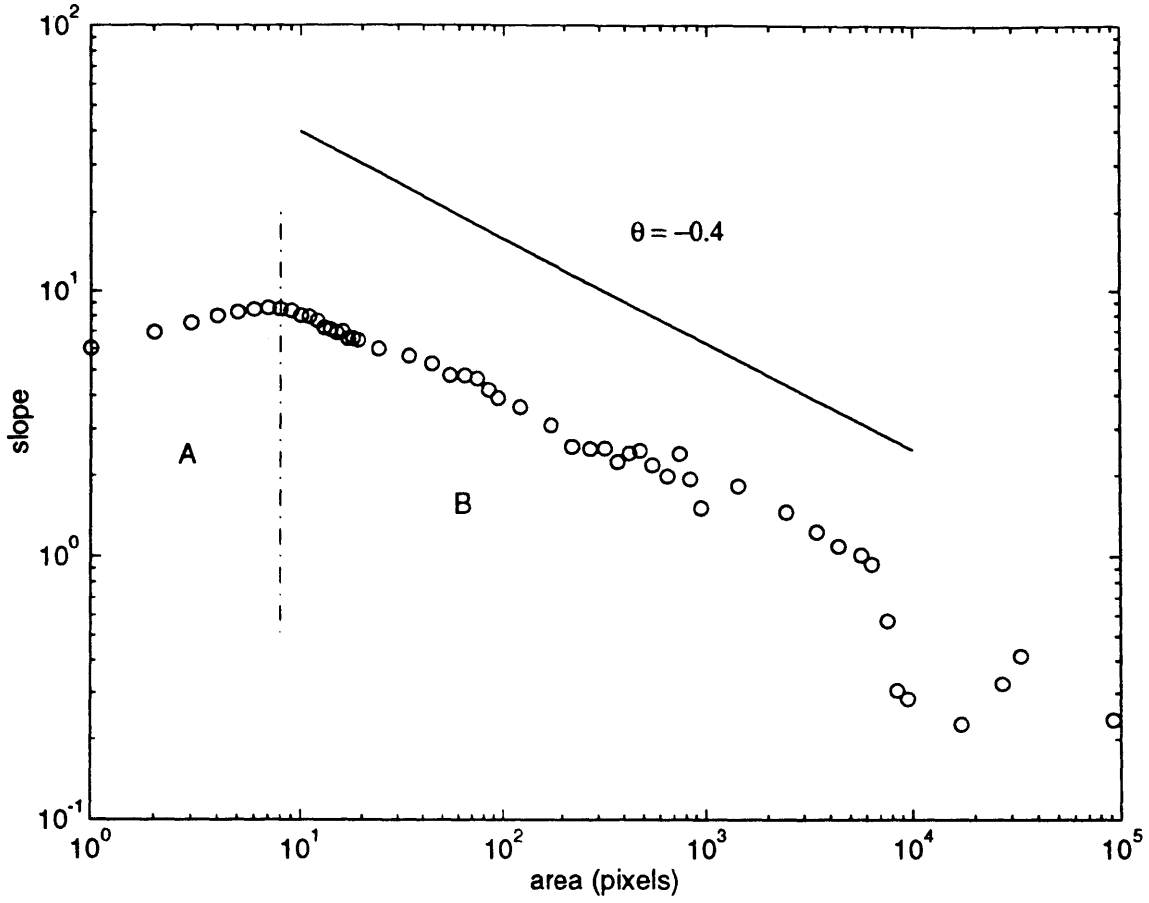

Figure 2-2: Observed slope-area relationship for Schoharie drainage basin, New York. (Line with slope-area scaling of $\theta = -0.4$ is shown for reference. Region A is dominated by diffusive erosion processes while region B is dominated by fluvial erosion processes.)

area relationship. Values of θ ranging from -0.3 to -0.6 were typically reported in Tarboton (1989, 1991).

It will be seen in subsequent chapters that this is perhaps the most fundamental geomorphic measure. It gives information about the relative strengths and magnitudes of both diffusive and fluvial transport processes and also implies the drainage density of the basin. Furthermore, it gives information about the relative degree of channel incision within the basin. The estimation of several basin evolution parameters directly from this relationship will be demonstrated.

2.3.3 The Cumulative Area Distribution

The cumulative area distribution measures the aggregation pattern of a drainage basin. This distribution was used by Rodriguez-Iturbe, *et al.* (1992) as a means of

characterizing the aggregation structure of the channel network. The distribution is calculated by determining the area which drains through each point in a system which has been discretized by a rectangular grid overlay. Each point (or pixel) has a cumulative area associated with it. A simple counting procedure generates the probability of a given pixel in the basin draining a cumulative area greater than or equal to a prescribed value:

$$P(A \geq a) = \frac{\#\ pixels\ with\ area,\ A \geq a}{\#\ pixels\ in\ basin} \tag{2.9}$$

Plotting these $P(A \geq a)$ against a in log-log gives the cumulative area distribution. A sample distribution is illustrated in Figure 2-3. Each distribution is characterized by three distinct regions also shown in in Figure 2-3. Region A corresponds to small areas and is physically indicative of the aggregation behavior of hillslope pixels. This is the primary region of focus in this study. Region B describes pixels which drain an intermediate area corresponding primarily to pixels which lie on the channel network. Pixels in region C lie entirely on the channel network. The rapid decrease in probability associated with region C pixels is due to domain constraints. A theoretical formulation describing the portion of the this curve corresponding to the channel network is presented in La Barbera and Roth (1993).

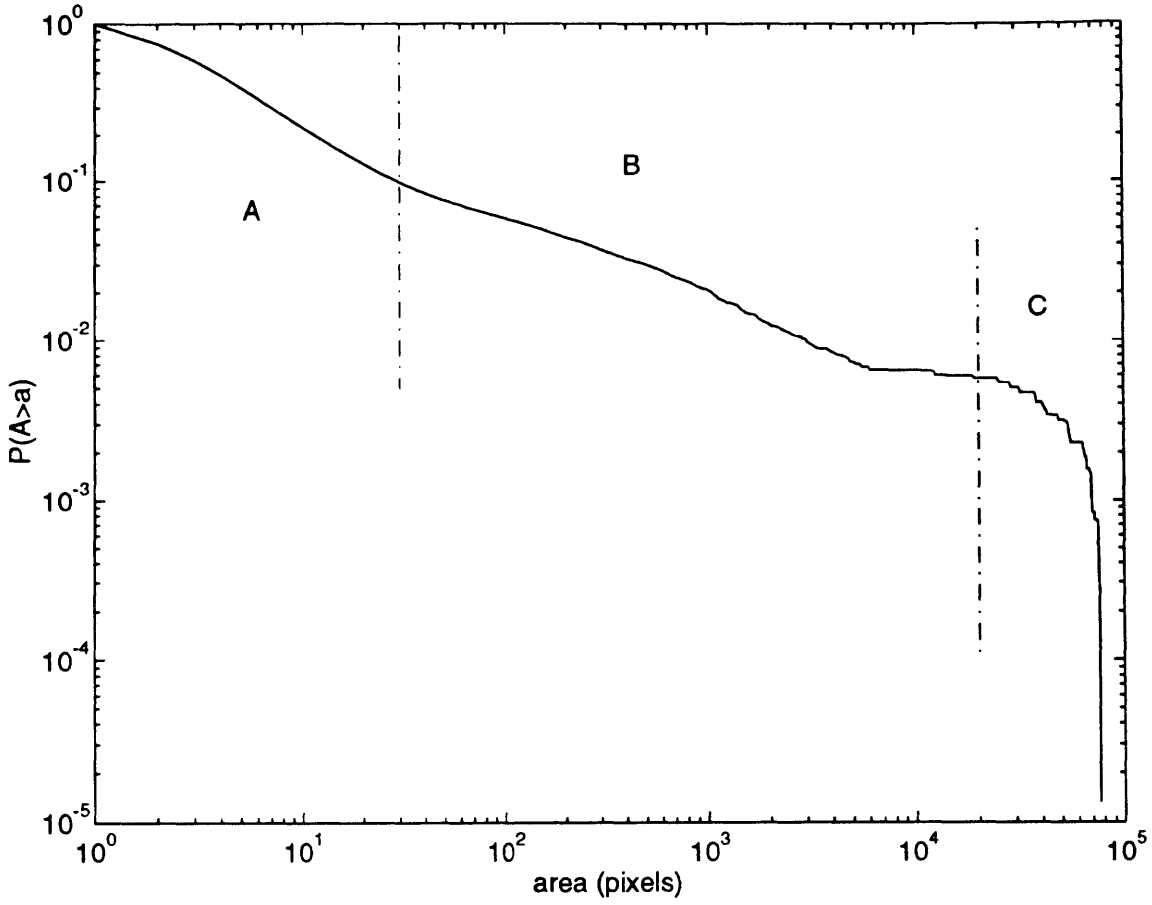

Figure 2-3: Observed cumulative area distribution for North Elk drainage basin, Idaho. Region A is dominated by diffusive erosion processes while regions B and C are subject to predominantly fluvial erosion.

2.3.4 The Hypsometric Curve

The hypsometric curve is a measure first introduced by Langbein *et al.* (1947), that describes the relative distribution of the basin area as a function of elevation. Area in the sense used here is a simple planar property and should not be confused with cumulative area referred to elsewhere in this work. The measure is best visualized by imagining many horizontal planes slicing through the drainage basin at equal elevation intervals such that the lowest plane slices through at the elevation of the outlet and the highest plane just touches the tip of the highest point in the basin. The the planar projection of the basin which lies above a given slicing plane is the quantity of interest. Thus the lowest plane at elevation z_0 will slice through a projected area, A_0, equal to the area of the entire basin. Likewise, the highest plane at elevation z_0 will slice through a projected area, A_n which is infinitesimally small. In between, a given plane z_i will slice through an area, A_i which is between zero and the area of the entire basin. The vertical axis corresponds to the z_i's normalized by the total relief of the basin. The horizontal axis corresponds to the A_i's normalized by the total basin area. Thus both axes range from 0 to 1 with the plot going from (1, 0) at the basin outlet, to (0, 1) at the highest point in the basin.

Figure 2-4 shows three hypothetical hypsometric distributions. The characteristic shape of most hypsometric curves is that of an "S" curve placed on its side. This is because the hypsometric distribution is essentially a cumulative probability distribution of elevations. The point at which the "S" curve levels out had been used by Strahler (1957) to infer whether a basin is young, mature, or monadnockian in terms of its geologic age. These are shown in Figure 2-4. Others have used different arguments to attribute a level of activity to a given hypsometric distribution. We will use this distribution to quantify the behavior of an observed system and, in subsequent chapters, we will show how different hypsometric distributions may also be indicative of horizontal or vertical variability in soil strength.

2.3.5 The Width Function

Developed by Surkan (1968), the width function measures the number of pixels located a given distance from the basin outlet. The horizontal axis gives the distance (measured along the drainage network) from the outlet, while the vertical axis gives the number of points contributing to the outlet located that distance from the outlet. The width function is a good measure of hydrologic response since it is strongly correlated with the instantaneous unit hydrograph. In the case where unit rainfall excess is routed with constant velocity from each pixel in the basin, the width function is synonymous with the instantaneous unit hydrograph.

Shown in Figure 2-5 is the observed width function for the North Elk drainage basin in Idaho. Also shown is a cubic spline smoothed version of this width function. A cubic spline was chosen for simplicity since it preserves the area under the width function, and conveys the most meaningful information content of the original curve. All width functions begin and end with an ordinate of essentially one pixel since there will be only one pixel located at the basin outlet and generally one pixel which is most

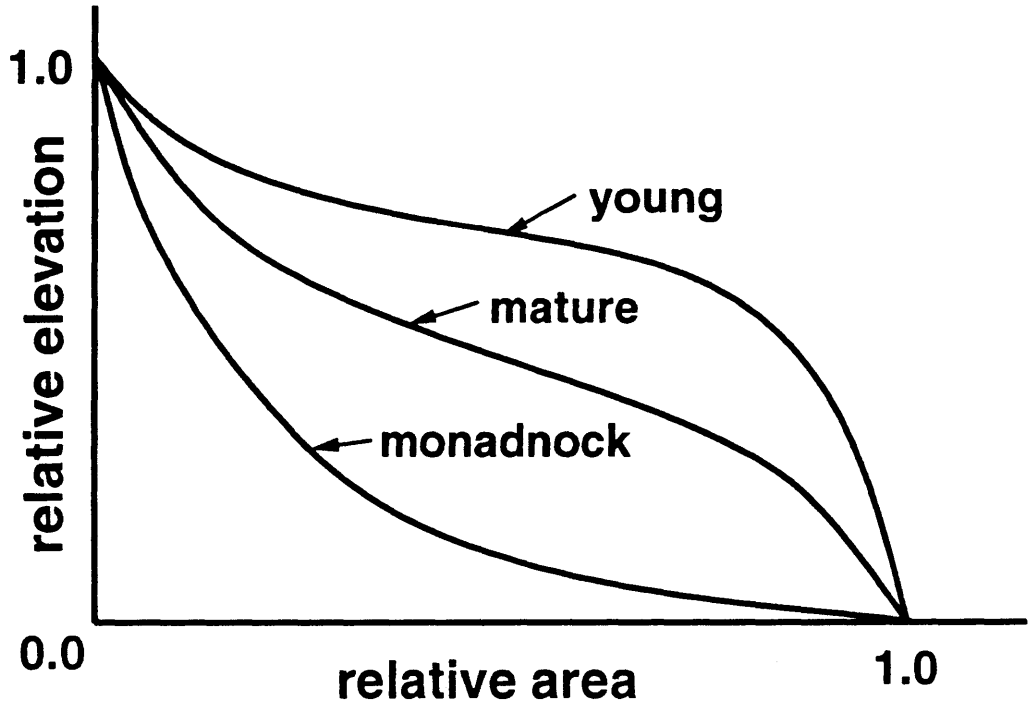

Figure 2-4: Several typical hypsometric distributions for basins of differing geologic age (after Strahler, 1957).

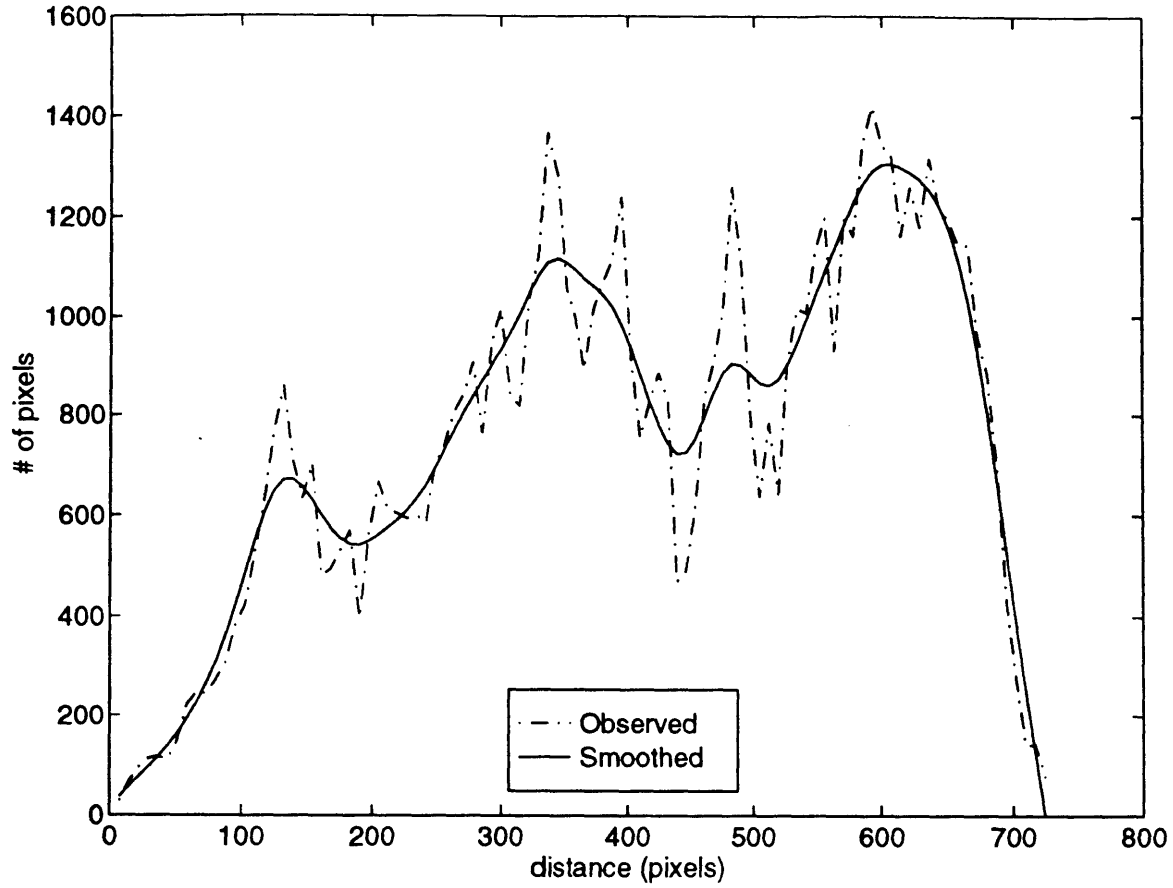

Figure 2-5: Observed(dash-dot line) and smoothed(solid line) width function for North Elk drainage basin, Idaho.

remotely located relative to the basin outlet. In between, the width function is largely dependent on the basin shape and also somewhat on the drainage structure.

2.3.6 Energy Dissipation

From hydraulic considerations, the energy dissipated at a point in the channel network is the product of the discharge passing through that point and the local drop in elevation. The energy dissipated by the entire network is then just the sum of all the local energy expenditures:

$$E = c_1 \sum Q_i \Delta h_i \tag{2.10}$$

where E is total energy dissipated by the system, Δh is the local drop in elevation, and the sum is taken over every pixel i within the system. Using cumulative area, A as a surrogate for discharge (i.e. $A \sim Q$) and the approximate slope-area scaling

relationship ($S \sim A^{-1/2}$), equation 2.10 can be rearranged:

$$E = c_2 \sum A_i^{1/2} L_i \tag{2.11}$$

where we have made use of the fact that $\Delta h_i = S_i L_i$.

This equation was used by Rinaldo *et al.* (1992) to generate optimal channel networks (OCNs) which are organized such that they minimize the sum given by equation 2.11. Their work shows that OCNs exhibit a number of natural characteristics even though the initial conditions from which the OCNs are generated may vary considerably from natural systems. By implication, an "objective" of natural systems is to aggregate flow in an efficient manner as defined by the minimization of equation 2.11. For our purposes, we will determine E for both natural and simulated systems and compare the values. We will not be so much interested in whether E is minimized, but rather if that E is a characteristic measure of a basin's aggregation pattern and provides a number which can be readily compared to other basins.

2.4 Channel Network Models

Many investigators have taken advantage of today's computational resources to simulate drainage basins and channel networks. These efforts have varied in their approach and in their physical bases.

Headward growth is the extension of a channel network from some initial site (the basin outlet) into a previously undrained region. The channel network extends into the basin and downcuts the topography eventually draining all area available to it. Howard (1971) was the first to numerically model the headward growth of a channel network. His model was essentially an Eden tree growth model (see Stark, 1991). He later (1990) improved his model to include stream piracy and channel junction alignments that were more consistent with observed systems.

Ahnert (1976) introduces a three-dimensional, physically based model of landform development. This model was among the first to move from slope profile modeling to the depiction of fully three dimensional features. The model incorporates a number of options for boundary conditions and erosion processes. Included are accelerating, constant, or decelerating base-level lowering, and splash, wash, plastic and viscous flow erosion processes. Ahnert also allows for different qualities of strata and a soil production function which deals with unweathered bedrock, fractured material, and unremoved waste. Ahnert illustrated several simple simulations with his model but was limited by the computer resources of the time, with typical simulation domains only 10 x 10 pixels in size.

The handling of eroded material within Ahnert's (1976) model varied with the erosional process being depicted. Ahnert made the distinction of point-to-point transfer and direct removal of waste transport. Direct removal was used for the wash process while point-to-point transfer was employed for all other remained erosion processes. Under direct removal, material that is set into motion is removed from the system without the possibility of redeposition. Point-to-point transfer moves material from

one node to its neighbor, where it may be moved again in a subsequent time step.

Cordova *et al.* (1982) used the equations of momentum, continuity, and a shear stress-based sediment transport equation to model the headward growth of channels. They illustrated how the introduction of perturbations in elevation produced a branched network which obeyed Horton's laws. In the absence of such perturbations only a single straight channel developed.

Willgoose, *et al.* (1991) present a physically based basin evolution model, SIBERIA. This model simulates drainage basin evolution based on discharge and sediment continuity. A unique feature of this model is the distinction it draws between hillslope and channels. The model utilizes a channel initiation function which governs the transition from hillslope to channel of a given pixel based on its slope and discharge. The model then applies different sediment transport capacities based on whether the pixel resides on a hillslope or a channel. The authors also present a non-dimensionalized analysis of their model and illustrate how similitude arguments can be applied to make comparisons among different basins. This work and model provide the foundation for the research presented in this thesis.

Stark (1991) produced channel networks by a specific form of headward growth he called "invasion percolation". He hypothesized that channel networks grow along a path of weakest "lattice bond strength". He also showed how anisotropy in the bond strength field could be used to form directional preference to the overall channel network geometry. Stark (1994) generalized his results from 1991 by lumping all drainage network evolution under the name of "cluster growth". He cites three forms of cluster growth: eden growth, invasion percolation, and Laplacian fingering. Eden growth is the dominant structure in a randomized area not strongly influenced by any controlling strata or exterior forces. Invasion percolation dominates where relative strengths or weaknesses of the substrate govern the evolution. Finally, Laplacian fingering (analogous to viscous fingering) dominates where groundwater sapping leads to preferred growth directions. Stark presents simulations for each growth mechanism and visually illustrates their resulting differences.

Kramer and Marder (1992) developed two models: one to assess channel cross-section stability and a second to assess the large scale features of channel networks. The latter model is similar in its conceptualization to that of Leheny and Nagel (1993). Both models traced individual units of water flowing across the landscape and applied some simple rules based on the path the water had taken to erode a landscape. For Leheny and Nagel, this erosion took two forms: a uniform removal (fluvial erosion) from all nodes visited along the drainage path, and a landslide form of diffusion at all sites with slopes exceeding a critical value. This diffusion term is physically realistic under some circumstances, however the fluvial term should not be uniform, but should be based on slopes and discharges. In this sense, both sets of researchers produced models which suffered from this lack of a physical basis.

Howard (1994) presents a physically-based model of basin evolution which has some components of erosion which are detachment (weathering) limited while others are transport limited. Similar to Willgoose *et al.* (1991a,b,c), he finds that individual details of a simulation are sensitive to initial perturbations in elevation, but general form (indicated by drainage density, and slope profile characteristics) is not sensitive.

Howard found that natural looking landscapes could be produced by simple additive models of various erosional processes. Howard also asserts that the stream network organization produced by his model and earlier optimality principle generated networks (discussed below) are similar. The implication is that optimality principles have imbedded within them the more physically-based approach presented by his current model.

Mentioned in the previous section and above by Howard (1994), another hypothesis concerning channel network organization is that their formation and structure is governed by some optimality principle. Rodriguez-Iturbe *et al.* (1992) propose a set of principles concerning energy dissipation in each link of a network and within the network as a whole. These principles lead to an overall minimization of energy dissipation over the network. In a series of papers they show how networks (OCNs) reproduce Horton ratios, cumulative area distributions, and multifractal distributions of power and area. that are consistent with natural observed behavior.

Ijjasz-Vasquez, *et al.* (1993) developed a simple model which generates drainage basins based solely on reproducing a power-law relationship between slope and area:

$$S \propto A^{\theta}$$

They showed how the resulting networks exhibit energy dissipation values comparable to those of OCNs, and also how the scaling exponent, θ, affects the network structure. In particular, values of θ close to -0.5 were necessary to produce channel networks with drainage patterns most like those observed in the field.

2.5 Interpretation of Digital Elevation Models

As stated earlier, a digital elevation model (or DEM) is a rectangular grid of elevation values which can be used to describe a topography and infer the drainage network. O'Callaghan and Mark (1984) give both a good review of early efforts in DEM interpretation and also provide algorithms for extracting information from DEMs. This procedure of identifying and isolating a drainage basin was followed by Tarboton (1989) and was the source of DEM data presented in this work. The procedure can be outlined as follows:

- **Step 1:** Using raw DEM data, determine drainage direction at each pixel. Drainage is in the steepest direction to one of each pixel's eight immediate neighbors. Local low points (pits) are removed by adjusting elevation upwards until all pixels drain.

- **Step 2:** Cumulative area is determined by calculating the number of pixels which drain through each pixel.

- **Step 3:** Channels are defined as pixels which have a cumulative area exceeding some threshold. (The determination of an appropriate threshold was the focus of Tarboton's (1989) work. No thresholds appear in our model. For illustrative purposes, we will identify the drainage network choosing an arbitrary threshold.)

- **Step 4:** Individual basins are identified and isolated by selecting a pixel on the drainage network and tracing upstream from there. All pixels which drain through the selected pixel are part of the basin. All other pixels in the DEM are flagged so their elevation, area, drainage direction, and slope are not recorded.

Other methods of characterizing the topography using irregularly spaced DEM data have been proposed including the use of triangular irregular networks (TINs) and networks with elements shaped by contour lines and flow tubes (O'Loughlin, 1986, Moore *et al.*, 1988).

Additionally, researchers have begun to consider the pixel size when processing DEM data. The procedure outlined above is correct provided the pixel size is infinitesimally small. However, since the pixels we are dealing with have a finite size it is not strictly true that all discharge (or area) draining through a given pixel will continue to flow to *only the one* pixel below that is in the steepest direction. Quinn, *et al.* (1991) propose allocating discharge (or area) downstream according to a weighted average of slopes. Each neighboring pixel with a downhill component from a given pixel receives some fraction of the drainage area according to:

$$Q_{ij} = Q_i \frac{S_{ij}}{\sum_{k=1}^{k=p} S_{ik}}$$

where Q_{ij} is the discharge from pixel i to j, and Q_i is the total discharge passing through pixel i. In this same spirit, Costa-Cabral and Burges (1994) developed an algorithm which views the elevations provided in a DEM as not defining the average elevation of a single pixel, but rather as defining the elevations of the four corners of a pixel. Based on these elevations, a value of the slope aspect is determined. Discharge, therefore, has some angle in the horizontal which can be resolved into a north-south and east-west component. In this way discharge (or contributing area) is allocated in fractional amounts among several pixels. Whether this method is superior to that used by Quinn, *et al.* (1991) is open to debate. Both methods are similar in that they apportion flow not according to steepest gradient, but rather by considering several values of slope in the flow field. In the next chapter we will show how we employ the method of Quinn, *et al.* largely because of its algorithmic simplicity.

Chapter 3

Description of Model

This chapter will introduce the model used to simulate the evolution of a landscape caused by erosional processes. The formulation of the model will be presented along with some sample simulations. Also included is a discussion concerning the two forms of limiting erosion behavior and the consequences of these forms on dynamic equilibrium. As stated previously, this model is very similar to that proposed by Willgoose *et al.* (1991a,b,c, 1994a,b,c). We will highlight those differences between the model presented here and the one used previously by Willgoose (in SIBERIA, version 6).

3.1 Model Formulation

In our model, the evolution of local elevation, z_i within a basin is governed by the equation:

$$\frac{\partial z_i}{\partial t} = U - \beta_i Q_i^m S_{ij}^n + D_i \nabla^2 z_i \tag{3.1}$$

where U is the rate of uplift, Q is the discharge, S is the slope. Node j lies in the steepest direction downhill from i, defining the slope from i to j. The parameters β_i, m, n, and D_i are calibrated to produce a specific topography. In the work presented here, we are concerned with regions on the order of 1 to 10 km^2. Uplift is assumed spatially constant at this scale. The last two terms on the right-hand-side of equation 3.1 describe erosion from fluvial processes and diffusive processes, respectively. Note that if β_i and D_i are spatially constant then we have homogeneous conditions, whereas if these parameters vary in space (with i), then the soil material is heterogeneous in its composition. We will define fluvial erosion as the process of soil removal due to a concentrated flow of water. Fluvial erosion tends to incise or carve the landscape. In contrast, we will define diffusive erosion as the process of soil redistribution due to local differences in elevation. Diffusive erosion tends to round and smooth the landscape. Figure 3-1 gives a schematic illustration of the forces of landscape evolution as conceptualized in this model.

Equation 3.1 is solved using an explicit finite difference method over a square grid. The grid divides the domain into a set of small square elements, or pixels, over

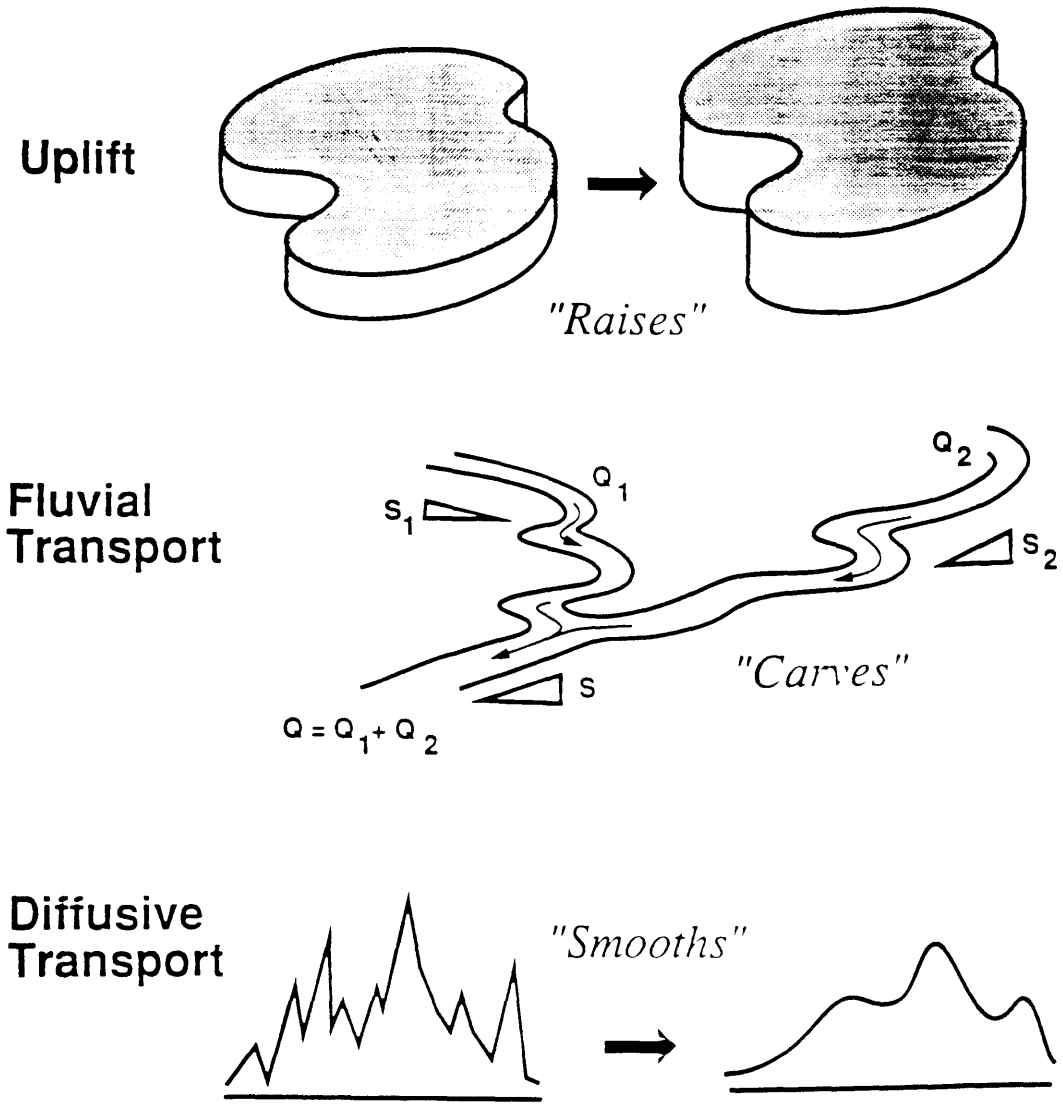

Figure 3-1: Schematic of the forces which govern drainage basin evolution.

which all properties are treated as locally constant. Direct exchanges of flow and sediment are allowed only between a given pixel and any one of its eight immediate neighbors. Water and sediment ultimately drain to an outlet pixel which retains a fixed elevation. A no-flux boundary condition is imposed at all other pixels on the boundary of the domain.

3.2 Multiple Flow Directions

The use of multiple flow directions (MFD) was mentioned earlier in Chapter 2. Our objective is to provide for a more precise distribution of flow in the downhill direction than simply have all flow from a pixel travel to its neighbor in the steepest downhill direction. Instead, discharge, Q is determined by accumulating flow along all paths which have a downhill component from a given pixel. Flow is apportioned to each downhill pixel according to the weighted average of slope in each downhill direction similar to the scheme developed by Quinn, *et al.* (1991):

$$Q_{ij} = Q_i \frac{S_{ij}}{\sum_{k=1}^{k=p} S_{ik}} \tag{3.2}$$

where Q_{ij} is the flow from pixel i to j, and Q_i is the total flow passing through pixel i. Note that when $p = 1$ the equation simplifies to the single flow direction (SFD) algorithm which routes all flow in the steepest downhill direction. The total flow is calculated by summing over all q pixels immediately uphill from pixel i:

$$Q_i = \sum_{k=1}^{k=q} Q_{ki} \tag{3.3}$$

Streamflow has often been indexed to contributing drainage area (Strahler, 1964) of the form,

$$Q_i = kA_i^b \tag{3.4}$$

where A_i is the cumulative area draining through location i. For our purposes, both k and b are taken as unity and thus discharge and cumulative area become interchangeable quantities within our model.

Although area is distributed according to the MFD algorithm, the fluvial component of sediment transport is determined as a combination of both SFD and MFD properties. The fluvial transport, given by $\beta A^m S^n$ uses the cumulative area, A, determined from the MFD algorithm as shown in equations 3.2 through 3.4. However the slope, S, is the *steepest* slope in the downhill direction from a given pixel. In this sense, slope is an SFD determined property.

Consider for a moment the consequences of allowing fluvial sediment transport to follow a pattern consistent with the MFD flow allocation methodology. The fluvial sediment transport from node j in an SFD system is given by:

$$Q_{s,j} = \beta A_j^m S_j^n \tag{3.5}$$

while under MFD conditions, this transport would be:

$$\begin{aligned} Q_{s,j} &= \Delta Q_{s,j1} + \Delta Q_{s,j2} + \Delta Q_{s,j3} + \dots \\ &= \beta A_{j1}^m S_{j1}^n + \beta A_{j2}^m S_{j2}^n + \beta A_{j3}^m S_{j3}^n + \dots \\ &= \beta \left(\frac{A_j S_{j1}}{\sum_{k=1}^{p} S_{jk}} \right)^m S_{j1}^n + \left(\frac{A_j S_{j2}}{\sum_{k=1}^{p} S_{jk}} \right)^m S_{j2}^n + \left(\frac{A_j S_{j3}}{\sum_{k=1}^{p} S_{jk}} \right)^m S_{j3}^n + \dots \end{aligned} \quad (3.6)$$

where the quantities in the parentheses are A_{j1}, A_{j2}, and A_{j3}. These are the portions of the flow to nodes 1, 2, and 3 from the uphill node, j.

For the case of a flat sloping plane (where elevations are identical across the width dimension) there are three downhill components to the multiple flow direction sediment transport out of any given node. One is directly downhill (and is the only one used in the single flow direction case) and the other two are diagonal to either side. If we allow the elevation loss in the steepest direction to be Δh then equation 3.6 becomes:

$$\begin{aligned} Q_s &= \beta A^m \frac{\left(\frac{\Delta h}{\sqrt{2}}\right)^{m+n} + (\Delta h)^{m+n} + \left(\frac{\Delta h}{\sqrt{2}}\right)^{m+n}}{\left(\frac{\Delta h}{\sqrt{2}} + \Delta h + \frac{\Delta h}{\sqrt{2}}\right)^m} \\ &= \beta A^m \Delta h^n \left[\frac{2\left(\frac{1}{\sqrt{2}}\right)^{m+n} + 1}{\left(\frac{2}{\sqrt{2}} + 1\right)^m} \right] \end{aligned} \quad (3.7)$$

Notice that since we are using unit nodal spacing the quantities Δh and S are the same. Therefore, the quantity in the square brackets of equation 3.7 represents the ratio of sediment transport using the multiple flow direction method compared to the single flow direction method:

$$\frac{Q_{s,MFD}}{Q_{s,SFD}} = \left[\frac{2\left(\frac{1}{\sqrt{2}}\right)^{m+n} + 1}{\left(\frac{2}{\sqrt{2}} + 1\right)^m} \right] \quad (3.8)$$

This relationship could be approached from the opposite angle. If our desire is to have the same amount of fluvial sediment transport, regardless of the method of flow allocation, we could adjust the β values accordingly:

$$\frac{\beta_{SFD}}{\beta_{MFD}} = \left[\frac{2\left(\frac{1}{\sqrt{2}}\right)^{m+n} + 1}{\left(\frac{2}{\sqrt{2}} + 1\right)^m} \right] \quad (3.9)$$

In either case, there is a difference in the sediment transport that is produced at a point depending on whether SFD or MFD methods are used. This is true even though the system geometries are identical. If we were to consider a diverging surface, one in which pixels tended to drain to more than three of their neighbors, the difference would be amplified even more. In general, the use of the MFD algorithm amplifies sediment transport on diverging or planar surfaces when compared to the same system under SFD transport. In actuality such surfaces diffuse flow rather than

concentrating flow. This shape of topography would not be expected to produce much fluvial transport. Therefore, SFD transport produces the more desirable result of the two possible transport methods. On converging surfaces, the two methods become equivalent because the number of downhill pixels, p becomes unity in equation 3.6.

The choice of the steepest slope method for computing sediment transport is also more convenient in the derivation of theoretical slope-area relationships. In an MFD system, several different values of slope are potentially available at many pixels. It is not clear how one would define the *average slope* when a pixel drains downhill in several directions. The SFD transport system avoids this ambiguity and allows for a simple analytical result (discussed in Section 3.3) which is consistent with observation. For these reasons, the fluvial transport component used in this model will be based on the steepest slope, even though multiple flow directions are used to determine the cumulative area.

The use of the MFD algorithm in our model is in contrast to the use of the SFD algorithm employed in SIBERIA. The SFD algorithm is used in Chapters 4 (all simulations) and 5 (where noted), with the MFD algorithm employed in all other simulations. The purpose of Chapter 5 is to directly address the implications of using one algorithm or the other. Based upon observed differences between simulations using the different methods, Chapter 5 will recommend the exclusive use of one of the algorithms for the ultimate objective of calibration.

3.3 Different Methods for Modeling Sediment Transport

There are two different methods for accounting for sediment once it has been set into motion as fluvial transport. The first, and simpler method allows for fluvial transport to be a power function of discharge and slope:

$$Q_{f,i} = -\beta_1 Q_i^{m_1} S_{ij}^{n_1} \tag{3.10}$$

where $Q_{f,i}$ represents the *local contribution* to fluvial transport from node i, Q_i is the flow leaving node i, S_{ij} is the slope in the *steepest* direction, and β_1, m_1, and n_1 are parameters to be calibrated. In contrast, the second method (used in SIBERIA) models the fluvial sediment transport as the divergence of the incoming and outgoing sediment fluxes:

$$Q_{f,i} = \sum_{k=1}^{q} \beta_2 Q_k^{m_2} S_{ki}^{n_2} - \beta_2 Q_i^{m_2} S_{ij}^{n_2} \tag{3.11}$$

where $Q_{f,i}$ is now the *total* fluvial transport from node i. The q in the summation is indicative of the number of points which contribute sediment to node i. A positive value of $Q_{f,i}$ indicates aggradation while a negative value indicates degradation. It should be noted that the β_x's, m_x's and n_x's are not necessarily the same between equations 3.10 and 3.11. Also, these parameters are constant in space so these comments apply to homogeneous conditions.

As stated in the previous chapter, Ahnert (1976) made a clear distinction between

Table 3.1: Comparison of direct removal and point-to-point transfer erosion terms

Erosion Term	Direct Removal	Point-to-Point Transfer
Sediment Influx	$\sum \beta_1 Q^{m_1} S^{n_1}$ †	$\sum_{k=1}^{k=q} \beta_2 Q_k^{m_2} S_{ki}^{n_2}$
Local Production	$\beta_1 Q_i^{m_1} S_{ij}^{n_1}$	$\sum_{k=1}^{k=q} \beta_2 Q_k^{m_2} S_{ki}^{n_2} - \beta_2 Q_i^{m_2} S_{ij}^{n_2}$ §
Transport Capacity	∞	$\beta_2 Q_i^{m_2} S_{ij}^{n_2}$
Sediment Efflux	$\sum \beta_1 Q^{m_1} S^{n_1}$ ‡	$\beta_2 Q_i^{m_2} S_{ij}^{n_2}$

† Summation is over all nodes which ultimately drain to pixel, **not** including the pixel itself. Quantity is not explicitly calculated by the model.

§ Quantity is not explicitly calculated by the model.

‡ Summation is over all nodes which ultimately drain to pixel, including the pixel itself. Quantity is not explicitly calculated by the model.

these two methods. He referred to the methods employed in equations 3.10 and 3.11 as direct removal and point-to-point transfer, respectively. Using direct removal, material that is set into motion is removed from the system without the possibility of redeposition. In contrast, point-to-point transfer moves material from an uphill pixel to the next adjacent downhill pixel. The material may be eroded from there during the same time interval, provided the downhill pixel has enough transport capacity to do so. Table 3.1 itemizes the differences between these two methods in terms of incoming and outgoing fluxes, local production, and transport capacity.

Let us now comment on the limitations of these two models. The greatest drawback of the direct removal model is that it inherently cannot reproduce physical features in the landscape which are the result of depositional processes that form alluvial fans, deltas, sandbars, etc. The major shortcoming of the point-to-point transfer model is its high numerical instability which necessitates extremely small time steps and thus requires large amounts of CPU per simulation.

Several questions that naturally arise are:

> *Does the assumption of one limiting behavior or the other affect the ultimate topography that is generated? Is it possible to determine which method would be more appropriate for modeling a given observed topography?*

To answer these questions one must be familiar with the dynamic equilibrium slope-area relationship. Using the point-to-point transfer model (neglecting diffusion)

the tectonic uplift input to an arbitrary sub-basin of area, A should be just balanced by the transport capacity out of the basin at the outlet:

$$UA = \beta_2 A^{m_2} S^{n_2}$$

$$S = \left(\frac{U}{\beta_2}\right)^{1/n_2} A^{(1-m_2)/n_2} \tag{3.12}$$

By contrast, using the direct removal model each pixel (with unit area, 1) should individually arrive at equilibrium with the tectonic input just balancing the fluvial transport out of that pixel:

$$(U)(1) = \beta_1 A^{m_1} S^{n_1}$$

$$S = \left(\frac{U}{\beta_1}\right)^{1/n_1} A^{-m_1/n_1} \tag{3.13}$$

where A is the cumulative area drained by the pixel in question.

So we see that both assumptions lead to the same general form of the slope-area relationship with the difference being in the exponent on area, θ:

$$S = kA^{\theta} \tag{3.14}$$

Under the point-to-point transfer model:

$$\theta = \frac{1 - m_2}{n_2} \tag{3.15}$$

while under the direct removal model:

$$\theta = \frac{-m_1}{n_1} \tag{3.16}$$

Because the parameters m_x and n_x may vary over a wide range of values (see Figure 2-1) it is difficult to discern from the observed data (usually in the form of a DEM) whether θ is better described by equation 3.15 or 3.16. It appears that only field reconnaissance and gaging could determine which would be more appropriate for a given basin.

Parallel to this argument is that observed data give no information about transient behavior. Transient behavior (because of the different emphasis on erosion at a point) differs between the two models even though they both arrive at the same form of dynamic equilibrium relationship. So although a given realization may take two different trajectories (depending on which model is employed) from its initial condition to a dynamic equilibrium form, the ultimate condition is consistent with either assumption. Therefore, neither model can be said to be more correct than the other.

Likewise the value of θ is all that is observable from a DEM rather than the unique, individual values of m and n. It is possible that flume or field experiments can determine the individual values of m and n, but it would also be crucially important

to observe whether intermediate deposition of material takes place as this would indicate the need to used the point-to-point transfer model. Otherwise, the direct removal model would be valid.

Since we will focus almost entirely on the equilibrium form of the topography and since the direct removal form of the model is more numerically stable than the point-to-point transfer model, we have selected the direct removal form for our fluvial transport term (except in Chapter 4). Moreover, we believe the characteristics of the model discussed in this thesis would broadly apply to any numerical model of landscape development provided the governing equations and initial conditions were comparable.

To put our work in the context of Ahnert's (1976) model, he employed direct removal for erosion he termed as "wash". This would correspond to the term we are calling fluvial transport. Likewise, Ahnert employed point-to-point transfer for all remaining erosion processes which are roughly akin to our diffusive transport term. This is identical to the handling of fluvial and diffusive transport within our model.

3.4 Sample Simulations

Before proceeding further, it is instructive to illustrate some sample simulations which represent different values of several of the key parameters of the evolution equation. In particular, this section will address the ramifications of the relative strength of D and β and the ratio of m/n.

Let us first consider the implications of D and β. From Figure 3-1 it should be clear that although diffusive and fluvial transport both are sources of erosion, they have very different signatures on the landscape and operate antagonistically. While fluvial erosion tends to carve topography and concentrate flow, diffusive erosion smoothes the landscape and disperses flow paths. Additionally, these two forces are dominant at different scales: fluvial erosion at large scales and diffusive erosion at small scales.

Figures 3-2 and 3-3 illustrate drainage basins generated with differing values of the diffusion coefficient, D. The first is with a relatively small value of $D = 0.04$ while in the second the value is relatively large, $D = 0.2$. Notice that this has a profound influence on the average hillslope scale and drainage density.

The relative strengths of these two processes determines the exact scale at which one force gives way to the other. This scale is directly related to the size of the average hillslope in a basin and the drainage density. We can analytically determine this scale by considering the asymptotic behavior for slope-area scaling of both diffusive and fluvial transport independently. Fluvial equilibrium was shown previously by equation 3.13. By a similar argument, diffusive equilibrium comes from:

$$UA = D\sum_{i}^{8} S_i = fDS$$

$$S = \frac{UA}{fD} \tag{3.17}$$

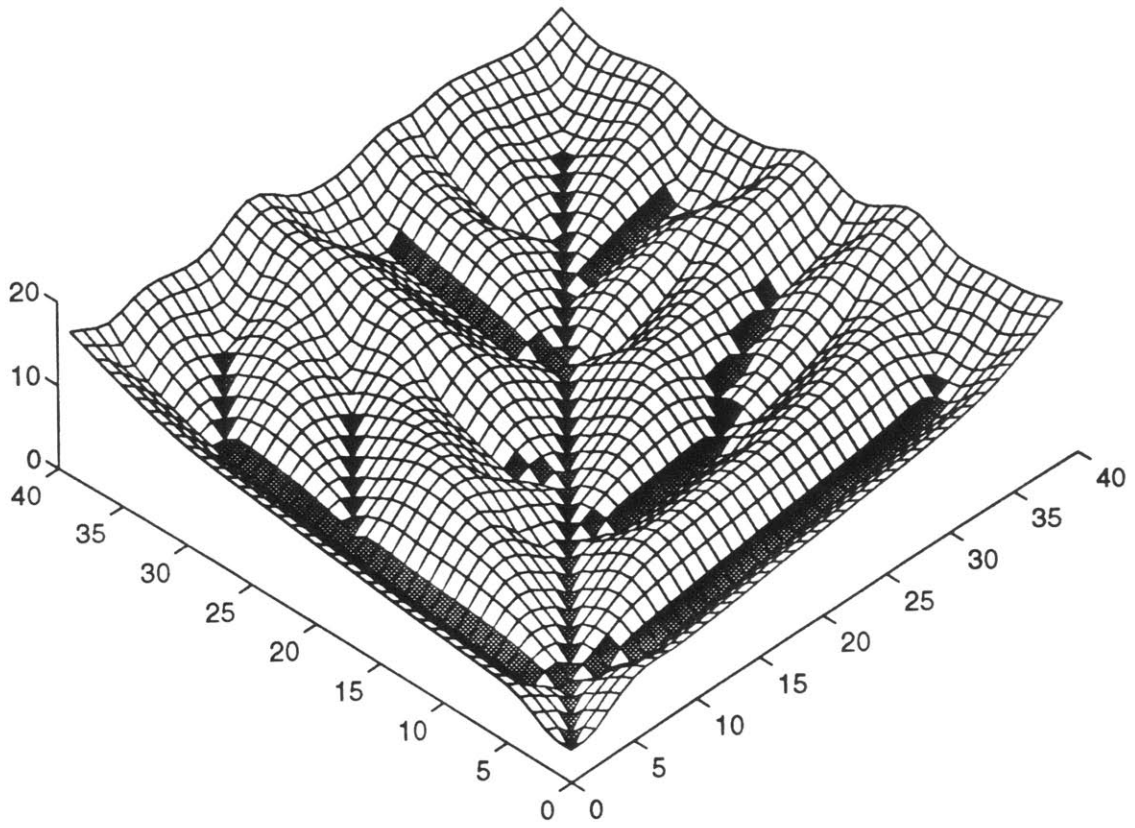

Figure 3-2: 3-D perspective of simulated basin with $D = 0.04$, $\beta = 0.01$, and $\theta = -0.5$.

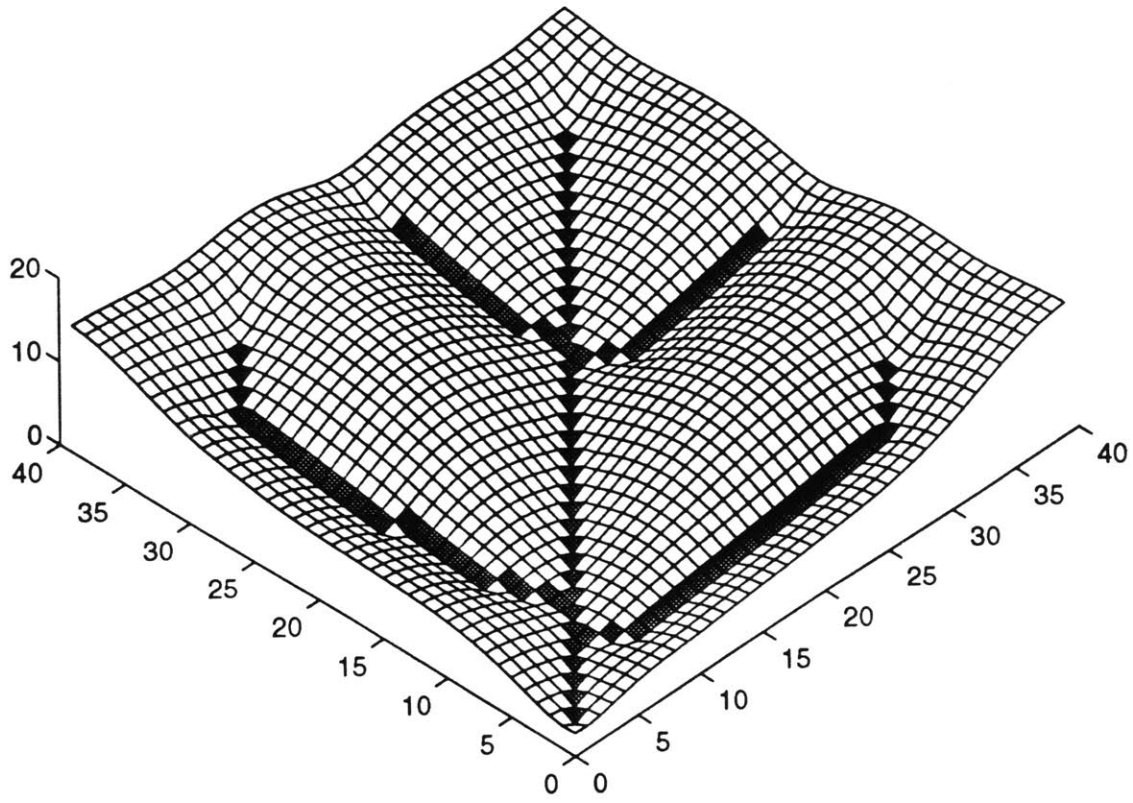

Figure 3-3: 3-D perspective of simulated basin with $D = 0.2$, $\beta = 0.01$, and $\theta = -0.5$.

Quantifying diffusion is complicated by the fact that transport is a function of local slopes in each neighboring direction rather than just the steepest slope. The quantity f in equation 3.17 represents an average sum of slopes expressed as a function of the steepest slope. From observation this quantity is typically about 2.5. If we set equations 3.13 and 3.17 equal to one another we get:

$$\frac{UA_*}{fD} = (\frac{U}{\beta})^{1/n} A_*^{-m/n}$$

$$A_* = U^{\frac{1-n}{n+m}} \beta^{\frac{-1}{n+m}} (fD)^{\frac{n}{n+m}} \tag{3.18}$$

The area given by A_* is the the characteristic area of the hillslope (in pixels) traveling from an average ridgetop to the channel. Note that this area increases as D increases and decreases as β increases, which would be expected. For the two simulations shown in Figures 3-2 and 3-3 the calculated values of A_* are: 2.15 and 6.30, respectively. Figure 3-4 shows the slope-area relationship for these two simulations. Notice that both systems tend towards the same fluvial equilibrium condition but that increasing D tends to reduce the slopes in the diffusion dominated portion of the relationship. This reduction also causes the scale at which A_* is located to increase. By inspection, this crossover point can be found at approximately 2 and 6 pixels for the given systems, confirming the analytical results derived above.

Differences in hillslope scale are also reflected in the cumulative area distribution. Figure 3-5 shows the cumulative area distributions for the two simulations shown in Figures 3-2 and 3-3. In general, as the value of β decreases or the value of D increases (i.e. A_* increases) there will be a shift to the right in the leftmost region of the cumulative area distribution. This is the region corresponding to hillslope pixels which drain relatively small areas.

Let us now consider the implications of the ratio m/n. From equation 3.16 we see that m/n controls the exponent on the area scaling in the fluvially dominated portion of the slope-area relationship. What *physically* does an exponent of say, -0.25 versus -0.5 indicate? Figure 3-6 illustrates a domain corresponding to the same values of β and D as that shown in Figure 3-2 but with θ equal to -0.25 rather than -0.5 of Figure 3-2. In this case we see that the domain with $\theta = -0.25$ has much greater relief and possesses channels which are not as incised as the domain corresponding to the domain with $\theta = -0.5$. The greater relief results purely from the fact that the $\theta = -0.25$ exhibits larger slopes at all areas than the other system. The integration of slopes along these drainage paths yields overall elevations that are much greater than those in the other system. The more interesting fact is that the channel is not as deeply incised into the material. This degree of channel incision is the most direct manifestation of the physical significance of m/n or θ.

The slope-area relationships for these two systems are shown in Figure 3-7. The values of A_* for the systems are 3.00 and 2.15 for θ=-0.25 and -0.5, respectively. This is evidenced in the figure by the turning point occurring at a slightly larger area for the system with θ=-0.25 compared to the system with θ=-0.5. This illustrates that, everything else being equal, a smaller (absolute) value of θ will result in a larger

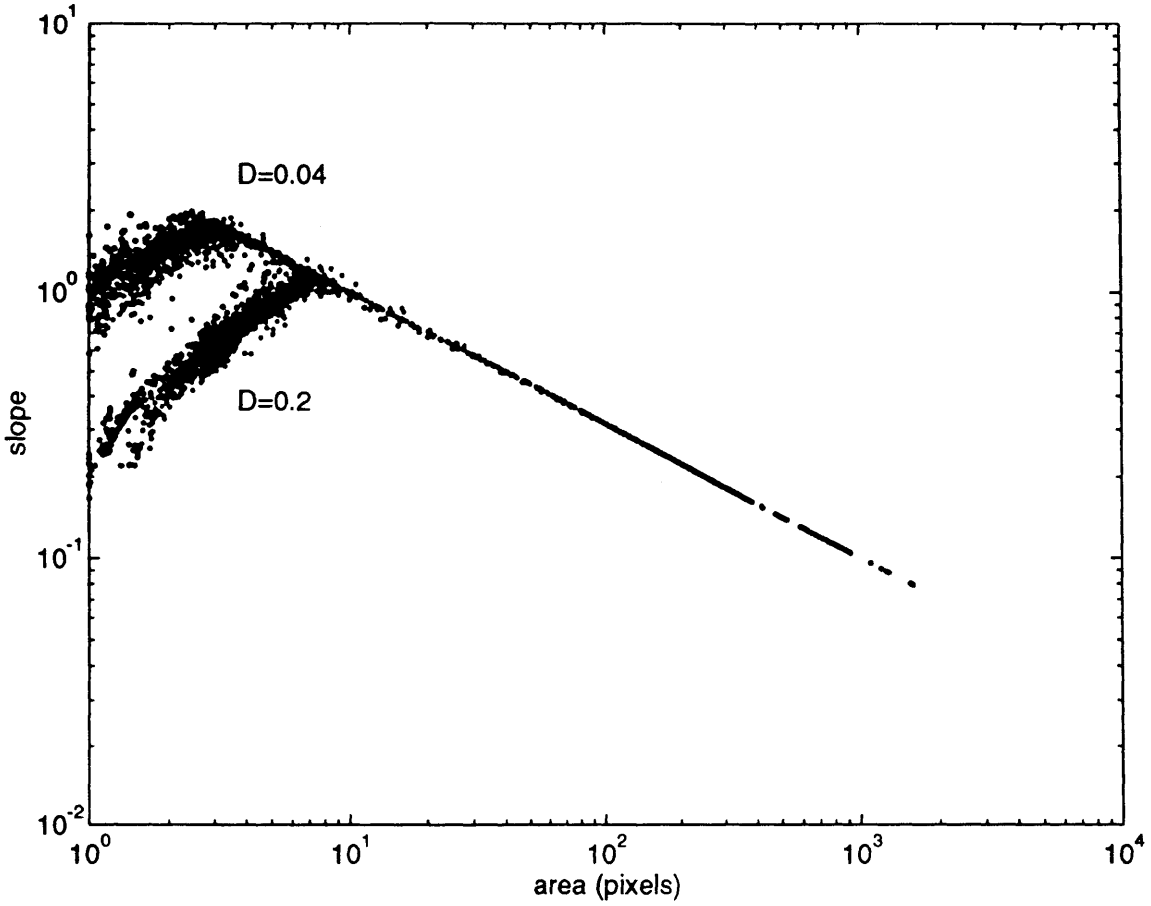

Figure 3-4: Slope-Area relationship for two sample distributions with varying values of the diffusion coefficient.

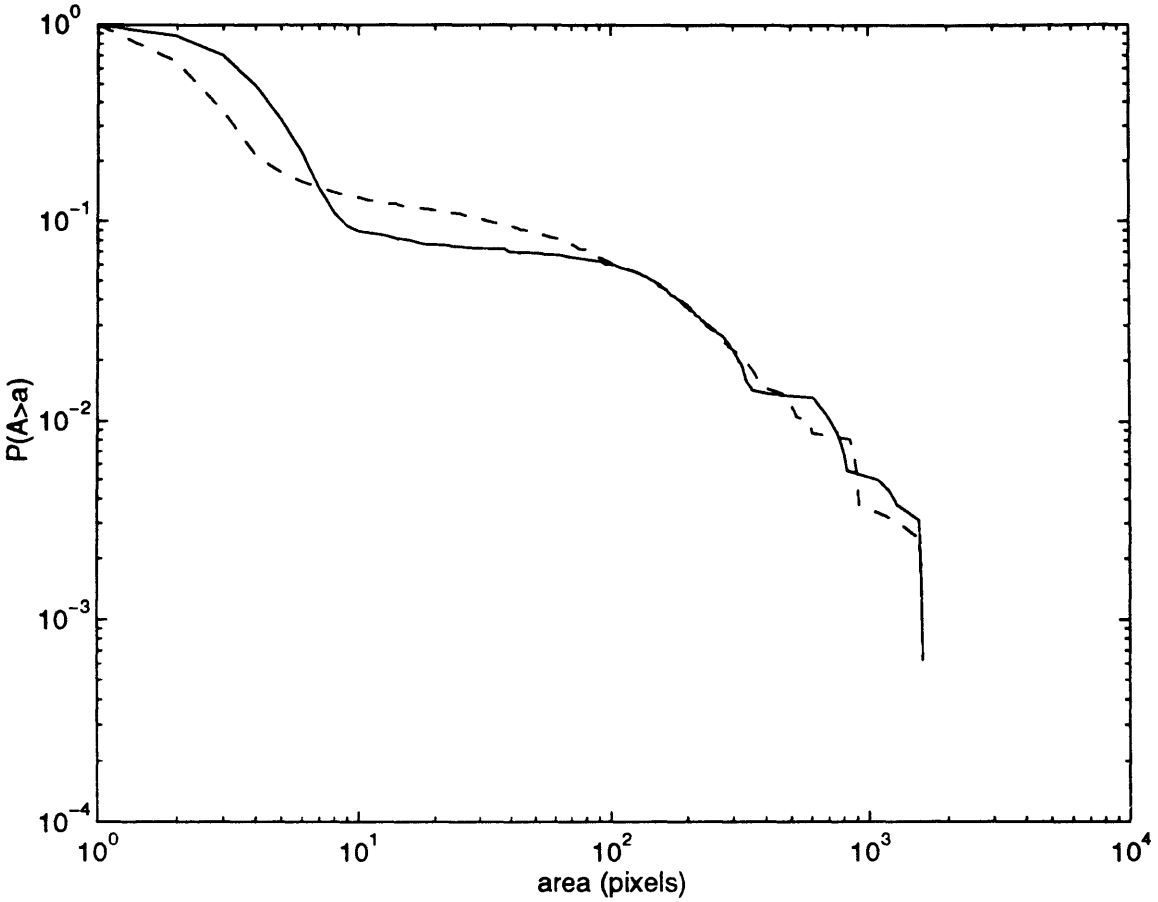

Figure 3-5: Cumulative area relationship for two sample distributions with varying values of the diffusion coefficient. (Solid line: $D = 0.2$ and $\beta = 0.01$, Dashed line: $D = 0.04$ and $\beta = 0.01$)

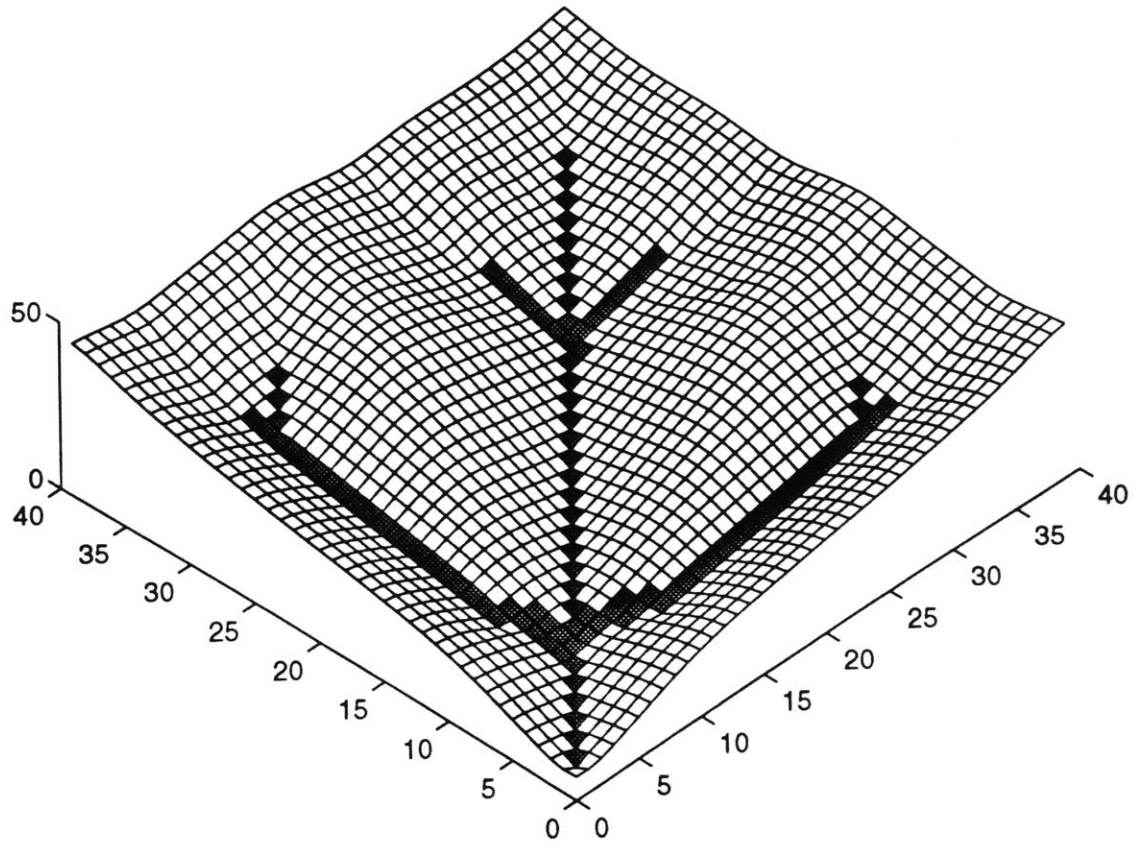

Figure 3-6: 3-D perspective of simulated basin with $D = 0.04$ and $\beta = 0.01$ and $\theta = -0.25$.

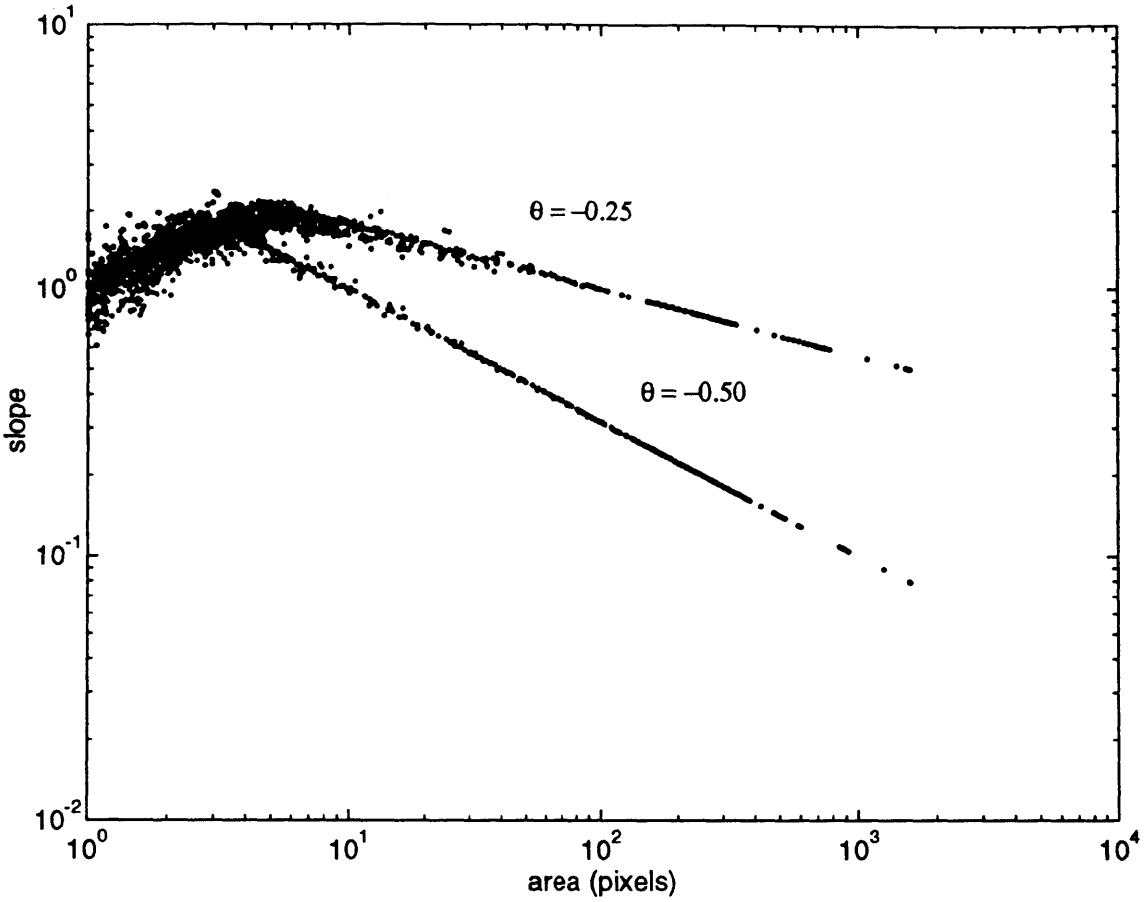

Figure 3-7: Slope-Area relationship for two sample distributions with different values of θ.

hillslope extent.

3.5 The Role of Tectonic Uplift

The tectonic uplift term of the evolution equation plays a number of roles in the evolution of a drainage basin. The most primary role is that $U > 0$ will ensure that the ultimate topography will exhibit some degree of relief whereas $U = 0$ will result in evolution to a flat, featureless surface. The greater the value of U the greater the degree of relief that will ultimately be produced.

In this study, uplift is considered uniform over the entire basin. The rationale for this assumption is that within the scale of most simulation domains, the uplift is essentially constant. If desired, uplift can be made a function of space to capture the effects of folding or it can be made a function of time to capture the effects of episodic uplift. For simplicity, all results presented in this work will be for constant uplift in space and time.

Table 3.2: Units of the parameters in equation 3.1.

Parameter	Dimensions	Metric Units
U	$\frac{length}{time}$	$\frac{m}{yr}$
β	$\frac{length^{1-2m}}{time}$	$\frac{m^{1-2m}}{yr}$
D	$\frac{length^2}{time}$	$\frac{m^2}{yr}$

Uplift also determines the time scales associated with the transient behavior of basin evolution. Unfortunately, uplift is an elusive quantity to measure and is only quantified in a few areas around the world, particularly those areas that are experiencing rapid growth such as the Himalayas, or to a lesser extent, the Rockies of North America. In general, uplift on the order of 1 cm/100 years is considered quite rapid.

Since uplift is so difficult to measure, its role in this study is often more of a mathematical entity than a physical parameter. Uplift is essentially a forcing function to which the different erosive processes respond. As such, the calibrated values of β and D, which will be determined in later chapters, are not informative by themselves, but become meaningful only when the value of U is known as well. In essence, it is the ratio of these different processes that is being calibrated, rather than absolute magnitudes.

To illustrate this point, imagine that we have a drainage basin that is in a state of dynamic equilibrium. This means that $\partial z_i/\partial t = 0$ for all i in equation 3.1. Thus:

$$0 = \Psi(U - \beta_i Q_i^m S_i^n + D_i \nabla^2 z_i) \tag{3.19}$$

which will be true for any Ψ. If we multiply Ψ through equation 3.19, this new equation will reflect the exact same topography as was generated earlier except now the uplift is ΨU, the fluvial erosion coefficient is $\Psi\beta$, and the diffusive erosion coefficient is ΨD. Thus it is the ratios: β/U and D/U that are relevant and not the precise choice of any one of these three parameters. As a matter of convention all numbers reported in this work will correspond to unit uplift.

3.6 The Role of Time

Equation 3.1 gives the rate of change of elevation per unit time. But what timescales are represented in this model? Consider the units of model parameters: U, β, and D given in Table 3.2:

The units of U and D are fixed by equation 3.1, but the units of β will vary depending on the value of the exponent on cumulative area in the fluvial transport

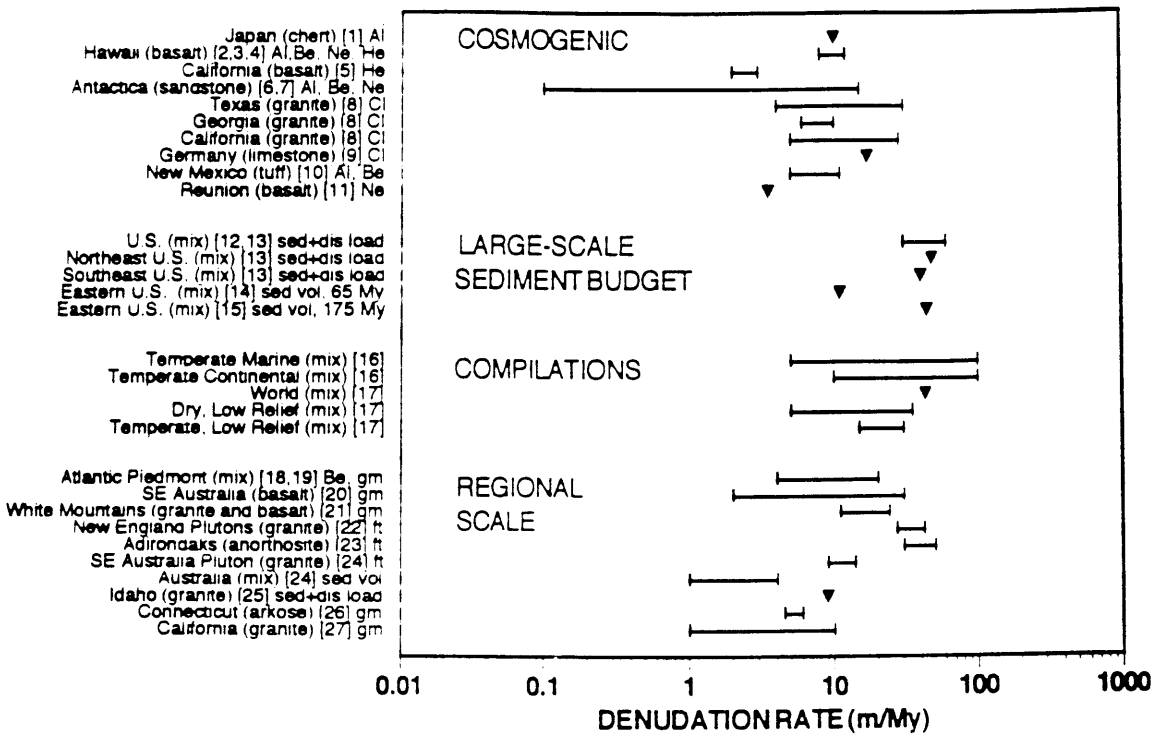

Figure 3-8: Typical rates of denudation determined by various means (from Bierman, 1994).

term. For values of m ranging from 0.5 to 1.0 the units of β will vary from $1/time$ to $1/(length - time)$.

Recalling the results from the previous section, the value of uplift regulates the values of β and D. Thus, the absolute dimensions that we choose our uplift to represent define the timescale of each iteration and the timescale of the evolution overall. We have said previously that all results as presented are for "unit uplift". Figure 3-8 illustrates some physically observed denudation rates as determined by several methods. As an approximation, let us take these denudation rates as being on the same order of magnitude as uplift rates. (This assumption is valid over very long timescales.)

A typical value taken from the denudation rates shown in Figure 3-8 is 1.0 m/My (or 0.1 mm/century). This is the unit uplift used in our experiments. Having selected and fixed this uplift rate, the values of β and D follow directly as discussed in the Section 3.5. If we use an uplift rate of 0.1 our timesteps represent 100 years. Since a given evolution may take 1000 to 10,000 timesteps to reach dynamic equilibrium the timescale of the evolution is 1 to 10 million years. If we increase the uplift to 1.0 (and hold β and D constant) then the evolution will reach dynamic equilibrium approximately ten times more quickly. Faster uplift results in a shorter evolution transient.

The reader might falsely conclude that increasing the uplift rate would be a simple way to perform simulations more quickly. This is not the case. A distinction must be

made between timesteps and iterations. It may take one or more iterations to simulate a single timestep. As the uplift defined by a timestep increases, more iterations per timestep become necessary to maintain a stable evolution. So although a simulation with rapid uplift may physically represent a shorter time period, the number of computer iterations (and the total computer simulation time) may be comparable to the the slower uplift case.

3.7 Summary

In this chapter the basic formulation of the basin evolution model was presented. Specific aspects of the model including the employment of multiple flow directions and the use of the direct removal algorithm were discussed. These aspects are some of the key differences between the model used in this study and the one presented previously by Willgoose *et al.* (1991a,b,c 1994a,b,c). One other key difference, incorporating heterogeneous erosivity into the model, will be discussed in Chapters 6-9. Sample simulations of the model were performed which illustrated the effect of the the fundamental evolution parameters: D, β and θ. The differences caused by these parameters were illustrated directly in the simulated topography, and also in the effect on the slope-area relationship. Finally, discussions of the meaning and influence of uplift and time was presented. We showed how the magnitude of the uplift, U, dictates the resulting values of β, and D. Furthermore, the units of U govern the timescales associated with a single timestep and with the overall evolution duration.

Chapter 4

Large Scale Simulations

Complementary to the primary goal of reproducing an observed topography is our ability to assert that topography has been reproduced. We make no pretense that a given observed system can be deterministically reproduced. To do this would be tantamount to knowing the precise initial conditions from which the actual system evolved, which is improbable. This is the point that Ijjasz-Vasquez, *et al.* (1992) demonstrate. They show the strong sensitivity to initial conditions of the Willgoose *et al.* (1991a,b,c) SIBERIA model to small perturbations in elevations. The conclusion to draw from this work is that, at best, we can attempt to *statistically* reproduce an observed system. This involves developing a set of measures which effectively and objectively quantify some characteristic of a drainage system.

If a simulated and observed system were to exhibit comparable values to each of this set of measures then we would assert that the two systems were statistically the same. The goal of reproducing the observed topography would thus be achieved. Naturally, the extent to which the simulated system actually resembles the observed system is dependent on the robustness of the measures. The quality of our work depends not only on our model, but also on our ability to critique and quantify discrepancies between the simulated systems and what is observed in nature.

The simulations shown in this chapter will be used to illustrate some of the measures introduced in Chapter 2. The value of each of these measures in quantifying differences between drainage networks will be discussed. Additionally, systematic shortcomings between simulations and the observed network will be highlighted as issues which will be addressed in later chapters.

4.1 Initial Conditions

A series of simulations were performed using the observed basin boundaries of the North Elk DEM data set. This basins contains about 75,000 pixels and has an area of approximately 410 km^2. It is located in east-central Idaho and exhibits fairly mountainous terrain. The observed relief of the basin is roughly 800 meters. Five simulations were performed varying only the nature of the initial elevation field. Table 4.1 summarizes the simulations that were done.

Table 4.1: Summary of simulations performed. ("x" in box indicates initial conditions, z_i: initial elevation at node, i, $\bar{z}$: arbitrary characteristic elevation, ϵ: uniformly distributed, small random perturbation, d_i: separation distance of node i from nearest point on the basin divide, α: arbitrary multiplicative constant.)

Overall Surface Shape	without Perturbations	with Perturbations	Initial Elevation Field Model
Flat	x		$z_i = \bar{z}$
Flat		x	$z_i = \bar{z} + \epsilon_i$
Drum	x		$z_i = \bar{z} - \alpha d_i^{1/2}$
Drum		x	$z_i = \bar{z} - \alpha d_i^{1/2} + \epsilon_i$

Owing to the large domain size, a prohibitive amount of CPU time is required to use the basin evolution model to simulate each case to dynamic equilibrium. Instead, a two-step procedure was employed to *approximate* the dynamic equilibrium form of the simulated basins.

- **Step 1 - Capture:** Initial conditions are from the initial elevation field specified in Table 4.1 along with the basin boundaries and identified outlet. The basin is captured by headward growth of the network originating from the outlet.

- **Step 2 - Imposing Equilibrium:** At the completion of step 1 the basin is dissected such that the drainage paths from each pixel to the outlet are defined. We assume now that these drainage paths will not change further as the evolution proceeds to dynamic equilibrium. This assumption is not strictly true, however in a set of smaller simulations it was observed that only a very small percentage of pixels (less than 1%) change their direction after capture. Elevations can then be defined at each point in the basin by equating the fluvial dynamic equilibrium result from equation 3.12 (which relates slope to cumulative area) to the observed slope-area relationship for the Nelk drainage basin. This observed slope-area relationship is shown in Figure 4-1.

  It should be acknowledged that the landscape produced by this method is still not strictly the same as would be produced by the evolution model since the diffusive transport term has been omitted. The intention here is to determine some approximation of the topographic distribution of elevations which will only be of importance in the determination of the hypsometric curve.

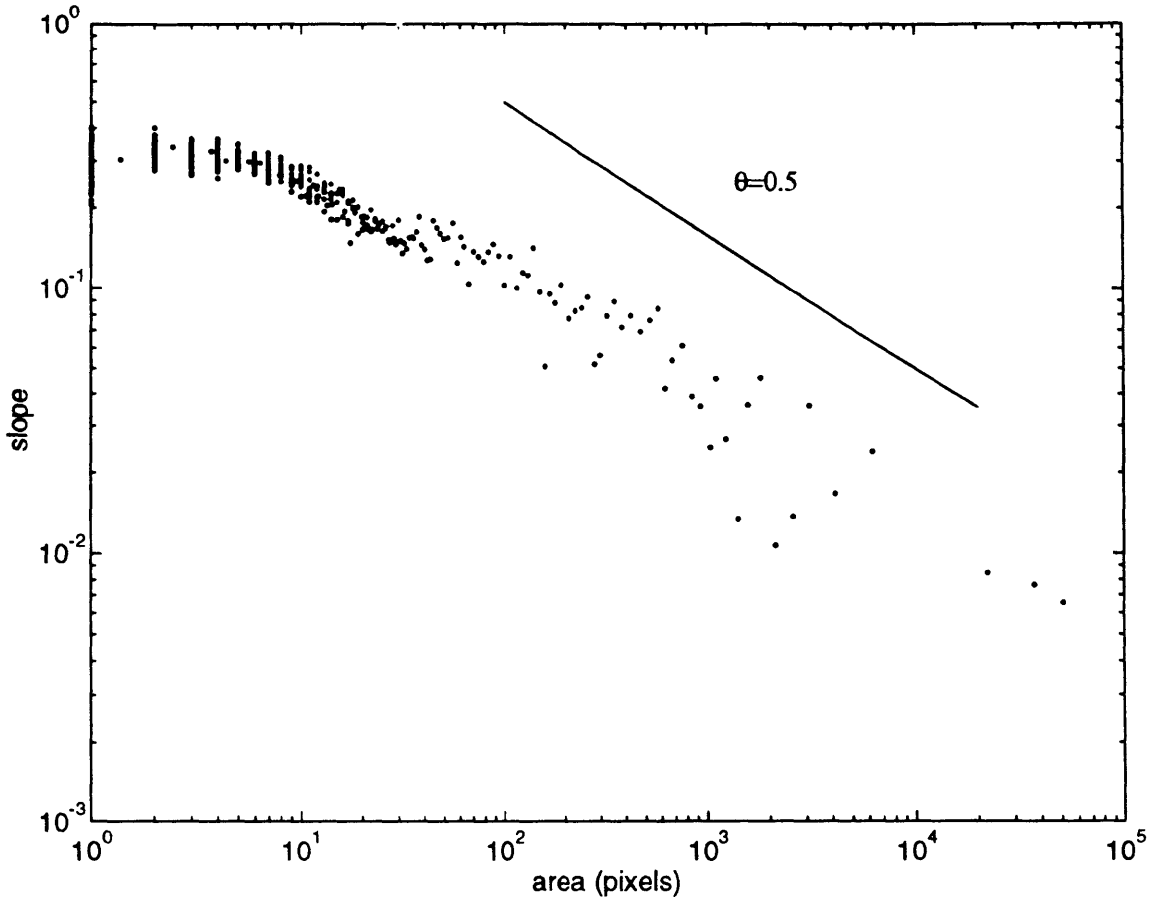

Figure 4-1: Observed slope-area relationship for Nelk, Idaho

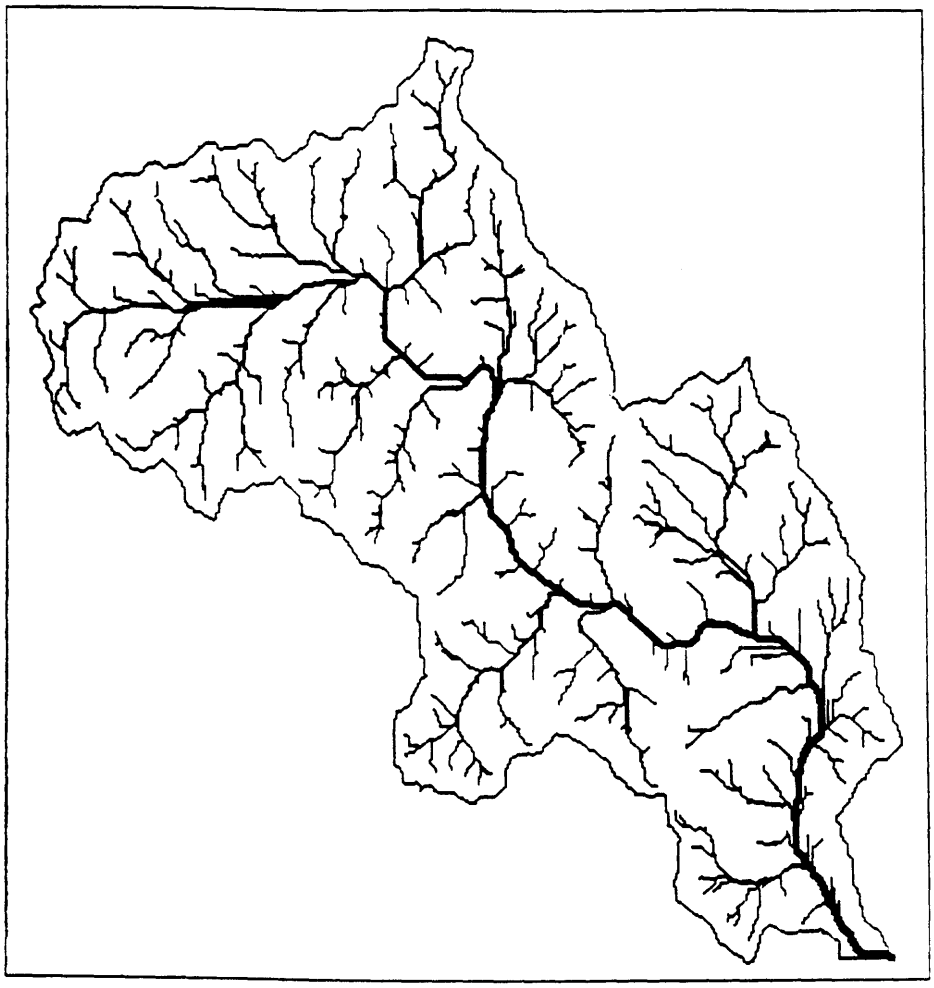

Figure 4-2: Observed channel network - Nelk river basin, Idaho.

4.2 Results: Qualitative Observations

The observed channel network along with the simulated networks are shown in Figures 4-2 through 4-6. All networks are shown with a threshold area of 50 pixels defining the beginning of channels. Stream width is plotted as a function of the square root of cumulative area for illustrative purposes only. The evolution model does not parameterize channel width in any way.

- **Observed Network (Figure 4-2):** this network has a single main channel which roughly traces through the middle of the basin although it does wind about the domain to a fair degree. Drainage begins perpendicular to the basin divides and tends to join the main channel at perpendicular confluences.

- **Simulated Network - flat, no perturbations (Figure 4-3):** A quick glance at this network immediately reveals that it does not look very realistic. Channel branches tend to be long and straight, with north-south and east-west drainage directions largely favored over northeast-southwest and northwest-southeast directions. However, the drainage pattern in the vicinity of the basin outlet is

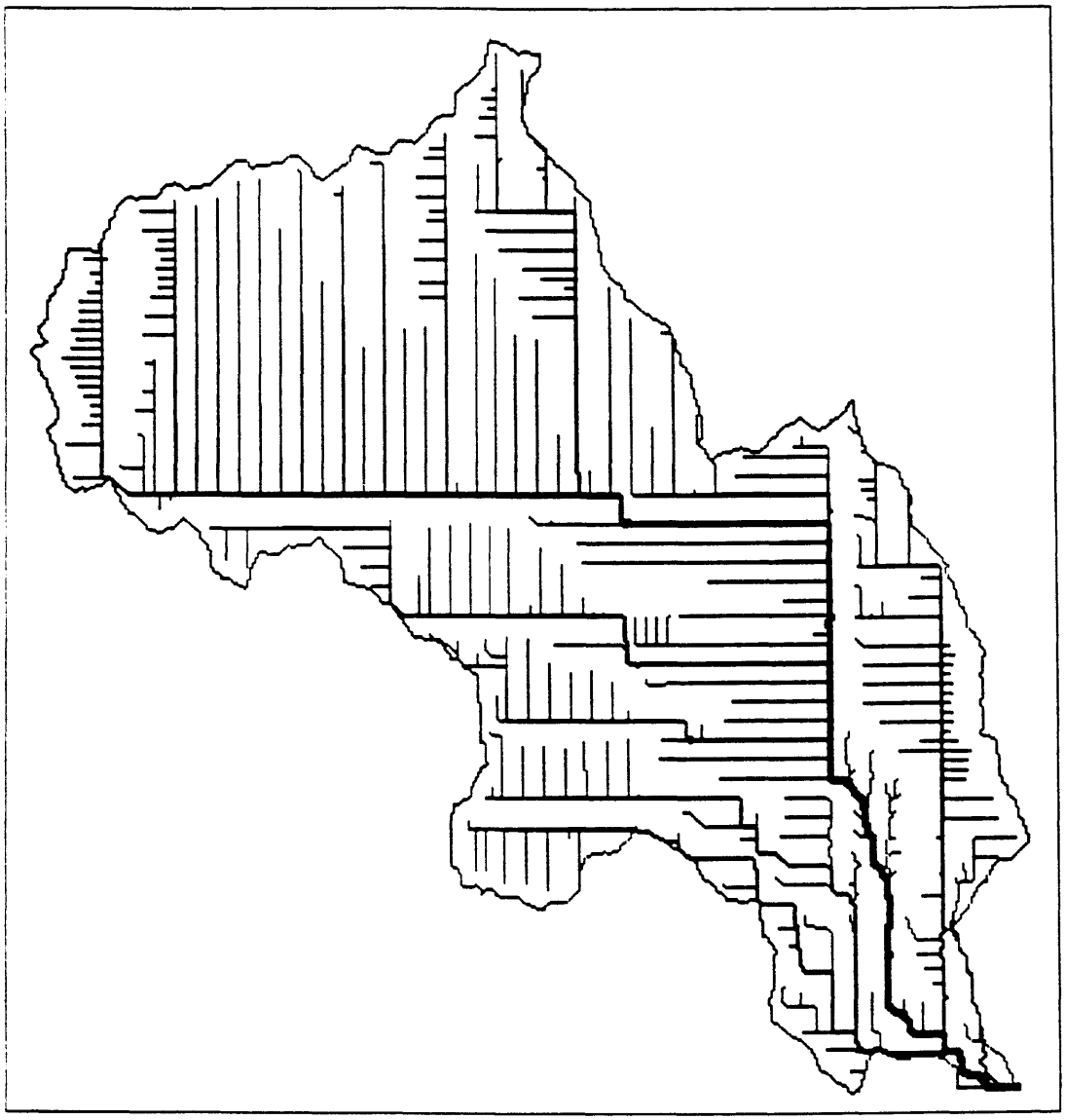

Figure 4-3: Simulated channel network - initial conditions: flat, no perturbations.

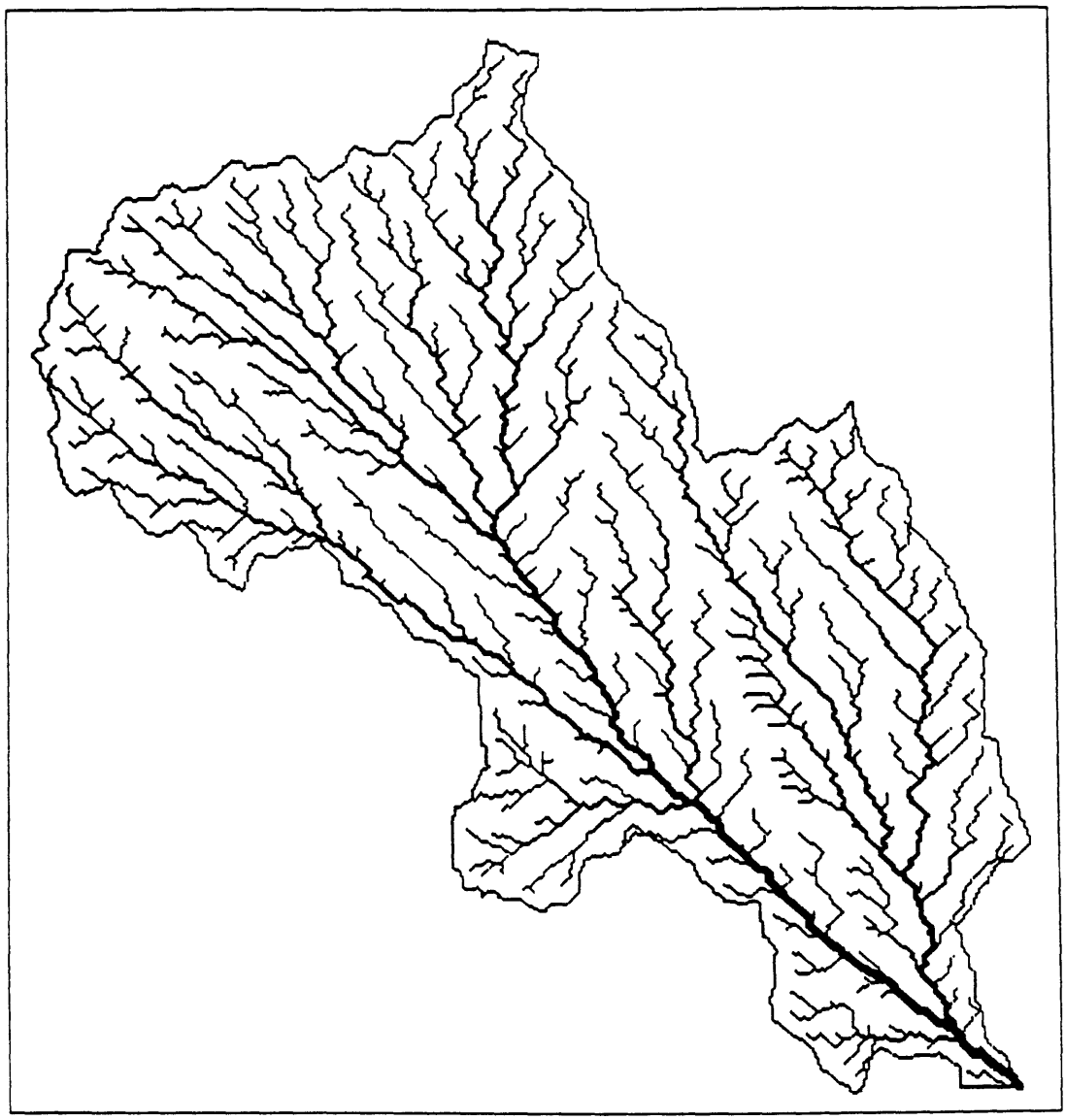

Figure 4-4: Simulated channel network - initial conditions: flat, with perturbations.

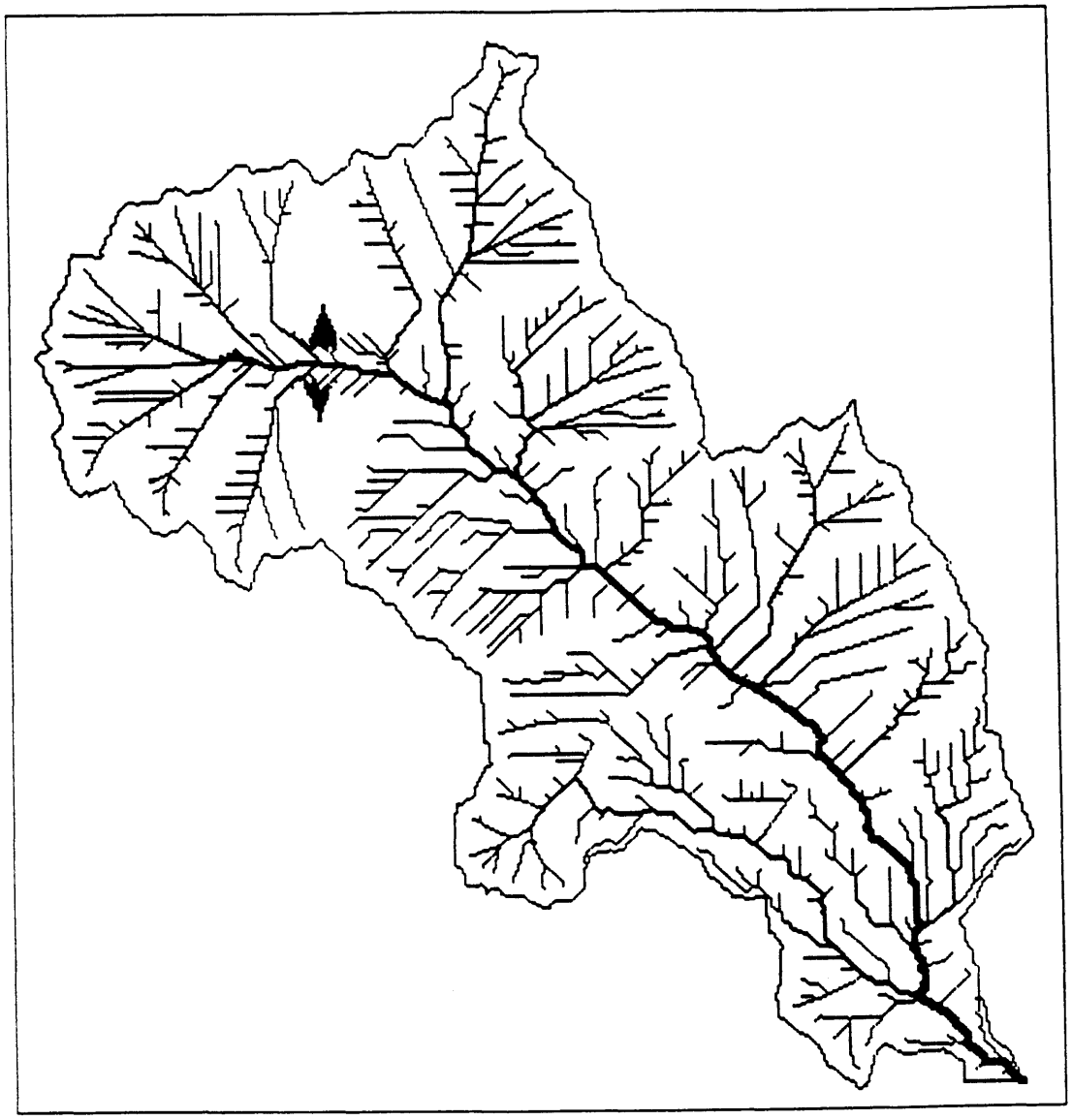

Figure 4-5: Simulated channel network - initial conditions: drum, no perturbations.

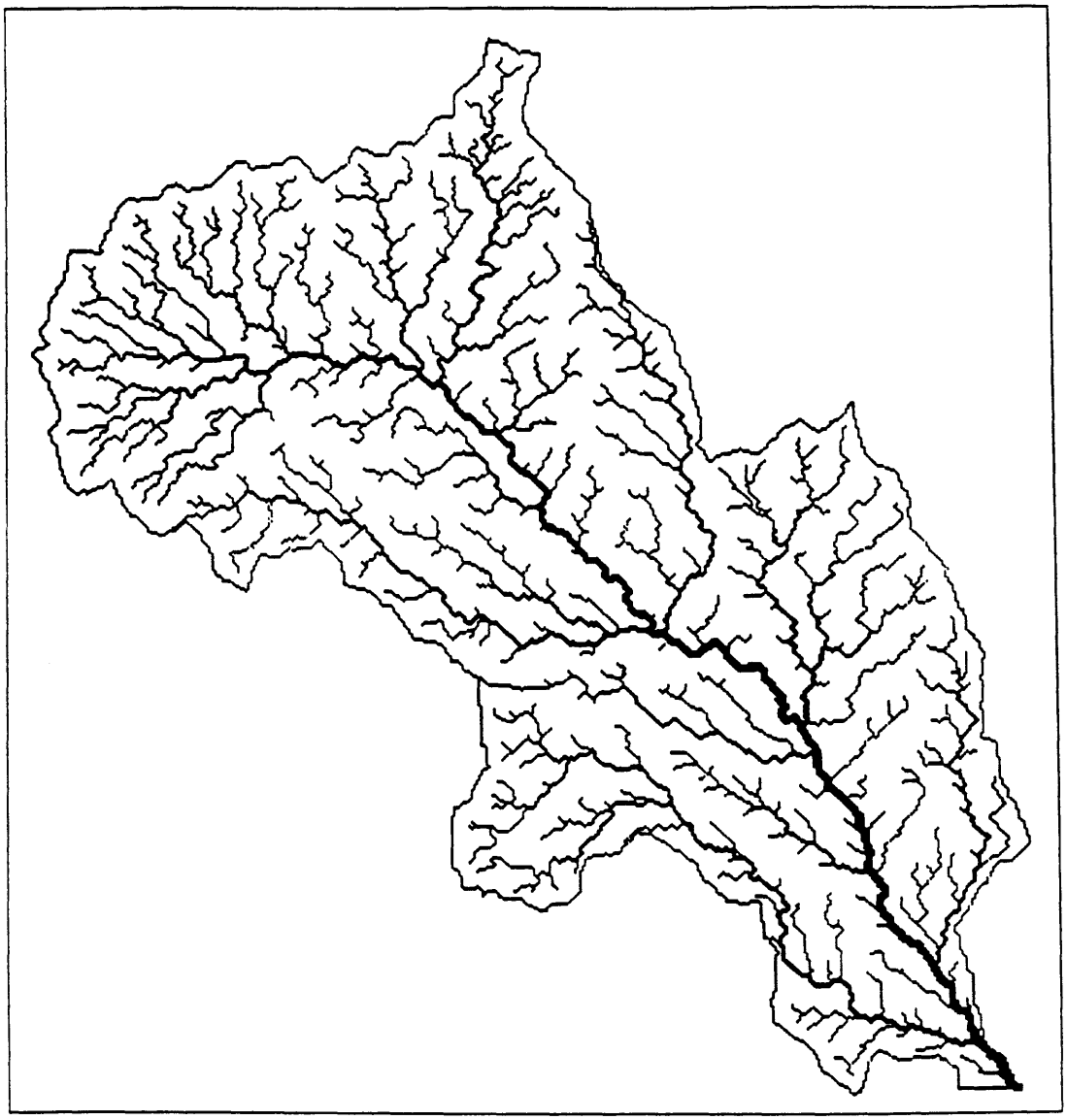

Figure 4-6: Simulated channel network - initial conditions: drum, with perturbations.

more realistically organized than the remainder of the basin. If the evolution history of the basin is examined it would be found that this region near the outlet is the site of competition and piracy which has led to this more natural appearance.

- **Simulated Network - flat, with perturbations (Figure 4-4):** The channel network is much more natural looking than in the previous simulation. However, channels are more elongated than in the observed simulation and confluences are characterized by acute junction angles. A northwest to southeast drainage direction dominates the basin, reflecting the general orientation of the outlet relative to the basin. Finally, the network doesn't seem to "feel" the presence of the basin divides until it is just upon them. Several cases of channels which trace along in an unrealistic path parallel to the divides are apparent.

- **Simulated Network - drum, no perturbations (Figure 4-5):** Because of its single main channel bisecting the basin and perpendicular drainage paths from divide to main channel, this network immediately seems more realistic than the previous two simulations. A closer examination, however, reveals that many smaller branches are too straight, without any small scale deviations from the drainage course to the main stream. This is due to the lack of perturbations in the initial elevation field which would have discouraged such straight drainage. The two triangular regions in the upper reach of the main channel are remnants of a large "lake" which had collected there since all points in this region are located a similar distance from the basin divides and therefore have similar initial elevations. The evolution model eventually captured this lake and bisected it into two smaller ones.

- **Simulated Network - drum, with perturbations (Figure 4-6):** This is probably the most realistic simulation although some degree of perpendicularity of drainage (from divide to main channel) seems to have been lost in comparison with the observed network. In this respect the simulation with drum initial conditions and no perturbations was better at reproducing the perpendicular drainage observed in the actual channel network.

There are two overall differences that are true for all simulations as compared to the observed network. First, the actual network is characterized by larger, continuous unchannelized regions, whereas the simulations seem to more evenly cover the entire basin allowing only smaller continuous hillslopes. This is achieved despite very similar drainage densities. The other difference results from the headward growth assumption of the evolution model. This assumption has the tendency to force all drainage paths to point back towards the outlet. There is little of this tendency exhibited in the actual network. In fact, many branches drain in a northerly direction, counter to the direction of the ultimate basin outlet.

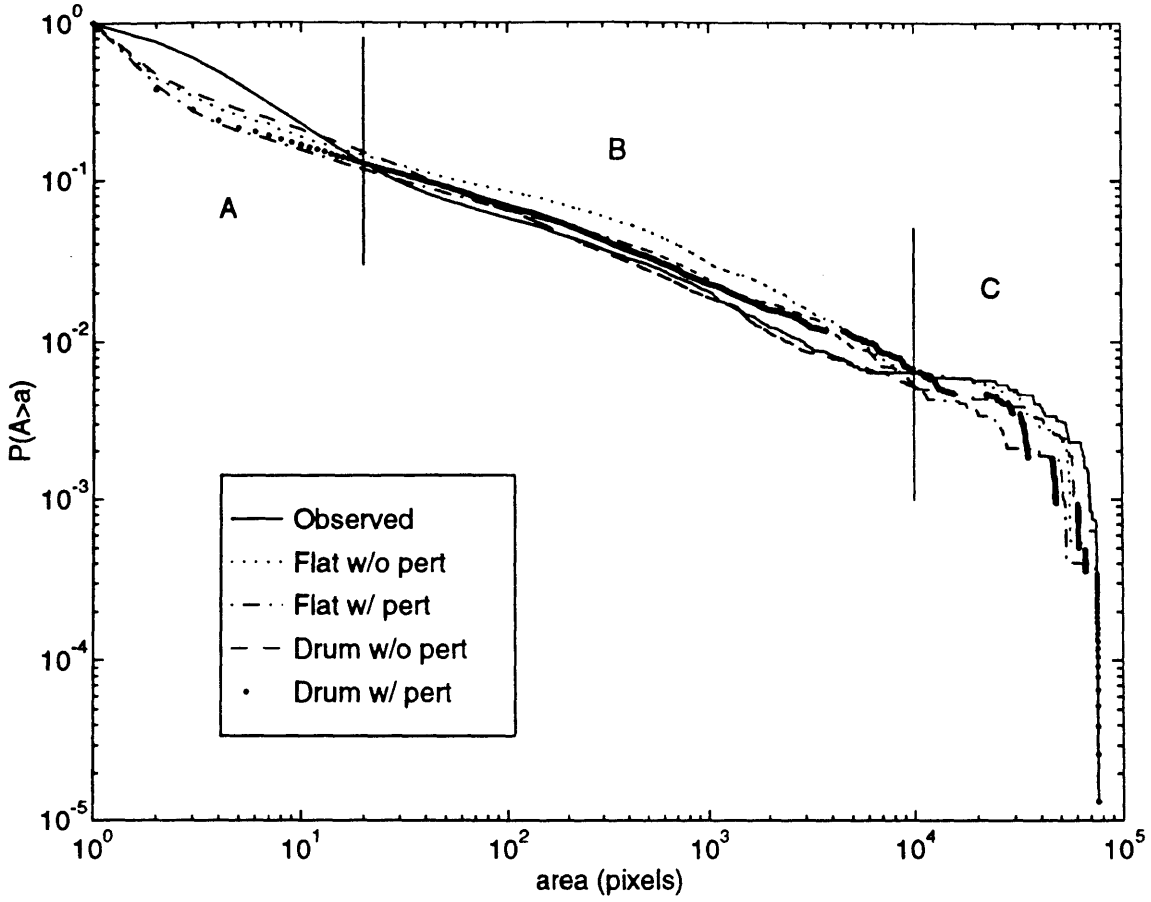

Figure 4-7: Observed and simulated cumulative area distributions for Nelk drainage basin.

4.3 Results: Quantitative Observations

The measures provided in Chapter 4 may now be applied to quantify differences between each of the systems illustrated in Figures 4-2 through 4-6.

4.3.1 The Cumulative Area Distribution

Figure 4-7 shows the probability of exceeding a given cumulative area plotted against area in log-log scale. These curves are of the observed and simulated drainage basins shown previously. Before discussing differences between these curves let us first consider the meaning of the figure itself.

There are three regions of interest. Moving from small to large cumulative area, these regions are: $A < 20$ pixels (Region A), 20 pixels $< A <$ 10,000 pixels, (Region B), and $A >$ 10,000 pixels (Region C). Region A is dominated by small scale, primarily diffusive transport, hillslope processes. Region B is characterized by branched channel aggregation dominated by fluvial transport processes. Region C corresponds to the

Table 4.2: Slopes of cumulative area distributions in fluvially-dominated region (Region B).

Data Set	Slope for $1.5 < \log(A) < 3.5$
Observed	-0.5227
Flat w/o pert	-0.4950
Flat w/ pert	-0.4617
Drum w/o pert	-0.5707
Drum w/ pert	-0.4920

largest areas very close to the basin outlet. The precipitous decline in probability in this region is a function of domain constraints. For purposes here, Regions A and B will be of the most interest.

The dissimilarities between the observed and simulated curves in Region A indicate that the evolution model in not capturing hillslope scale aggregation patterns well. The exceedence probability associated with the interface between Regions A and B is approximately 0.1 to 0.2 for all systems (observed and simulated). In other words, 80% to 90% of the basin is draining cumulative areas less than 20, or 80% to 90% of the basin is comprised of hillslope pixels. This means that failing to capture the aggregation pattern indicated by the observed drainage basin is equivalent to failing to capture the aggregation pattern of the vast majority of the basin. This is true despite the rather insignificant looking difference indicated in Figure 4-7.

In contrast, there is relatively good agreement in Region B. The simulated distributions all demonstrate a similar slope to the observed distribution as shown in Table 4.2. This is remarkable since we know how different the various simulation channel networks are in appearance. The conclusion we draw is that the good agreement in the Region B aggregation pattern is owed not so much to a well calibrated model, but rather to the fact that most dendritic drainage patterns tend to reproduce the observed cumulative area distribution for cumulative areas corresponding to branched, channel network aggregation.

4.3.2 The Hypsometric Curve

Figure 4-8 shows the observed and simulated hypsometric curves for the Nelk drainage basin. All the curves are quite similar. The jaggedness of the observed curve is caused by the DEM data format which gives only integer values for elevation at 1 meter

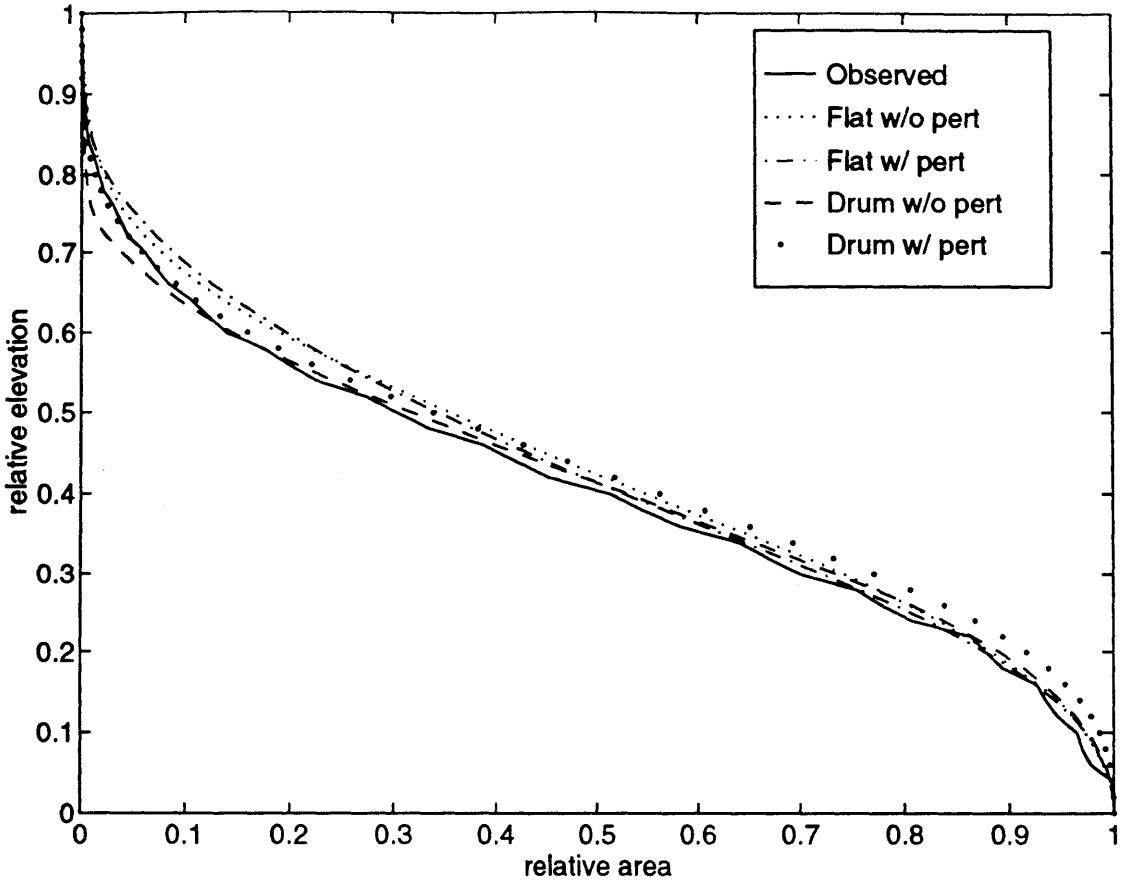

Figure 4-8: Observed and simulated hypsometric curves for Nelk drainage basin.

resolution. The discrepancies here are quite small and are difficult to measure.

The good agreement between the observed and simulated networks is a function of two things. First, we have imposed the observed slope-area relationship upon the simulations. Since the hypsometric curve and the slope-area relationships are both measures of the vertical behavior of the basin it is not surprising that such good agreement should exist. However, as we will see later in Chapter 7, it is probably that there is not significant stratification of soil types in this basin. Stratification of soils occurs during the natural process of deposition and leads to a basin which will exhibit different resistance to erosion as a channel incises. If this were the case for the current basin under study, the imposition of the slope-area relationship alone would not be enough to achieve good hypsometric curve agreement.

Although, the hypsometric curve appears to be a poor discriminator between systems in this set of simulations, this is not generally the case. This will be shown more explicitly in Chapter 7.

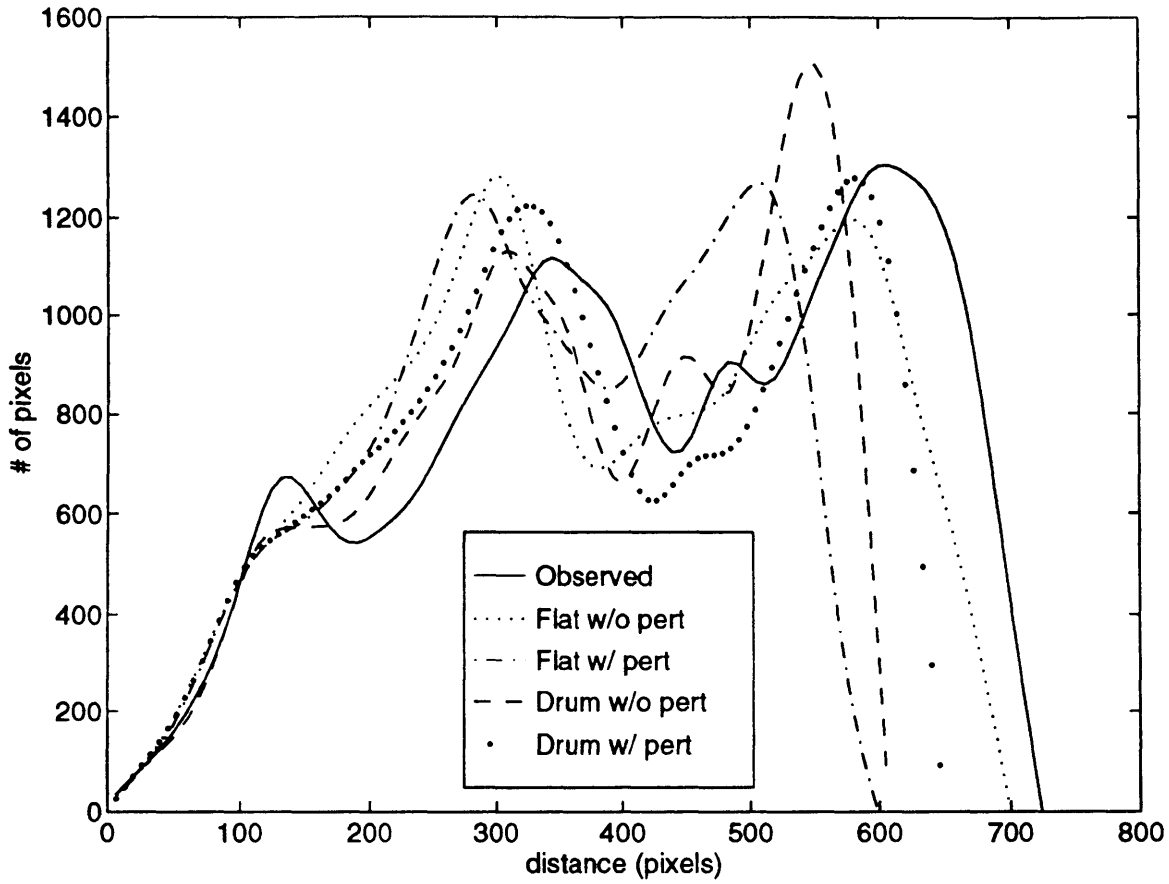

Figure 4-9: Observed and simulated smoothed width functions for Nelk drainage basin.

4.3.3 The Width Function

Figure 4-9 shows the smoothed width functions for each of pictured observed and simulated Nelk drainage systems. Again, we are using a cubic spline function to smooth the width functions corresponding to each system. The cubic splines preserve the total area under the width function while still conveying the primary information content of the original curve.

Comparison between the width functions for various networks is difficult since all exhibit roughly the same shape. The primary observable difference is the total distance spanned by each width function. For each system, this distance is indicative of how long it takes for the most hydrologically remote pixel to contribute runoff to the outlet. The more direct flow patterns described by the channel network, the shorter the distance that the most remote pixel is removed from the outlet.

Table 4.3 shows the mean and maximum travel distance associated with each width function. The longest mean travel time is exhibited by the observed network while the shortest is produced by the "Drum w/o pert" simulation. It is reasonable that the

Table 4.3: Width function statistics.

Data Set	Mean Distance (pixels)	Maximum Distance (pixels)
Observed	420.5	724.3
Flat w/o pert	385.7	699.7
Flat w/ pert	342.4	606.8
Drum w/o pert	365.9	605.1
Drum w/ pert	374.4	670.2

"Drum w/o pert" case produces the smallest mean since examination of Figure 4-4 shows very direct drainage paths from all points in the network to the outlet. Likewise, the observed network contains a main stream which takes a winding course through the basin and has some flow directions which (as previously mentioned) initially drain away from the basin outlet before joining the main channel. It is noteworthy that the width function of the "Flat w/o pert" case is both reasonable in shape and has comparable statistics to those of the other simulations. This case produced the mean distance that is most similar to that of the observed value although all simulations exhibit mean distances smaller than those of the observed system.

The width function is of value in discriminating between the observed system and the simulations. This is indicated by the systematically shorter travel distances of the simulations when compared to the observed system. The width function, however, does not seem to capture visually observable differences in the channel network structure. Each of the systems analyzed has an observably different structure yet the shape of the width functions themselves and the means and maxima of these distributions do not vary considerably. The shape of the width function seems to be controlled by the basin shape. Since all the systems drain the same basin, their width functions are constrained to be comparable in this regard.

4.3.4 Horton Ratios

The Horton bifurcation, length, and area ratios were calculated for the observed and simulated systems. These values are tabulated in Table 4.4. The bifurcation ratio value was determined two ways. The first way is to perform a simple log-log regression with number of streams plotted against order. This gives the value of R_B (free) shown in the table. The second way is to constrain the regression line to go through unity at the highest order stream since all drainage systems must, by definition, have only

Table 4.4: Horton ratios for observed and simulated networks.

Data Set	R_B (free)	R_B (fixed)	R_L	R_A
Observed	4.1496	3.9389	1.8220	4.1441
Flat w/o pert	4.7634	3.9042	1.8630	5.1129
Flat w/ pert	4.5851	4.1207	2.1296	4.8241
Drum w/o pert	4.5575	4.1503	2.1626	4.8621
Drum w/ pert	4.5664	4.1517	2.2168	4.7101

one highest order stream. This gives the value for R_B (fixed).

Although Table 4.4 clearly shows some degree of variation for these measures, all values fall within recognized and acceptable ranges for observed channel networks. Some general observations can be made. In every case but one (R_B fixed for "Flat w/o pert") the simulated network Horton ratio is greater than the observed ratio for that quantity. Among the simulated networks, the "Flat w/o pert" network produced measures for the R_B (free) and R_A that deviated the most from those measures of the observed system. This stands to reason since this network was visually the most different and unrealistic of all the simulations. Interestingly, it is the same network that produced the two closest matches with the observed (for R_B (fixed) and R_L). Finally, all networks were of order, $\omega = 8$, resulting in large standard errors in the regressions to determine the value of a particular Horton ratio. This makes any comparison between measures tenuous, at best. Despite the many qualitative differences cited earlier, these results indicate that the Horton ratios are not effective in quantifying them. There are differences between the Horton ratio's determined, but they are not large, especially among the simulated systems. That the "Flat w/o pert" simulation produces reasonable statistics at all damages the credibility of Horton ratios to yield any meaningful information about a network. The results here reinforce Shreve's (1966) and Kirchner's (1993) notions that Horton's ratios are statistical artifacts of topological constraints on a dendritic channel network.

4.3.5 Energy Dissipation

The energy dissipation as defined in Chapter 2 was determined for the observed and simulated basins. These values are shown in Table 4.5. Equation 2.11 was used to generate this table. As discussed earlier in this chapter, dynamic equilibrium was artificially imposed in Step 2 of section 4.1. This makes the slopes, by definition, scale

Table 4.5: Energy dissipation values for the study networks.

Data Set	Total Energy Dissipation
Flat w/o pert	418,400
Flat w/ pert	407,200
Drum w/o pert	389,900
Drum w/ pert	414,200

proportional to $A^{-0.5}$ which was the exact assumption used to transform equation 2.10 to 2.11.

The energy values shown in Table 4.5 do not vary greatly. The smallest value, corresponding to the "Drum w/o pert" case is still 93% of the largest value, corresponding to the "Flat w/o pert" case. What kind of system would minimize the sum described by equation 2.11? From an OCN standpoint, it appears that a system which favors a single main stream tends to produce a smaller sum. Additionally, direct drainage to the main stream is important to minimize this sum even more. Not surprisingly, the "Drum w/o pert" case produces the minimum sum among the simulations since the drum condition essentially imposes a single main stream, and the lack of small surface perturbations provides for straight, direct drainage to the main stream.

The observed system is comprised of hillslopes and channels. The hillslopes make up a large portion of the basin and but do not scale with $A^{-0.5}$ as indicated for $A < 10 - 20$ pixels in Figure 4-1. Hence, the use of equation 2.11 is inappropriate. On the other hand, using equation 2.10 will produce biased results because resolution limitations yield many pixels with zero elevation drop.

Our objective is to illustrate the application of several geomorphic measures to observed and simulated networks. In so doing, the goal is to find measures which effectively quantify differences between simulated and observed drainage networks. From these results, it appears that energy dissipation would not be an effective measure since all the simulated systems have quite comparable values, and direct comparison of energy values is hampered by slope scaling issues in hillslopes and channels.

4.4 Conclusions

This chapter illustrated the application of the slope-area relationship, the cumulative area distribution, the hypsometric curve, the width function, Horton's ratios, and the

energy dissipation function to a series of simulations of a large river basin. The slope-area relationship was not measured for each of the simulations, but rather, used with each simulated domain in the form of an imposed dynamic equilibrium constraint. Imposing this rule had the effect of causing very good agreement between each of the simulations and the observed hypsometric curve. The cumulative area distribution indicated that none of the simulations were adequately reproducing the aggregation structure of the observed system at the hillslope scale. The width function showed that the observed system is characterized by longer travel distances to the outlet than any of the simulations. Horton's ratios and the energy dissipation function were note effective in discriminating among qualitatively different looking systems.

These results indicate that the slope-area relationship, the hypsometric curve, the cumulative area distribution, and the width function are valuable measures of the basin organization. Although its importance was not explicitly demonstrated, the imposition of the slope-area relationship throughout this chapter was used to generate a realistic linkage between the horizontal and vertical dimensions. Additionally, by the imposition of the slope-area relationship, the agreement between observed and simulated hypsometric distributions was largely imposed. Had this not been done, the hypsometric distributions might have varied considerably indicating the value of this measure as an effective discriminator. The remaining measures: the cumulative area distribution and the width function quantify more horizontal organization characteristics and were shown to vary in a systematic way from the observed system's measures. These results indicate that the small scale organization and the overall travel distances to the outlet of the simulated systems must be improved and that these measures will be useful in verifying that such improvement has been achieved.

The measures considered and illustrated here do not constitute an exhaustive list of geomorphic quantities. Other quantities, most notably fractal and multifractal measures, could be applied as well. We have chosen to use the masures outlined above because we felt that they adequately quantified different characteristics of drainage basins both in the planar and vertical dimensions.

Finally, this chapter illustrated how the structure of the initial conditions produced fundamentally different looking drainage basins. The simulations performed here indicate that trends in the initial elevation field are evident in the ultimate drainage structure. This was true both at the small scale (through the presence or lack of small perturbations in elevation) and at the large scale (through a flat or "drum" trend to the initial topography).

Chapter 5

Evaluating Model Behavior in Basic Topographic Elements

This chapter will employ the basin evolution model to examine the effects of parameter selection and the flow allocation method on two basic topographic elements: a 1-D hillslope profile, and a 2-D diverging hillslope (spur). In studying such simple systems we will address the issue of appropriate magnitudes for m and n in the fluvial erosion term of the evolution equation, and also compare the differences between single flow direction and multiple flow direction area accumulation algorithms. Simulated topography is sensitively dependent on these parameter and algorithm choices, yet there may be no physical basis for this dependency. This sensitivity is an artifact of the modeling procedure itself. This chapter will document these artifacts and will develop criteria for minimizing their influence on simulated drainage basins. These criteria will be applied in the remaining chapters, especially where issues of parameter estimation are concerned.

5.1 Hillslope Profiles

Hillslope profiles provide a basic geomorphic feature which is instructive to study. A hillslope profile is a slope draining an unchannelized area which aggregates flow only in the longitudinal direction (in the direction of flow). This sort of topographic element will be found in regions where flow directions are predominantly parallel, with neither diverging nor converging flow paths.

At dynamic equilibrium equation 3.13 in Chapter 3 shows that the ratio m/n governs the slope-area scaling exponent, θ. This indicates that it is not the absolute magnitude of either of these exponents, but rather the ratio of these two that controls the fluvial portion of the slope-area relationship. Also from equation 3.13 the multiplicative factor:

$$k = \left(\frac{U}{\beta}\right)^{1/n}$$

controls the slope steepness with area. Given these relationships, an infinite number of sets of values $\{\beta, m, n\}$ can be determined which result in the same fluvial scaling

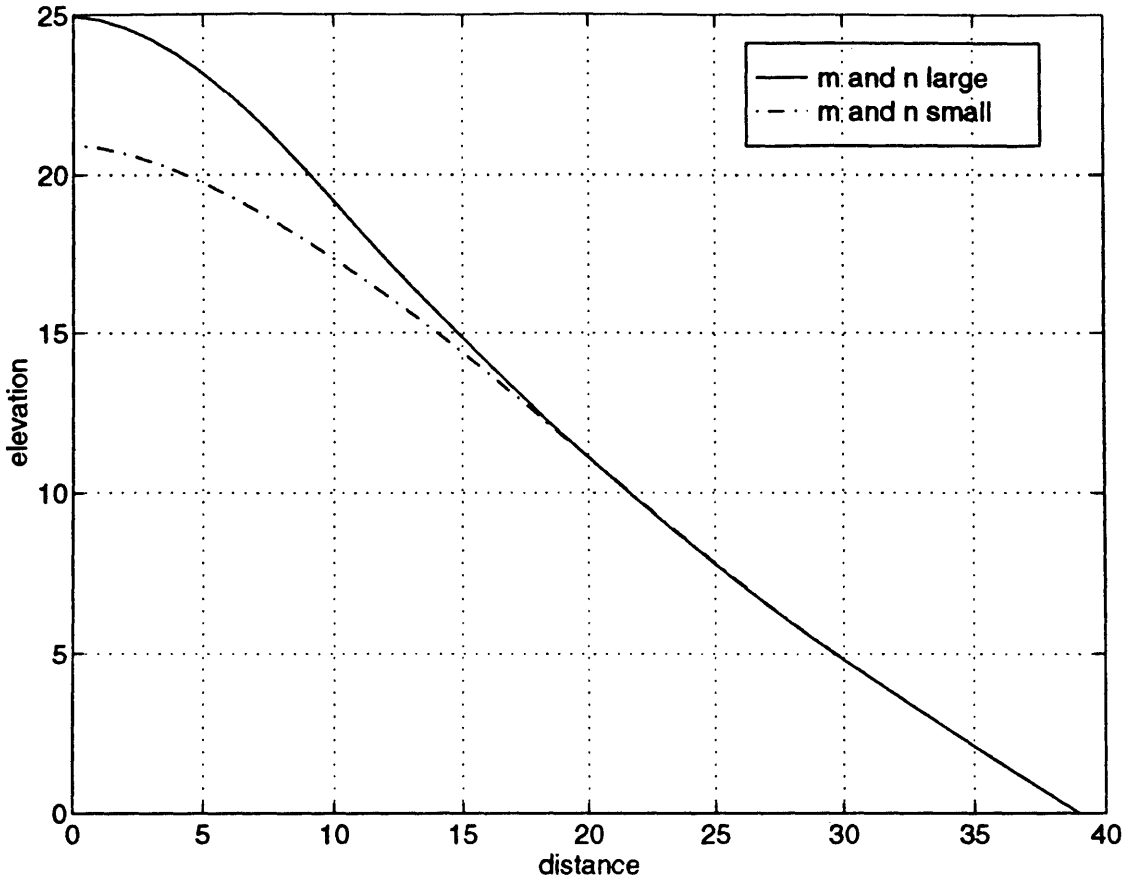

Figure 5-1: Hillslope profiles generated for β, m, and n values which yield theoretically identical behavior.

asymptote. Two such sets of values are: {0.01, 1.0, 2.0} and {0.063, 0.2, 0.4}. Figure 5-1 shows the resulting slope profiles for these two parameter sets. Although both figures were generated with parameters which yield the same theoretical fluvial behavior, the resulting profiles differ in the convex (diffusion dominated) portion of the hillslope. This occurs despite the use of the same value of the diffusion coefficient, $D = 0.1$. Why are the profiles different? Figure 5-2 shows the slope area relationship for these two parameter sets. This figure implies that, although both systems obey the same asymptotic behavior, the system with the smaller values of m and n exhibits slopes which are smaller than those due to either pure diffusive or fluvial equilibrium over a broader range of areas. The systems with the larger m and n values exhibits almost pure diffusive or fluvial equilibrium except over a much smaller range of areas. Figure 5-3 shows schematically the effect of increasing m and n on the slope-area relationship.

Figure 5-4 shows the fraction of diffusive erosion/total erosion for each of the two systems pictured in Figure 5-1. The reach over which diffusion contributes to a significant fraction of the total erosion is contained to the upper portion (the convex

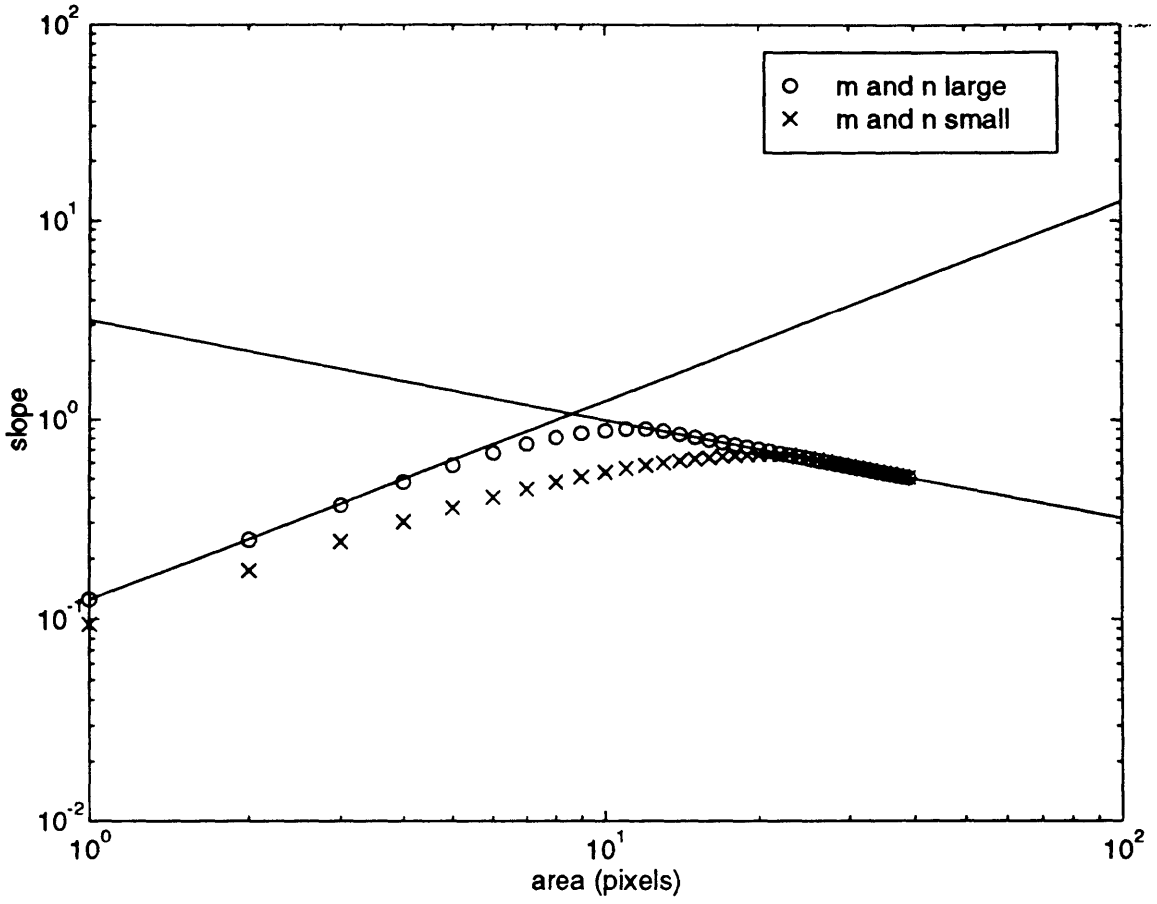

Figure 5-2: Slope-area relationship for hillslope profiles with β, m, and n values which yield theoretically identical behavior.

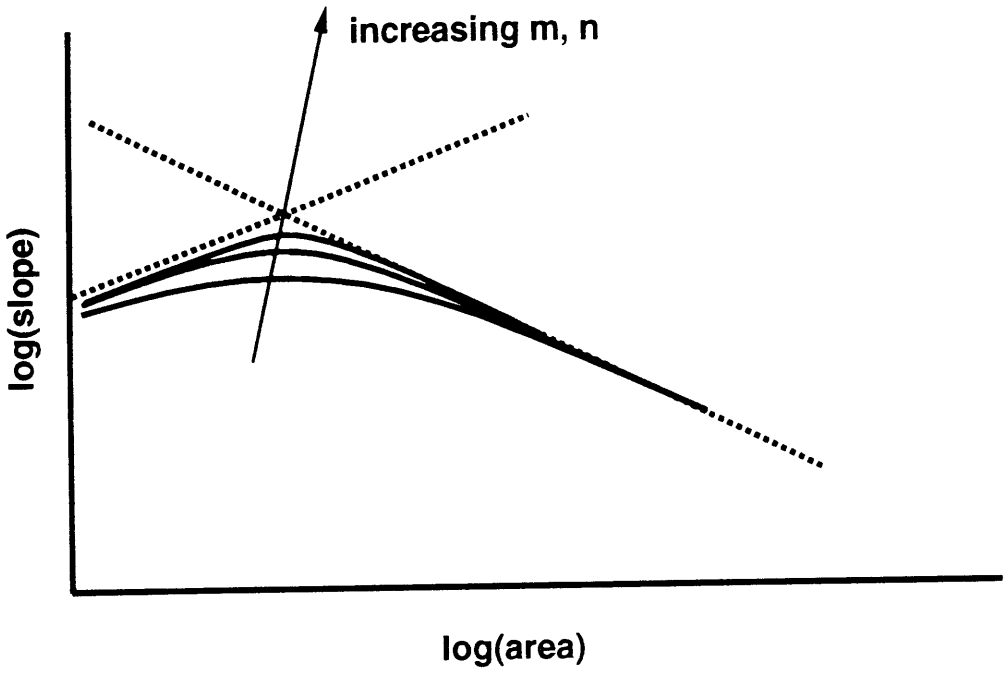

Figure 5-3: Effect of increasing m and n on slope-area relationship.

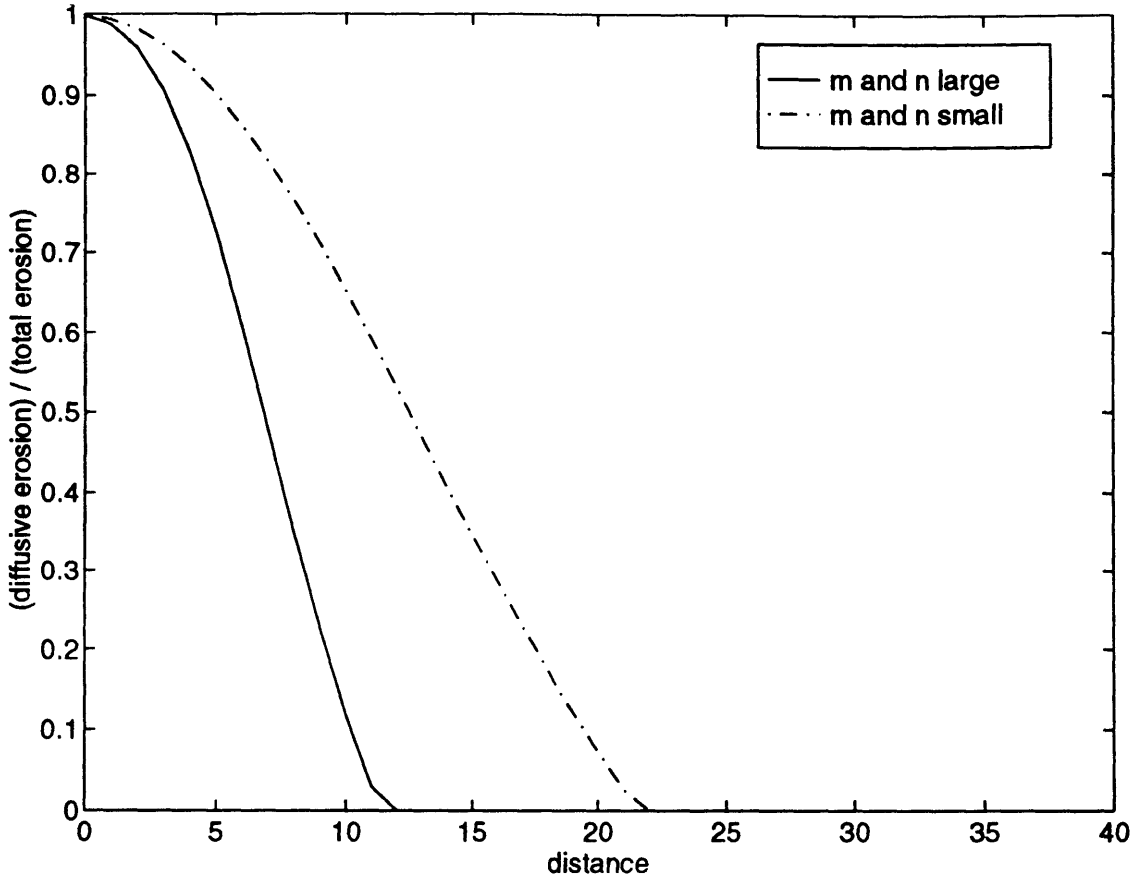

Figure 5-4: Fraction of contribution to dynamic equilibrium from diffusive transport term for hillslope profiles with β, m, and n values which yield theoretically identical behavior.

part) of the hillslope profile. Fluvial erosion makes up the remainder of the erosion at each point. Notice that the system with m and n small has a much greater range (longer transition reach) over which the diffusive transport term is a significant percentage of total erosion. Thus, the effect of using smaller values of m and n is to increase the range over which diffusive transport is effective within a system. This happens because as m and n get smaller, the dependence of the fluvial transport term on cumulative area is diminished and the so-called fluvial transport becomes more like a second form of diffusive transport.

5.1.1 Equivalent Diffusion: $D(n)$

Given that we observe this enhanced diffusive transport as m and n decrease, it is possible to define an equivalent diffusion parameter, $D(n)$ where there is now an explicit dependence of D on n. (Recall that m is also related to n from $\theta = -m/n$.) Owing to the non-linearity of the evolution equation, it is not possible to analytically

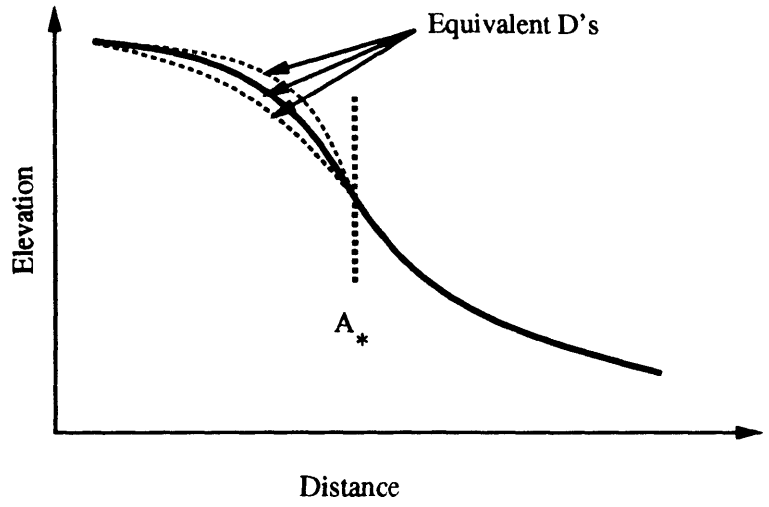

Figure 5-5: Equivalent D values shown for an arbitrary slope profile.

determine values of D for various m and n that will lead to exactly identical hillslope profiles. Nevertheless, it is still useful to define some equivalency criteria so that we can quantify how D is a function of n. We will use those values of D which yield the same elevation drop between the top of the hillslope and the point, A_* the point of inflection along the hillslope profile. This definition is illustrated in Figure 5-5.

An iterative search procedure using the basin evolution model was employed to determine the relationship between n and D over a range of values for n. This relationship is shown in Figure 5-6 for two different values of A_*. This figure illustrates that as n decreases, the value of the diffusion coefficient, $D(n)$ needed to achieve a fixed amount of elevation drop decreases. In addition, Figure 5-6 illustrates that as n gets larger, the sensitivity of D to n grows smaller. For $n \geq 2$ the value of D is changing quite slowly.

Admittedly, this definition of equivalent diffusion is arbitrary. However, the effect being documented is real and is due to the longer transition reach associated with smaller values of m and n. Any definition which attempts to quantify the effect of this longer transition reach on simulated topography will result in a similar relationship for $D(n)$.

5.1.2 Choosing an appropriate m and n

Given that the magnitude of m and n influence the role of diffusion within the basin evolution model, what is an appropriate range for these parameters to use? There are two ways to answer this question. First, the literature (See Figure 2-1 typically quotes values ranging from 0 to 3 for m and 1 to 3 for n. The value for both parameters tends to increase with the scale of the process being modeled. For example, ($m = 0$, $n = 1$) is precisely the diffusive term used in our evolution equation and has been found to

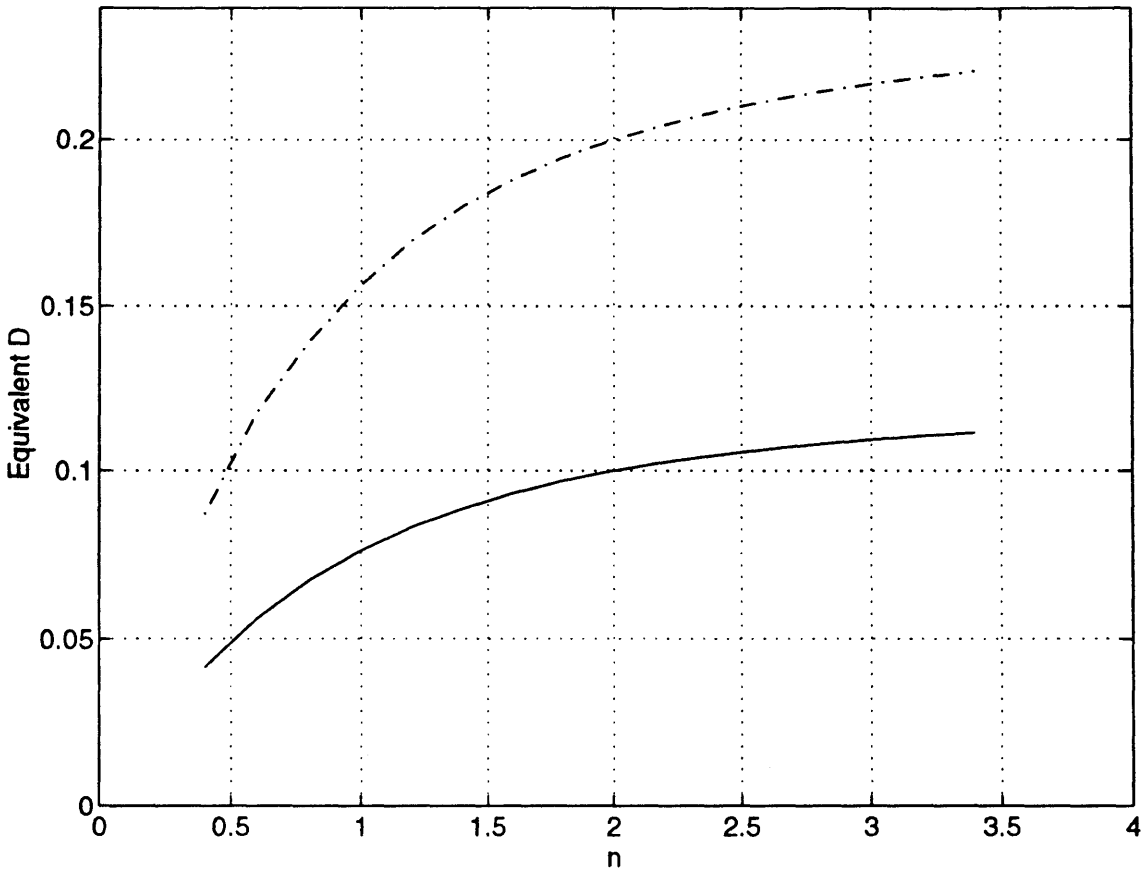

Figure 5-6: Relationship between n and D for $A_* = 5$ (solid line) and $A_* = 8$ (dashed line). A value of $m/n = 0.5$ is used in throughout.

correspond well to soil creep and rainsplash processes. A value of $n = 2$ appears applicable over a wide range of larger scale processes including soil wash and rivers. The value of m varies over a broader range of values because of the increasing nonlinear dependence on area at these scales.

The second way to answer this question is simply from a standpoint of numerical sensitivity. There is a strong degree of sensitivity of the generated profiles on the magnitudes of m and n when these exponents are small (i.e. both parameters less than 1.0), but as these parameter values increase, the simulated profiles converge towards a single solution. Evidence of this convergence is shown in Figure 5-7. The solution that is being converged upon is that represented by the pure diffusive and pure fluvial asymptotes pictured in this same figure. There is little change in the solution between the systems with $m = 1$, $n = 2$ and $m = 2$, $n = 4$. Likewise, the profiles that are generated differ very little. This is equivalent to the results in the previous section which showed that $D(n)$ was not strongly sensitive to n for values greater than 2. Given this decreased sensitivity to fluvial transport exponents and the support of reported values in the literature, we will hereafter use $n = 2$ and select m such that the desired value of θ is produced.

5.2 Hillslope Spurs

Hillslope spurs are the second drainage element we will consider. A hillslope spur will be found located between two channels and their point of confluence. Spurs characteristically are sites of *diverging* flow paths. Such a configuration is depicted in Figure 5-8. Two drops of water originating at almost identical locations will tend to flow *away* from one another as they travel downhill. Not surprisingly, a hillslope spur becomes an ideal feature upon which to compare differing flow allocation algorithms.

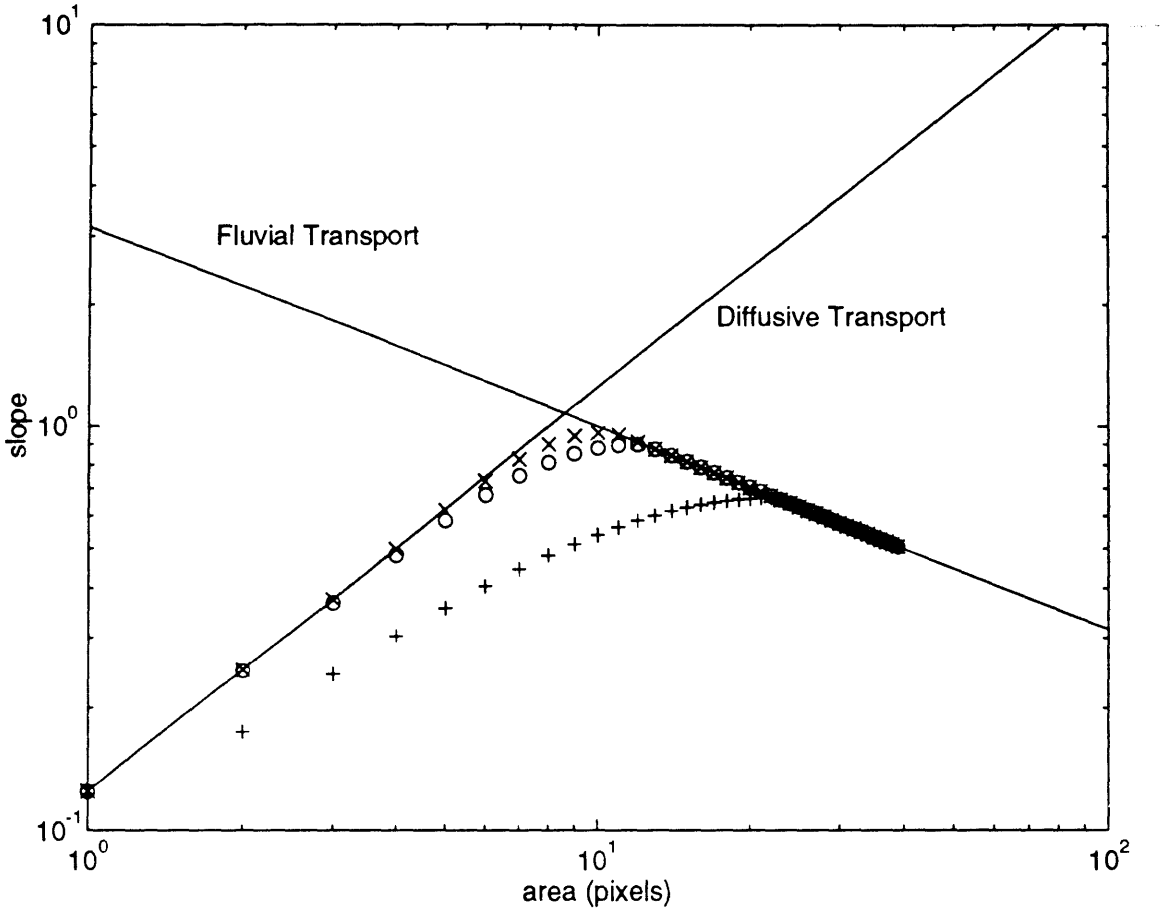

Figure 5-7: Convergence of slope-area relationship to diffusive and fluvial transport asymptotes. With (β, m, n): "+": (0.063, 0.2, 0.4), "o": (0.01, 1.0, 2.0), and "x": (0.001, 2.0, 4.0).

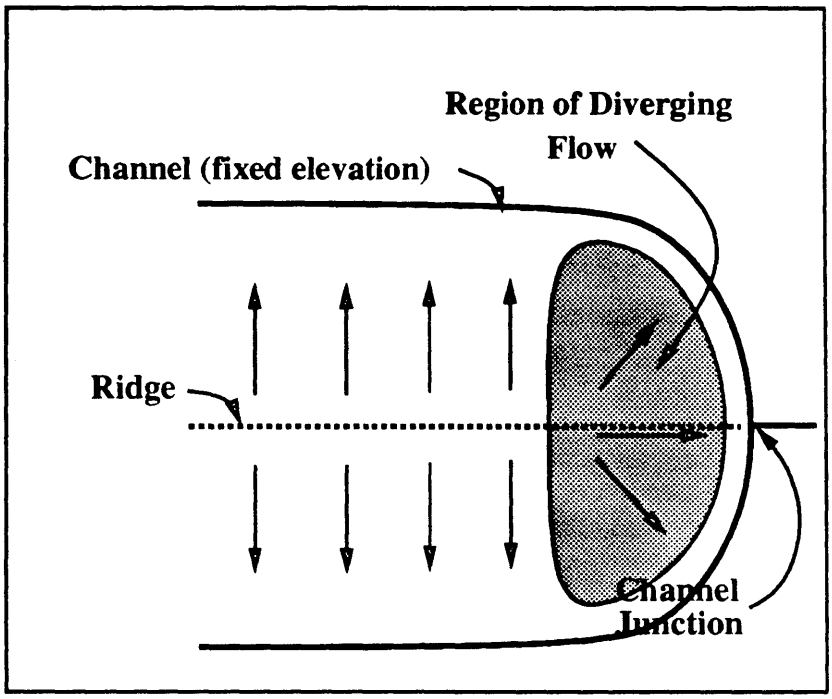

Figure 5-8: Definition sketch of a hypothetical hillslope spur.

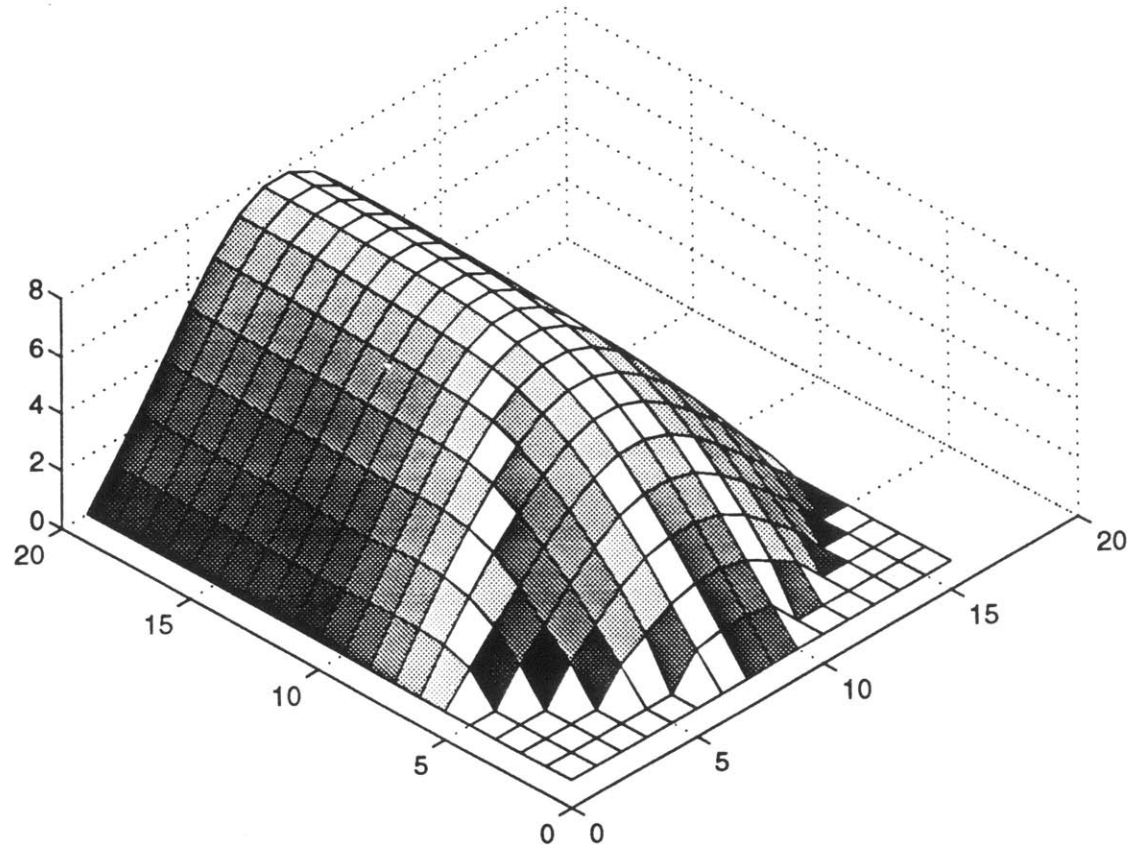

Figure 5-9: Hillslope spur generated using single flow direction algorithm. Shading of each pixel is proportional to drainage area.

5.2.1 Consequences of Flow Algorithm

Figures 5-9 and 5-10 show hillslope spurs generated under identical conditions except for the use different flow allocation algorithms. Figure 5-9 was generated using the single flow direction (SFD) algorithm which assigns all flow from a given pixel to the one pixel downhill of it which lies in the direction of the steepest slope. Figure 5-10, in contrast, was generated using the multiple flow direction (MFD) algorithm which assigns flow to each downhill pixel in proportion to the slope in each direction. Both figures are shaded in proportion to the drainage area flowing through each pixel. Comparison between the figures indicates that the drainage areas in the region of diverging flow paths are quite different. The SFD surface is characterized by white "streak" lines where cumulative drainage area seems suspiciously small, and disproportionately dark pixels where the drainage area is suspiciously large (black pixels at 45 degrees to the ridge line). In comparison, the MFD surface exhibits an even distribution of increasing area as flow accumulates downhill.

To appreciate the differences these flow algorithms cause, it is informative to

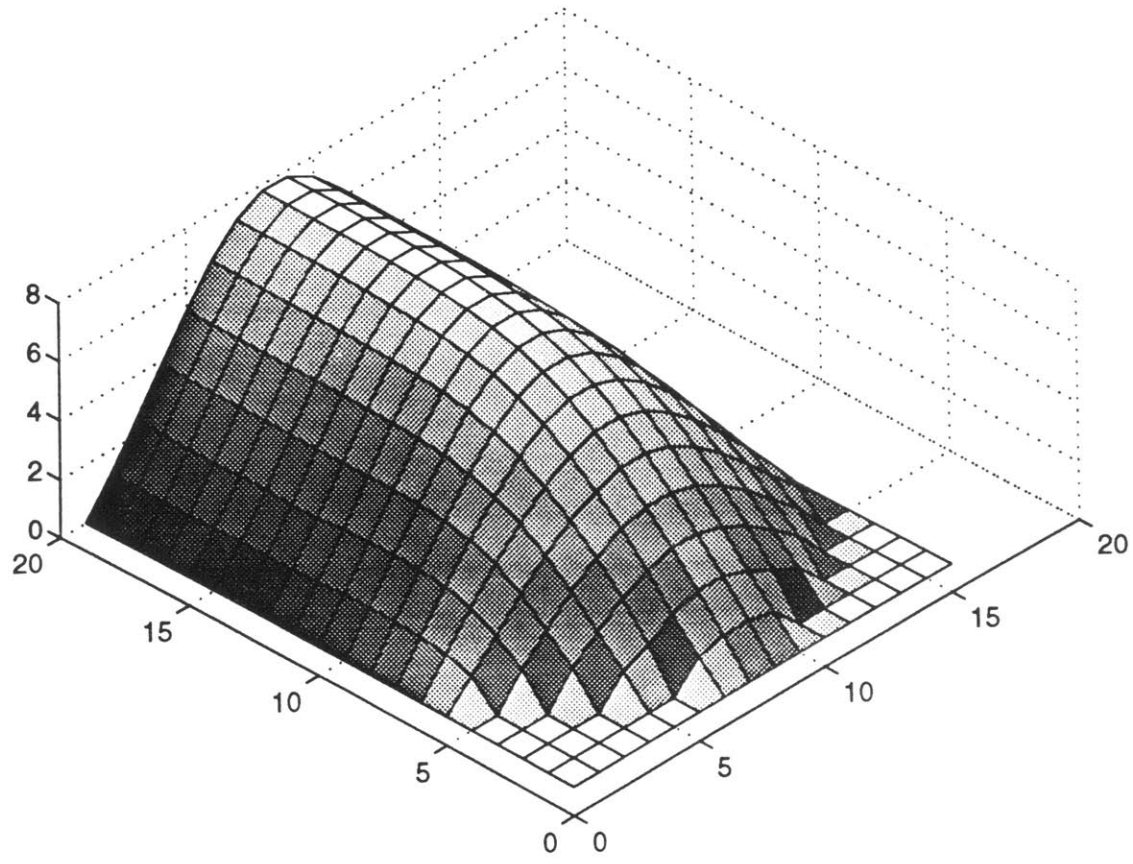

Figure 5-10: Hillslope spur generated using multiple flow direction algorithm. Shading of each pixel is proportional to drainage area.

analyze the residual elevation difference between the two simulated spurs pictured in Figures 5-9 and 5-10. Let us define a new surface, $\mho$:

$$\mho(i,j) = \frac{z_{SFD}(i,j) - z_{MFD}(i,j)}{\Re_{spur}} \tag{5.1}$$

where the numerator is simply the difference between the MFD and SFD generated spur surfaces and the denominator is the total relief of either system (both systems have the same overall relief to within 0.07%). Thus, $\mho$ gives the percent difference between the two spur surfaces. Figure 5-11 shows a perspective plot of $\mho$ with the shading of the figure proportional to the SFD generated cumulative area. The largest errors (approximately 3% to 4%) occur in the region of diverging flow. In addition, it is possible to discern a pattern to these errors. First, all the errors are positive, indicating that the SFD generated spur was everywhere greater in elevation than the MFD spur in the region of diverging flow. Second, the errors are greatest where the shading of the surface is lightest. This is not surprising since shading is proportional to area, we would expect the lightly shaded areas on the SFD spur to be subject to less fluvial erosion than the corresponding points on the MFD spur.

One might argue that the 3% to 4% errors caused by the different algorithms are not large enough to be of concern. Consider that this experiment is constrained more rigorously than a typical evolution is: the boundaries which would normally correspond to movable channels are instead fixed in elevation. Additionally, both surfaces were generated without any perturbations in the initial elevation field. These constraints allow for very direct measurement between the generated systems, but act to diminish differences between the surfaces. In an actual simulation, any irregularities present in the initial elevation field would be handled differently by the two area accumulation algorithms and would be amplified as the system evolved. Large differences would have a likely influence on channel growth and location. For these reasons we will employ the MFD algorithm in all future simulations and especially during the model calibration process.

5.3 Conclusions

This chapter employed two simple topographic elements: a hillslope profile and a hillslope spur to analyze the effect of parameter and algorithm choice on the basin evolution model. It was found that smaller values of m and n led to an effective increase in the amount of diffusive erosion present in a simulation. By defining equivalent diffusion and allowing m and n to vary, a relationship quantifying the value of the diffusion coefficient needed to produce a fixed amount of diffusion was developed. This relationship illustrated how the diffusion and the magnitude of m and n are interrelated. This $D(n)$ relationship and direct analysis of the slope-area relations for varying m and n indicated that the model became less sensitive for larger m and n. In consideration of this decreased sensitivity and also the reported values in the literature, it was determined that a value of $n = 2$ would be an appropriate choice. The parameter, m would then be determined by the desired value of θ for a given

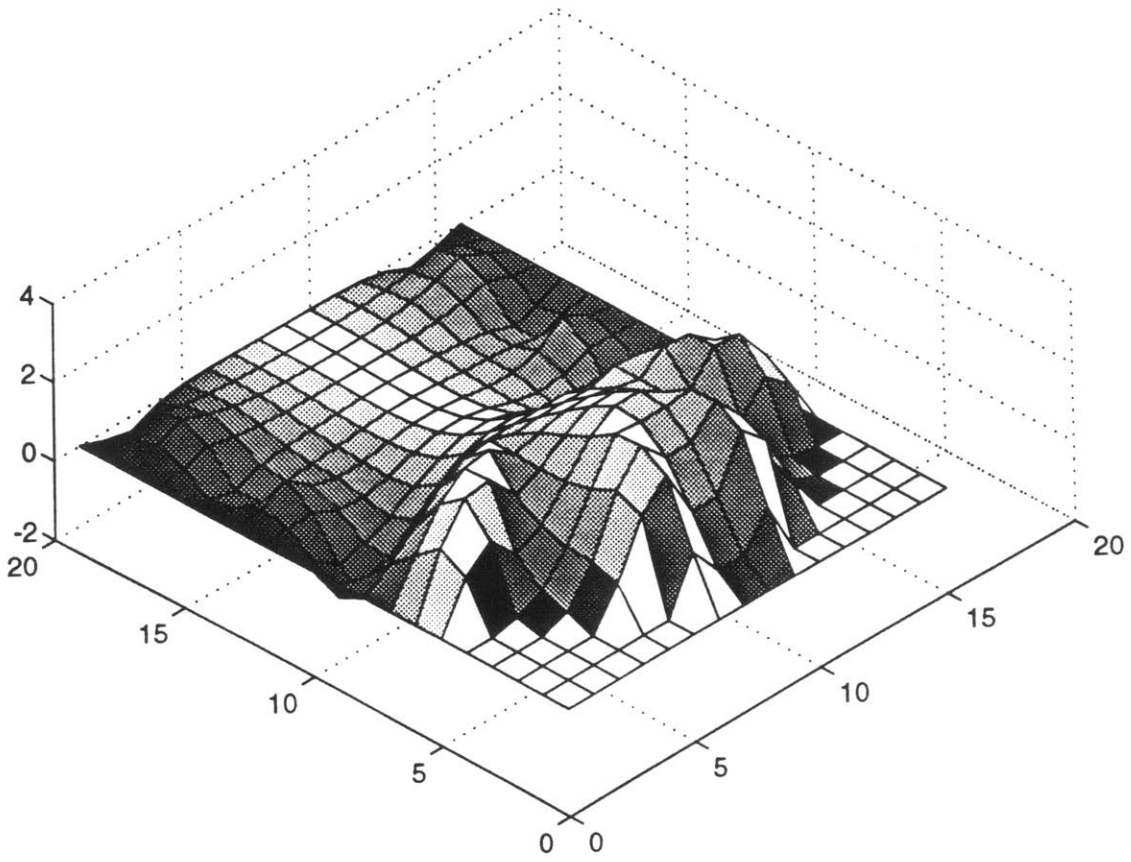

Figure 5-11: Percent difference between the SFD and MFD generated hillslope spurs. Shading of each pixel is proportional to SFD drainage area.

simulation.

A study of hillslope spurs was performed to compare the effects of the area accumulation algorithm on simulated topography. It was shown that both cumulative areas and ultimately the simulated elevation were dependent on the algorithm used. The MFD algorithm was shown to give a more evenly distributed representation of the cumulative areas along a smooth, diverging surface when compared to the SFD representation. For this reason, the MFD algorithm was chosen for use in all future simulations.

Chapter 6

Heterogeneity in Soil Erosivity

The presence of spatial heterogeneity is an integral part of almost all natural systems. To assume that soil material is eroded everywhere with the same degree of ease is to neglect that vegetation and geology play any role in affecting the topography. Tree and plant roots cling to the earth preventing slides and resisting wash. Sands, clay lenses, alluvial deposits, and countless other distributions of material are all subject to erosion at different rates. These are just a few examples of natural phenomena which induce spatial variability.

6.1 Implementation of Spatial Variability into the Model

The model presented here characterizes the spatial heterogeneity of erosivity in a very simple fashion. The erosivity of the material is assumed to be log-uniformly distributed in space as a white noise process. Thus the fluvial erosion coefficient, β varies as a function of space,

$$\beta_i = \beta_0 10^{\alpha\eta_i} \tag{6.1}$$

and likewise for the diffusion coefficient,

$$D_i = D_0 10^{\alpha\eta_i} \tag{6.2}$$

where β_0 and D_0 are some nominal fluvial and diffusive transport coefficients, η_i is a uniformly distributed property on [-0.5,0.5] which characterizes the spatial variability of soil "softness" at location, i, and α is a parameter which controls the variance of the erosion heterogeneity. The values of α and η_i are the same in equations 6.1 and 6.2. If $\eta_i < 0$ then the material is more resistant to erosion than average, while $\eta_i > 0$ corresponds to material that is more readily eroded. As α increases the material grows more variable in its resistance to erosion. When α=0 the material is homogeneous. Note that the means of the distributions (μ_β or μ_D) cited above are *not* the nominal

values above but are instead calculated by:

$$\mu_X = \mu_{X_0} \left[\frac{10^{\alpha y}}{\alpha \ln(10)} \right]_{y=-0.5}^{y=0.5} \tag{6.3}$$

Where μ_{X_0} is the nominal value of either the fluvial or diffusion transport coefficient. Thus the mean of both distributions varies as a function of α which will be an important consideration during the calibration process.

Other distribution models, such as ones which allow for spatially correlated fields or for log-normally distributed soil erosivity, are possible. The case of vertical stratification and horizontally correlated erosivity fields will be discussed later in Chapter 7. The particular geology and vegetation cover would determine the most appropriate distribution characteristics for simulation of a given system. Depending on the specific distribution employed, the material will vary in its spread around a central value, and in its sensitivity to the α parameter. The model chosen in equations 6.1 and 6.2 above illustrates the general behavior of the response of simulated domains to spatial heterogeneity. One could easily conceive of a multitude of other formulations. For instance α could vary between equations 6.1 and 6.2, a multiplicative rather than exponential form to the hardness could be used, etc. Again, these issues would be best addressed by the observed structure of the heterogeneities themselves.

Figures 6-2 and 6-3 illustrate basins simulated with the same nominal values of the fluvial and diffusion coefficients as those shown previously in Figure 6-1 (namely, $U = 0.1$, $\beta = 0.01$, and $D = 0.1$). Figure 6-1 was generated under homogeneous ($\alpha = 0.0$) conditions, while Figures 6-2 and 6-3 correspond to values of ($\alpha = 1.5$) and ($\alpha = 2.0$), respectively.

Figure 6-4 shows two slices of the drainage systems pictured in Figures 6-1 and 6-2. We see how the introduction of spatial heterogeneities in erosivity leads to a rough-textured topography compared to the smoother and more regular homogeneous erosivity topography. We also notice the occurrence of convex-concave profiles in the heterogeneous system whereas only convex profiles are evident in the homogeneous system.

6.2 Effect of Spatial Variability

In Chapter 3, we illustrated how relative changes in the transport coefficients, β and D, influenced the magnitude of the hillslope scale. These changes corresponded to a shift in the small-area region of the cumulative area distribution. Spatial heterogeneity also has an influence on the simulated topography and cumulative area distribution. As heterogeneities increase (α increasing) the path taken by the channel network becomes more tortuous and even the diffusion dominated hillslopes exhibit a small-scale roughness or irregularity. Spatially variable erosivity forces the channel network to take a more irregular path because the incising river will preferentially seek points in the terrain that are more readily eroded than neighboring points. At the fine scale, differences in erodibility result in small differences in the equilibrium slope

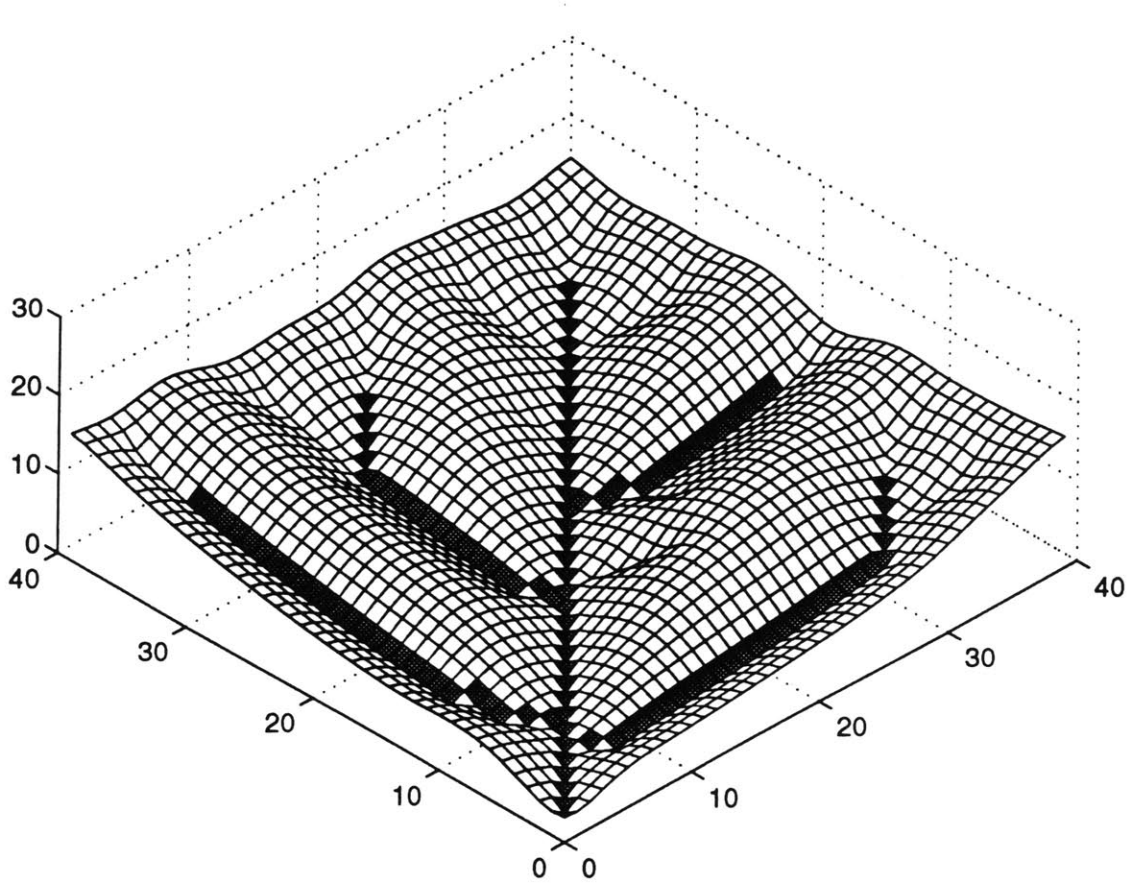

Figure 6-1: Perspective plot of simulated domain under homogeneous erosivity conditions.

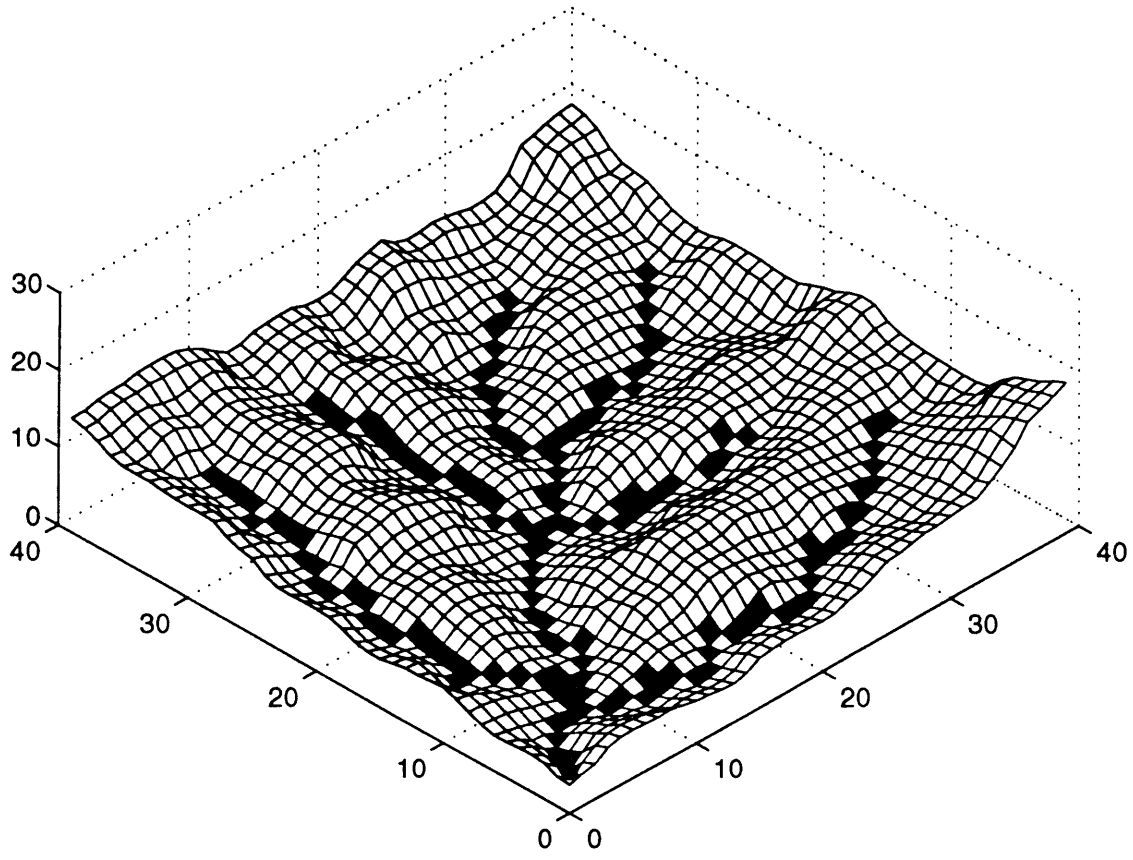

Figure 6-2: Perspective plot of simulated domain under heterogeneous erosivity conditions ($\alpha = 1.5$).

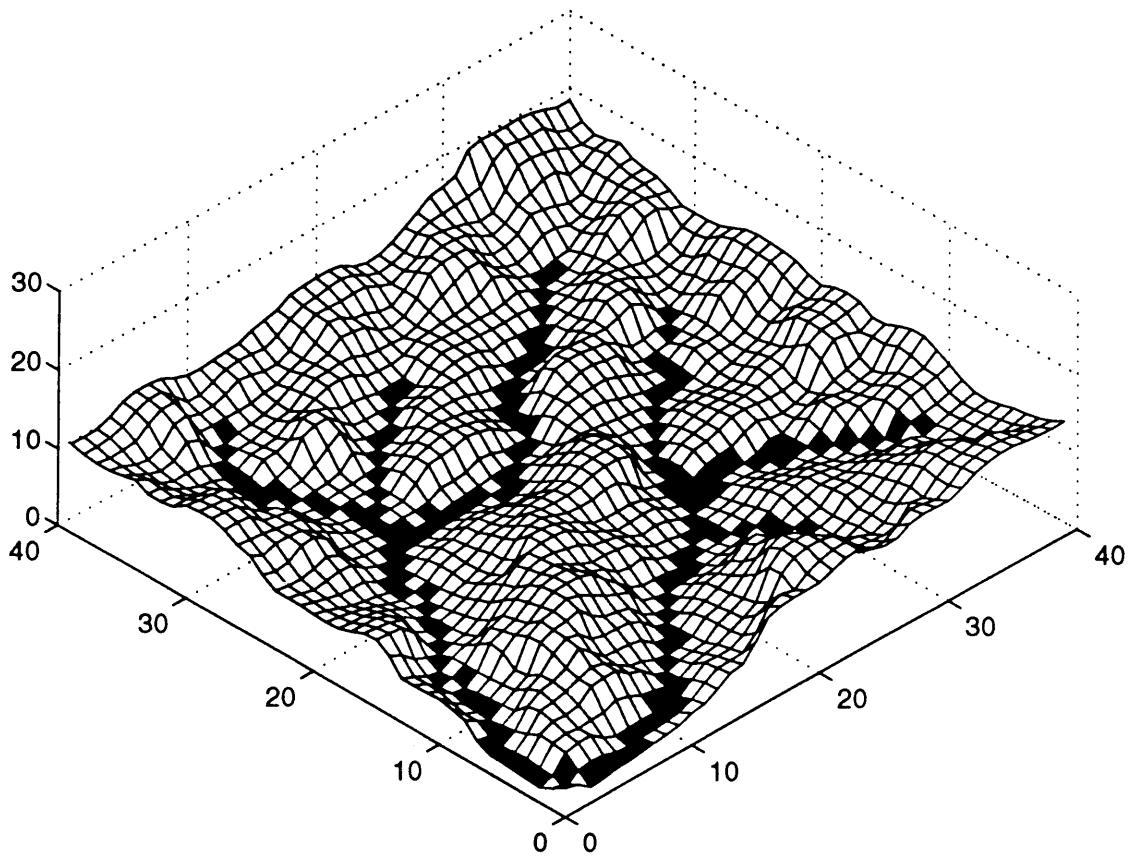

Figure 6-3: Perspective plot of simulated domain under heterogeneous erosivity conditions ($\alpha = 2.0$).

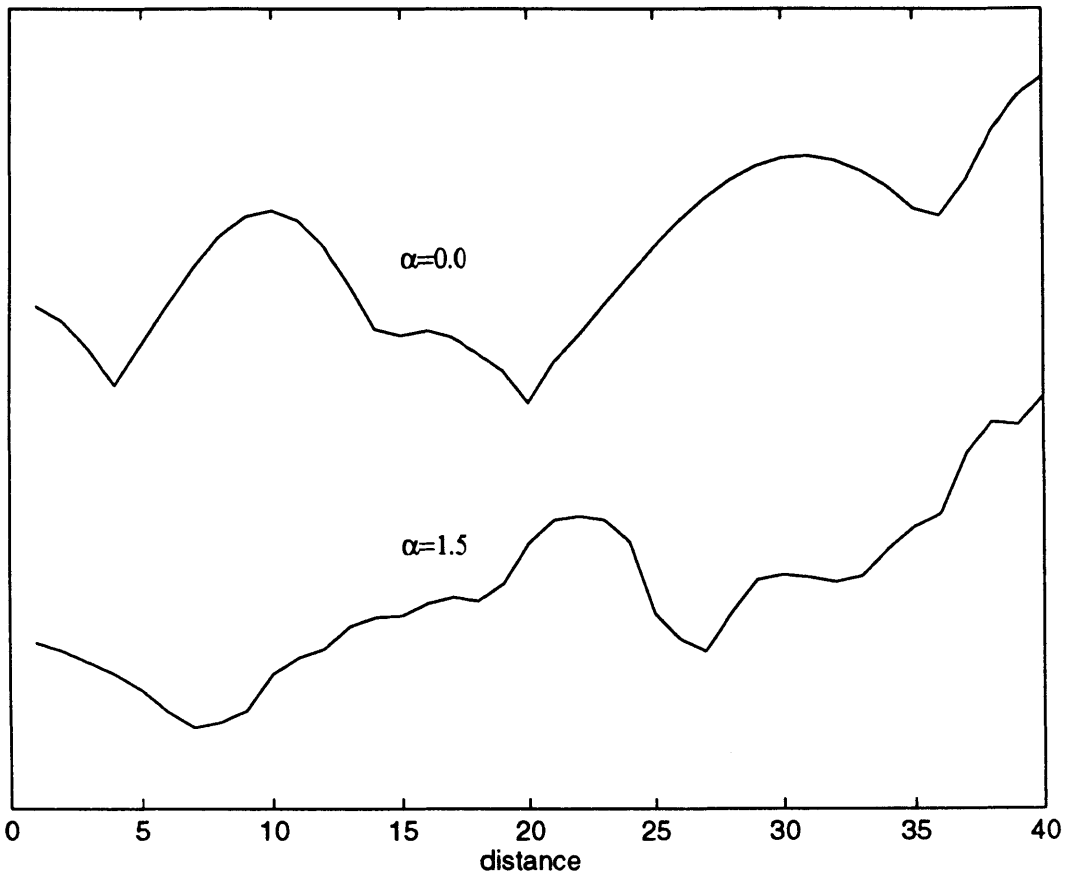

Figure 6-4: 1-D cuts of simulations for $\alpha = 0.0$ and $\alpha = 1.5$.

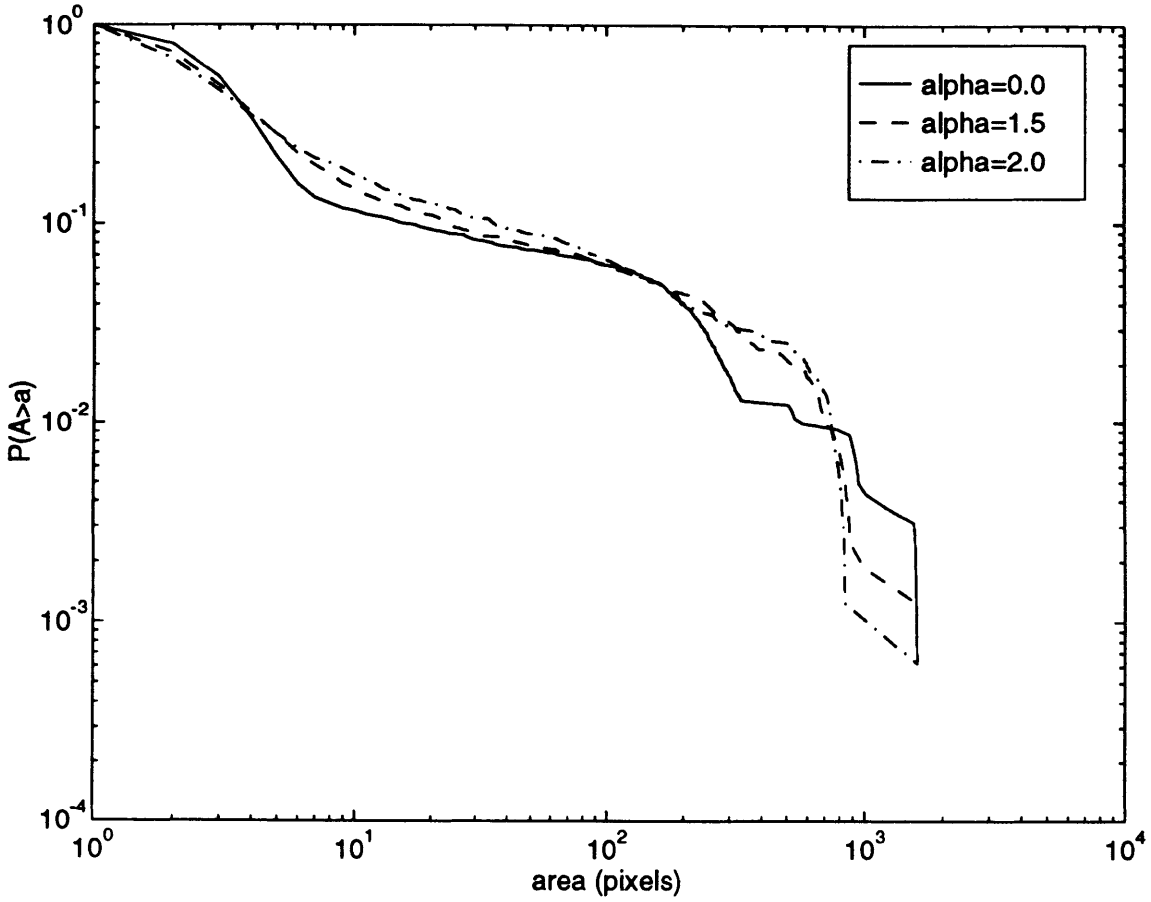

Figure 6-5: Cumulative area distributions for simulations with $\alpha = 0.0$, 1.5, and 2.0.

and cause small elevation perturbations on the otherwise smooth hillslope elements.

Figure 6-5 shows the cumulative area distributions for the three simulations with α=0.0, 1.5, and 2.0. From Figure 6-5 we see that varying α affects the rate of decrease of exceedence probabilities with increasing cumulative area. This is in contrast to β and D which predominantly determine the cumulative area at which there is a sharp drop in exceedence probabilities. Spatial variability in the soil erosivity adds a roughness which limits the ease with which rapid aggregation can take place. The result is that a greater fraction of pixels exist which drain areas of 10 to 50 pixels. If the material is homogeneous, aggregation from small ($A < 10$) to larger areas ($A > 50$) is more immediate, causing the sharp drop in exceedence probabilities.

Figure 6-5 illustrates how the the presence of heterogeneities increases the scales over which a power-law distribution of cumulative areas is valid. This is a result which is very useful, since most natural systems exhibit power-law behavior. Chapter 8 will explore this issue show how we can make use of heterogeneities to reproduce observed topography.

Figures 6-6 and 6-8 show the principal drainage directions for the simulated

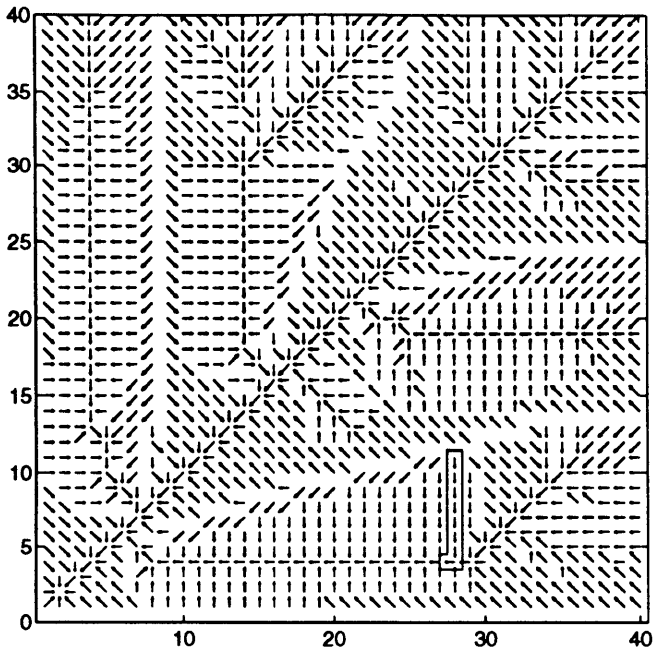

Figure 6-6: Plot of principal drainage directions for $\alpha = 0.0$. Highlighted box shows area emphasized in Figure 6-9.

drainage basins shown previously for $\alpha = 0.0$ and $\alpha = 2.0$, respectively. By principal, we mean the steepest drainage direction. One immediately notices that the introduction of heterogeneities in Figure 6-8 leads to a more complex drainage structure. We have highlighted within a box on both figures a small drainage segment. These segments were chosen as representative of the drainage in both systems. Figure 6-7 shows the first system (with $\alpha = 0.0$). We can trace due south from the pixel located on a ridge at (28,11) to (28,4) where we encounter a channel. Along this trajectory the cumulative area (in pixels) increases as follows: {1.21, 1.90, 2.59, 3.20, 3.73, 4.17, 4.76, 160.49} where the last area (160.49) is indicative of having encountered a channel. In the second system (shown in Figure 6-9) we can trace (roughly) from east to west from the ridge at (18,20) to the channel at (11,20). The areas change as follows: {1.32, 2.25, 6.27, 14.03, 21.41, 15.29, 12.52, 267.02}.

These two area accumulation patterns reflect the overall cumulative area distributions that were previously shown in Figure 6-5. In the case when $\alpha = 0.0$, we see that the areas increase roughly linearly (about 0.6 to 0.7 per pixel) along the direction of flow. In contrast, the cumulative area first increases, then decreases as we travel along the drainage path for the case of $\alpha = 2.0$. The decrease in cumulative area along the principal drainage path is due to a diverging flow field. Not only is the aggregation pattern non-linear in the heterogeneous case, but we see that the cumulative areas may be much larger than the value of 4 or 5 pixels observed in the homogeneous simulation. This illustrates how the roughness of the heterogeneous surface limits the rate at which aggregation occurs along a flow path and allows for larger cumulative areas before channel aggregation is encountered.

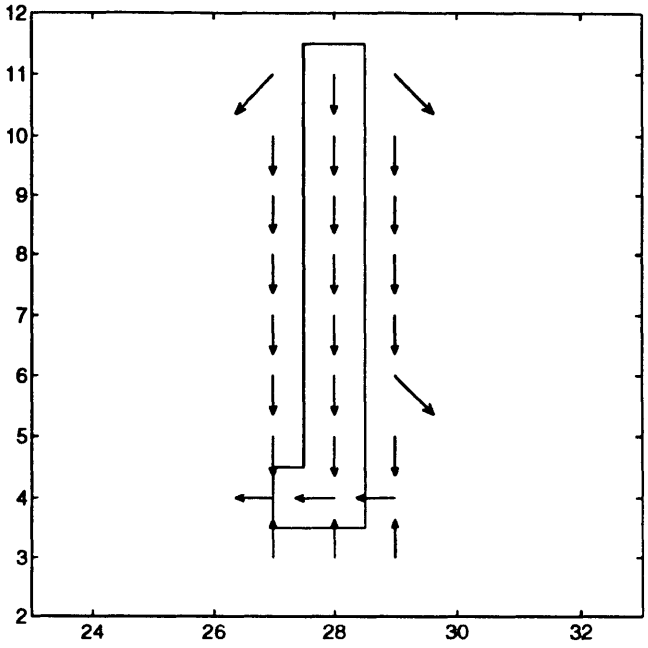

Figure 6-7: Plot of principal drainage directions for $\alpha = 0.0$ for highlighted area in Figure 6-8.

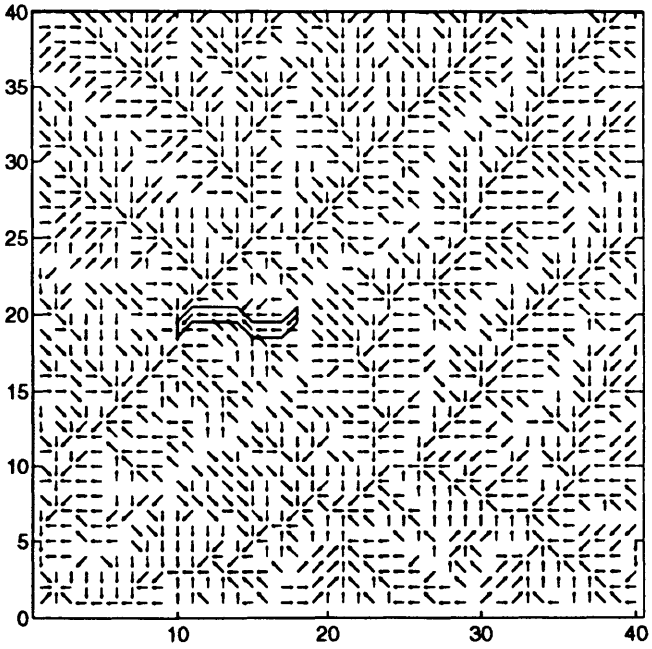

Figure 6-8: Plot of principal drainage directions for $\alpha = 2.0$. Highlighted box shows area emphasized in Figure 6-11.

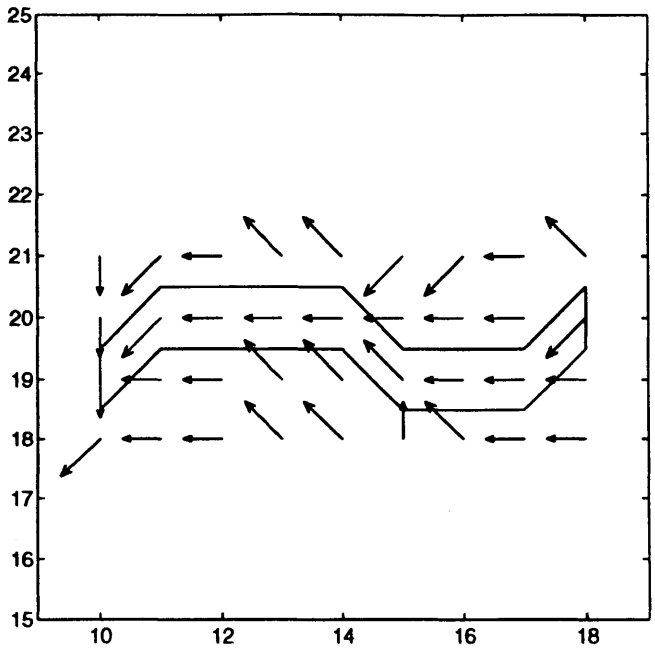

Figure 6-9: Plot of principal drainage directions for $\alpha = 2.0$ for highlighted area in Figure 6-10.

The slope-area relationship is also effected by the presence of heterogeneity. Figure 6-10 shows the slope-area relationship for the simulation pictured in Figure 6-1. In contrast, Figure 6-11 shows the slope-area relationship for the simulation pictured in Figure 6-2. The presence of heterogeneity caused by $\alpha > 0$ introduces scatter in the slope-area relationship. The greater the value of α, the greater the magnitude of the scatter.

6.3 Channel Selectivity in a White Noise Field

It has been stated earlier that the growing and extending channel head will naturally "seek" out softer material and preferentially grow in that direction. If the channels naturally select softer material it would be expected that the mean slope-area relationship is not simply a matter of knowing the mean erosivity behavior of the basin. This section will address the issue of biases that result from channel selectivity.

Figure 6-12 shows the scatter in soil erosivity as a function of area for a simulation with $\alpha = 1.0$. Careful examination of the scatter reveals that there is a positive trend with increasing area. Also shown on the plot is a moving average of the scatter. The moving average indicates that there is an initial decline in the softness index (the value of the η_i's) with area (Region A), followed by a strong positive trend (Region B), and then finally a long stretch with essentially no trend as area continues to increase (Region C).

Let us first address the large area convergence of the moving average to an ap-

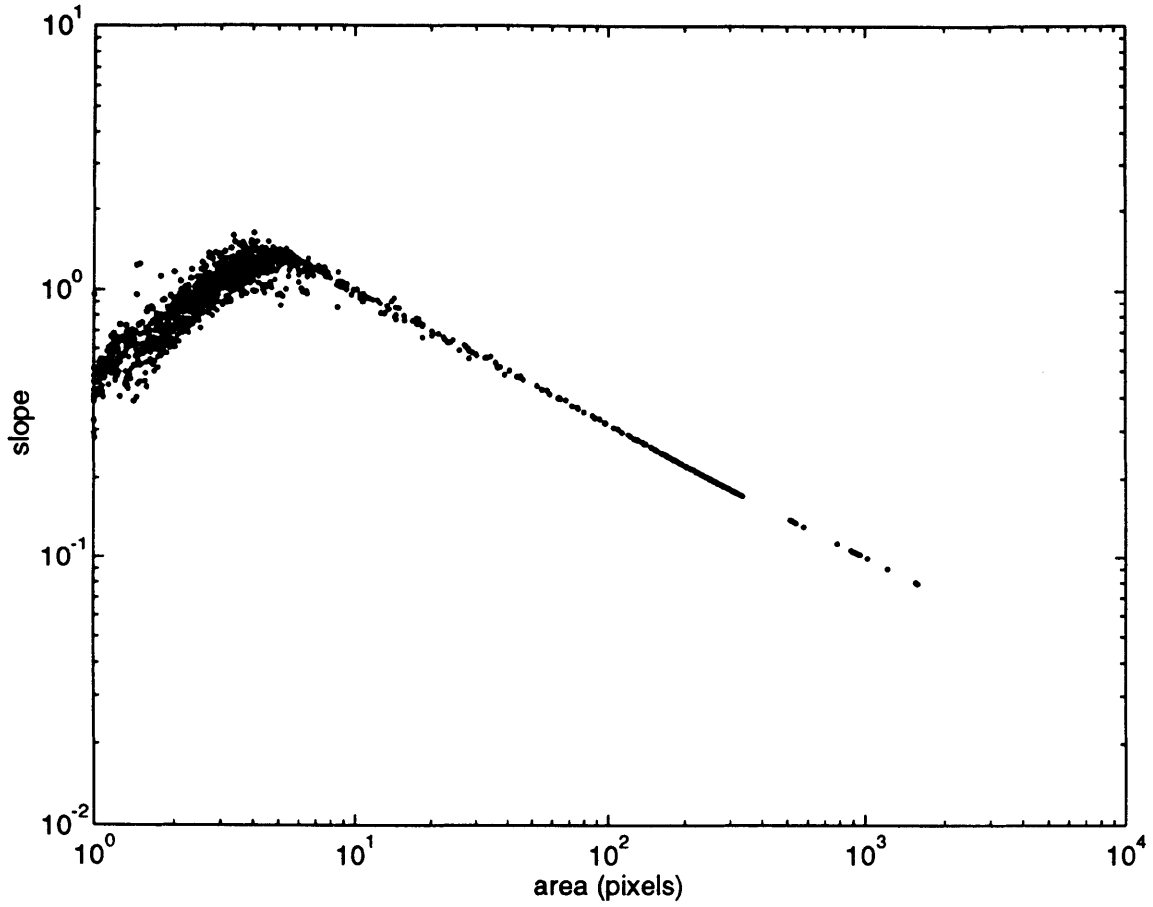

Figure 6-10: Slope-area relationship for homogeneous conditions.

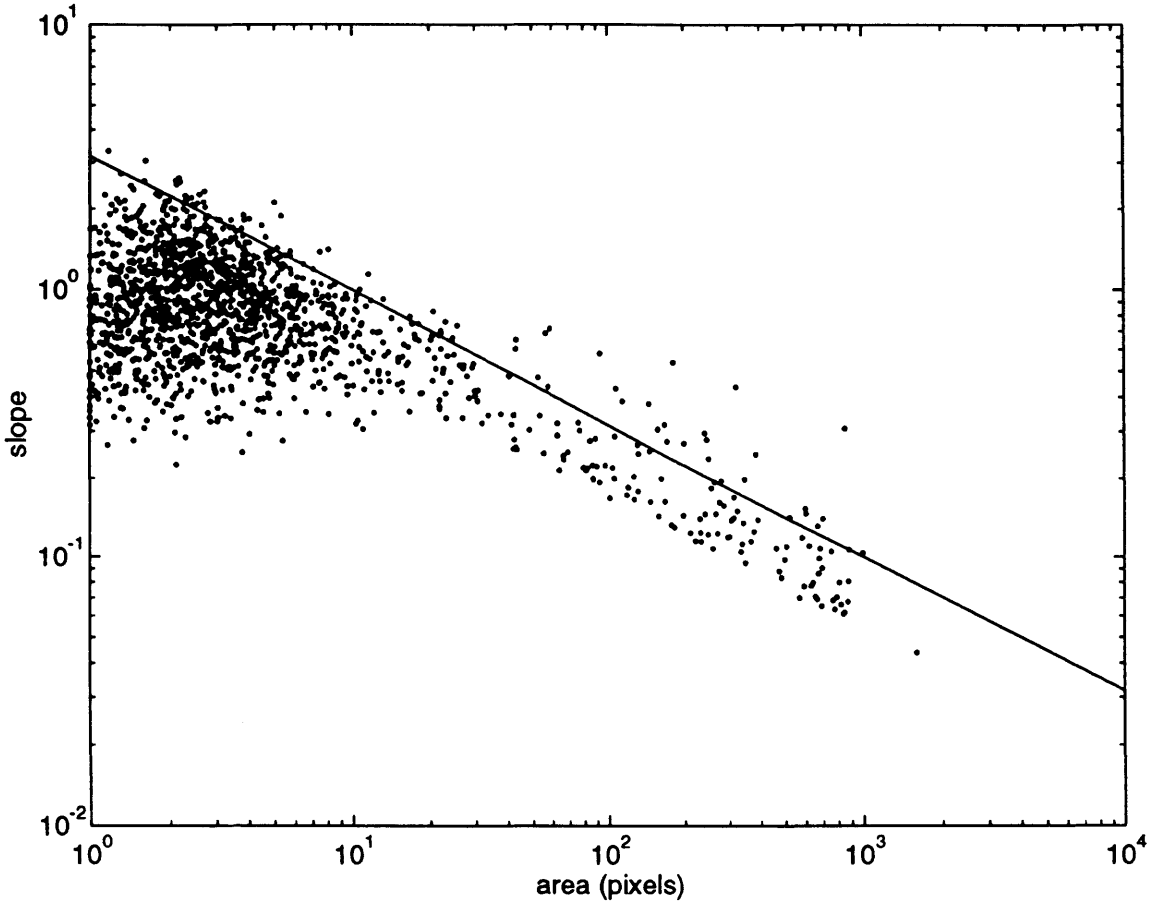

Figure 6-11: Slope-area relationship when $\alpha = 1.5$. Solid line corresponds to fluvial dominated slope-area relationship under homogeneous conditions.

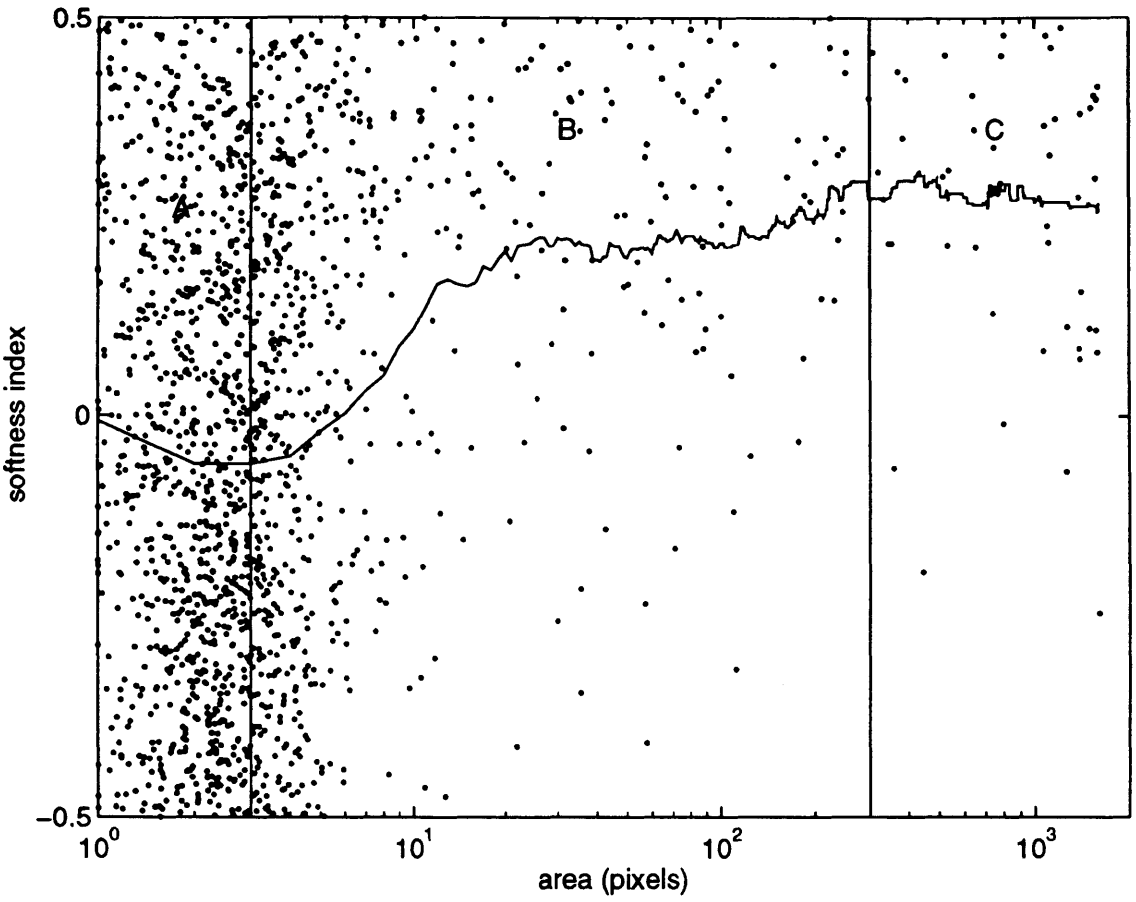

Figure 6-12: Scatter plot of softness index as a function of area and moving average of scatter for $\alpha = 1.0$.

parent fixed value (Region C). We can abstract the channel growth process to the following rules:

- The channel head examines the elevations of each of its neighbors (ignoring the one pixel which is already downstream of the channel head).
- The channel will tend to grow towards the neighbor that is currently attracting the greatest amount of flow (or area).
- The pixel with the greatest amount of flow will likely be the one with the lowest current elevation
- The pixel with the lowest current elevation will likely be the one with the largest relative value of the softness index, η_i

Following this logic, the channel head is most likely to grow towards the neighboring pixel which has the largest relative value of the softness index. Since our softness index is uniformly distributed on [-0.5, 0.5], this amounts to asking the question:

> *What is the expected value of the maximum of ζ uniformly distributed random variables on* [-0.5, 0.5]*?*

The answer is:

$$E[\text{max of } \zeta \text{ values}] = U_{min} + (U_{max} - U_{min})\frac{\zeta}{\zeta + 1} \tag{6.4}$$

where U_{min} and U_{max} are the values of the lower and upper bounds of the uniform distribution in question. For our particular situation $U_{min} = -0.5$ and $U_{max} = 0.5$. If $\zeta = 3$ then equation 6.4 gives $E = 0.25$ which is consistent with the moving average results.

In other words the channel head is choosing from among three pixels as it extends into the unchannelized domain. This seems like a reasonable value as indicated by Figure 6-13. This figure illustrates the two possible channel head configurations (diagonal and cardinal) and shows the potential sites for future growth which are three pixels.

One might argue that the convergence of the moving average to 0.25 for large area is due to some other phenomena. Appendix A addresses this issue with a small study, analogous to the one shown here except for normally ($N(0, 0.083)$) distributed erosivity. (A variance of σ^2=0.083 is used to be consistent with the variance of uniformly distributed noise on the interval [0, 1]. The conclusions of this appendix are twofold:

- Channel head is choosing from among three points in which to grow.
- The maxima of ζ=2, 3, and 4 uniformly or normally distributed values are roughly equivalent provided that the mean and variance of both distributions are the same. This suggests that channel selectivity behavior will be comparable for either uniformly or normally distributed erosivity under these conditions.

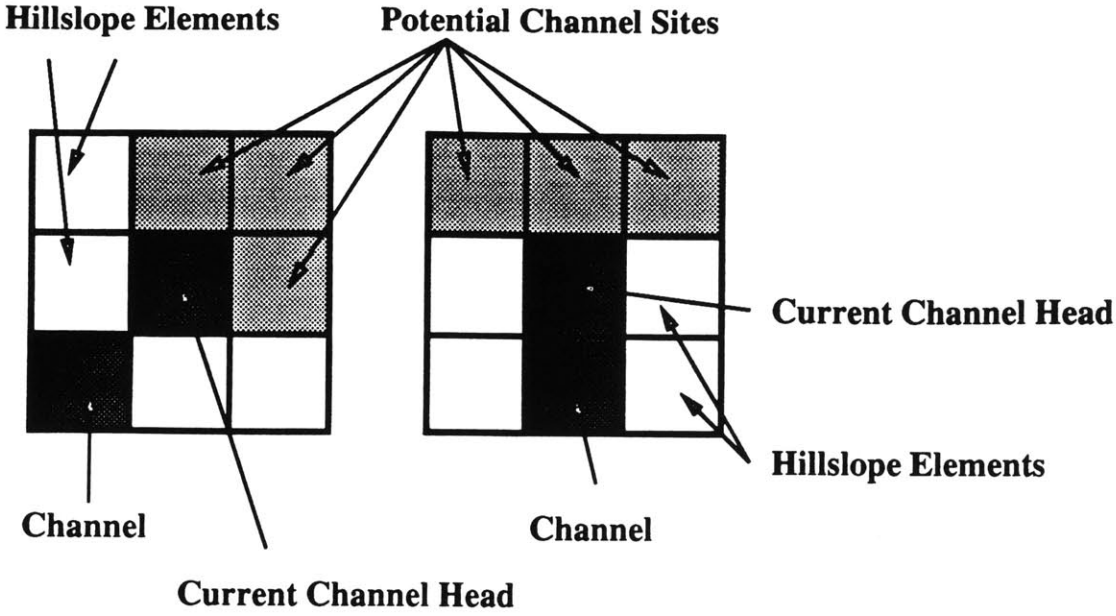

Figure 6-13: Schematic diagram showing the two possible channel head configurations and potential sites of future growth.

We are also interested in any dependence the scatter of softness indices may have on α. Multiple realizations for α=1.0, 1.5, 2.0, and, 2.5 were performed and ensemble averages taken for the moving averages of the scatter associated with these cases. Figure 6-14 shows these ensemble averages. The reader will note that there are again, three distinct regions to each ensemble average curve. For small area there is an initial decline in softness index (Region A), followed by a positive trend to the scatter for intermediate areas (Region B), and finally a zero trend section for large areas (Region C).

Notice that Region C tends towards the limiting value of 0.25 regardless of α. In other words, the magnitude of the variance has no bearing on this limiting value. Region B, in contrast, shows different behavior for each value of α. Simulations in which α is small reach the limiting value of 0.25 at a smaller cumulative area than those in which α is large. This is reminiscent of the cumulative area distributions which showed that as α increased, the scale of influence of the hillslope aggregation structure increased. Finally, Region A is characterized by the smallest values of the softness index. This indicates that the hillslopes are comprised of material that is, on the average, harder than anywhere else in the basin. This is caused primarily from the fact that the channels are tending towards softer material on average, so the hillslopes are left with the remaining area which tends to be harder than average.

With this understanding of the structure of the scatter in the softness index we are now prepared to examine the effect of channel selectivity on the slope-area relationship. We have shown that the average value of the softness index for large area ($A >$ 200 to 300 pixels) is a constant with no dependence on cumulative area or

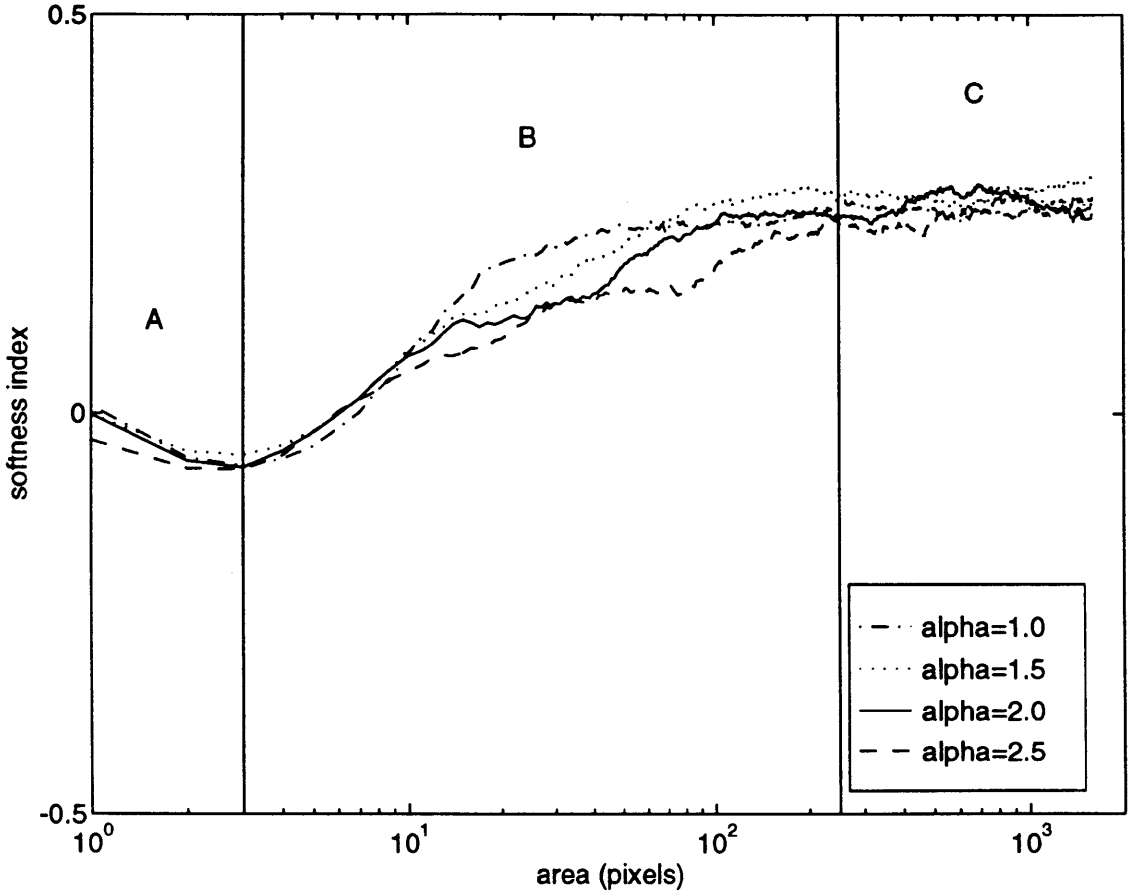

Figure 6-14: Ensemble averages of moving averages of scatter in softness index for varying α.

α. For uniformly distributed softness index this constant value 0.25. This implies that the slope-area scaling exponent, θ will be the same values as that determined by theory under homogeneous conditions. However, the multiplicative constant relating slope to area will differ. Under homogeneous conditions this constant is determined from:

$$c = (\frac{U}{\beta_0})^{1/n} \tag{6.5}$$

but when β is allowed to vary, the mean value of β for large areas will be (on average):

$$\bar{\beta_0} = \beta_0 10^{0.25\alpha} \tag{6.6}$$

Combining equations 6.5 and 6.6, the result is that the mean channel slope will be reduced by a factor of:

$$\frac{\beta_{0,homogeneous}}{\beta_{0,heterogeneous}} = 10^{\alpha/4n} \tag{6.7}$$

This effect is shown in Figure 6-15 which shows the reduction in slope from that expected for homogeneous conditions for an ensemble average of five simulations with $\alpha = 1.5$. This difference should be considered during the calibration procedure (discussed in a following chapter) as β will need to be made proportionately smaller to compensate for this bias.

6.4 Summary

This chapter has illustrated the effect of white noise variability in erosivity on simulated topography. A physical justification for this variability was given and a small simulation showed how this form of erosivity gives rise to the small scale roughness characteristic of natural topography, previously impossible to produce under homogeneous conditions within the model. The effect of varying the magnitude of the heterogeneity through the parameter, α, was illustrated through 3-D perspective plots, the slope-area relationship, and most importantly, on the cumulative area distribution. Finally, the issue of channels preferentially choosing material that is more readily eroded was discussed. This channel selectivity was shown to have a minimal effect on θ but a significant effect on the mean value of β for pixels draining large areas. This has implications on the future objective of calibrating the model to an observed topography.

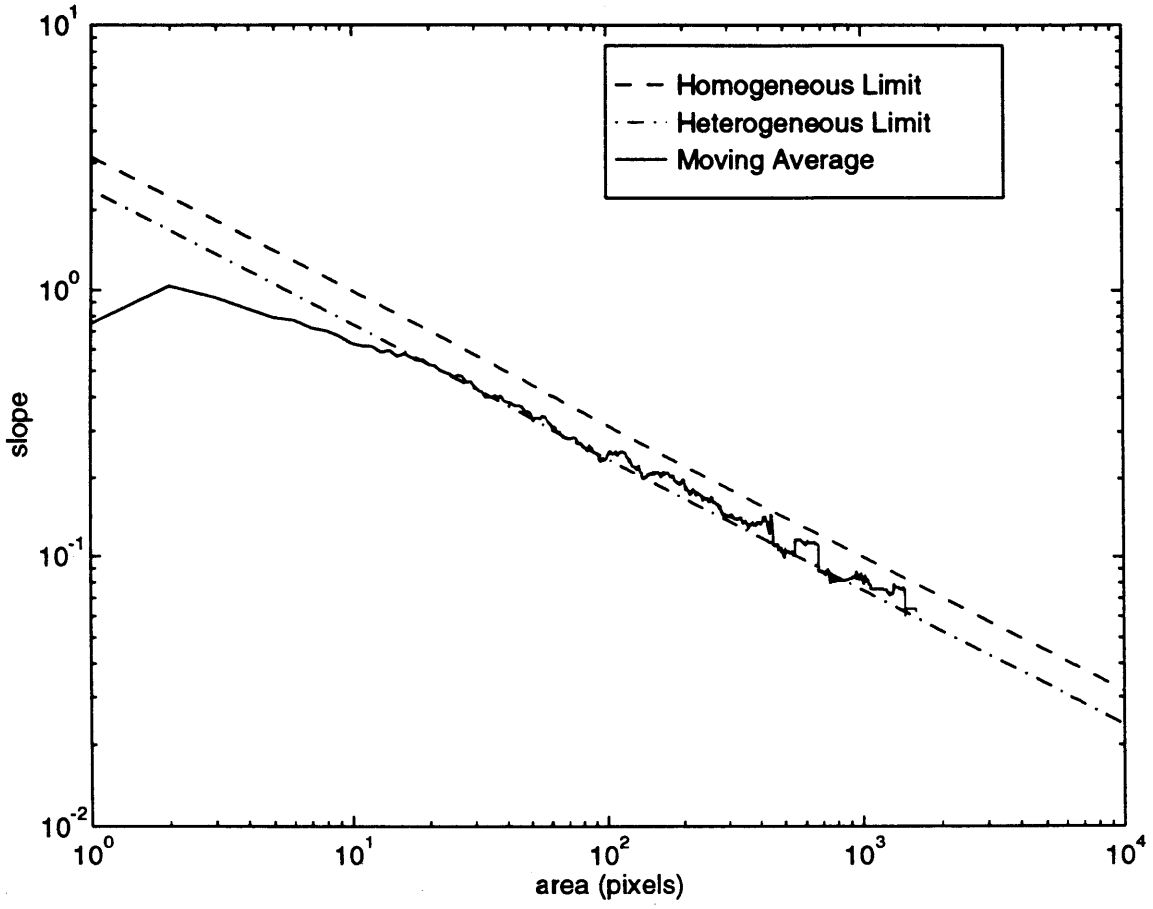

Figure 6-15: Plot of moving average of slope versus area. The upper straight line corresponds to expected slope-area scaling under homogeneous conditions while the lower straight line corresponds to expected slope-area scaling under heterogeneous conditions ($\alpha = 1.5$)

Chapter 7

Erosion Variability and the Hypsometric Curve

The hypsometric curve was introduced earlier in Chapter 2. Here we will discuss how the hypsometric curve of simulated domains is dependent on the structure of the softness index field. In particular, two different types of structures will be examined: correlated fields in the horizontal, and vertically stratified fields. It will be shown that the softness index field can be used to dictate the desired form of the hypsometric curve.

7.1 The Prototypical Hypsometric Curve

The prototypical hypsometric curve (shown in Figure 7-1) is defined here to provide a means of comparison with the other hypsometric curves that will be presented in this chapter. The hypsometric curve reflects basin shape, drainage network organization, geology, structure of heterogeneities, and dominant transport processes. If we perform multiple realizations of networks which all have the same domain shape, comparable networks, geology, and heterogeneities, and the same transport processes, then we would expect their hypsometric distributions to be very similar. We will define the ensemble average of these similar hypsometric distributions to be our **prototypical** hypsometric curve and conditions which produce this curve will be referred to as **normal** conditions. This curve will serve as a useful benchmark against which we can compare other hypsometric curves which result from systems with a different structure of soil heterogeneity.

Interestingly, the prototypical hypsometric curve will result from spatial variability at both ends of the spectrum of correlation scales. This will be discussed in a later section. In both cases the prototypical hypsometric curve results for the same reason: namely, that the growing channel network develops under conditions where the extending channel head encounters an erosivity field which is essentially invariant in space. The result is that the channel network extends into the basin without being biased in any one direction and produces a distribution of elevations that is fairly evenly distributed from the outlet elevation to the highest reaches of the divides.

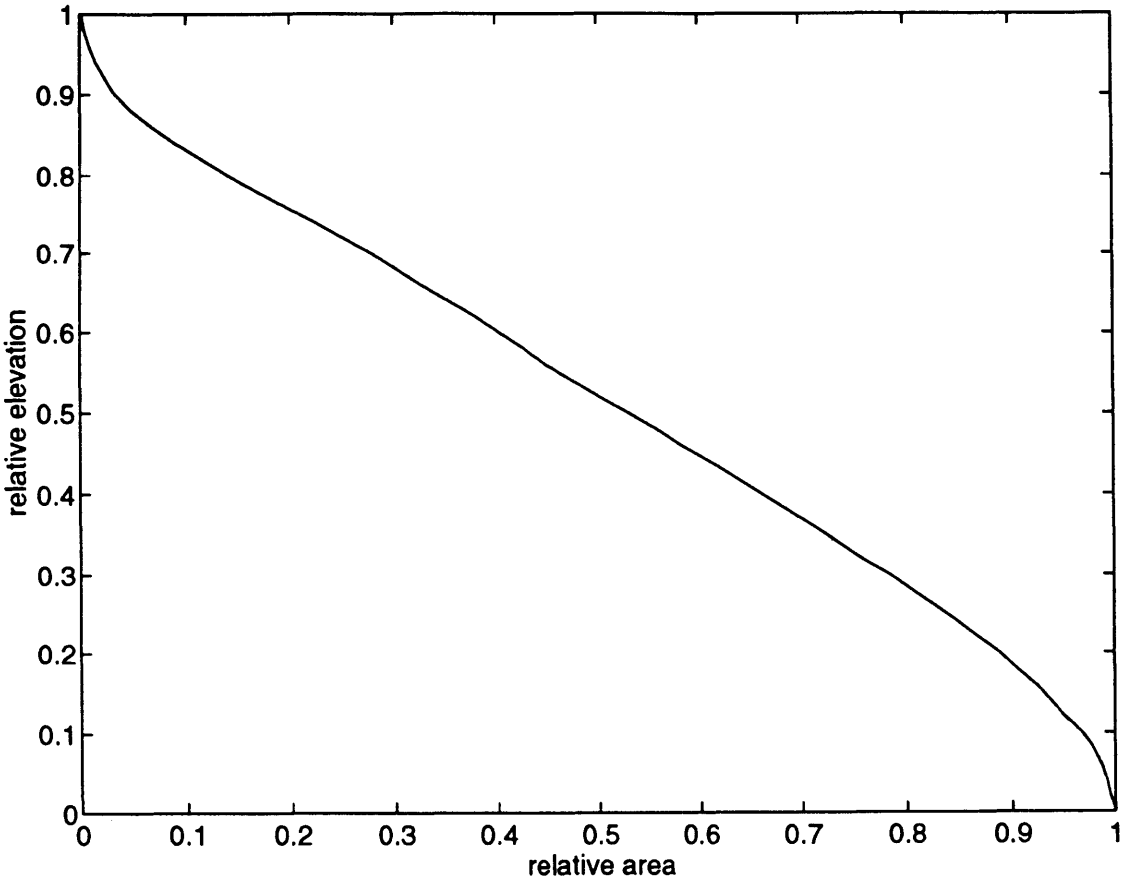

Figure 7-1: The prototypical hypsometric curve.

This distinction will become more evident when this prototypical hypsometric curve is contrasted with those presented in the following sections.

7.2 Vertically Stratified Fields

Deposition by wind and water over many years produces a stratified geology. Examples of this layering are readily apparent at large road cuts or to any hiker descending into the Grand Canyon, for instance. Since the composition and depositional conditions vary from layer to layer, it is natural to expect that one property that would vary among the layers is the softness (degree of resistance to erosion) associated with that layer. The simulations discussed here are based on this premise.

For purposes of simplification two cases will be considered. The first case that we will study involves the structure of a basin which has developed in a region where two distinct layers of material are present; one much more resistant to erosion than the other. The second case is at the opposite extreme and involves a continuously varying stratification structure.

7.2.1 Case 1: Two distinct layers

The initial conditions for this study involve a 40x40 domain at equilibrium with a top layer of heterogeneous material with mean softness, $\bar{\eta}_1$ and variability, $\alpha = 2.0$. At the onset of the simulation the outlet is just at the interface between the two the layers. As the evolution proceeds the basin begins to erode into the lower layer with mean softness, $\bar{\eta}_2$. Two sub-cases are considered:

- Case 1a: $\bar{\eta}_1 = \bar{\eta}_2 + 0.5$, i.e. soft material overlying hard material. Since $\alpha = 2.0$, $\bar{\beta}_1 = 10\bar{\beta}_2$ and $\bar{D}_1 = 10\bar{D}_2$.

- Case 1b: $\bar{\eta}_1 = \bar{\eta}_2 - 0.5$, i.e. hard material overlying soft material. Since $\alpha = 2.0$, $\bar{\beta}_1 = 0.1\bar{\beta}_2$ and $\bar{D}_1 = 0.1\bar{D}_2$.

These cases are illustrated in Figure 7-2. Figures 7-3 and 7-4 show 3-D perspectives of the topography resulting from cases 1a and 1b respectively. Figure 7-5 shows the hypsometric curve for each case with the prototypical curve shown for comparative purposes.

The resulting drainage networks (at least in plan view) are very similar. However, in case 1a the topography is canyon-like with a deeply incised channel cutting into a relatively flat upper surface. In case 1b the opposite is true. The channel network does not cut significantly into the landscape and the greatest portion of the relief lies at the basin divides where the material still corresponds to the harder, upper layer. This yields the characteristic monadnock profile shown as the lower curve in Figure 7-5. We may generalize the results by observing that:

- Hard material supports steeper slopes, while soft material results in milder slopes or,

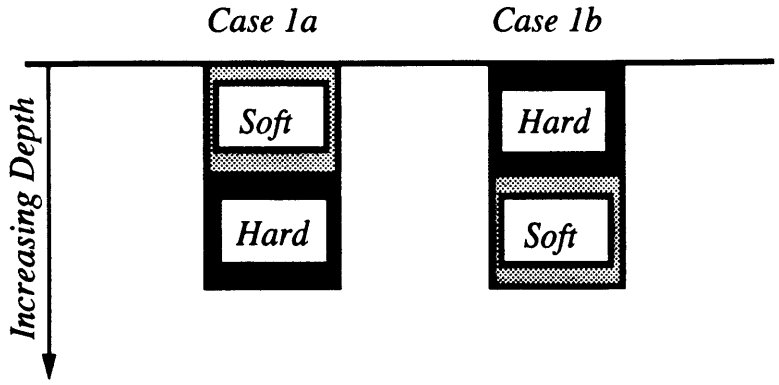

Figure 7-2: Schematic diagram for case of two distinct layer stratification.

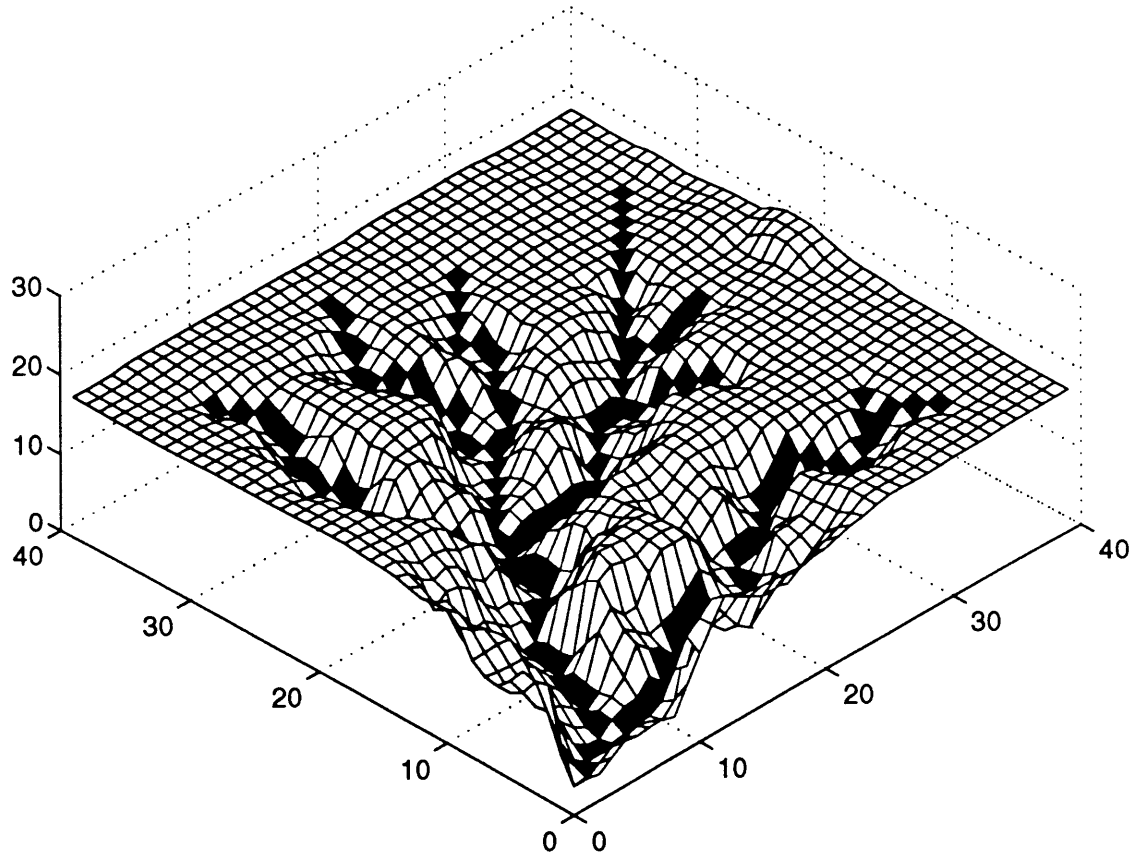

Figure 7-3: 3-D perspective of two layer stratification (soft material underlaid by hard).

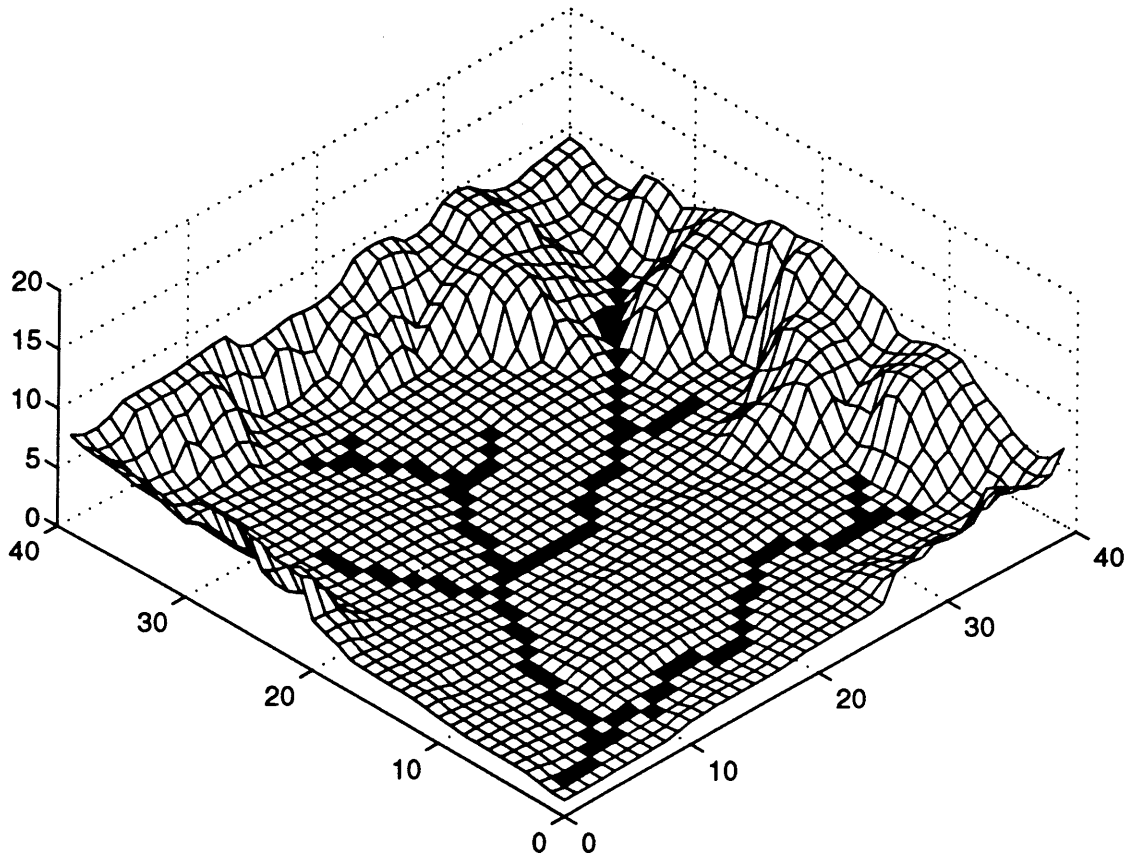

Figure 7-4: 3-D perspective of two layer stratification (hard material underlaid by soft).

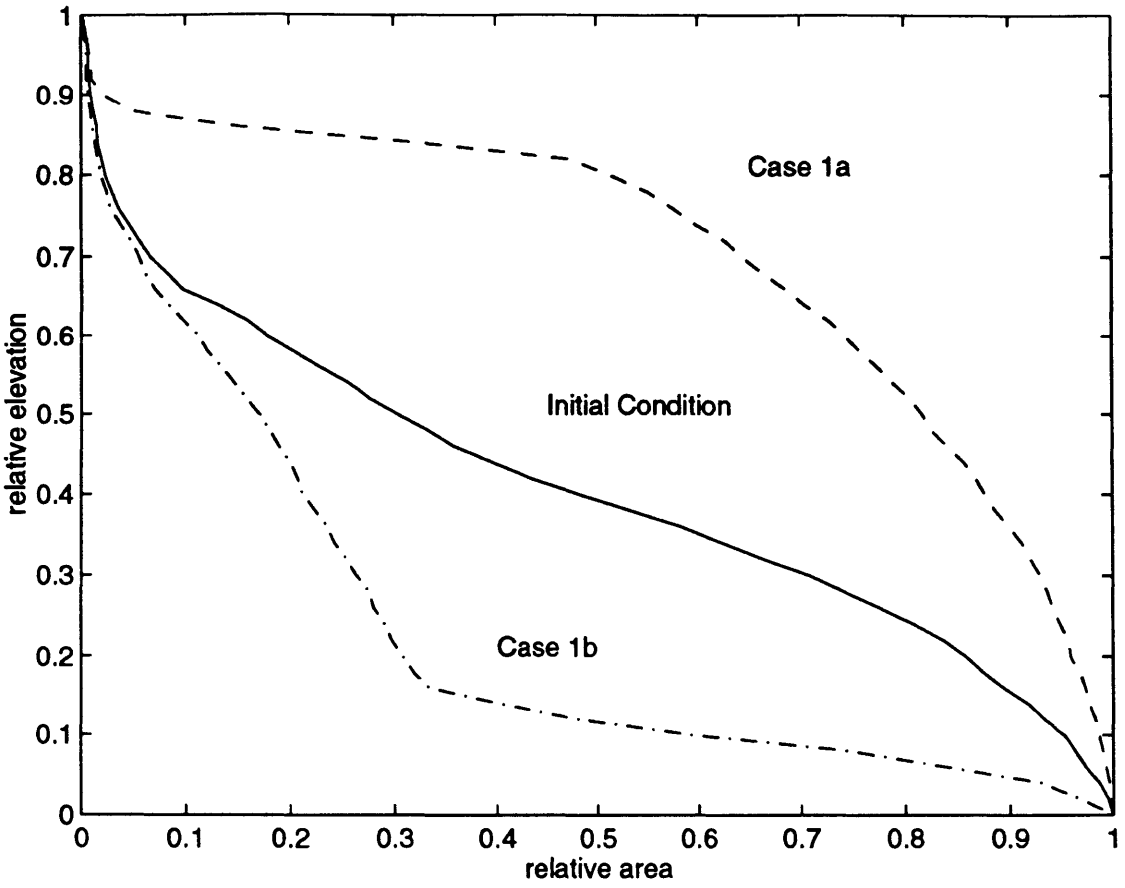

Figure 7-5: Hypsometric curves corresponding to the two layer stratification cases and contrasted with the initial condition for both cases.

- Hard material implies smaller β values which result in steeper slopes while soft material implies larger β values which result in milder slopes.

The first statement gives the *physical* cause of the steep (or mild) slopes as the relative softness of the material. The second statement explains *mathematically* how the steep (or mild) slopes come about.

7.2.2 Case 2: Continuously varying stratification

This case is a generalization of the cases shown in 1a and 1b. Here we allow the material softness to vary continuously according to:

$$\eta_{i,j}(d) = 2.0^{\xi d}\eta_{surface}(i,j) \tag{7.1}$$

In this equation, d denotes the depth of cutting into the layer from the beginning of the simulation and the sign convention is positive downwards. The parameter, ξ, represents the doubling rate of the softness of the material. The consequences of

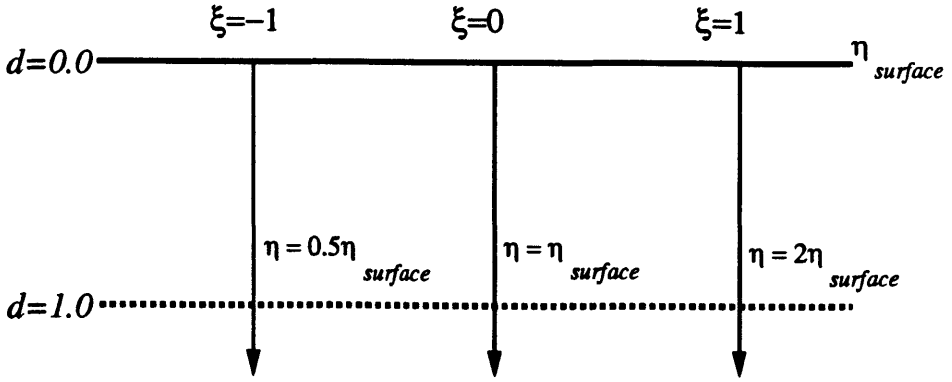

Figure 7-6: Schematic diagram for case of continuously varying stratification.

this equation are illustrated in a schematic diagram in Figure 7-6. The larger the magnitude of ξ the more rapidly the material softness changes with depth. If ξ is positive then the material gets softer with increasing depth, and if ξ is negative then the material gets harder with increasing depth. When $\xi = 0$ the material softness does not change with depth.

Figure 7-7 shows the variation in hypsometric curves as ξ varies from positive to negative. The general behavior shown here is similar to that in the two layer case in that a monadnock profile is generated when harder material overlies softer material and a canyon-like profile results from the opposite orientation. There are, however, two key differences. First, the profiles shown in cases 1a and 1b illustrate transient effects that will vanish once the upper layer (whether soft or hard) has completely eroded. In contrast, the continuously varying stratification lithology permanently affects the hypsometric distribution. And second, the degree of variation from the no stratification hypsometric curve is controllable, purely through variations in ξ. This fact will be exploited in the following chapter where stratification will be used as a means of model calibration to reproduce an observed hypsometric distribution.

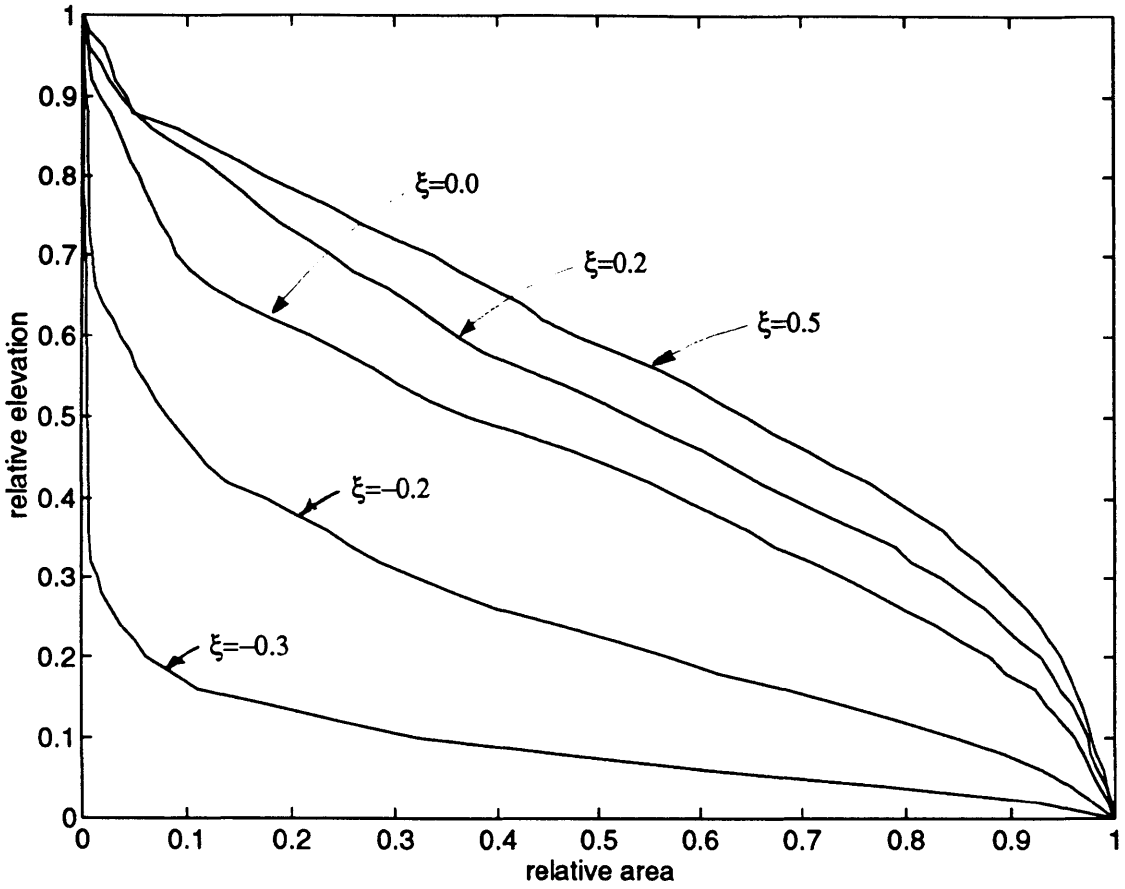

Figure 7-7: Hypsometric curves corresponding to continuously changing softness in stratification.

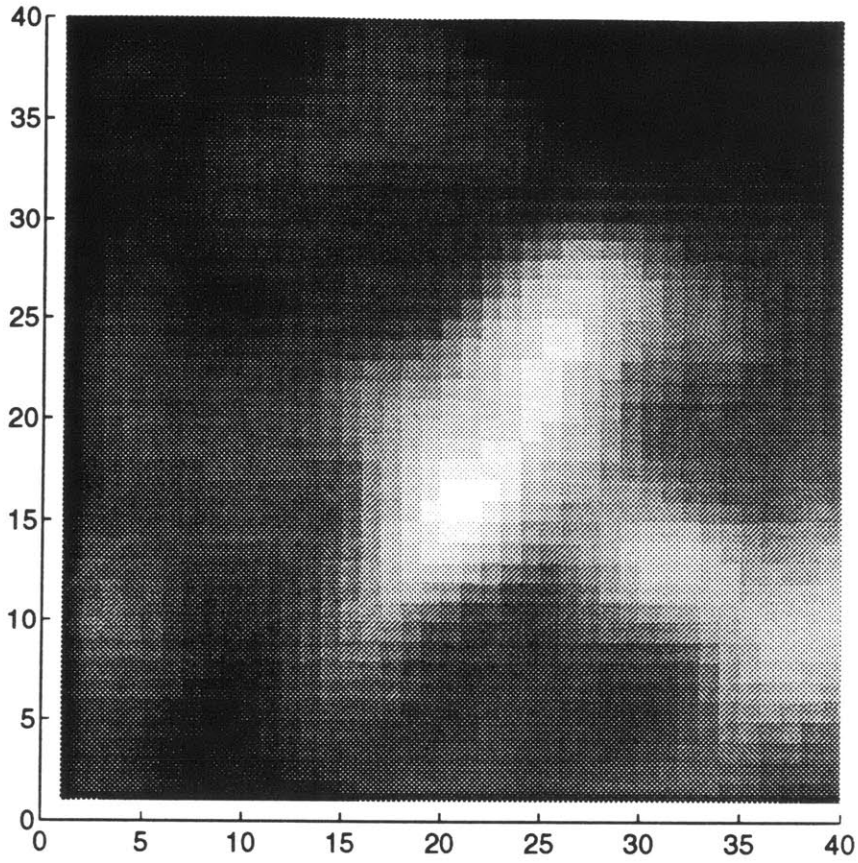

Figure 7-8: Sample correlated erosivity field ($\lambda = 10$).

7.3 Horizontally Correlated Fields

The previous section considers the case of material softness varying in the vertical dimension only. In reality, material properties will vary in the horizontal dimension as well, as the geologic forces that have brought material to a given area vary in their spatial extent. The premise of this section is that there is some scale which describes the distance within which the material properties should be similar. The magnitude of this scale may vary from region to region as the geologic history of each region varies. This section will examine how the hypsometric curve varies as the correlation scale of the soil softness changes.

The spatially correlated fields should be contrasted with the white noise used previously in Chapter 6 and with the homogeneous studies presented in Chapters 3, 4, and 5. In the white noise case, the correlation scale is zero whereas the correlation scale of homogeneous material is infinite. We are now studying the effect of noise which lies somewhere in between these two limiting cases. As an example, a correlated field is shown in Figure 7-8. The correlation scale in this figure is 10.

The correlation structure used to generate the erosivity fields in this study is:

$$\rho(r) = e^{-r/\lambda} \tag{7.2}$$

where $\rho(r)$ is the correlation between points separated by horizontal distance, r, and λ is the correlation scale. Note that as λ increases the correlation between points within a given domain becomes greater.

The characteristics of the simulated topography generated with correlated erosivity fields are due to two properties of the erosivity field:

- As λ increases, the variation in erosivity from point to point diminishes. As a result the drainage structure becomes more regular and the simulated topography reflects more directly regions where the material is much softer or harder than average.

- As λ increases (for a given area), the overall variation and/or range of erosivity values diminishes. The result is that the erosivity field tends to become increasingly homogeneous as λ increases. This behavior is illustrated in Figure 7-9.

The structure of the variance as indicated by Figure 7-9 is dependent on the spatial scale of the domain being simulated. If the domain were very large then the variance would not depend strongly on the correlation scale of the erosivity. Indeed, if the domain were infinite, Figure 7-9 would be a horizontal line with σ^2 equal to some constant. This is clearly not the case in the simulations performed since we are limited in the domain size that can be simulated by the speed of the computer being used. Nevertheless, it is not a computational artifact, but rather a well-documented phenomenon known as variance reduction. See Vanmarcke (1983) or Gelhar (1993) for a more complete discussion of variance dependence on correlation scale.

The function shown in Figure 7-9 reflects the 40x40 domain size of the simulations. When λ is very small ($\lambda < 10$) the variance is not profoundly affected by the domain size. As λ increases the domain size becomes significant and the variance decays exponentially with λ. Each data point in Figure 7-9 represents an average variance for ten fields simulated with a given correlation scale. Additionally, ten different correlation scales were examined to determine the variance as a function of λ. The solid line is a fitted function of the form:

$$\sigma^2(\lambda) = \sigma_0^2 - a\lambda^2 \quad \text{where } \lambda \leq \lambda_0 \tag{7.3}$$

$$\sigma^2(\lambda) = be^{c\lambda} \quad \text{where } \lambda > \lambda_0 \tag{7.4}$$

The particular values of the fitting coefficients are: $\sigma_0^2 = 0.0236$, $a = 5.64 \times 10^{-6}$, $b = 0.0366$, $c = 0.0225$, and $\lambda_0 = 34.8$.

The values of η created by the random field generator are normally distributed and the variance was chosen to be $\sigma^2(0) = 0.0236$ since this yields a range of values of approximately 1.0. Since both β and D are determined by taking $10^{c+\eta}$ the ensuing

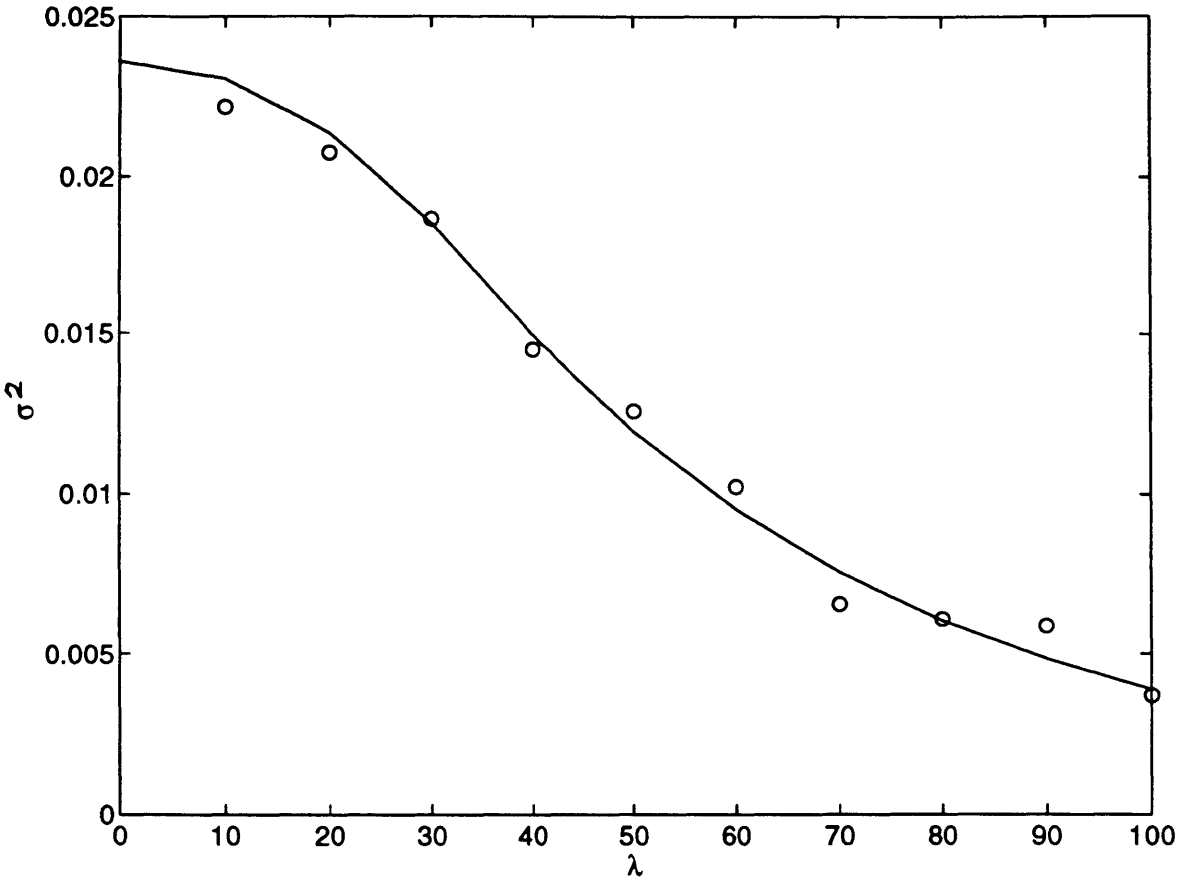

Figure 7-9: Relationship between variance and correlation scale for 40x40 spatial domain.

erosivity field will be log-normal. The domain is allowed to drain to any of the four corners of the system. This is done to eliminate biases that may occur by random chance should the region adjacent to the outlet be surrounded by material that is below average in softness. In the end, the the largest of the basins draining to each corner is isolated and its hypsometric curve is determined.

Four sets of simulations were performed:

- **Set #1** One set of simulations with λ varying and the variance of the generated erosivity fields following the function shown in Figure 7-9. (24 simulations)
- **Set #2** One set of simulations with λ varying and the variance of the generated erosivity fields fixed to the variance at $\lambda = 0$. (24 simulations)
- **Set #3** One set of simulations with $\lambda = 0$ and the variance of the generated erosivity fields varying analogously to those from the first set. (24 simulations)
- **Set #4** One set of simulations with $\lambda = 0$ and the variance of the generated erosivity fields fixed to the variance at $\lambda = 0$. (3 simulations)

In each case, three replicates were generated so stable averages could be computed and reported.

Before we consider the results from topographies generated in the simulations enumerated above, it is first interesting to consider the hypsometric curve for $\lambda = 0$ and $\lambda = \infty$. When $\lambda = 0$ we have white noise for our erosivity field. Since there is no organization to this field the channel network simply picks its way from the outlet along the path of least resistance (softest material). Since the soft and hard material are completely intermingled, topography is distributed fairly evenly among all elevations producing the prototypical hypsometric curve. When $\lambda = \infty$ we have completely homogeneous conditions which similarly result in the same prototypical hypsometric curve. Thus, if there is any effect of λ on the hypsometric curve, this effect must develop and then vanish as λ increases from 0 to ∞.

It will be shown in the following simulations that the two effects of λ (itemized earlier) actually compete with one another and result in transitioning from a prototypical hypsometric curve to some intermediate form and then back again as λ increases still further.

Figure 7-10 presents the hypsometric curves for the four sets of simulations itemized above. Simulations from sets 3 and 4 (indicated by the dashed and dot-dashed lines, respectively) indicate that there is essentially no effect of the variance on the simulated hypsometric curve when the correlation scale is zero and both sets yield the prototypical hypsometric distribution. Results from sets 1 and 2 indicate that the correlation scale does have a measurable effect on the hypsometric curve. Examining set 1 (solid line) indicates that as the variance is allowed to decrease naturally (with increasing λ), the generated hypsometric distribution tends towards prototypical. In contrast, set 2 (dotted line) shows that fixing the variance helps the effect of the correlation structure on the hypsometric distribution to persist much longer, although by the time $\lambda = 100$ it is evident that even the fixed variance simulations are tending toward normal conditions.

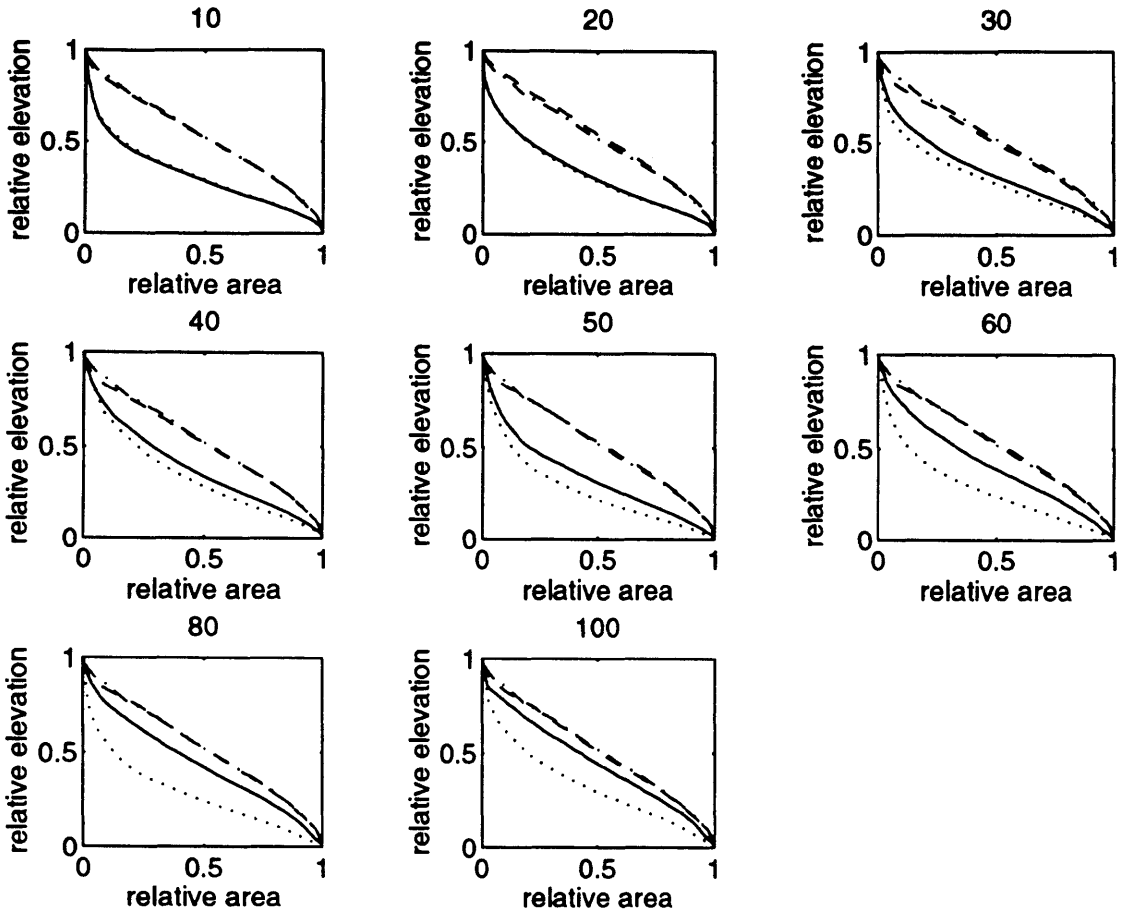

Figure 7-10: Hypsometric curves for varying horizontal correlation scales. {Solid line: varying λ - natural variance (Set #1), Dotted line: varying λ - fixed variance (Set #2), Dashed line: $\lambda = 0$ - natural variance (Set #3), Dot-Dash line: $\lambda = 0$ - fixed variance (Set #4)}

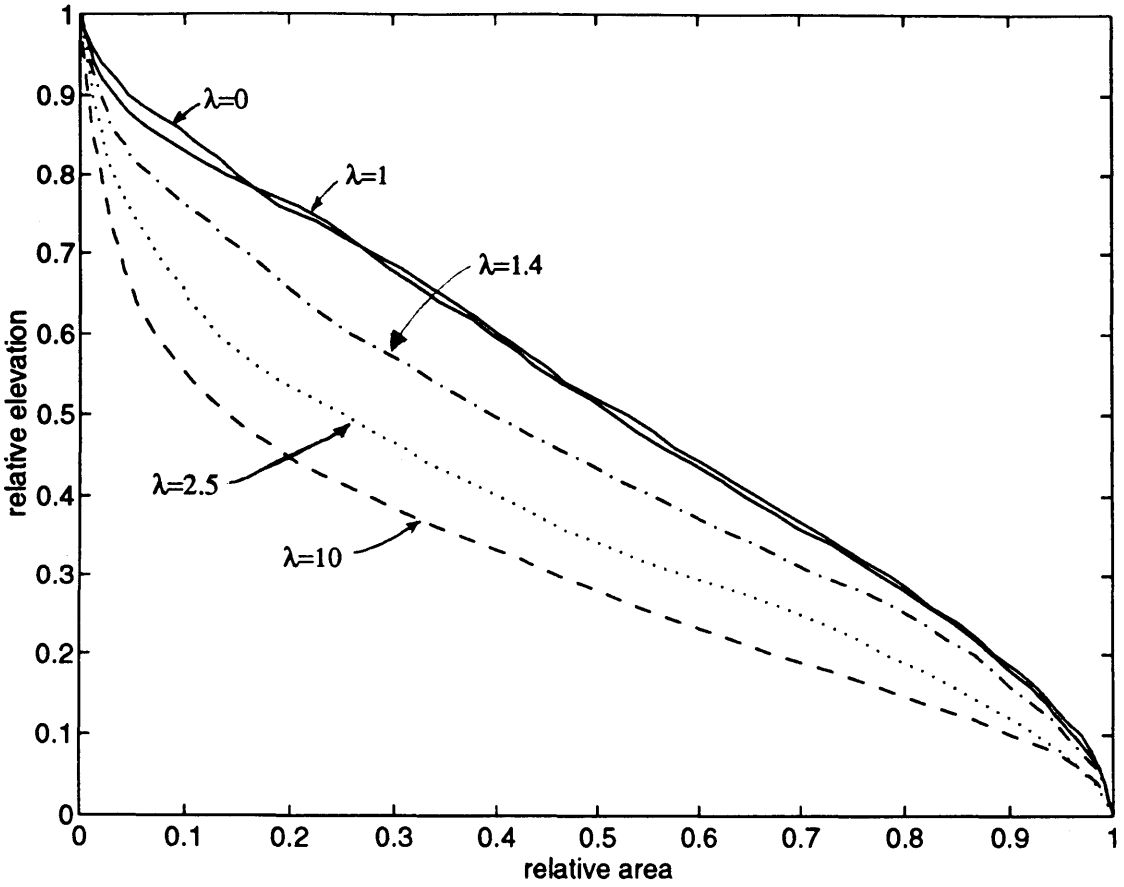

Figure 7-11: Hypsometric curves for small correlation scales.

The reader will notice that the hypsometric curve corresponding to $\lambda = 10$ seems to produce the largest excursion from normal conditions. As stated earlier, it would be expected that as λ increases the hypsometric curves should first transition away from normal conditions and then back to normal conditions as λ grows very large relative to the domain size. This implies that for $0 \leq \lambda \leq 10$ the transition away from the prototypical hypsometric curve must take place. In this range of λ there is essentially no change in the value of $\sigma^2(\lambda)$ as indicated by equation 7.3. Thus there is essentially no difference in the variance between simulations with natural variance and fixed variance corresponding to sets #3 and #4, respectively. We will show only those simulations corresponding to a fixed variance of $\sigma_0^2 = 0.0236$. Figure 7-11 shows the hypsometric curves for several judiciously chosen correlation scales which illustrate the transition from the prototypical hypsometric curve to the hypsometric curve corresponding to $\lambda = 10$. Notice that $\lambda = 0$ and $\lambda = 1$ are very similar and approximate the prototypical hypsometric curve. As λ increases further the hypsometric curve tends towards a lower distribution of elevation ultimately arriving at the $\lambda = 10$ distribution.

7.4 Correlated Erosivity and θ

In the last chapter we illustrated how channel selectivity led to the tendency for the extending channel head to seek out the softest material in which to incise. It was shown that in a field with $\lambda = 0$ (white noise) the slope-area relationship was shifted downwards towards smaller channel slopes by a factor of $10^{\alpha/4n}$. There was, however, no effect on the scaling exponent, θ.

Imagine now that we have a correlated erosivity field in which the relative softness of the material is a strictly increasing or decreasing function of distance from the outlet. This will occur in the event of vertical stratification and may also occur in simulations where the value of λ is comparable in magnitude to the scale of the domain. Consider three consecutive pixels located along the channel network. Let us number these three pixels 1, 2, and 3 starting from the pixel located furthest from the outlet. We will consider first the case of material softness *decreasing* with distance from the outlet. In this case, the value of $\beta_1 < \beta_2 < \beta_3$ and at dynamic equilibrium conditions we can determine the fluvial dominated slope-area relation from:

$$S = \left(\frac{U}{\beta_x}\right)^{\frac{1}{n}} A^{\frac{-m}{n}} \tag{7.5}$$

which results in the slope-area relationship being shifted vertically consistent with the softness corresponding to each pixel. We can consider each of these points to define a "line of constant geology" which would be the overall slope-area relationship if the material were homogeneous. However, since a trend in the geology exists, each pixel will individually satisfy its own fluvial equilibrium relationship. At the same time, cumulative area will be increasing as we travel towards the outlet from pixel 1 to pixel 3. Thus, $A_1 < A_2 < A_3$, so there will also be a decrease in slope as we travel from pixel 1 to 3 simply because slope decreases with increasing cumulative area. The resulting value of θ thus represents a composite effect of both the rate at which cumulative area is increasing along the channel network and the rate at which the material softness is changing. One possible realization of this effect is shown in Figure 7-12. In this case, it is clear that the observed value of $|\theta|$ for the correlated erosivity system is greater than that for any of the "constant geology" systems ($|\theta_{obs}| > |\theta_{const}|$). By a similar argument, we would observe a decrease in the observed value of $|\theta|$ if the material softness is uniformly *increasing* with distance from the outlet.

To summarize the situations that will influence the value of θ:

- $|\theta_{obs}| < |\theta_{const}|$ when:
    1. Vertical stratification with $\xi > 0$.
    2. Horizontal correlation with material softness increasing with distance from the outlet.
- $|\theta_{obs}| > |\theta_{const}|$ when:
    1. Vertical stratification with $\xi < 0$.

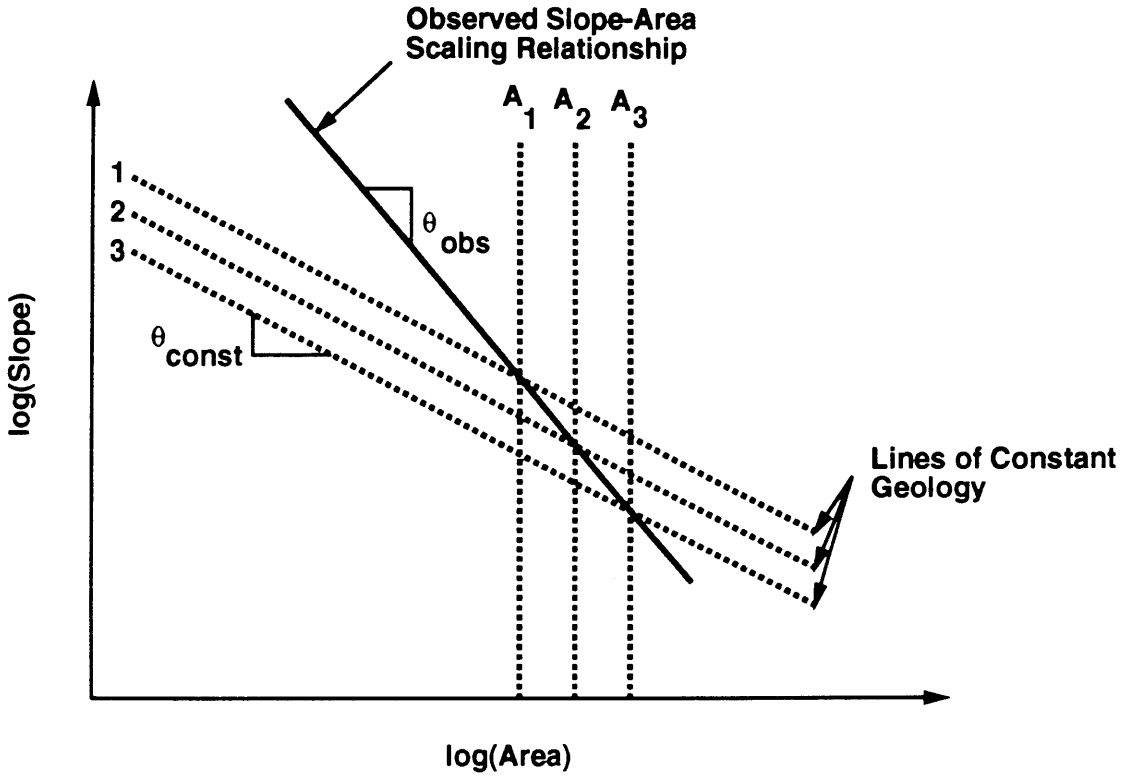

Figure 7-12: Slope-Area relationship effect on θ in an erosivity field which is strictly decreasing in its softness as one travels away from the outlet.

2. Horizontal correlation with material softness decreasing with distance from the outlet.

The case enumerated above in which $|\theta_{obs}| > |\theta_{const}|$ leads to an interesting result if taken to the extreme. If the change in material strength is great enough, it is possible to develop conditions in which slope would actually increase with cumulative area (i.e. $\theta > 0$). This is certainly not observed in any of the terrain we have analyzed. Most likely, it occurs over very short horizontal scales but is not persistent enough to influence analysis of basins at the scale we are investigating.

Both the aggregation pattern and the structure of the erosivity field will affect the actual value of θ_{obs}. The aggregation pattern will influence the horizontal spacing of A_1, A_2, and A_3. The rate at which the softness is changing with distance will influence the vertical spacing of the "lines of constant geology" associated with systems 1, 2, and 3. For the case of material decreasing in softness with distance from the outlet, both a slower rate of aggregation and a faster rate of change of material softness will tend to make θ more negative. The opposite is true if material softness is increasing with distance from the outlet. Notice also, that depending on the regularity of the aggregation rate and the change in material softness, the observed slope-area relationship may not be a simple power law relation. This argument is consistent with the results shown by Willgoose (1994c).

7.5 Observed Hypsometric Curves

Observed hypsometric curves vary considerably depending on the geology of the region under study. Figure 7-13 illustrates just a few hypsometric curves derived from observed data. These basins will appear again in the next chapter as they form the bases for five case studies. These observed distributions illustrate the degree of variability among observed hypsometric curves.

The two uppermost curves in Figure 7-13 correspond to the Moshannon and Racoon basins. From the results presented earlier, the characteristic shape of these two curves may suggest that these basins have developed in strata which decreases in softness with depth (i.e. $\xi > 0$). This hypothesis will be confirmed during the calibration process in the next chapter. In contrast, the lowest 40 percent of the Brushy basin may be characterized by the opposite stratification pattern in which softness increases with depth.

The lithology of both the Moshannon and Racoon basins is quite similar. Both basins consist of cyclic sequences of shale, sandstone, siltstone, red beds, clay, and limestone and both are located in central to western Pennsylvania. Thus it is not surprising that they would both exhibit higher relative distributions of elevation. The lithology of the Brushy basin is shale and sandstone with thin coal beds. The land cover is relatively sparse vegetation and shallow, sandy soils. From this information, it is not possible to infer any trend in the stratigraphy.

One advantage of the basin evolution model is its potential as a tool to suggest trends in the stratigraphy. The typical mode of operations (which is explicitly illus-

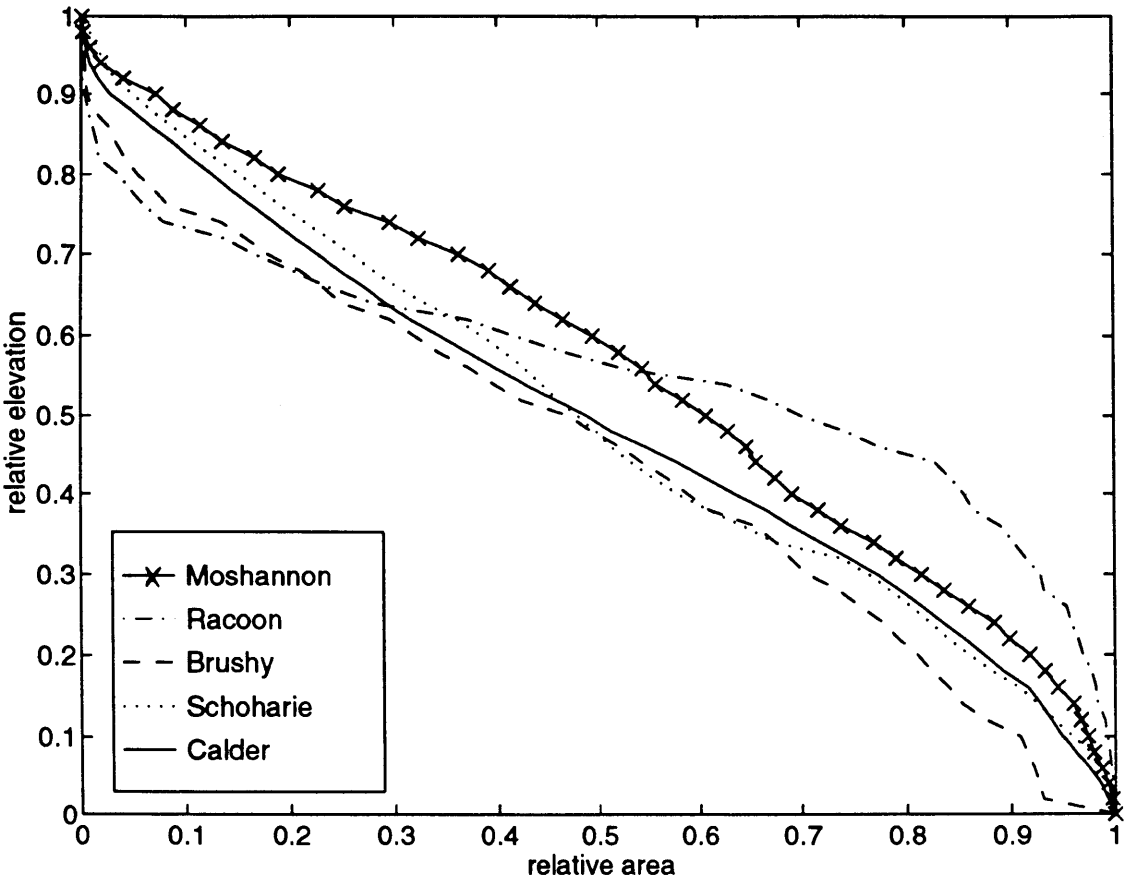

Figure 7-13: Observed hypsometric curves for various basins within the United States

trated in Appendix B) is to initially assume no trend in the stratification pattern. A simulation is performed and the hypsometric curve determined. Direct comparison of the observed and simulated hypsometric curves will indicate whether the assumption that "no-trend" assumption is appropriate. If it is not, the value of the model parameter, ξ can be modified to produce the desired shift (either towards higher or lower relative elevations) in subsequent simulations. The precise value of ξ depends on the magnitude and direction of the desired shift, and on the total relief of the basin that is to be reproduced.

7.6 Summary

The presence and form of spatially variable erosivity has a strong effect on the hypsometric curve. Two different forms of varying erosivity were considered: vertical stratification and horizontal correlation. Both structures produced hypsometric distributions which could vary considerably from the prototypical distribution.

Vertical stratification may shift the hypsometric curve towards a higher or lower distribution of elevations depending primarily on whether soft material underlies hard or vice versa. Hard material underlying soft tends to shift the distribution of elevations higher while the opposite is true when soft material underlies hard.

Correlation in the horizontal tends to shift the hypsometric curve towards lower elevations when the correlation scale is comparable to the scale of simulation. As correlation scale increases or decreases from this intermediate value the tendency of the hypsometric distribution is to approach the prototypical distribution. This tendency was shown to depend on two competing forces: the raw correlation scale of the erosivity field and the dependency of the variance of the erosivity scale on this correlation scale.

The issue of correlated erosivity and its effect on θ was addressed and it was shown that the value of θ_{obs} will be increased or decreased relative to $\theta = m/n$ in systems where the material softness is strictly increasing or decreasing, respectively as one travels away from the outlet.

Examination of hypsometric curves obtained from observed DEMs indicates that there is a fair degree of variation in the hypsometric distributions observed in nature. The results presented in this chapter imply several different erosivity field structures which may be employed to account for these natural variations.

Chapter 8

Estimation of Model Parameters

In the previous chapters we have seen the influence of each of the model parameters on simulated domains. We have seen how the balance between diffusive and fluvial sediment transport affects the hillslope scale, how the value of the slope-area scaling exponent, θ influences the degree of channel incision, and finally we have seen how heterogeneity in soil erosivity introduces variability with a structure quite similar to that observed in natural systems. This chapter will address the issue of how to estimate optimal values of each of the model parameters from observed data.

As stated previously and demonstrated in Ijjasz-Vasquez *et al.* (1992), the deterministic reproduction of topography is an impossibility due to the lack of knowledge of initial conditions and the inherent sensitivity of the basin evolution process to the initial state of a system. Since deterministic reproduction cannot be achieved, we must resort to producing a topography which matches the primary statistics of the observed basin. We will assert that a simulated domain which matches the observed domain in measures of its slope-area relationship, its cumulative area distribution, and its hypsometric distribution is well calibrated. Satisfying the slope-area relationship is a rather simple matter of determining the observed value of β and θ by inspection of the slope-area relationship for the observed basin. This issue is clouded somewhat by the presence of heterogeneity and stratification which introduces a bias in β and also possibly in θ although as a first estimate these problems can be neglected. Satisfying the hypsometric distribution is also a rather simple matter of introducing stratification although this too can be neglected initially. The real issue is matching the cumulative area distribution which is sensitive to the relative strengths of D and β and to the degree of heterogeneity quantified by the parameter α. We will see that matching this distribution is at the heart of producing simulated domains which are comparable to observed ones.

From the argument given above, the major task in the goal to estimate model parameters is to match the cumulative area distribution. In a numerical optimization sense this amounts to:

$$min\ f = \sum_{A} [P_{sim}(A \geq a) - P_{obs}(A \geq a)]^2 \tag{8.1}$$

where a certain set of values of $(\theta, D, \beta, \alpha, \lambda, \xi)$ produce the cumulative area distribu-

tion denoted by $P_{sim}(A \geq a)$. A set of parameter values which minimizes the value of f in equation 8.1 would be the optimized parameter values.

8.1 An Off-Line Version of the Evolution Model

In theory, the basin evolution model could be incorporated into an optimization program whose objective function would be precisely that shown in equation 8.1. The optimization would proceed from some initial set of parameter estimates and systematically perturb each parameter in an effort to minimize f. Depending on the quality of the initial parameter estimates the optimization could easily involve 20-100 perturbation steps before reaching an optimum, even if the initial estimates were quite good. Considering each simulation takes several hours to perform, this method of optimization could take more than a week to complete. This method of calibration does not represent a tractable alternative.

An off-line version of the model was created which contains the same information as that of the actual evolution model. This information was determined from a series of 120 simulations in which D, β, α, and θ were varied over a physically realistic range of values. Each simulation involved evolution of a 30x30 domain from initially flat conditions to dynamic equilibrium. The cumulative area distribution for each simulation was then determined. Although a 30x30 drainage system is not large, our area of concern is the aggregation pattern of pixels draining relatively small areas ($A \leq 20$). The aggregation pattern of these pixels is crucially dependent on the chosen values of D, β, α, and θ. A 30x30 system is adequate to properly define the distribution of these pixels.

Using the data collected from these 120 simulations, a series of regression models were calibrated with the following form:

$$P_{sim}(A \geq a) = c(A, \alpha, \theta) D^{\gamma_1(A,\alpha,\theta)} \beta^{\gamma_2(A,\alpha,\theta)} \tag{8.2}$$

where ($2 \leq A \leq 20$). No model is needed for $A = 1$ since $P(A \geq 1))$ is unity for all systems. The calibrated coefficients: c, γ_1, and γ_2 describe functions which vary with A, α, and θ. Figures 8-1, 8-2, and 8-3 show the calibrated coefficients as a function of area, A, and varying among a family of curves corresponding to different values of α.

Figure 8-1 shows how $c(A, \alpha, \theta)$ describes the mean behavior of the cumulative area distribution. Figures 8-2 and 8-3 illustrate how $D^{\gamma_1(A,\alpha,\theta)}$ and $\beta^{\gamma_2(A,\alpha,\theta)}$ contribute multiplicative factors which adjust the distribution up or down in opposition to one another. The largest variations in γ_1 and γ_2, which occur when $\alpha = 0$ indicate that D and β have the greatest influence on the cumulative area distribution when the material is spatially homogeneous. As α increases, their effect is diminished as had been observed from direct examination of the cumulative area distributions of the simulated domains. Figures 8-1 through 8-3 were generated with $\theta = 0.50$. To illustrate the effect of θ, Figure 8-4 shows the γ_2 function for $\theta = 0.25$.

The curves shown in Figures 8-1 through 8-4, which are determined directly from the observed model performance, now become an off-line representation of the cumulative area distribution that would be expected from a given combination of D, β,

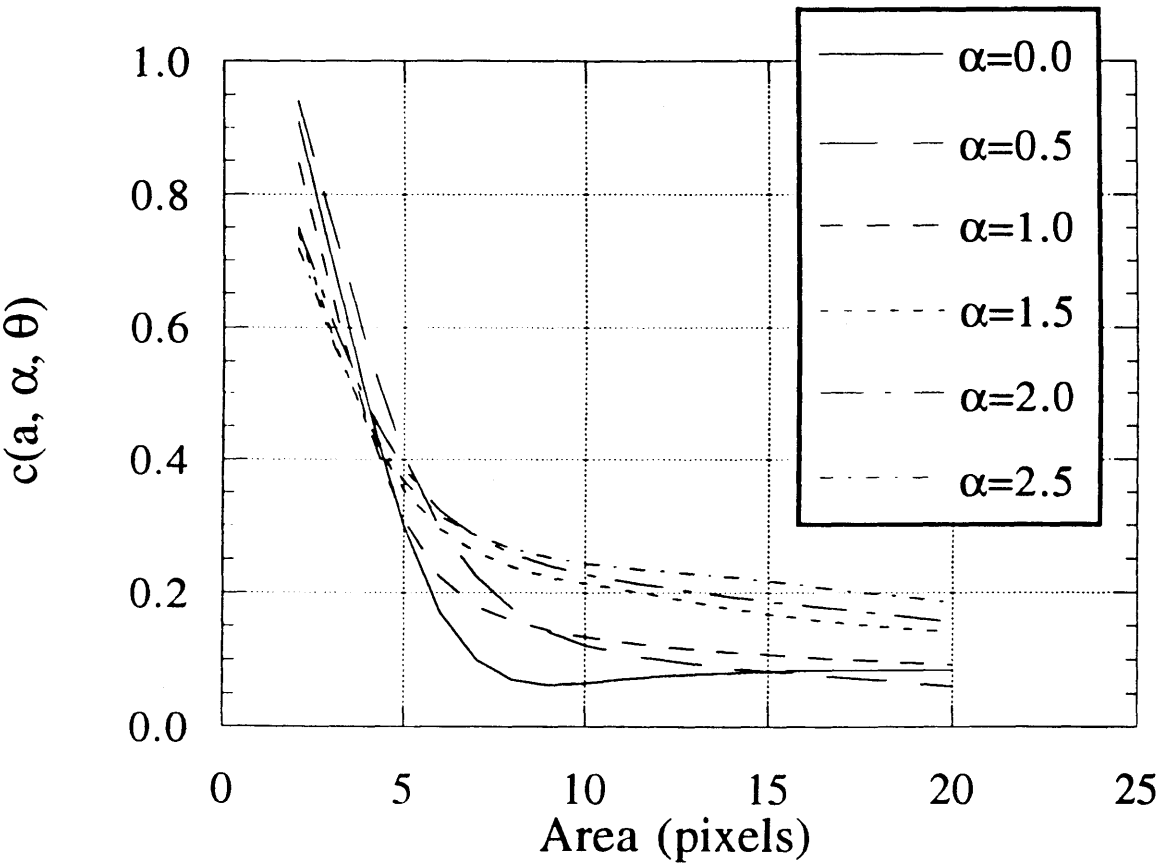

Figure 8-1: Derived $c(A, \alpha, \theta)$ relationship for $\theta = 0.5$.

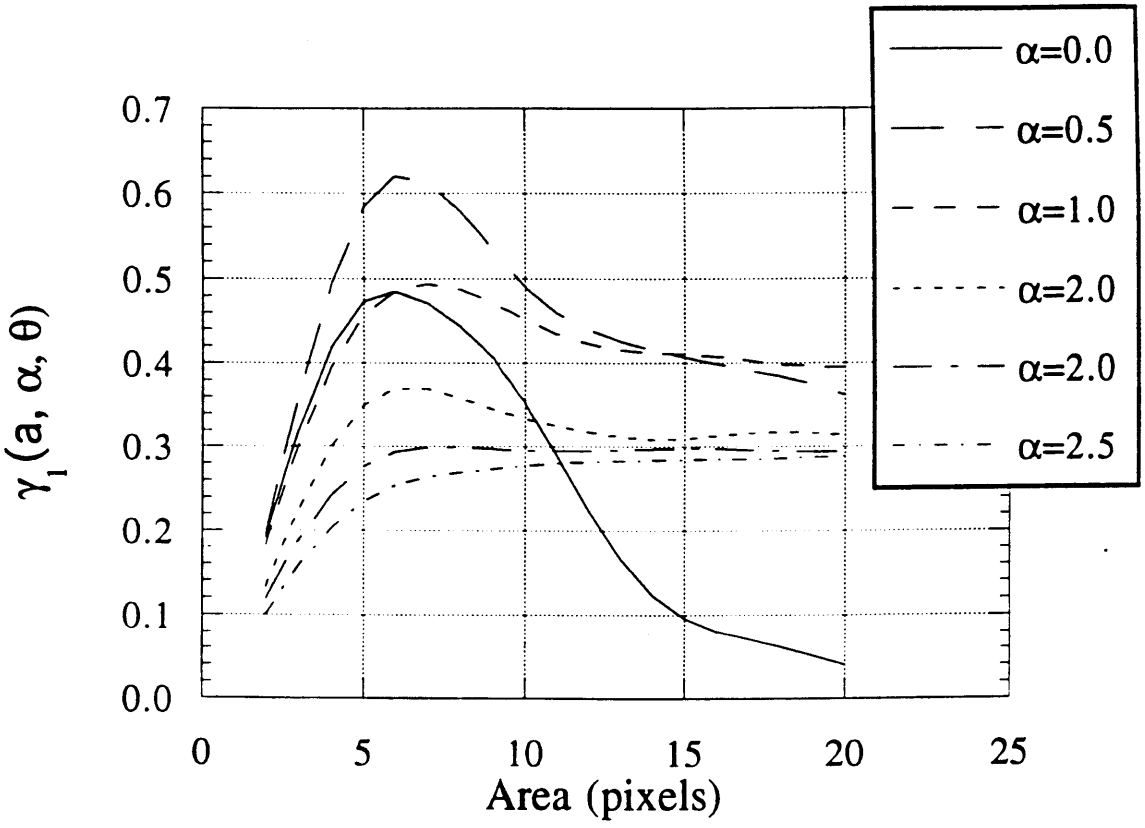

Figure 8-2: Derived $\gamma_1(A, \alpha, \theta)$ relationship for $\theta = 0.5$.

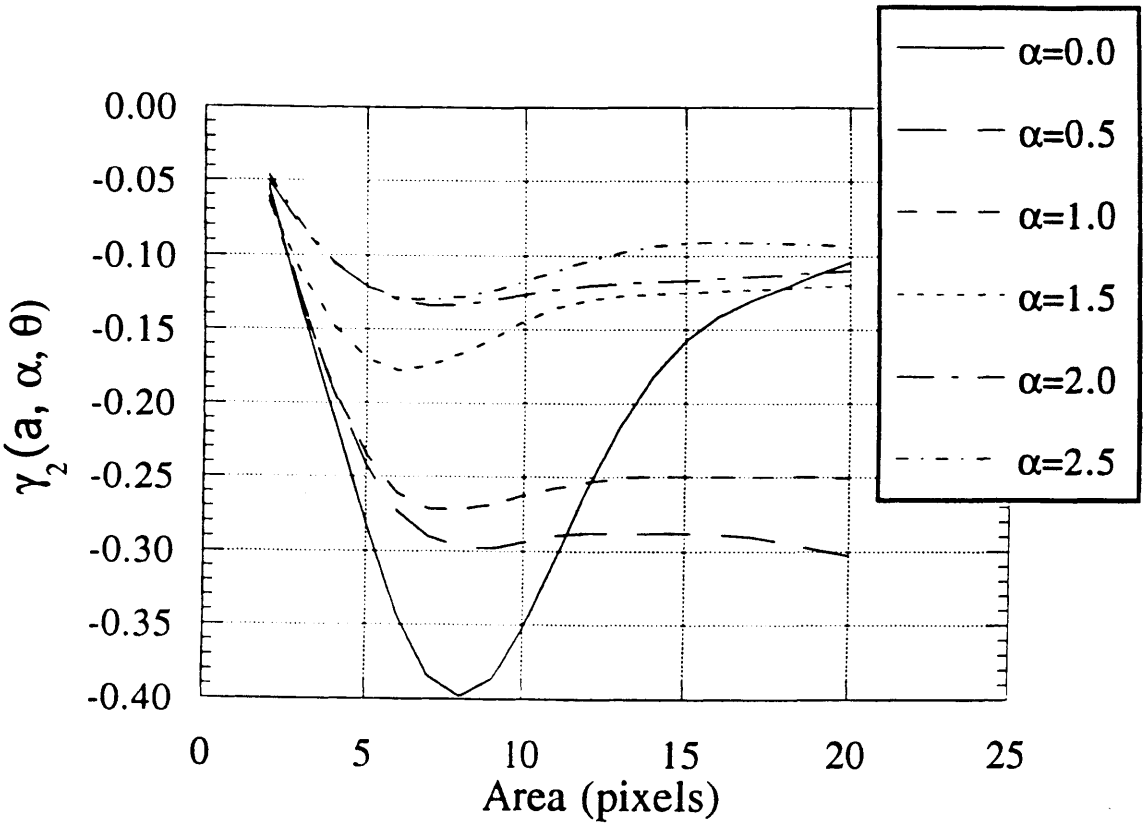

Figure 8-3: Derived $\gamma_2(A, \alpha, \theta)$ relationship for $\theta = 0.5$.

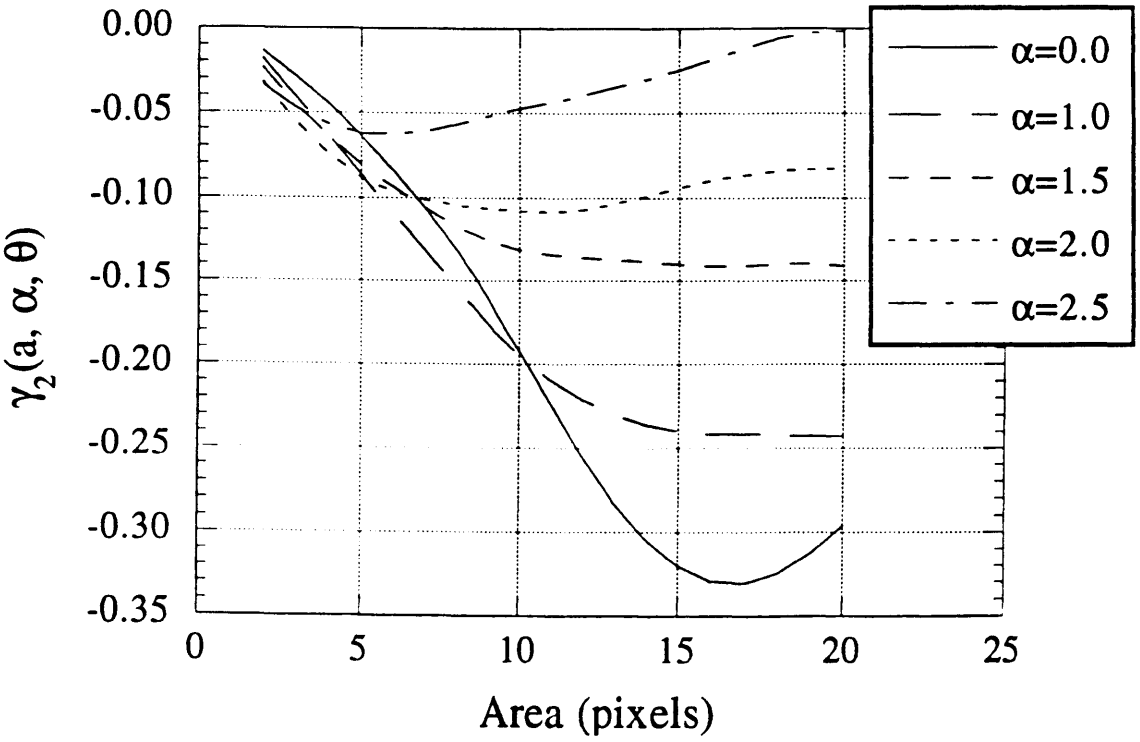

Figure 8-4: Derived $\gamma_2(A, \alpha, \theta)$ relationship for $\theta = 0.25$.

and α. We are now prepared to perform the optimization cited in equation 8.1. The difference now is that we are not dependent on a slow evolution model to optimize upon, but rather we have a fast parameterization of how the evolution model would behave. The optimization now becomes:

$$min\ f = \sum_{A=2}^{20} \left[c(A, \hat{\alpha}, \hat{\theta}) \hat{D}^{\gamma_1(A,\hat{\alpha},\hat{\theta})} \hat{\beta}^{\gamma_2(A,\hat{\alpha},\hat{\theta})} - P_{obs}(A \geq a) \right]^2 \tag{8.3}$$

with $\hat{\beta}$ and $\hat{\theta}$ coming from the observed slope-area relationship and $\hat{D}$, and $\hat{\alpha}$ resulting from the optimization of f in equation 8.3. $P_{obs}(A \geq a)$ is the exceedence probability associated with the observed cumulative area distribution. Since a family of curves for varying α and θ was previously developed, linear interpolation is used to determine the value of c, γ_1, and γ_2 for α and θ between a given pair of curves shown in Figures 8-1 through 8-4.

In the final step the calibrated parameters become input to the basin evolution model and the simulated topography is measured to quantify the quality of the optimized parameter estimates in reproduction of the observed topography.

8.2 Case Studies: Reproduction of Observed Topography

Five drainage basins were chosen from different locations within the United States. Table 8.1 summarizes some information about these basins and their calibrated optimal parameter values. These basins were selected because they exhibit different topographic signatures and therefore provide a test of the robustness of the calibration procedure described in the previous section and Appendix B. Each data set was derived from U.S.G.S. digital elevation model (DEM) data sampled at a resolution of 30 meters. Basins of approximately 2000 pixels in size (roughly 1.8 km^2) were arbitrarily isolated because this size is both large enough to provide accurate measures of aggregation behavior and small enough that the evolution model can simulate the domain in a tractable length of time. Simulations presented here were performed on a DECstation 5000/200 and took 3 to 12 hours to complete, depending on the parameters of the evolution.

8.2.1 Moshannon, Pennsylvania Basin

The Moshannon drainage basin is located in central Pennsylvania on the Allegheny Front of the Appalachian Plateau. The lithology of the area is cyclic sequences of shale, sandstone, siltstone, red beds, clay, and limestone. Figure 8-5 shows a 3-D perspective of this basin. The basin is characterized by a long angular shape with a single main channel roughly centered between the basin divides. The topography is fairly diffuse with fine scale roughness. Figures 8-6 through 8-9 illustrate the simulated topography, the slope-area relationship, the cumulative area relationship, and the hypsometric distribution.

Table 8.1: Summary of Case Study Simulation Statistics

	Moshannon, PA	Racoon, PA	Brushy, AL	Schoharie, NY	Calder, ID
Calibration #	12	16	31	24	10
Area (pixels)	2025	1998	2020	2034	2066
Relief (obs, m)	141	62	59	438	572
Relief (sim, m)	142.1	65.7	60.4	417.3	572.3
θ (obs)/R^2	-0.26/0.79	-0.29/0.52	-0.43/0.85	-0.22/0.87	-0.47/0.62
θ (sim)/R^2	-0.22/0.94	-0.29/0.87	-0.41/0.96	-0.21/0.83	-0.27/0.94
$\beta^{\dagger}$	1.23×10^{-4}	2.8×10^{-4}	8.14×10^{-4}	3.81×10^{-5}	5.13×10^{-5}
$D^{\dagger}$	1.43×10^{-2}	8.4×10^{-3}	9.5×10^{-3}	6.22×10^{-2}	1.11×10^{-2}
m	0.7	0.8	0.86	0.66	0.55
α	1.6	2.0	1.9	1.5	1.0
ξ	0.02	0.04	0.0	-0.0025	-0.002
A_*	6.75	3.52	2.51	31.9	7.76

†-Nominal β and D values are given. Mean values can be calculated using equation 6.3.

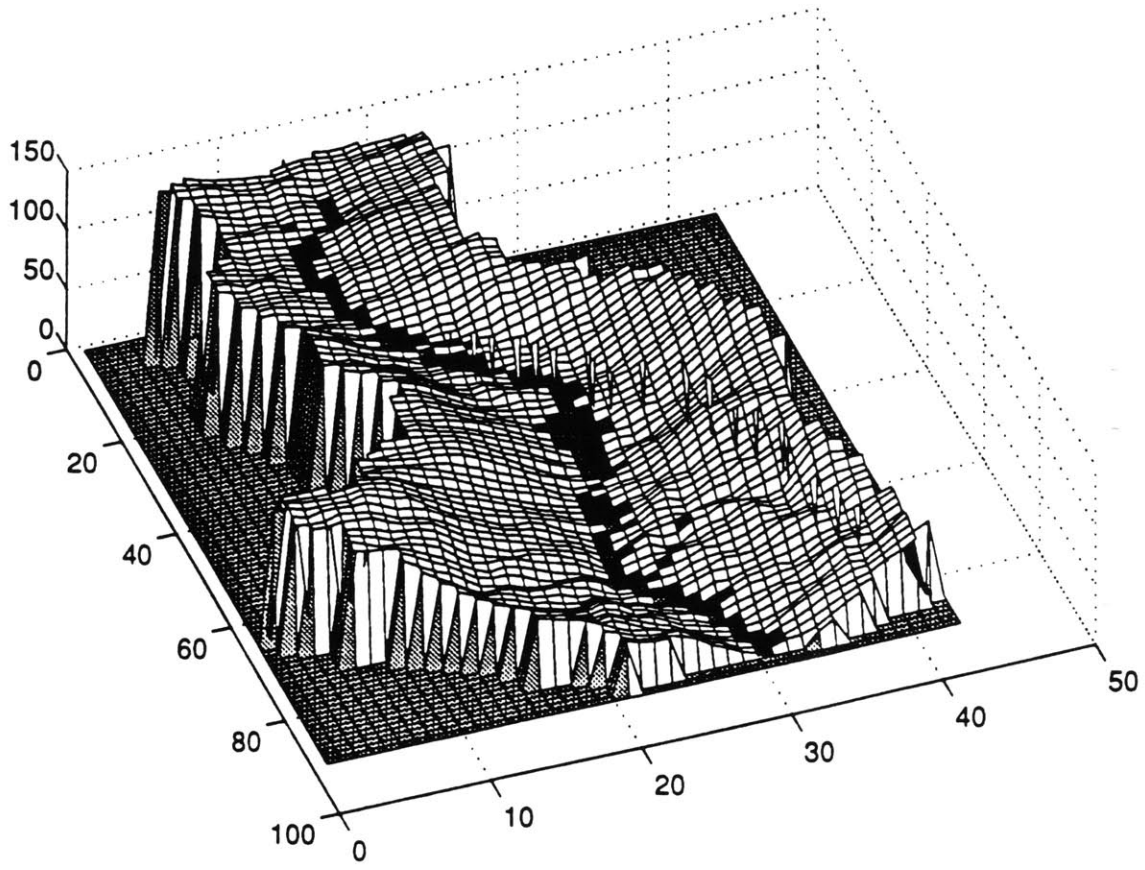

Figure 8-5: 3-D perspective of observed topography for Moshannon data set.

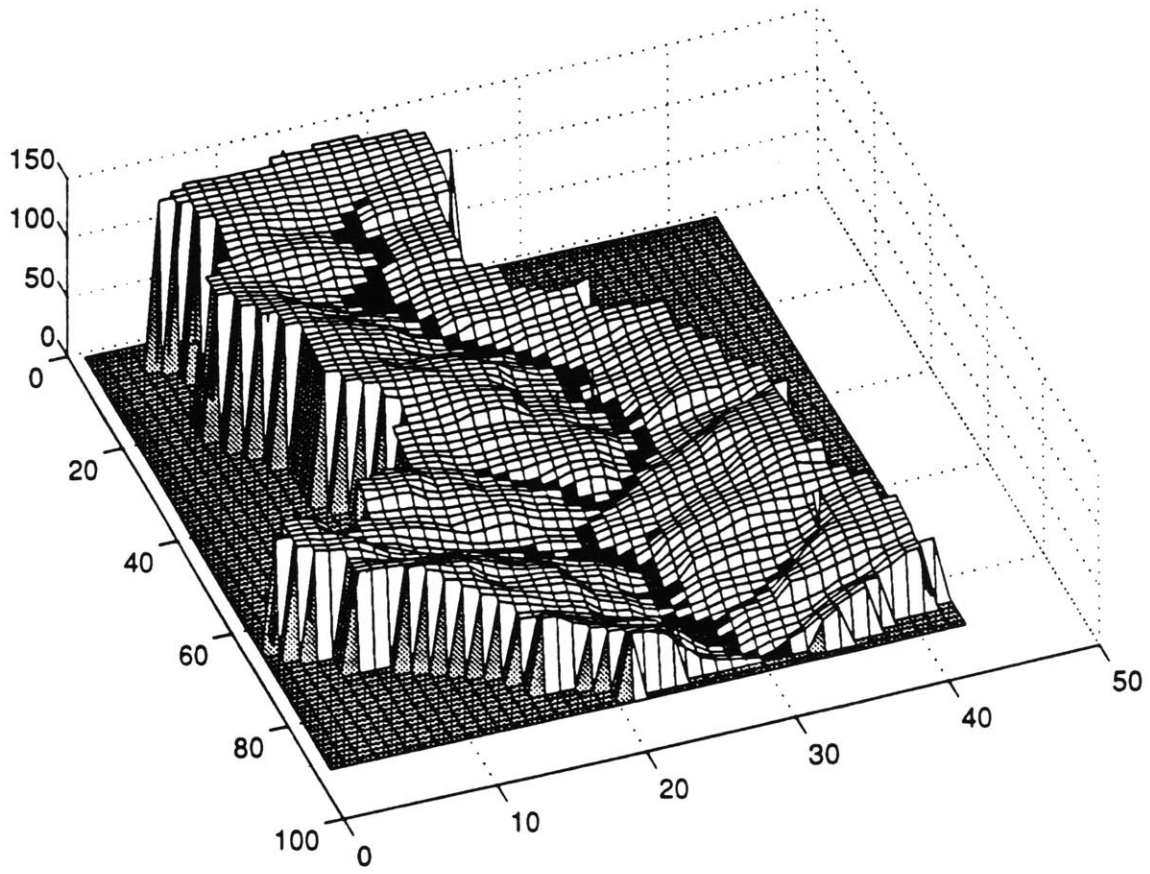

Figure 8-6: 3-D perspective of simulated topography for Moshannon domain.

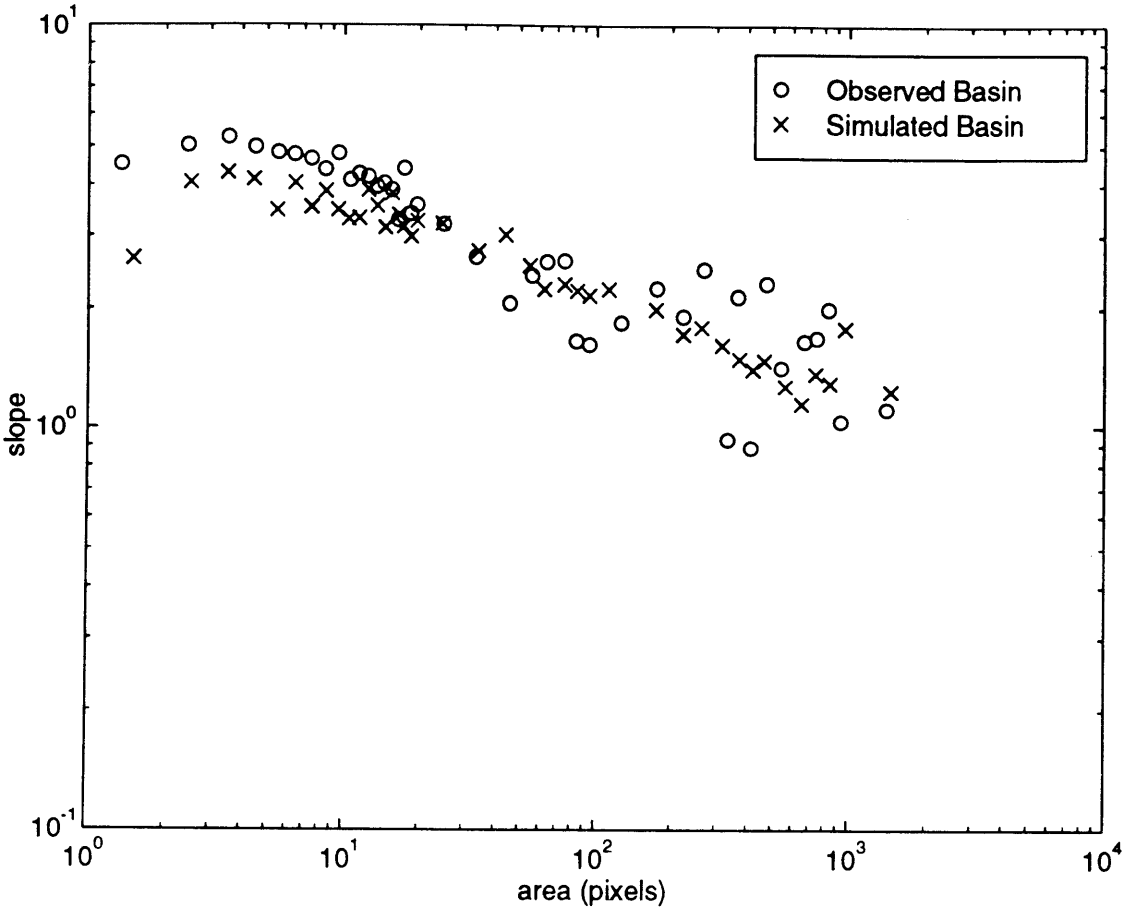

Figure 8-7: Slope-area relationships for Moshannon data set. (Shown are the relationships for the observed "o" and simulated basin "x".)

Table 8.1 shows calibrated values for β and D of 1.23 x 10^{-4} and 1.43 x 10^{-2}, respectively. These values lead to a moderate hillslope scale, A_* of 6.75 pixels. Given this hillslope scale and the long, narrow shape of the Moshannon basin, the resulting channel is essentially constrained to lie roughly centered between the drainage divides to either side.

The observed slope-area scaling exponent, $\theta_{obs} = -0.26$ is the second smallest (in absolute value) among the case studies. We observed earlier in Chapter 3 how the smaller θ values lead to less incised channels, and this is the case on examination of either the observed or simulated topographies.

We see that a positive value of $\xi = 0.02$ is used. This indicates that some vertical stratification was needed to help reproduce the hypsometric distribution. Since ξ is positive this indicates that the strata becomes increasingly harder with depth. Over the depth of the simulated domain this would lead to an increase in material hardness of:

$$2^{(\Re)(\xi)} = 2^{(142.1)(0.02)} = 7.2$$

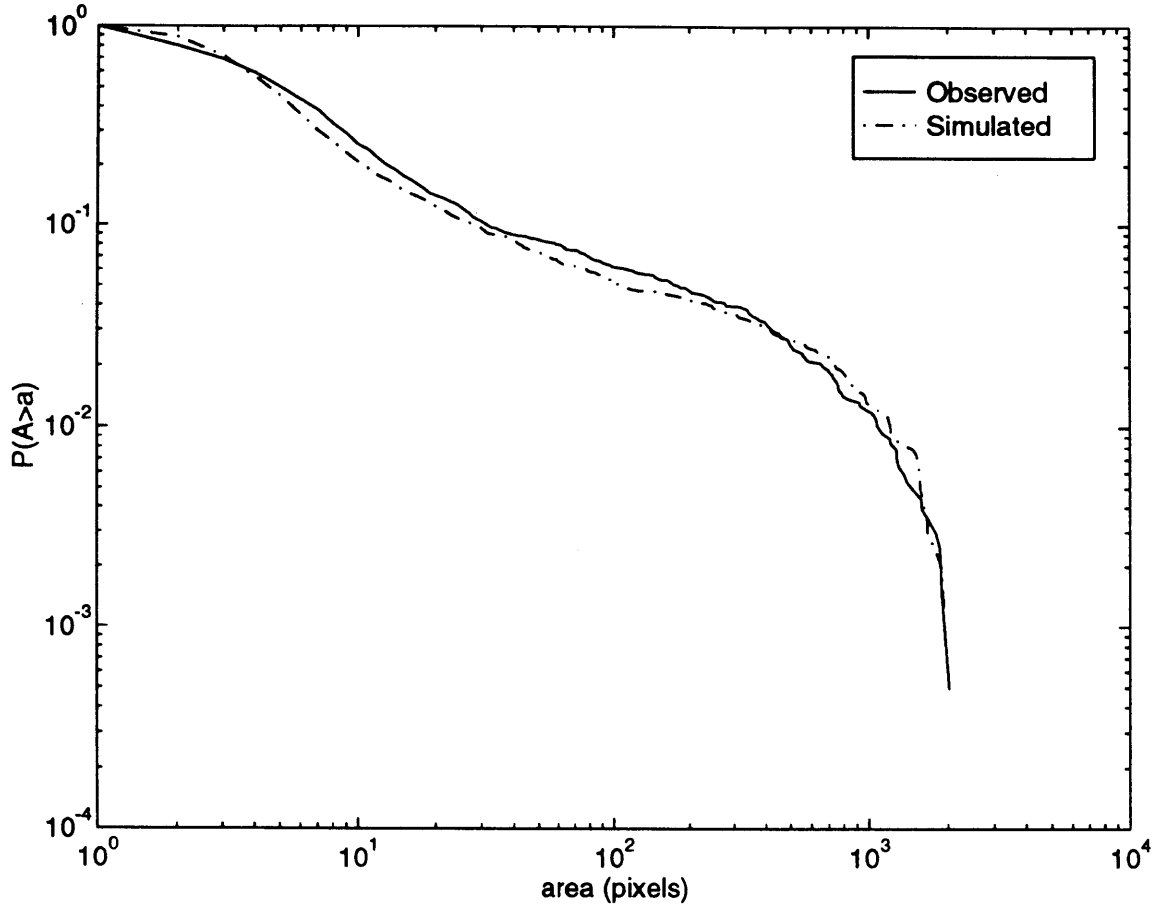

Figure 8-8: Observed and simulated cumulative area distributions for Moshannon data set.

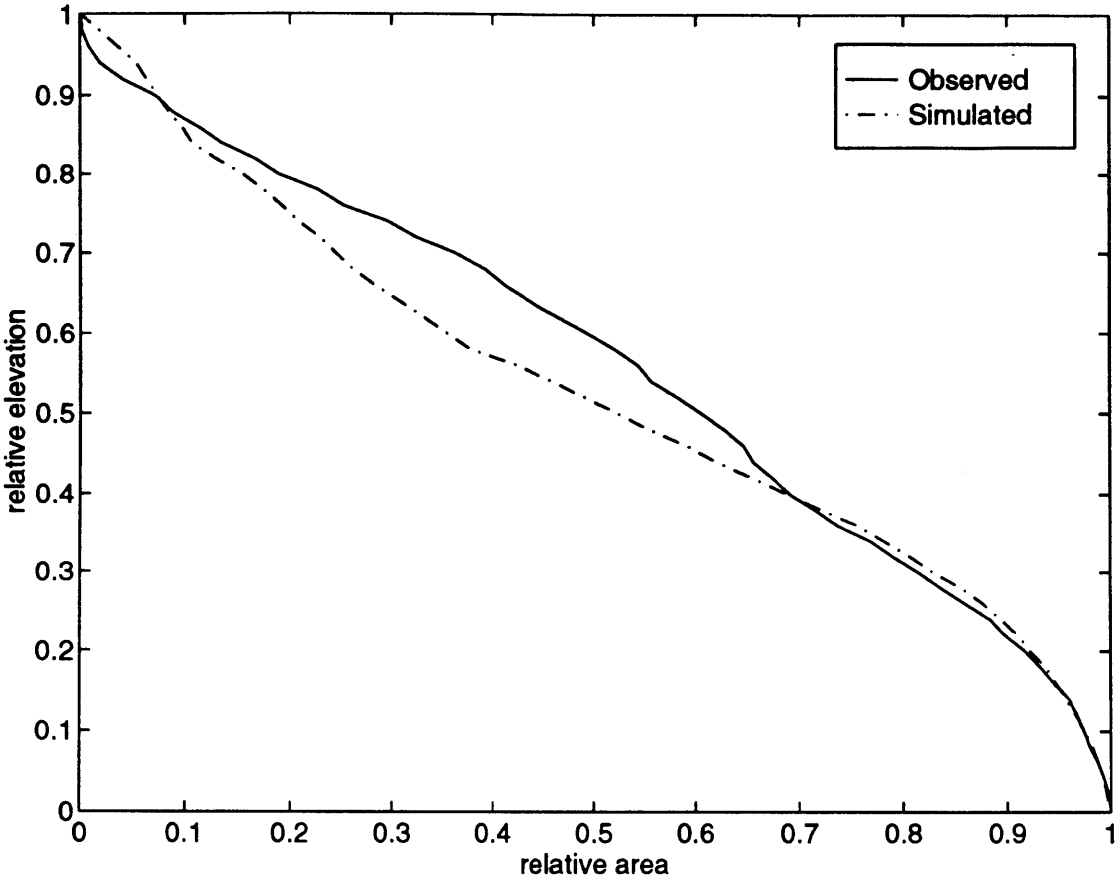

Figure 8-9: Observed and simulated hypsometric distributions for Moshannon data set.

over the vertical range of the basin. In other words the material at the outlet is, on average, 7.2 times harder than the material at the highest elevations within the basin.

This also has an effect on θ. From theory, θ would be given by:

$$\theta = \frac{-m}{n} = \frac{-0.7}{2.0} = -0.35$$

However, the observed and simulated values of θ are both approximately -0.25. This is the bias previously discussed in Chapter 7 and illustrated in Figure 7-12. When ξ is positive the simulated value of $|\theta|$ will be smaller than the theoretical value.

Concerning the quality of the reproduction of the observed topography, we see that the overall relief of the observed system is 141 meters versus the simulated relief of 142.1 meters, which is quite comparable. The observed and simulated cumulative area distributions are quite comparable as shown in Figure 8-7. There is some discrepancy between the observed and simulated hypsometric distributions as indicated by Figure 8-9. From relative elevations of 0.4 to 0.8 the observed system has significantly

greater elevations than the simulated system. This discrepancy could be reduced by introducing a more complicated stratification structure to the simulated system. For instance, if we allowed the material softness to decrease more rapidly with depth for relative elevations 0.4 to 0.8, this would shift the simulated hypsometric towards the observed one. Whether or not it is merited to introduce such vertical structure to the simulation, given our knowledge of the lithography, is another matter.

8.2.2 Racoon, Pennsylvania Basin

The Racoon drainage basin is located in western Pennsylvania just northeast of Pittsburgh. The lithology of the area is similar to that of the Moshannon basin with cyclic sequences of shale, sandstone, siltstone, red beds, clay, and limestone.

This basin is the subject of the explicit parameter estimation process demonstrated in Appendix B. We refer the reader to this appendix for the observed data and simulated results.

In contrast to the Moshannon basin, the Racoon basin exhibits a much more complex channel structure and more rugged terrain. This is reflected primarily in the value of the hillslope scale, A_* which is 3.52 pixels; almost half that of the Moshannon simulation and the second smallest hillslope scale of any of the case studies. Given the broader shape of the Racoon basin (as compared to the Moshannon basin) and the smaller hillslope scale, it is not surprising to see that both the observed and simulated channel networks are much more complex in structure than the single main stream that drains the Moshannon basin.

8.2.3 Brushy, Alabama Basin

Located in Bawkhead National Forest, the Brushy drainage basin (pictured in Figure 8-10) is located in north-central Alabama on the Cumberland Plateau. The lithology of the area is shale and sandstone with thin coal beds. The land cover is relatively sparse vegetation and shallow, sandy soils.

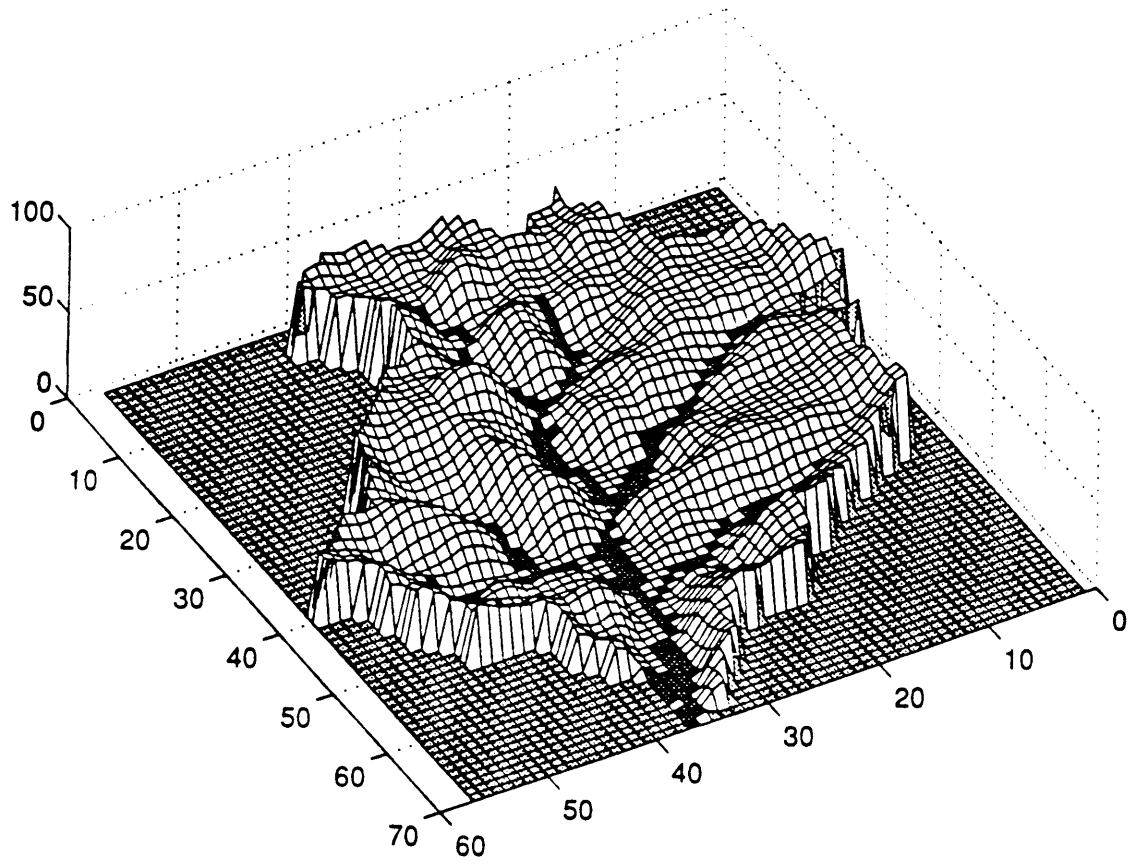

Figure 8-10: 3-D perspective of observed topography for Brushy data set.

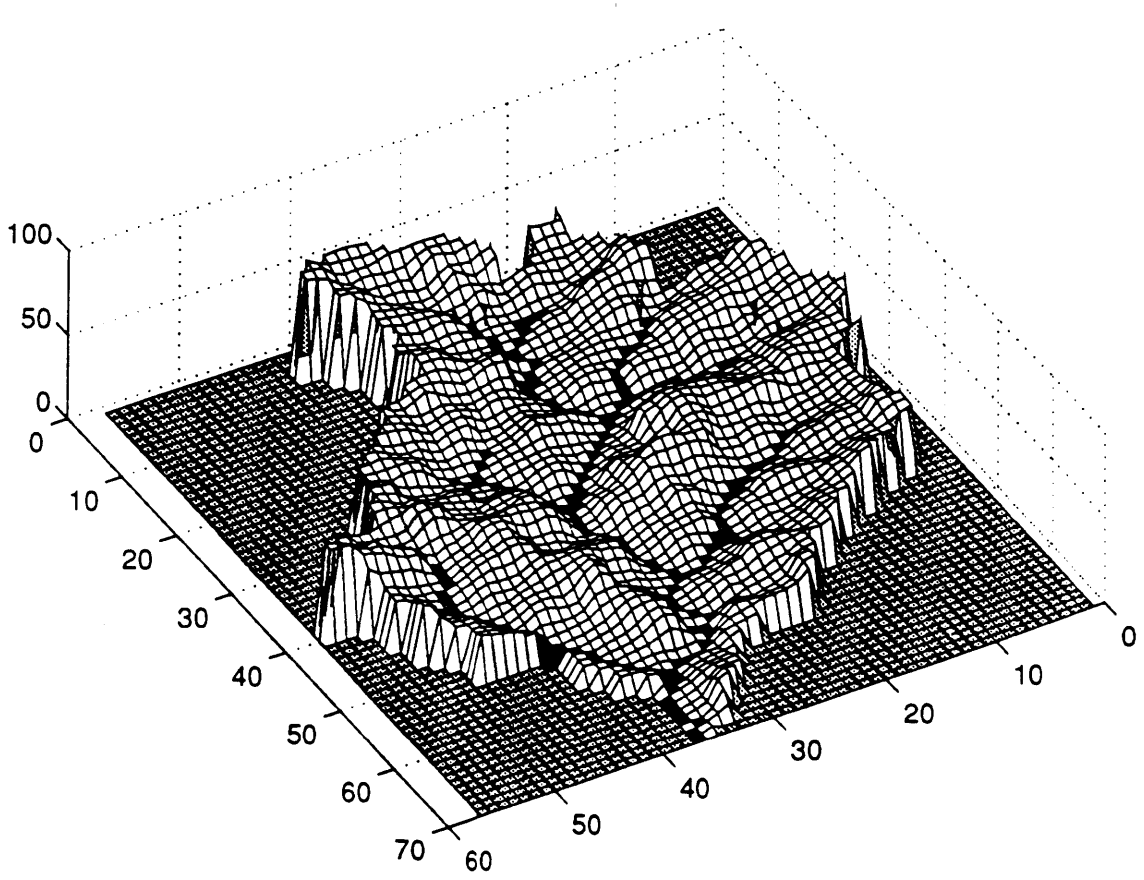

Figure 8-11: 3-D perspective of simulated topography for Brushy domain.

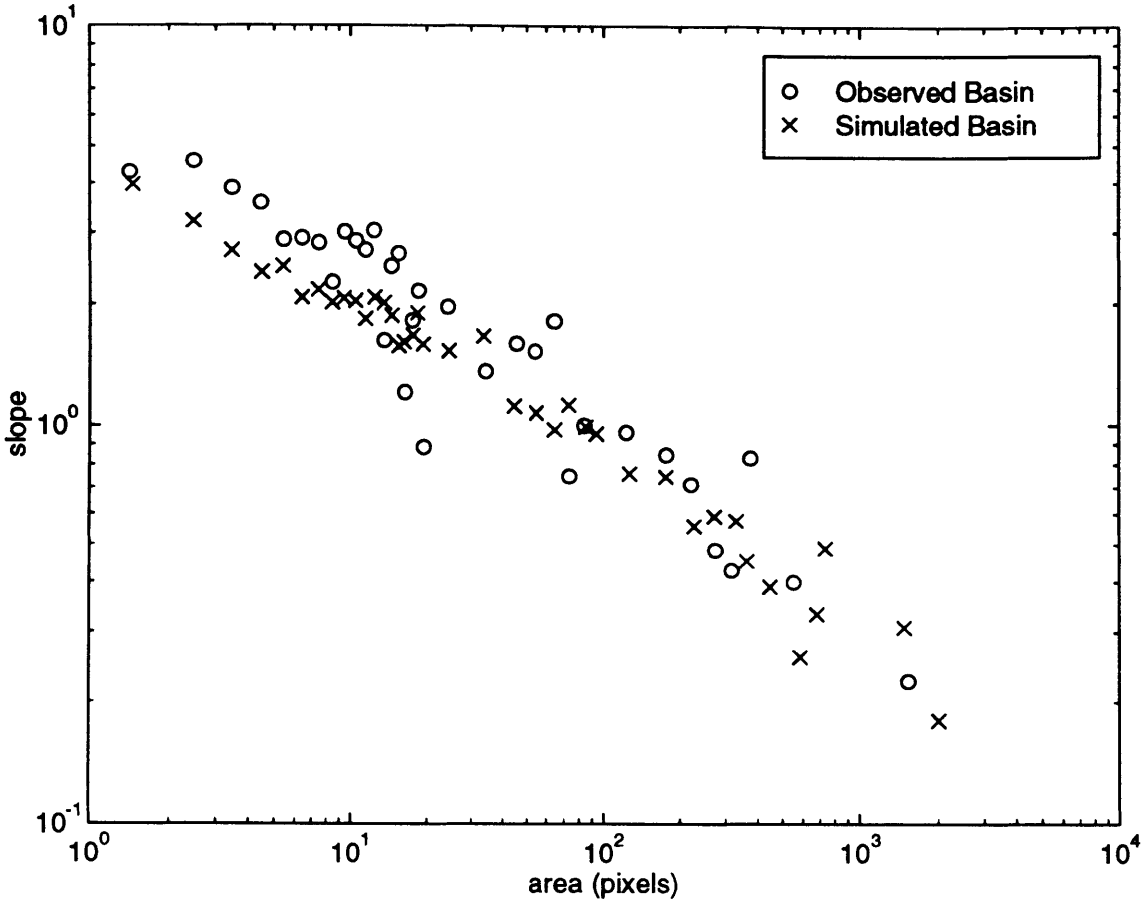

Figure 8-12: Slope-area relationships for Brushy data set. (Shown are the relationships for the observed "o" and simulated basin "x".)

Table 8.1 shows that β and D are 8.14×10^{-4} and 9.5×10^{-3}, respectively. This leads to a hillslope scale of $A_* = 2.51$ pixels which is the smallest of the five case study simulations. We would therefore expect the Brushy observed and simulated basins to be the most dissected by channels of any of the case studies. This qualitatively holds true from examination of the four other observed drainage basins.

The observed and simulated values of θ are -0.43 and -0.41, respectively. These are the largest values in absolute terms (omitting the unrealistically large value for the Calder basin, discussed later) of any of the five case studies. These large values for θ are reflected in the topography which exhibits the deepest degree of channel incision of any of the five case studies.

As was the case for the Racoon basin, a relatively high value of $\alpha = 1.9$ is necessary to produce the more complicated channel network and also the essentially power-law distribution of cumulative areas as indicated in Figure 8-13. When A_* is relatively small and α is relatively large, the resulting cumulative area distribution is most likely to be power-law distributed, even at the smallest cumulative areas.

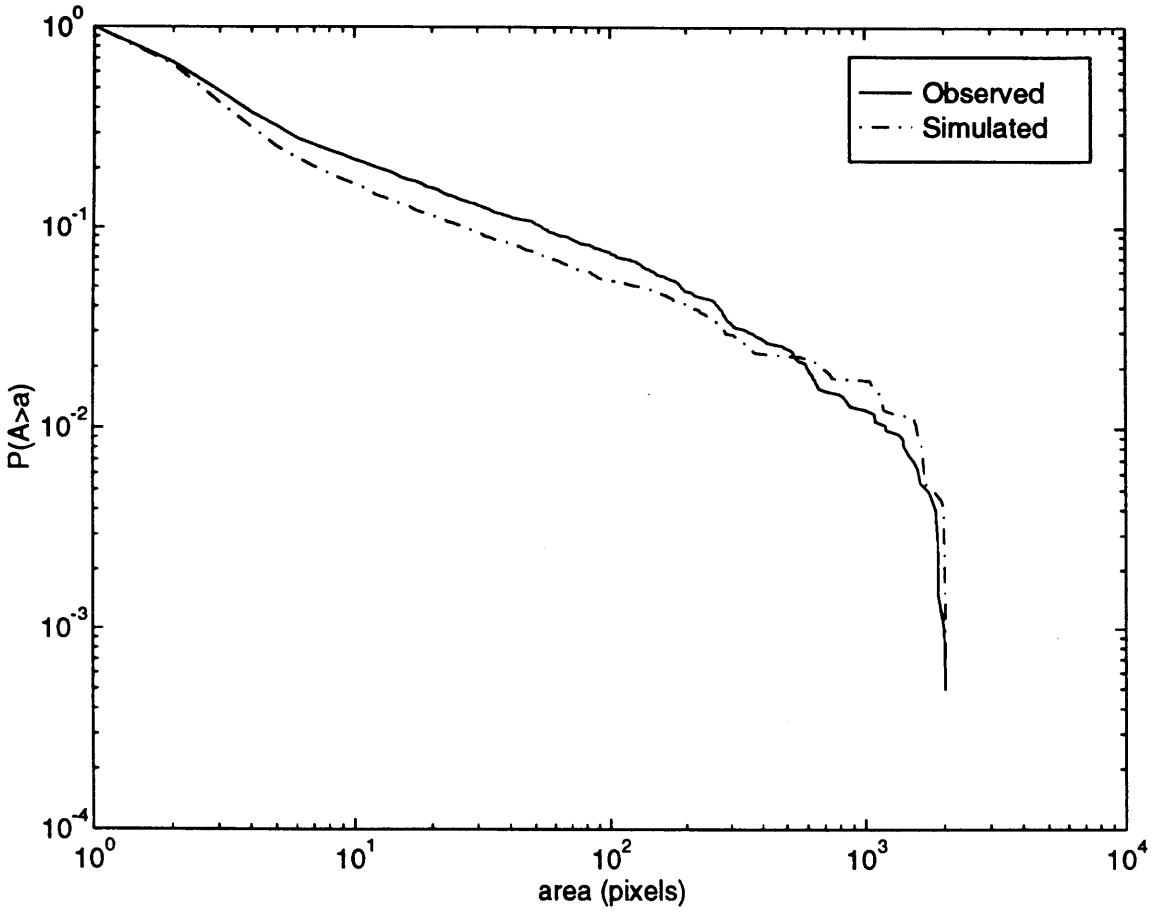

Figure 8-13: Observed and simulated cumulative area distributions for Brushy data set.

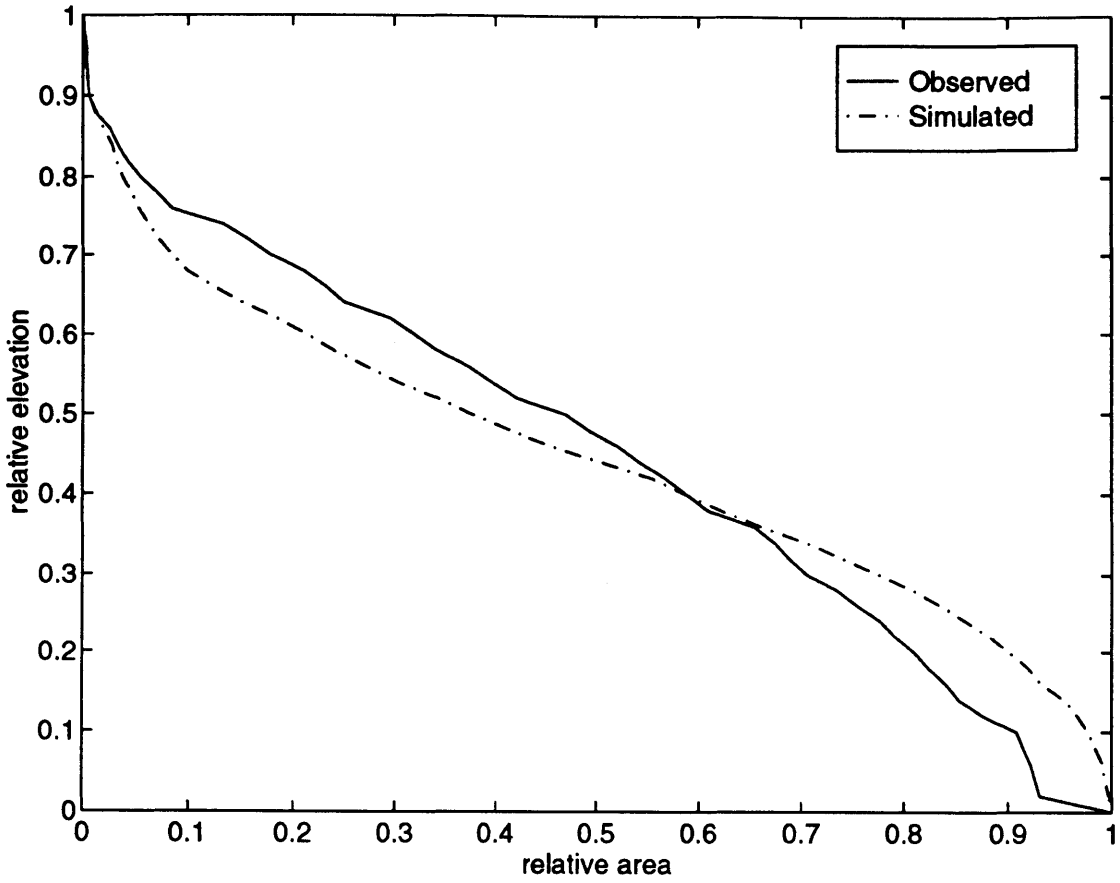

Figure 8-14: Observed and simulated hypsometric distributions for Brushy data set.

The observed and simulated relief for the Brushy basin compare favorably at 59 and 60.4 meters, respectively. The calibrated value of $\xi = 0.0$ indicates that no significant trend in vertical stratification was needed to reproduce the observed hypsometric distribution. As in the case for the Moshannon case study, we might argue that the portions of the simulated basin show significant deviation from the observed hypsometric distribution, shown in Figure 8-14. This could be rectified by modifying the soil strata to include a harder, upper 60 percent of the basin and a softer, lower 40 percent of the basin.

8.2.4 Schoharie, New York Basin

The Schoharie drainage basin (pictured in Figure 8-15) is located in east-central New York state in the Catskill mountains. This basin exhibits the largest hillslope scale (by far), $A_* = 31.9$, of any of the case studies. This large hillslope scale indicates a topography which should be quite smooth.

The Schoharie basin exhibits the second greatest relief of 438 meters (simulated 417.3 meters). Modeling this magnitude of relief is achieved by using a very small

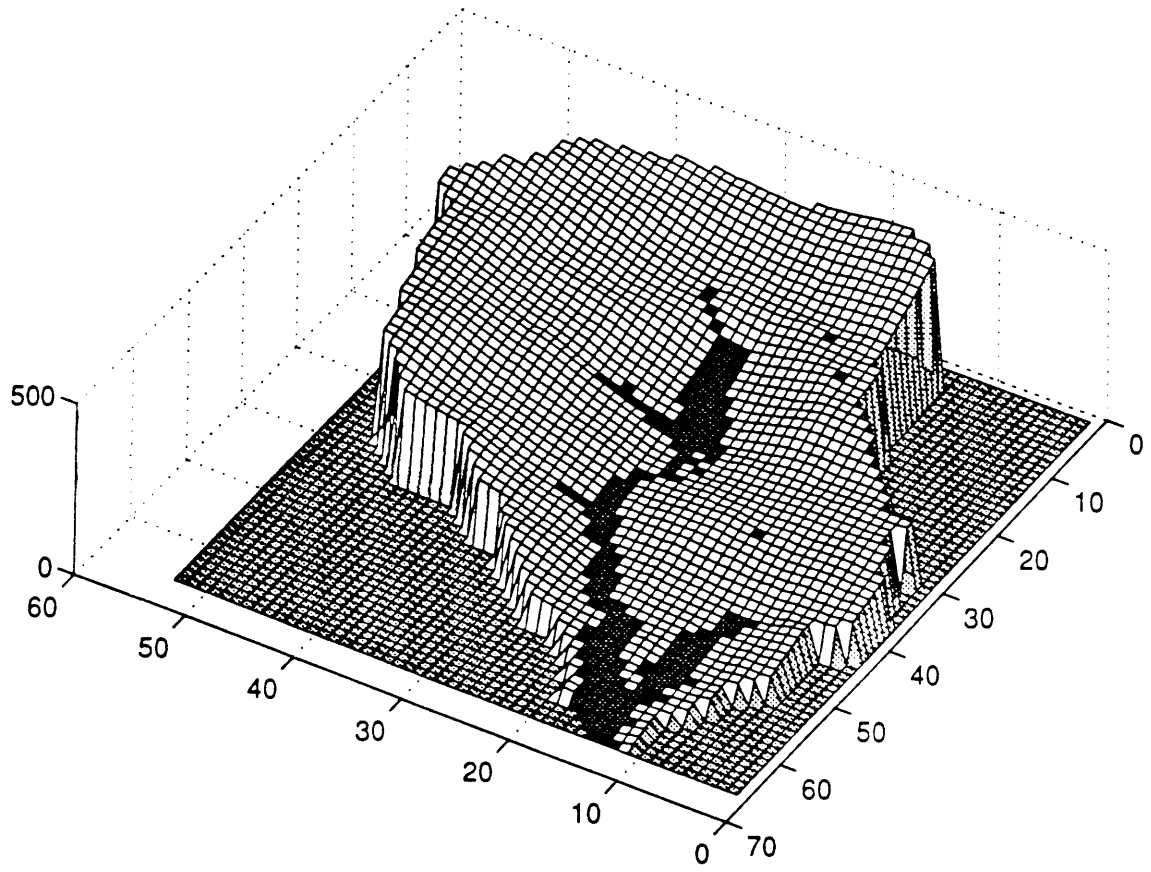

Figure 8-15: 3-D perspective of observed topography for Schoharie data set.

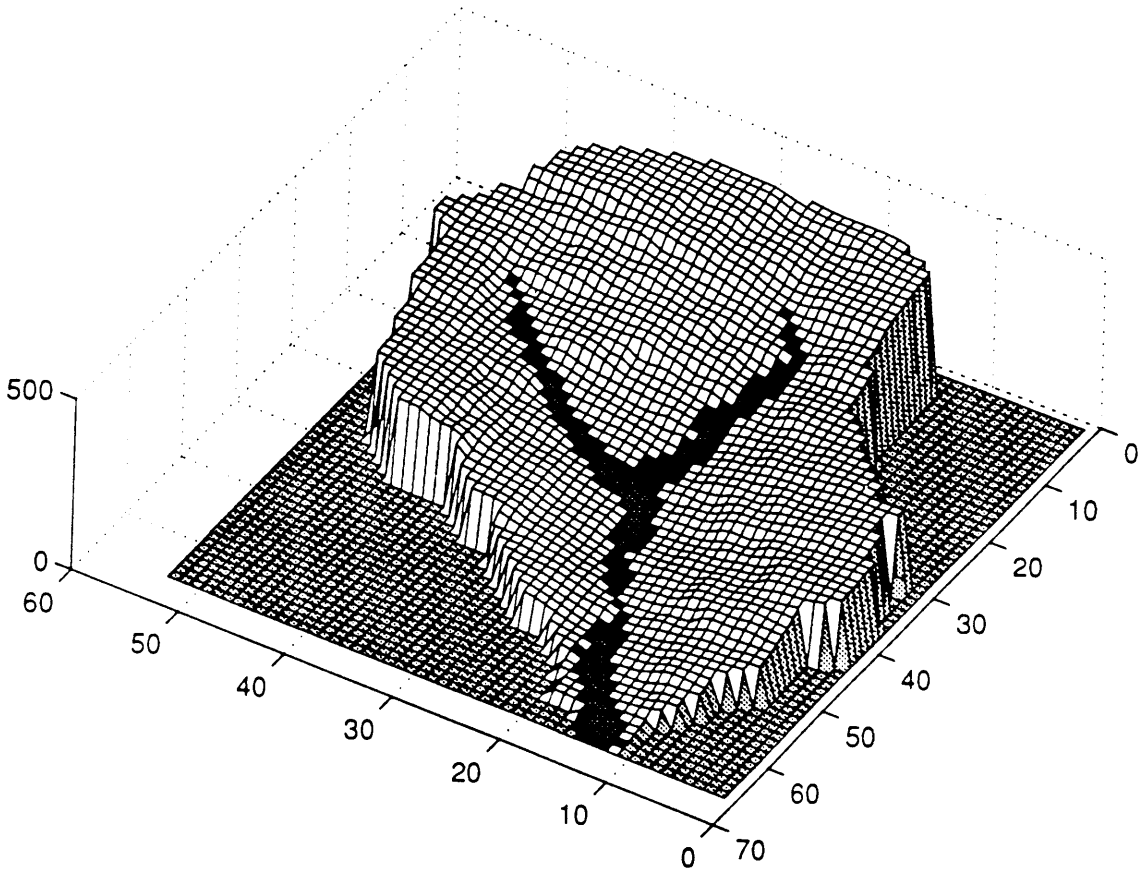

Figure 8-16: 3-D perspective of simulated topography for Schoharie domain.

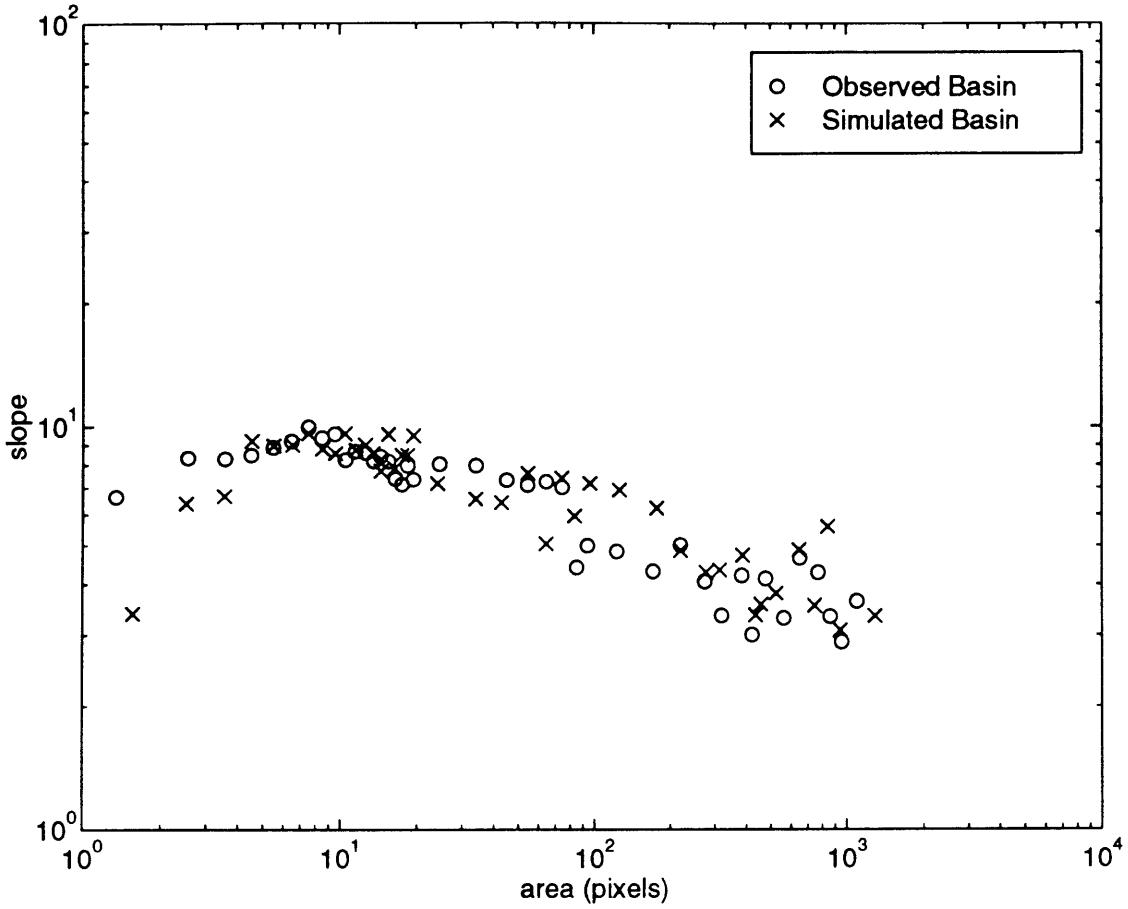

Figure 8-17: Slope-area relationships for Schoharie data set. (Shown are the relationships for the observed "o" and simulated basin "x".)

value of β. This result follows from:

$$\Delta H \sim \frac{\Delta H}{\Delta L} = S = \left(\frac{U}{\beta}\right)^{1/n} A^{-m/n} \tag{8.4}$$

Relief is essentially related to a summation of ΔH values. Thus, relief, $\Re$ is roughly equivalent to a function of U, β, and n:

$$\beta \sim \frac{U}{\Re^n} \tag{8.5}$$

Since uplift is a fixed quantity in our simulations, β will decrease as relief increases and we would expect to have the smallest values of β corresponding to basins with the highest overall relief.

The Schoharie Creek data set exhibits a small degree of negative stratification which corresponds to the case of material getting softer with increasing depth. In

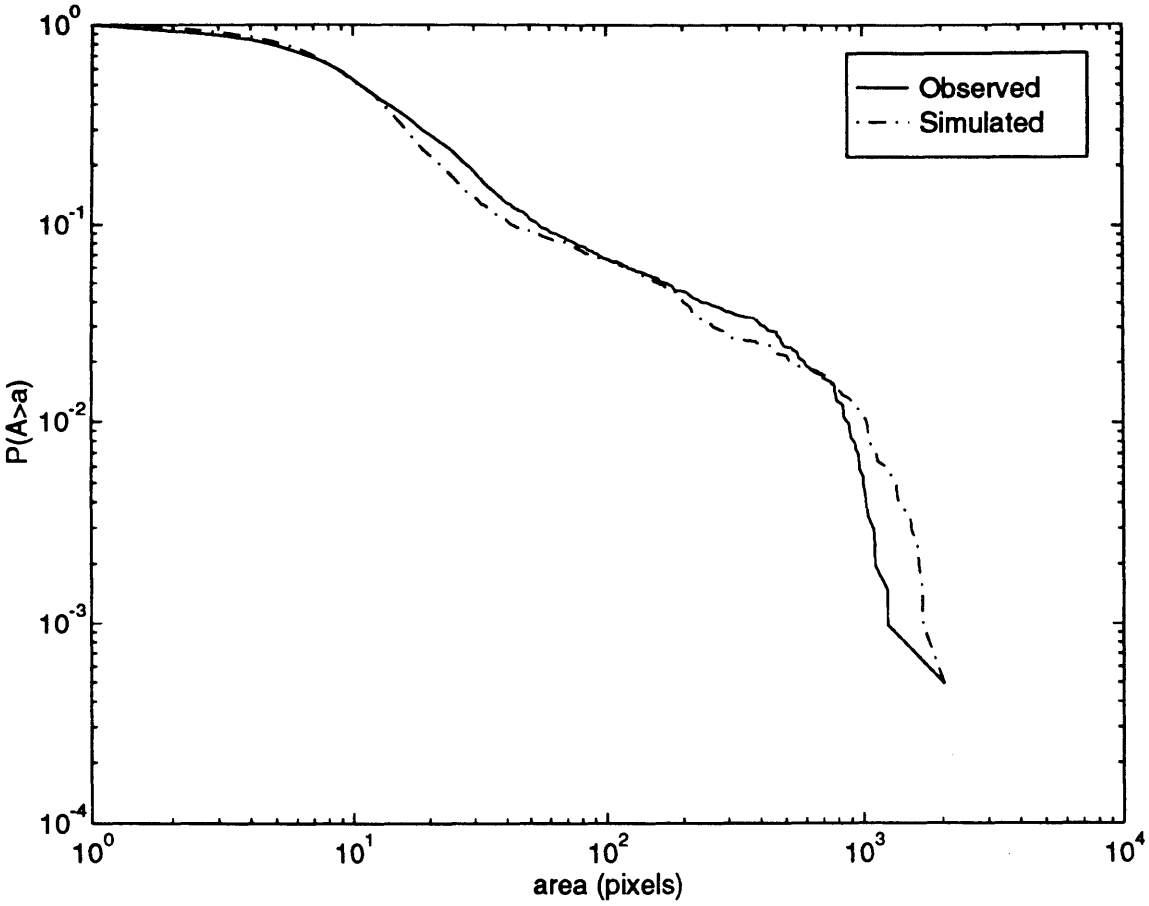

Figure 8-18: Observed and simulated cumulative area distributions for Schoharie data set.

this case, the overall increase in softness is calculated by:

$$2^{(\Re)(\xi)} = 2^{(417.3)(-0.0025)} = 0.49$$

meaning that the material at the outlet is only about half as hard as the material at the highest elevations in the basin. This raises an interesting conflict with the theoretical derivation presented in Chapter 7. In Figure 7-12 we argued that the absolute value of θ would **increase** for negative values of ξ. However, in this simulation our theoretical value for θ (ignoring effects of stratification) is given by:

$$\theta = \frac{-m}{n} = \frac{-0.66}{2.0} = -0.33 < -0.22 = \theta_{obs}$$

while the simulated value for $\theta = -0.21$. Because of the negative stratification, we would have expected that $\theta < -0.33$, which is not the case. The reason for this is two-fold. First, the stratification is only slightly negative, so the effect on θ should be minimal. Second, and more importantly, the hillslope scale in this simulation is very large ($A_* = 31.9$). Because of this large hillslope scale, the preponderance of the domain of the Schoharie basin simulation is subject to diffusive forces which blur and reduce (in absolute value) the slope-area scaling exponent. Fluvially dominated channels remain still somewhere downstream of the basin that is pictured. Therefore, the θ value predicted by theory remains somewhere off to the right of the observed and simulated data points shown in Figure 8-17.

8.2.5 Calder, Idaho Basin

The Calder drainage basin is located in northeastern Idaho on the Coeur d'Alene river in Shoshone National Forest. The lithology of the area is quartzitic and argillaceous, calcareous rocks, and some lava. Physically, the watershed is characterized by a single, main-channel which roughly bisects the basin as shown in Figure 8-20. Emanating from this main channel are several small side branches. The topography is smooth and the main channel is weakly incised. Overall, the Calder basin is somewhat similar to the Schoharie basin with its large relief (572 meters) and relatively large hillslope scale ($A_* = 7.76$).

The slope-area relationship, illustrated in Figure 8-22, was found to have a scaling exponent of $\theta_{obs} = -0.47$. However, closer examination of Figure 8-22 shows that there there are several data points which serve to reduce θ_{obs} unrealistically. If these outliers are removed, the resulting value of $\theta_{obs} = 0.3$ more accurately represents the data overall. This smaller θ is more consistent with the perspective plot of the observed topography which shows a main channel that is only weakly incised.

This simulation employed the smallest value of $\alpha = 1.0$ among the five case studies. This small value is most evident from examination of the simulated topography which appears to be the smoothest of all five of the simulations. Physically, this would indicate that the Calder basin is characterized by fairly homogeneous material.

Overall, reproduction of the slope-area relationship, cumulative area relationship, and hypsometric distribution is quite good as indicated by Figures 8-22 through 8-

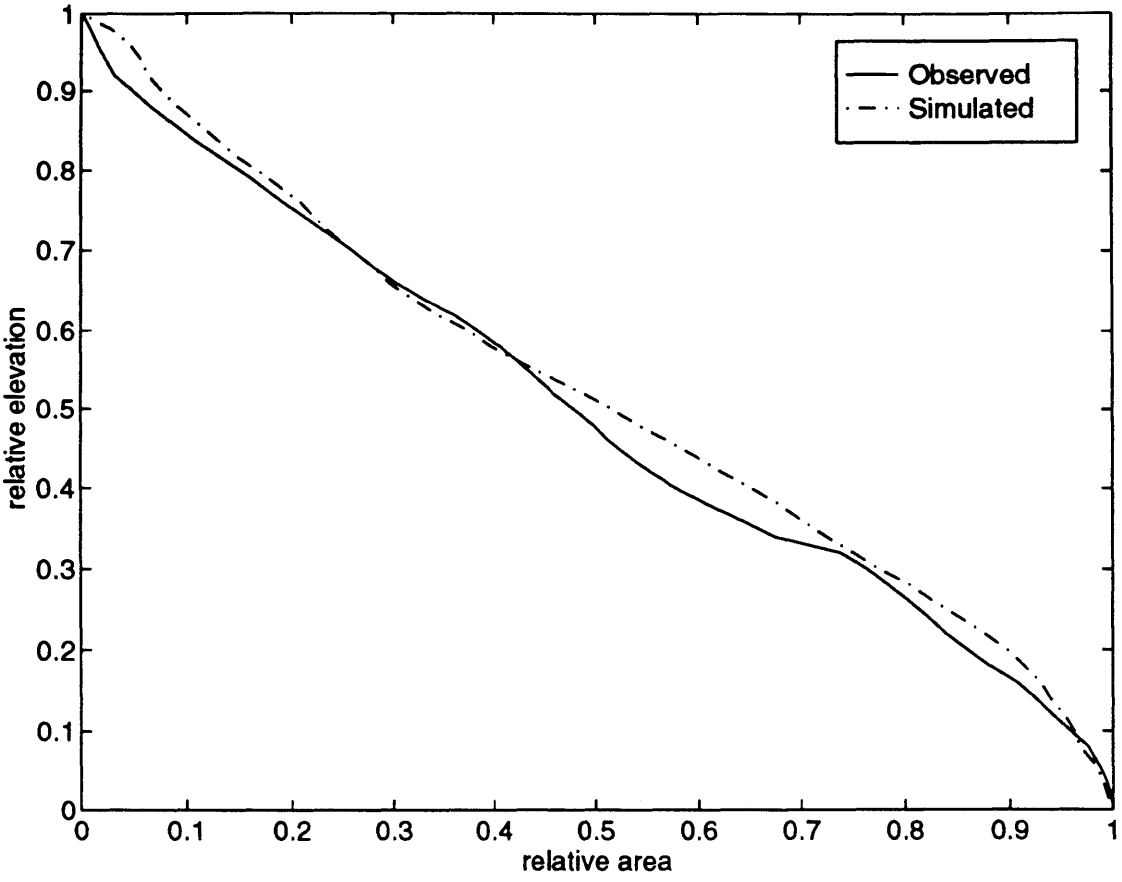

Figure 8-19: Observed and simulated hypsometric distributions for Schoharie data set.

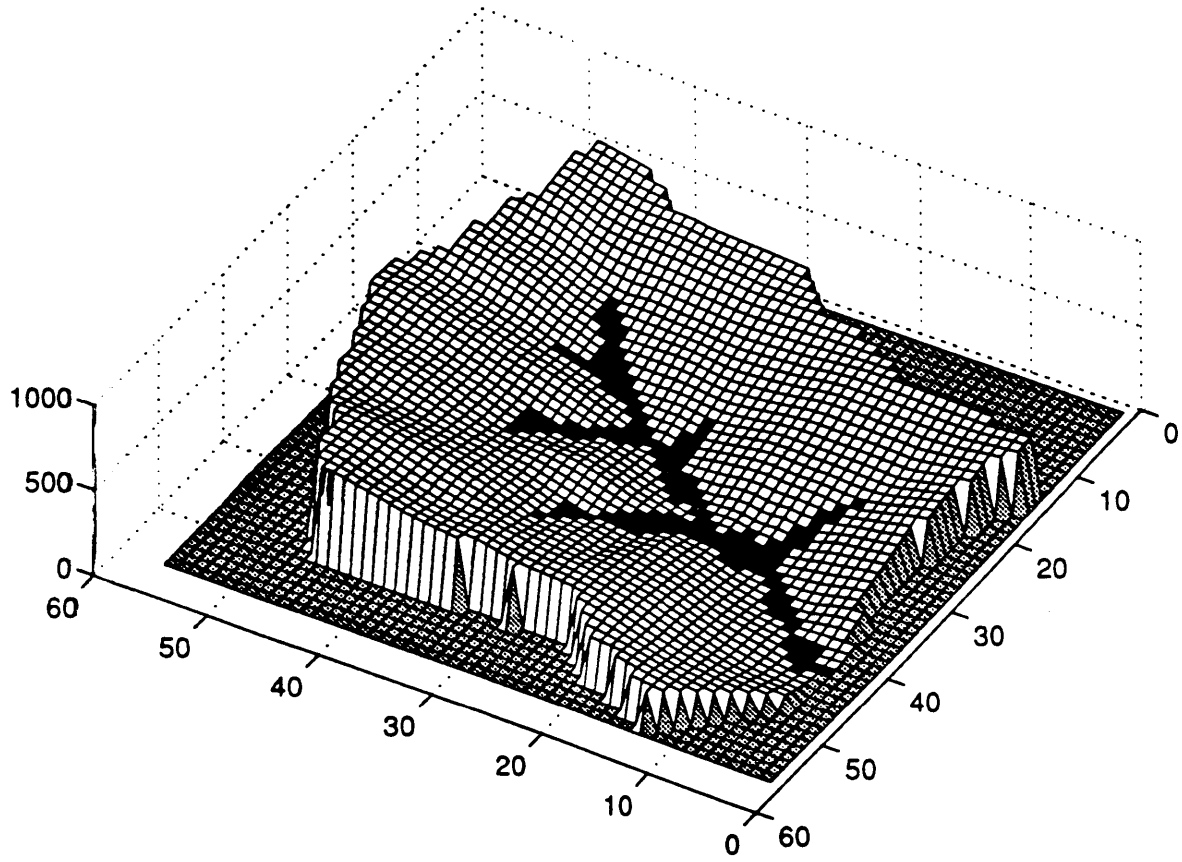

Figure 8-20: 3-D perspective of observed topography for Calder data set.

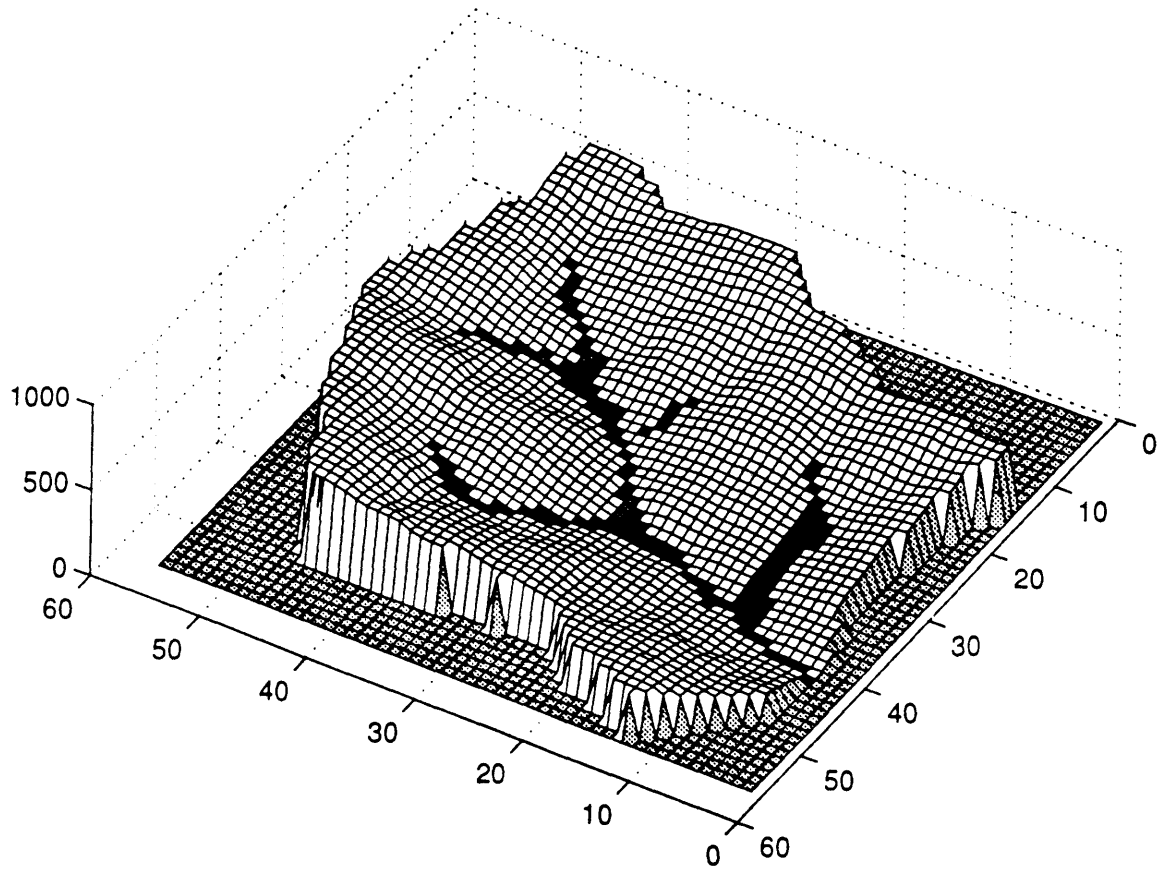

Figure 8-21: 3-D perspective of simulated topography for Calder domain.

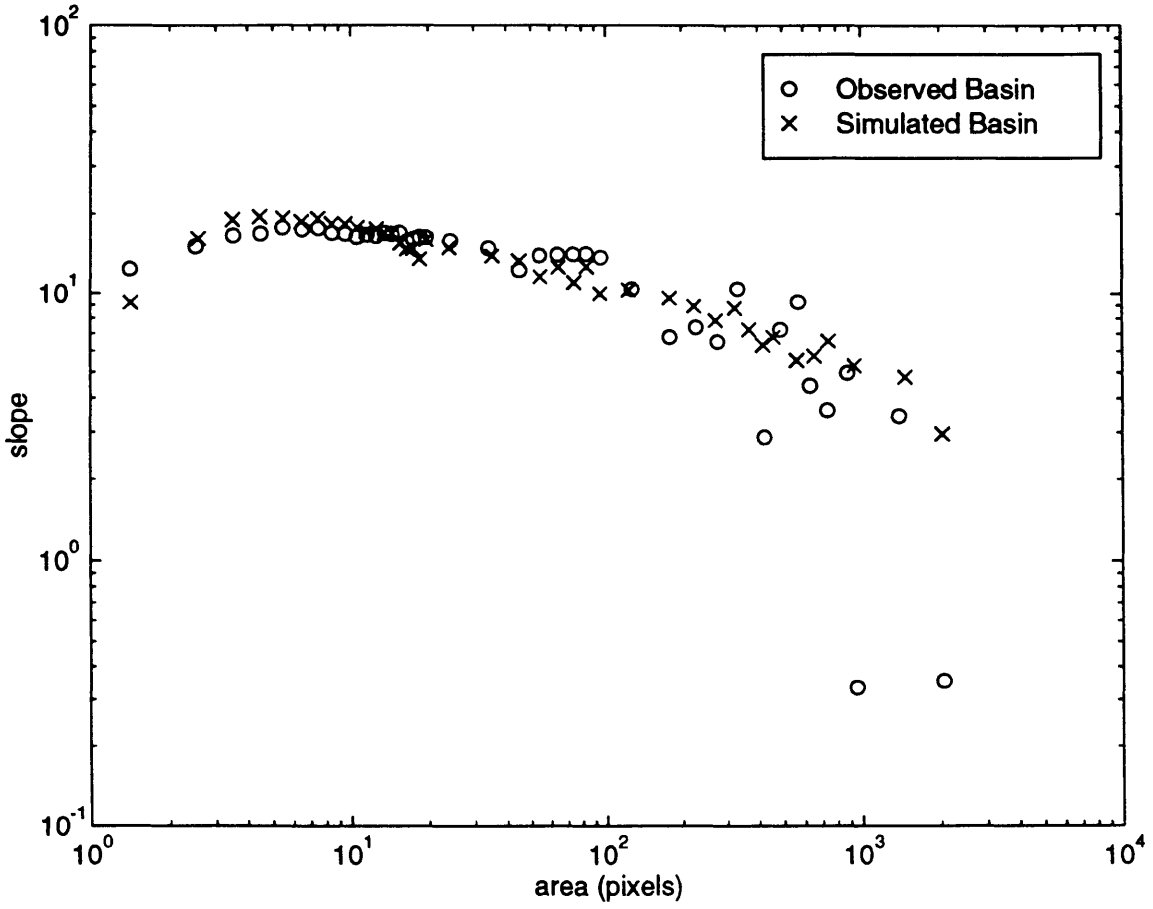

Figure 8-22: Slope-area relationships for Calder data set. (Shown are the relationships for the observed "o" and simulated basin "x".)

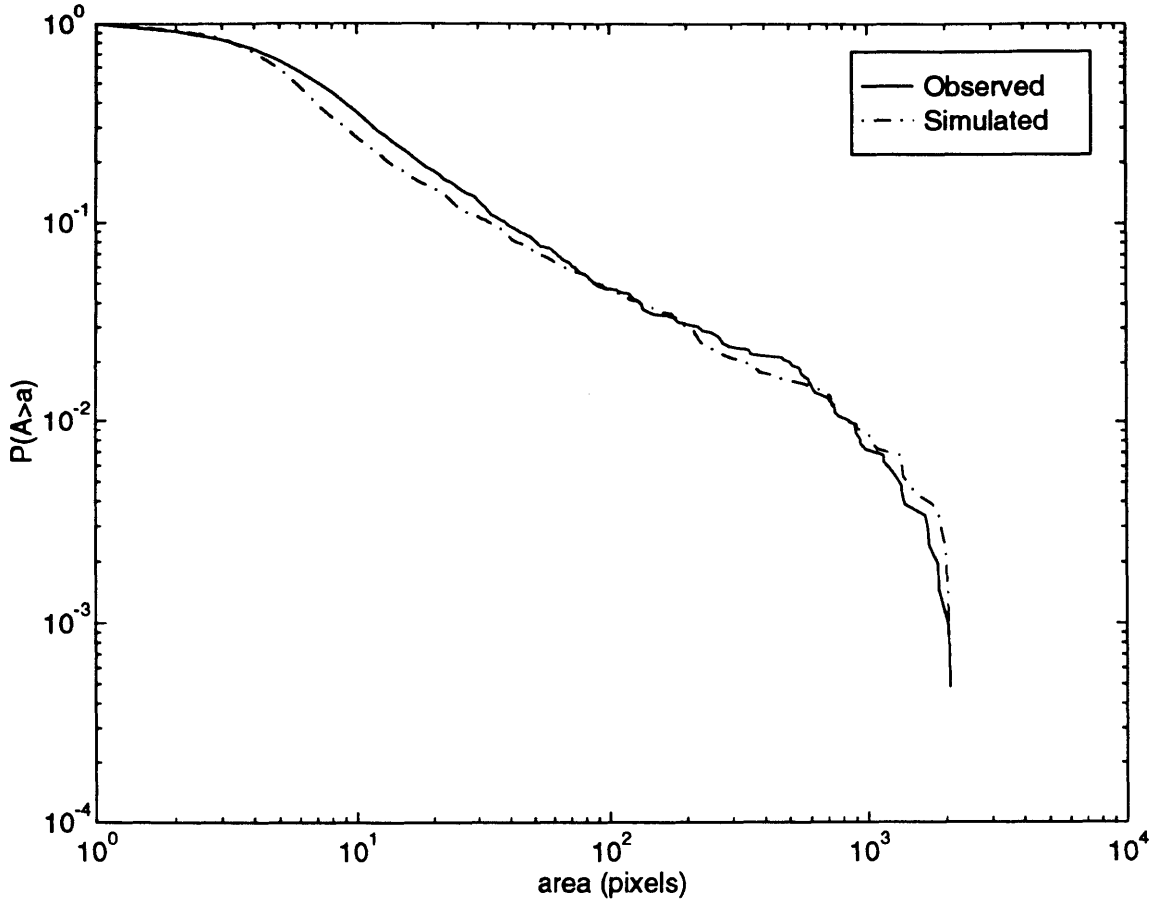

Figure 8-23: Observed and simulated cumulative area distributions for Calder data set.

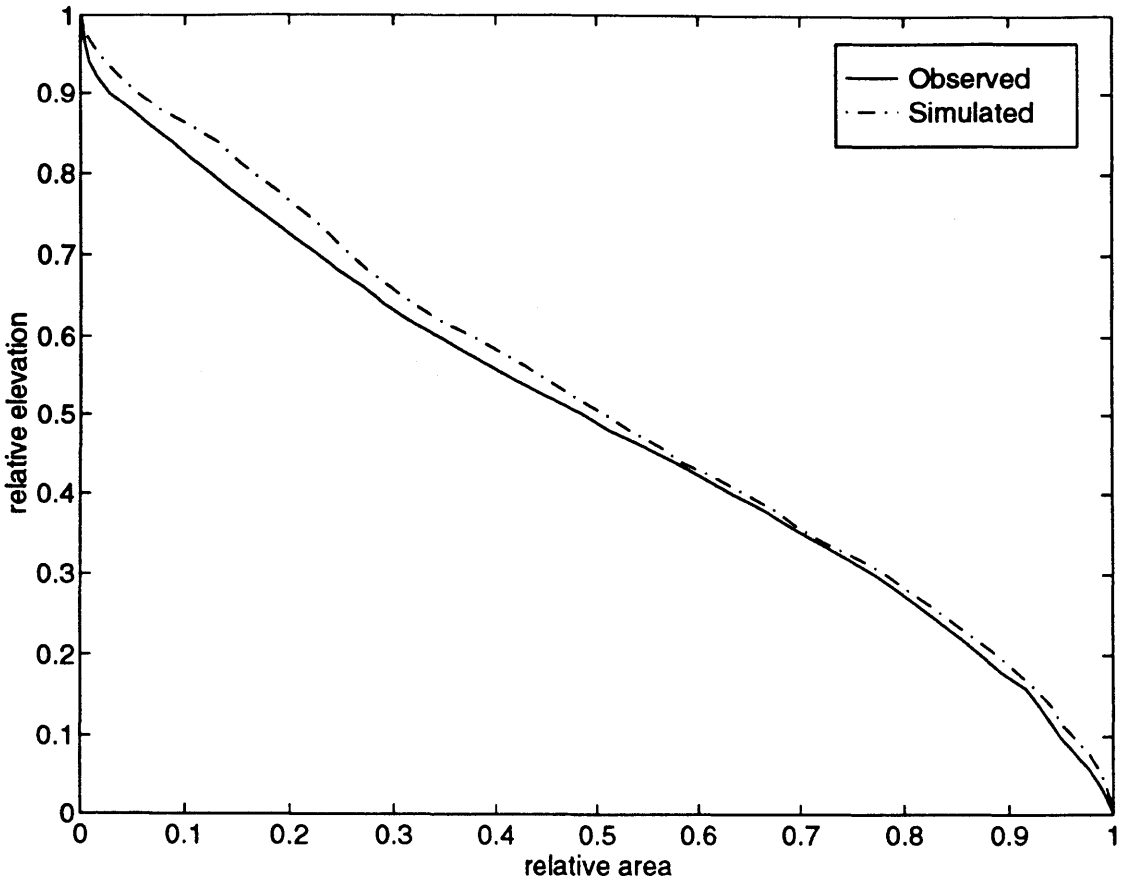

Figure 8-24: Observed and simulated hypsometric distributions for Calder data set.

24. Similarly to the Schoharie basin, it was found necessary to use a small degree of negative stratification, $\xi = -0.002$ which results in material that is a little more than twice as soft at the outlet than at the highest basin elevations. And, again, the simulated value of $\theta = -0.27$ is smaller in absolute value than would be predicted given the negative stratification, since:

$$\theta = \frac{-m}{n} = \frac{-0.55}{2.0} = -0.275 < -0.27 = \theta_{obs}$$

The difference is not as profound as in the previous case because the hillslope scale is not nearly as large as in the Schoharie basin. The θ value predicted by theory lies somewhere off to the right of the observed and simulated data points shown in Figure 8-22.

8.3 Discussion of Case Study Results

There are some trends that are consistent across the five case studies illustrated here. In each case study the R^2 value for the simulated basin was greater than that of the observed basin. Ideally, reproduction of the basin would include having comparable R^2 values. That $R^2_{sim} > R^2_{obs}$ indicates that the assumed log-uniform distribution of heterogeneities may not be appropriate. Perhaps some other distribution would work better. One obvious choice would be to assume the heterogeneities are log-normally distributed. This distribution was used for some preliminary simulations but poor results were obtained. The log-normal distribution was found to not have enough overall variability near the mean of the distribution while having far too much variability near the tails of the distribution. The result was that much of the basin was subject to essentially the same values for β and D while a few pixels had profoundly hard or soft material and had correspondingly small or large values for β and D.

In several of the simulations the quality of the fit to the observed hypsometric distribution was poor, at least in some portion of the distribution. As was suggested in the individual discussions, a better fit would be obtained if a more sophisticated model for basin stratification was used. Such a model might allow for stratification to be characterized by blocks of different mean hardness and depth, for example. This is discussed in Chapter 10 as a possible future direction.

As illustrated in Appendix B, the calibration of the model to an observed topography is not generally a one-step process. Initial estimates of all the model parameters may be obtained from examination of the observed slope-area distribution and the use of the off-line version of the model. However, refinements to these estimates are generally needed especially with regards to the parameter, ξ, which is initially taken as zero and then modified to bring the simulated hypsometric distribution more in line with the observed one.

8.4 Summary

This chapter first presented an off-line version of the basin evolution model. This model was calibrated from a series of simulations covering a range of parameter values. Once calibrated, the model was coupled with a non-linear optimization program which could be used to determine optimal initial estimates of D and α for use in the actual evolution model. Initial estimates of θ and β were obtained from the observed slope-area relationship.

The calibration of the basin evolution model to five different drainage basins. was illustrated. For each case we presented a perspective plot of the observed and simulated topographies, and comparisons of the slope-area, cumulative area, and hypsometric distributions for both the observed and simulated systems. Reproductions of the slope-area and cumulative area statistics were generally quite comparable to the observed system.

The introduction of vertical stratification was shown to achieve good first-order correspondence between observed and simulated hypsometric distributions. Discrep-

ancies were still found to exist between observed and simulated distributions. These discrepancies probably indicate that the stratification pattern would be more accurately represented by a more complicated structure than that given in equation 7.1.

Chapter 9

Relationship between Hydrologic Response and Geomorphology

The results presented in the previous chapters show that we can describe the topography in terms of the relative strengths of diffusive and fluvial transport. Additionally it was shown that the basin organization is sensitive to the amplitude and structure of variations in the erosivity field. We now want to address the simple question:

> *Is hydrologic response directly related to the parameters describing geomorphic structure? If so, what is this relationship?*

In essence, this chapter seeks to bring the research presented in earlier chapters full circle. As hydrologists, we are interested in the factors that affect hydrologic response. The hypothesis at the beginning of this work was that the geomorphology of a basin has a direct effect on the hydrologic response. As such, we have spent a considerable amount of effort quantifying geomorphic expression. With this collected knowledge, we now wish to apply what we have learned to the original intent: to understand the hydrology of the basin more clearly.

Before we can do this we must first define our methodology for inferring hydrologic response from what is essentially a field of elevation values. First, the term "Hydrologic Response" is being used here to define the timing and magnitude of the runoff from the outlet of the basin due to a simple storm - a hydrograph. A hydrograph is produced by two separate phenomena:

- Water exists (e.g. rainfall excess) at a location.
- Water drains downhill along flowpaths defined by the drainage structure of the basin.

We will parameterize rainfall excess to occur similarly to Beven & Kirkby (1979). In their work, Beven & Kirkby converted rainfall to runoff through the use of a topographic index. This index, was argued to quantify the tendency towards saturation at a given point, (i, j):

$$\frac{A_{i,j}}{S_{i,j}} > T \tag{9.1}$$

where T represents some threshold which when exceeded indicates that a location is saturated. This mechanism is quite rational since it would be expected that pixels draining relatively large areas would be more likely to saturate than pixels draining smaller areas. Likewise, a pixel residing in a relatively flat region will more likely saturate than one in a sloped region. It would be expected that the saturation threshold, T would vary geographically and may even vary on the scale of the basin itself. For illustrative purposes we will consider T to be spatially constant in the analysis presented here.

We will use a modified form of the width function to transform these saturated regions into a hydrograph. Recall from Chapter 2 that the width function is a measure of the spatial distribution of pixels located at a given distance (along the drainage path) from the basin outlet. We assign a drainage velocity to each pixel dependent on whether it is located on a hillslope or channel. This transforms the width function into a hydrograph. Hydrographs will have a total volume (area under the curve) equal to the area (in pixels) of the drainage basin. In some instances, we will modify the procedure for determining the hydrograph to count only saturated pixels (as defined by equation 9.1). In this way, this modified hydrograph reflects the runoff associated only with those pixels that are saturated.

9.1 Distribution of Saturation Indices

Let us look first at the distribution of saturation behavior within a basin. Every point in the basin has some cumulative area, $A_{i,j}$, and slope, $S_{i,j}$, associated with it. Therefore, it is possible to calculate the saturation index, $T_{i,j}$:

$$T_{i,j} = \frac{A_{i,j}}{S_{i,j}} \tag{9.2}$$

If $T_{i,j} = T$ in equation 9.1, the pixel is on the verge of saturation. Analogously to the cumulative area distribution, we can plot the cumulative probability distribution of A/S. The difference now is that we are plotting cumulative probability versus A/S rather than A. Not surprisingly, the distributions are similarly shaped, although the spread of the values of A/S in the plots that follow is larger than that of A itself. Figure 9-1 shows two sample A/S distributions.

The saturation threshold of equation 9.1 would manifest itself as a vertical line as is shown for $T = 3$ and $T = 5$ in Figure 9-1. Notice from this figure that the lines cross the two distributions at distinctly different locations. This suggests that very different proportions of the two basins would be saturated at these thresholds. Consider the $T = 5$ threshold. The basin marked "homogeneous" has only a very small (about 15%) fraction which exceeds this threshold, while the "heterogeneous" basin exhibits almost 50% saturation. These two basins were simulated under identical conditions, the only difference being the value of α. In the homogeneous case $\alpha = 0$, while in the heterogeneous case $\alpha = 2$. This suggests a great difference in the hydrologic response that would be expected from the two basins, since one that is almost 50% saturated

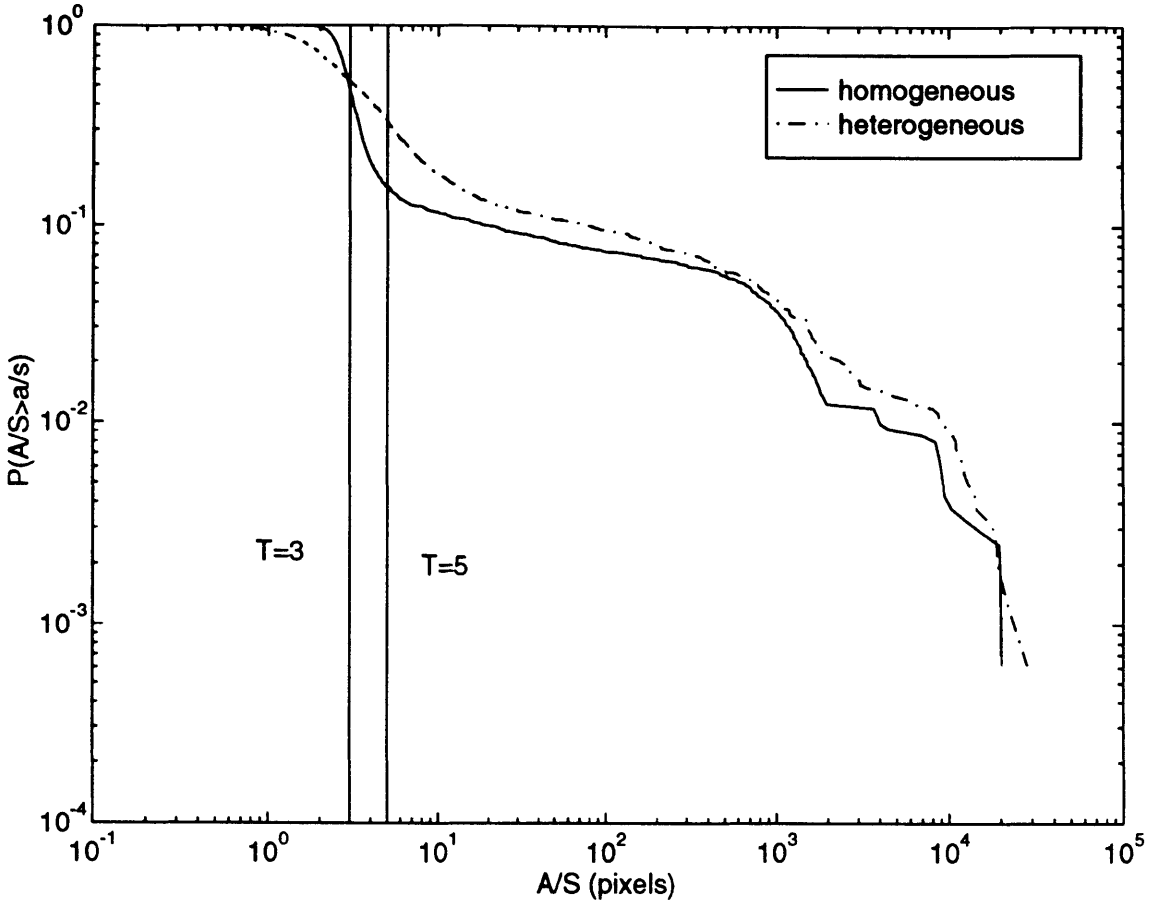

Figure 9-1: Distribution of A/S for two different basins. (Vertical lines indicates hypothetical saturation thresholds at $T = 3$ and $T = 5$.)

Table 9.1: Percent saturation as a function of saturation threshold and degree of heterogeneity.

Threshold (pixels)	Homogeneous $\alpha = 0.0$	Heterogeneous $\alpha = 2.0$
3	46.8	52.6
5	15.6	37.7

would be expected to produce much more runoff than one that is 15% saturated, all other things being equal.

Table 9.1 shows more precisely the saturation behavior of these two distributions at the two hypothetical saturation thresholds.

Owing to the drainage structure that is characteristic of a homogeneous basin, there is a precipitous decline in the number of pixels with a topographic index exceeding a threshold of approximately 5 for the particular parameters chosen in this simulation. The heterogeneous system exhibits, by contrast, a more gradual decline in number of pixels with a given topographic index. The degree of saturation of a basin with homogeneous erosivity will be extremely sensitive to saturation threshold.

9.2 Hillslope Scale and Saturated Areas

In Chapter 3 a method was presented for determining the average hillslope length by determining the intersection of the asymptotic behavior for diffusive and fluvial transport. Figures 9-2 through 9-5 illustrate the spatial distribution of saturated areas for the two drainage basins and two thresholds previously identified in Figure 9-1. These perspective plots show pictorially what was observed in the distribution of topographic indices. As the saturation threshold increases, the saturated areas decline in number much more rapidly for the homogeneous system than for the heterogeneous one.

Within the homogeneous simulations another property of the saturated areas is apparent. The saturated areas are largely concentrated immediately adjacent to the channelized pixels. As the threshold decreases the areas of saturation extend laterally from the channels. Moving laterally from the channel onto the hillslope, both cumulative area and slope decrease. Diffusive sediment transport enhances the likelihood of saturation by reducing slopes and extending the lengths of flowpaths from ridge to channel. Diffusive transport has the same effect in heterogeneous systems, although the effect is not as obvious due to the scatter in topographic indices resulting from soil heterogeneity.

The parallel between the cumulative area distribution and the distribution of topographic indices may also be useful to understand the relative roles of D and β. Just as increasing D or decreasing β tended to increase the dominance of diffusive transport and hillslope scale aggregation, these parameters play the same role in

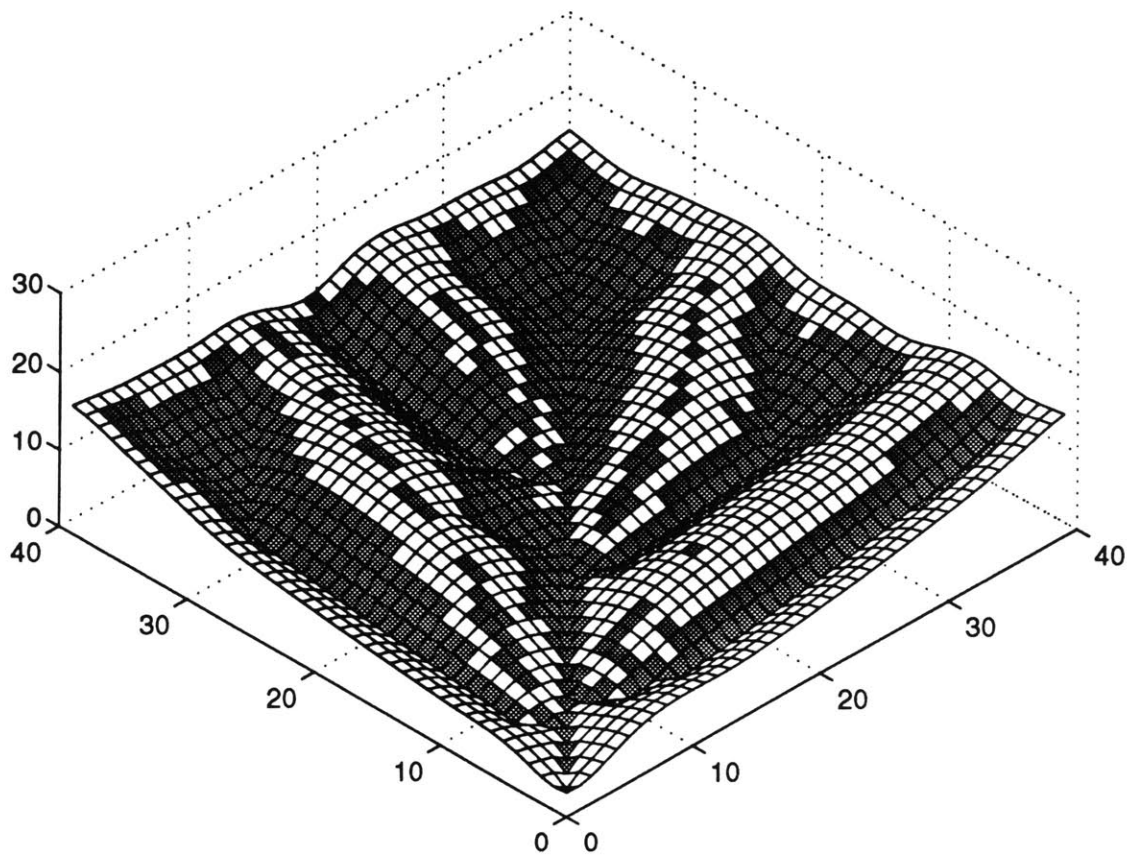

Figure 9-2: 3-D perspective plot of homogeneous system with saturated pixels shaded ($A/S > 3$ and 46.8% saturated).

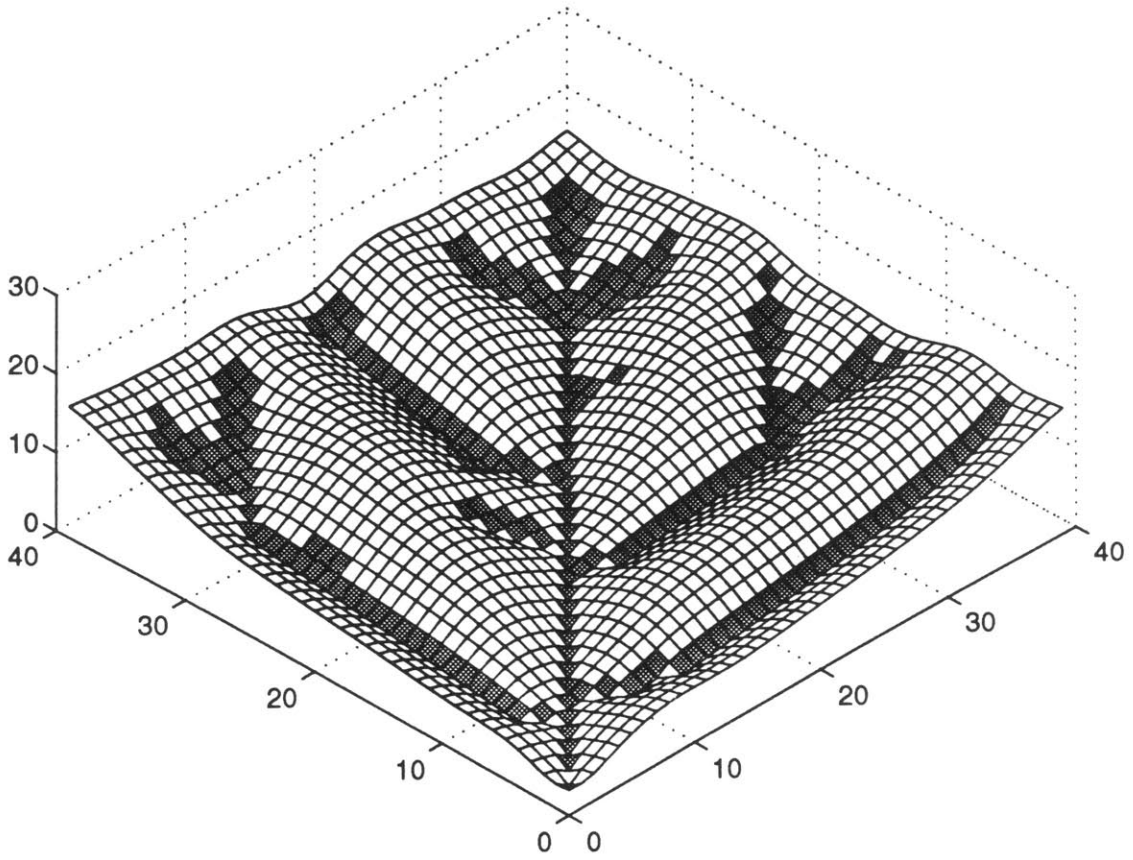

Figure 9-3: 3-D perspective plot of homogeneous system with saturated pixels shaded ($A/S > 5$ and 15.6% saturated).

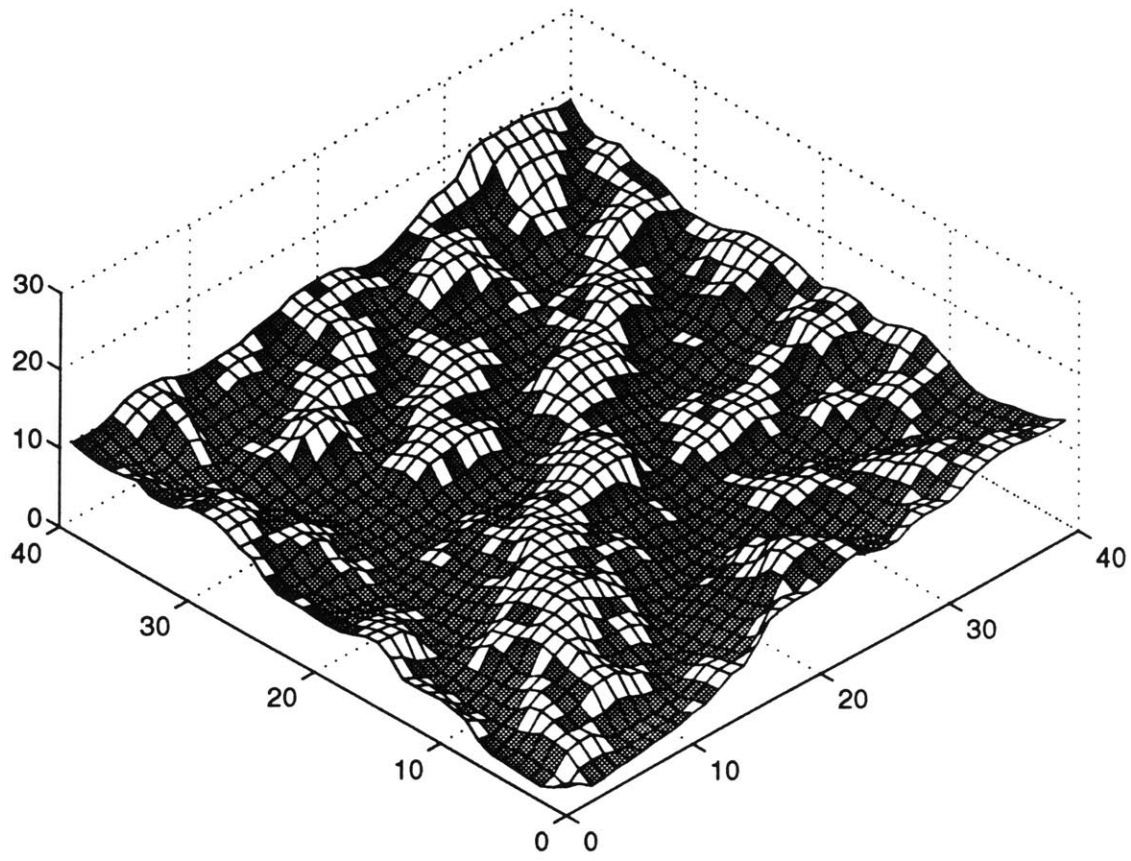

Figure 9-4: 3-D perspective plot of heterogeneous system with saturated pixels shaded ($A/S > 3$ and 52.6% saturated).

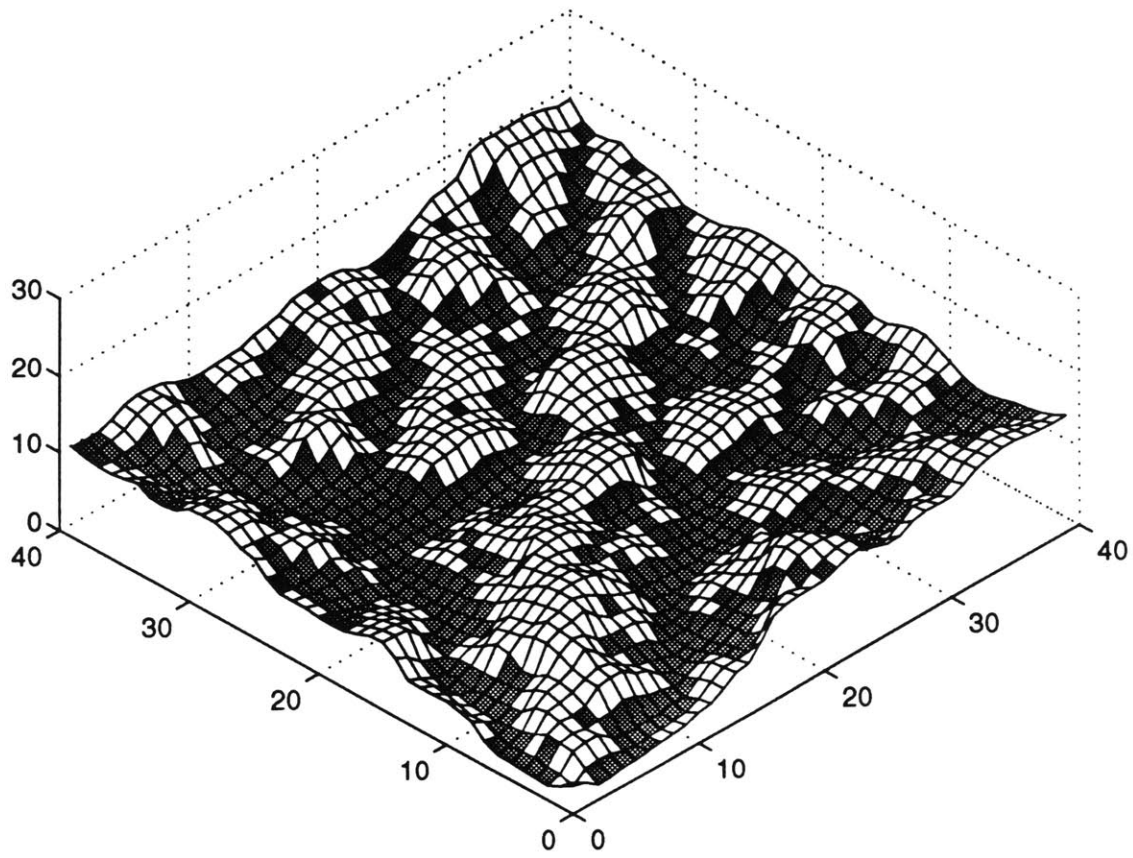

Figure 9-5: 3-D perspective plot of heterogeneous system with saturated pixels shaded ($A/S > 5$ and 37.7% saturated).

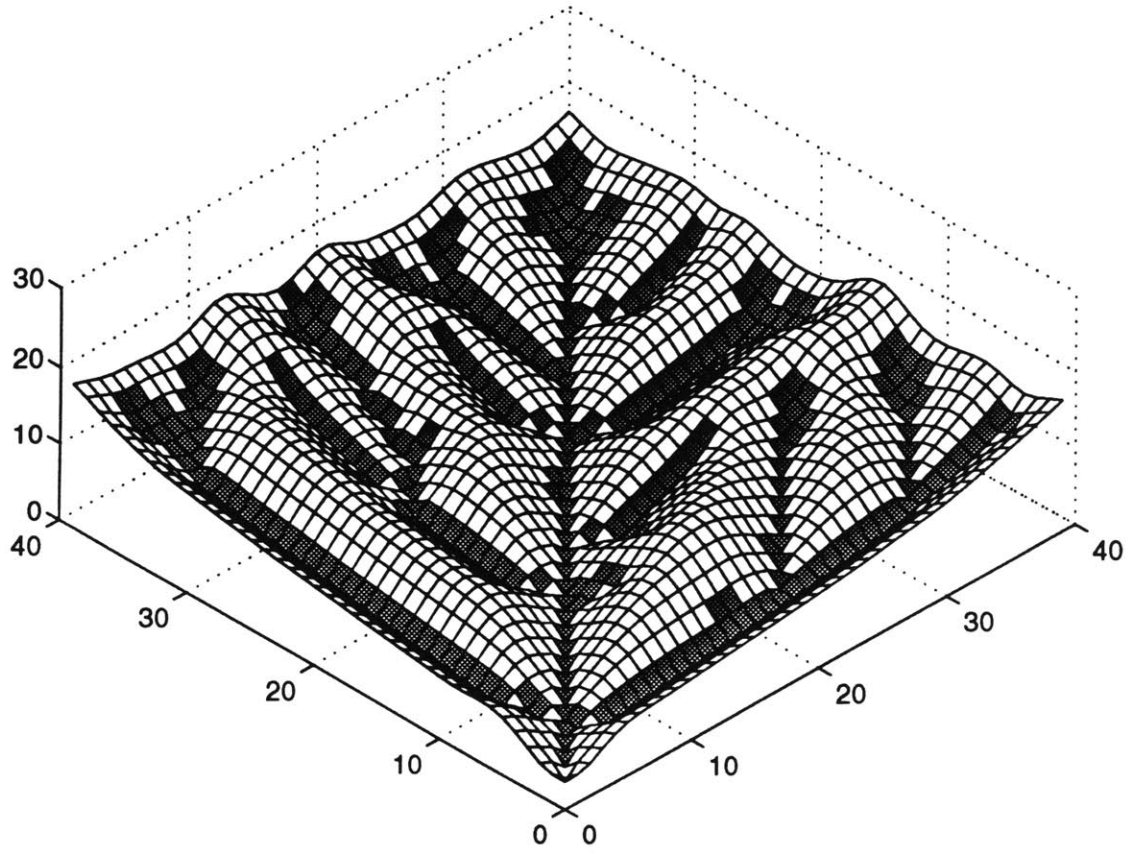

Figure 9-6: 3-D perspective plot of homogeneous system with saturated pixels shaded ($A/S > 3$, $D = 0.04$, and 19.2% saturated).

controlling the distribution of topographic indices. Thus, increasing D or decreasing β will tend to create topography that is more readily saturated. This is illustrated by the system pictured in Figure 9-6 which has a much smaller value of D than the system shown in Figure 9-2. Figure 9-7 gives the distribution of topographic indices for the systems pictured in these two figures and shows how the same saturation threshold results in very different degrees of saturation.

This hillslope scale was defined earlier in Chapter 3 as:

$$A_* = U^{\frac{1-n}{n+m}} \beta^{\frac{-1}{n+m}} (fD)^{\frac{n}{n+m}} \tag{9.3}$$

This scale, A_* marks the range of values at which the saturation threshold is most sensitive. This is apparent from inspection of 9-7 which shows the distribution of topographic indices for two systems with very different hillslope scales. By increasing D from 0.04 to 0.1 a clear shift to the right of the distribution of topographic indices is evident. For the systems pictured in Figures 9-2 and 9-6 the values of A_* are 3.97 and 2.15, respectively. Inspection of Figure 9-7 shows that these two values of

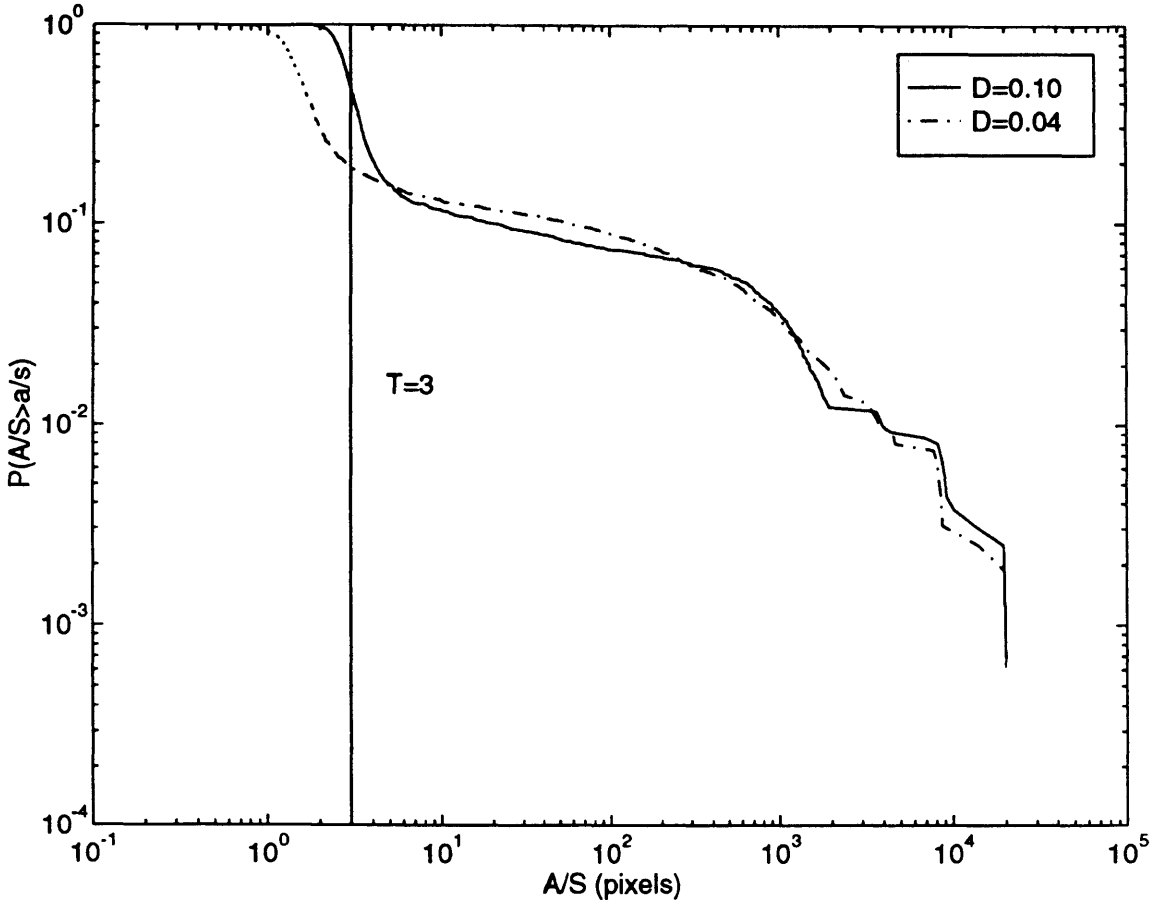

Figure 9-7: Distribution of A/S for two homogeneous basins with different magnitudes of diffusive transport.

A_* correspond to threshold values which roughly mark the center of the region of rapid decline for both distributions. This fact holds true because the value of slope just before channelization is approximately unity for these simulations so $A_* \simeq A/S$. More generally, the value A_*/S_* (where S_* is the value of the slope at A_*) marks the region over which the distribution of topographic indices is most rapidly changing.

9.3 Hydrographs of Simulated Basins

Now that we have a mechanism for characterizing saturation, the next step is to address the issue of how the saturated pixels will contribute to the hydrologic response. As stated previously, we will transform the width function to produce a characteristic hydrograph for each basin. In some cases, we will be interested in the hydrograph of only those pixels which are saturated.

Our method for determining the characteristic hydrograph for a given basin is to first determine the width function as shown previously in Chapters 2 and 4. Next, flow velocity at each pixel is assigned using Manning's equation:

$$v_{i,j} = \frac{1}{n_{i,j}} R_{i,j}^{2/3} S_{i,j}^{1/2} \tag{9.4}$$

where $v_{i,j}$ is velocity, $n_{i,j}$ is the Manning roughness, $R_{i,j}$ is the hydraulic radius (cross-sectional area/wetted perimeter), and $S_{i,j}$ is the slope, all located at pixel (i,j). As an approximation, we will use the "wide channel assumption", which equates the hydraulic radius to the depth of flow. This approximation is certainly valid for the overland flow that would be anticipated on hillslopes, and is probably acceptable in the channels as well. From Leopold and Maddock (1953) we have:

$$d_{i,j} = cQ_{i,j}^b \tag{9.5}$$

where $d_{i,j}$ is the depth of flow and $Q_{i,j}$ is the discharge at pixel (i,j). Leopold and Maddock give the value of $b = 0.4$. Using cumulative saturated area ($A_{s(i,j)}$) as a surrogate for discharge we obtain:

$$v_{i,j} = \frac{1}{n_{i,j}} A_{s(i,j)}^{0.27} S_{i,j}^{1/2} \tag{9.6}$$

Finally, we will simplify the characteristic roughness of the basin into a hillslope roughness and a channel roughness. The assignment of this roughness is determined from equation 9.3. If the cumulative area of a given pixel exceeds A_* then we treat the pixel as a channel and the Manning roughness is small. Likewise, if the cumulative area of the pixel is less than the hillslope scale, then the pixel is located on a hillslope and the roughness is large. This argument is quantified in equation 9.7:

$$\begin{aligned} n_{i,j} &= n_0 \quad \text{if } A_{i,j} \leq A_* \\ n_{i,j} &= \Gamma n_0 \quad \text{if } A_{i,j} > A_* \end{aligned} \tag{9.7}$$

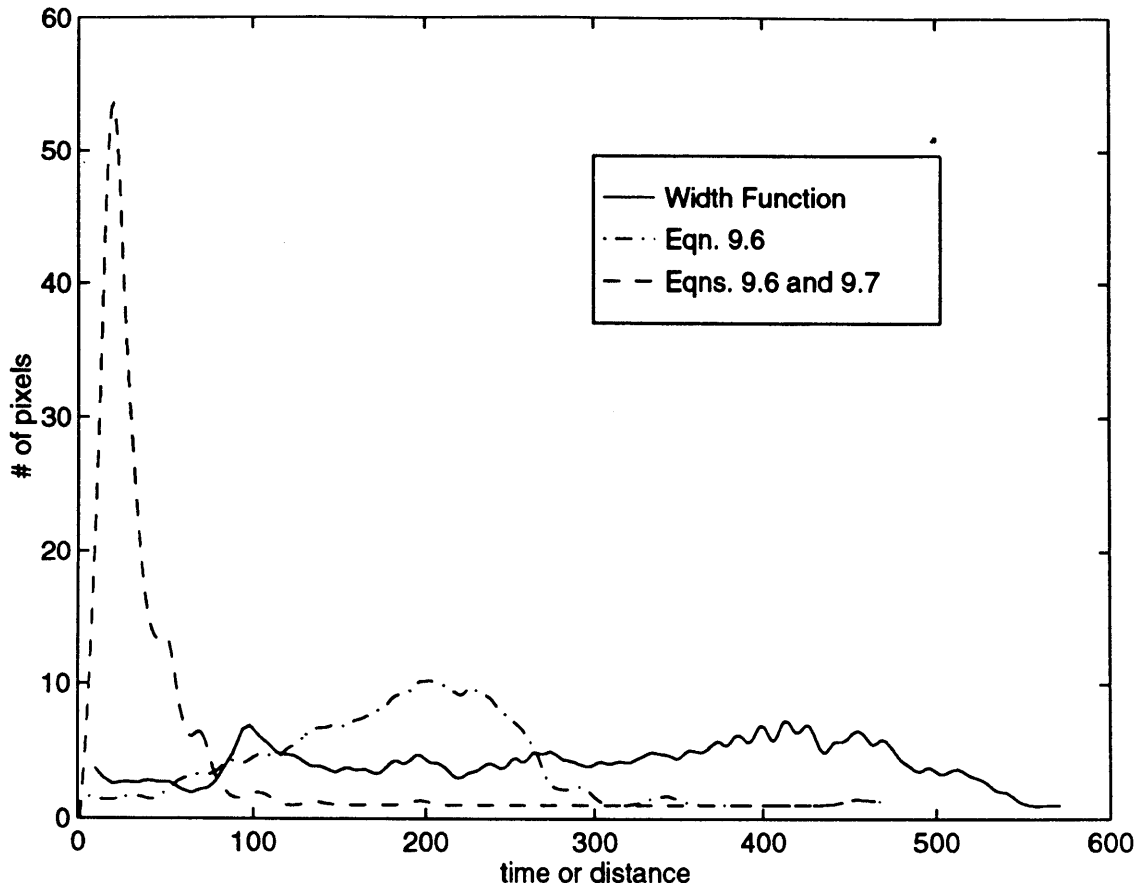

Figure 9-8: Transformation of width function to a hydrograph for basin pictured in Figure 9-2 and 9-3. (All pixels assumed contributing.)

Manning's roughness typically varies from 0.01 for smooth, concrete lined irrigation ditches to 0.15 for very irregular, natural streams. We will use a value of 0.1 for Γ to account for the difference in roughness between hillslope and channel pixels. The final step is to again apply a cubic spline smoothing function to the resulting hydrograph. Figure 9-8 illustrates the width function and hydrograph resulting from the transformation equations described above. As shown in this figure, the main effect of equation 9.6 is to increase velocities producing a distribution similar in shape to the original width function. Equation 9.7 transforms the negatively skewed function output from equation 9.6 into the positively skewed hydrograph.

Equation 9.6 may seem relatively inconsequential in this example since it has little effect on the shape of the original width function. This is because this illustration does not highlight the characteristics which 9.6 emphasizes. Equation 9.6 is important when comparing systems which differ in their cumulative area and slope characteristics. For example, imagine we have two identical systems except that the elevations of the first system (System A) are double that of the second system (System B). From

equation 9.6, the velocities of System A would be a factor of $\sqrt{2}$ greater than System B. This would be the expected result given System A's greater relief. Likewise, the more channelized a basin is, the greater the proportion of the basin's area that would contain pixels with high cumulative area. This too, would lead to larger velocities from the positive dependence of 9.6 on cumulative area.

The simplifications here are arbitrary assumptions used to transform the width function into a hydrograph. Other methods are equally justifiable. Our goal is not to determine the precise hydrograph corresponding to each system, but to produce hydrographs for comparison among basins generated with different model parameters. Our hypothesis is that the different topographies of these basins translate into different hydrographs. Since we are using equations 9.6 and 9.7 for purposes of comparison only, actual magnitudes are meaningless. However, relative differences in the peaks, times to peak, and overall shapes are meaningful and would probably be similar regardless of the precise equations that are used.

9.3.1 Effect of Saturation on Hydrologic Response

Figures 9-9 and 9-10 show the hydrographs at varying levels of saturation for the two systems illustrated in Figures 9-2 through 9-5. These figures confirm relationships that we have seen earlier in this chapter. Both figures show the total and saturated-only hydrographs for the simulated domains. The uppermost curves correspond to hydrographs for a completely saturated basin. The two lower curves show the hydrographs at saturation thresholds: $T = 3$ and $T = 5$ which correspond to the saturated areas shown in Figures 9-2 through 9-5. Notice the much more rapid decline in both hydrograph peak and volume for the homogeneous system when compared to the heterogeneous system. This illustrates the greater sensitivity of the homogeneous system to the saturation threshold and is consistent with Table 9.1. Additionally, the peak of the hydrographs are delayed as the saturation threshold increases. This is caused by the smaller discharges (and the resulting lower velocities) associated with a partially saturated basin. This is observed for both the homogeneous and heterogeneous systems, although it is particularly pronounced in the homogeneous case.

Additionally, we observe that the absence or presence of spatial heterogeneities has an observable effect on their corresponding hydrographs. Figure 9-11 illustrates this effect. The hydrographs corresponding to the simulated homogeneous systems consistently exhibit a quicker and larger peak than those for the heterogeneous systems. This is because the drainage path of the heterogeneous systems is more tortuous than the rather straight and angular ones of the homogeneous systems. Recall from Chapter 4 that this was one of the tendencies of the simulations relative to the observed width function. It appears that the introduction of heterogeneous erosivity has a realistic influence on the hydrologic response in this regard. Physically, the implication is that the presence of spatial heterogeneity reduces the peak and delays the expected time to peak of the hydrograph.

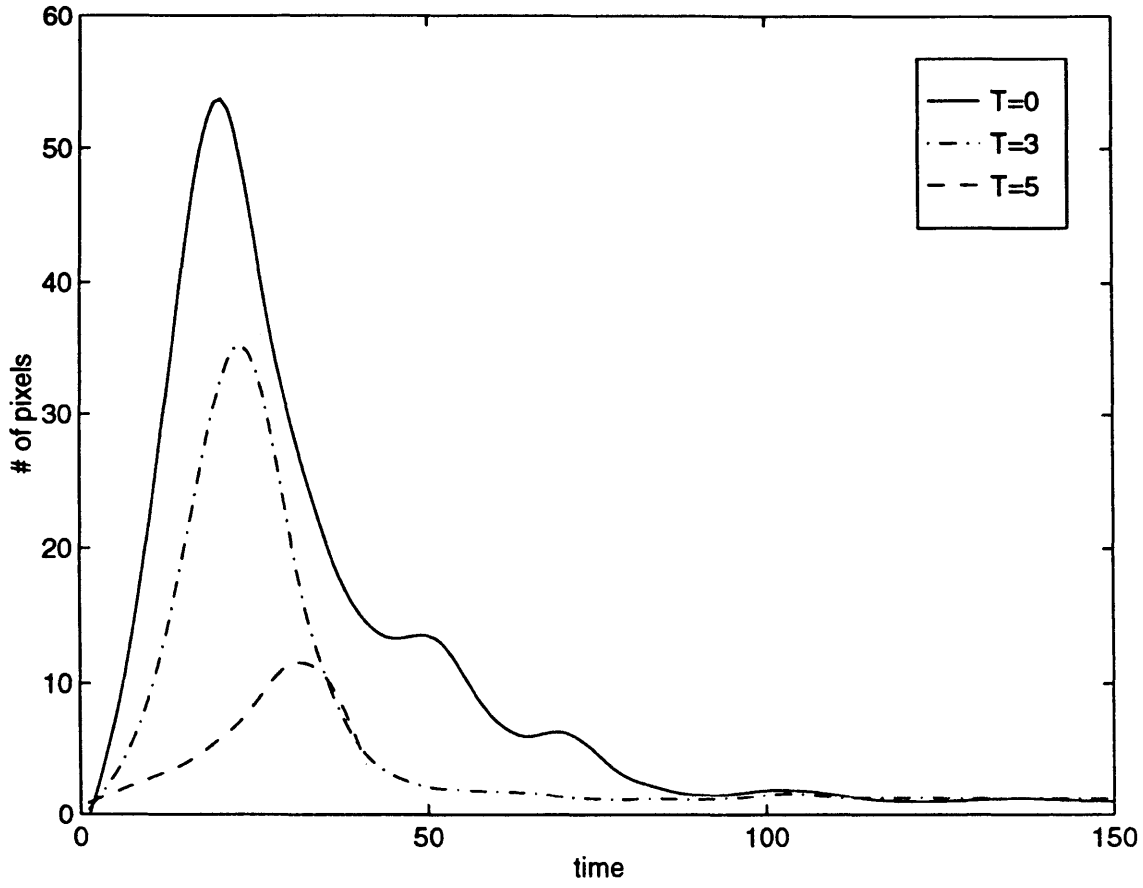

Figure 9-9: Hydrographs for homogeneous ($\alpha = 0.0$) system at three different saturation thresholds.

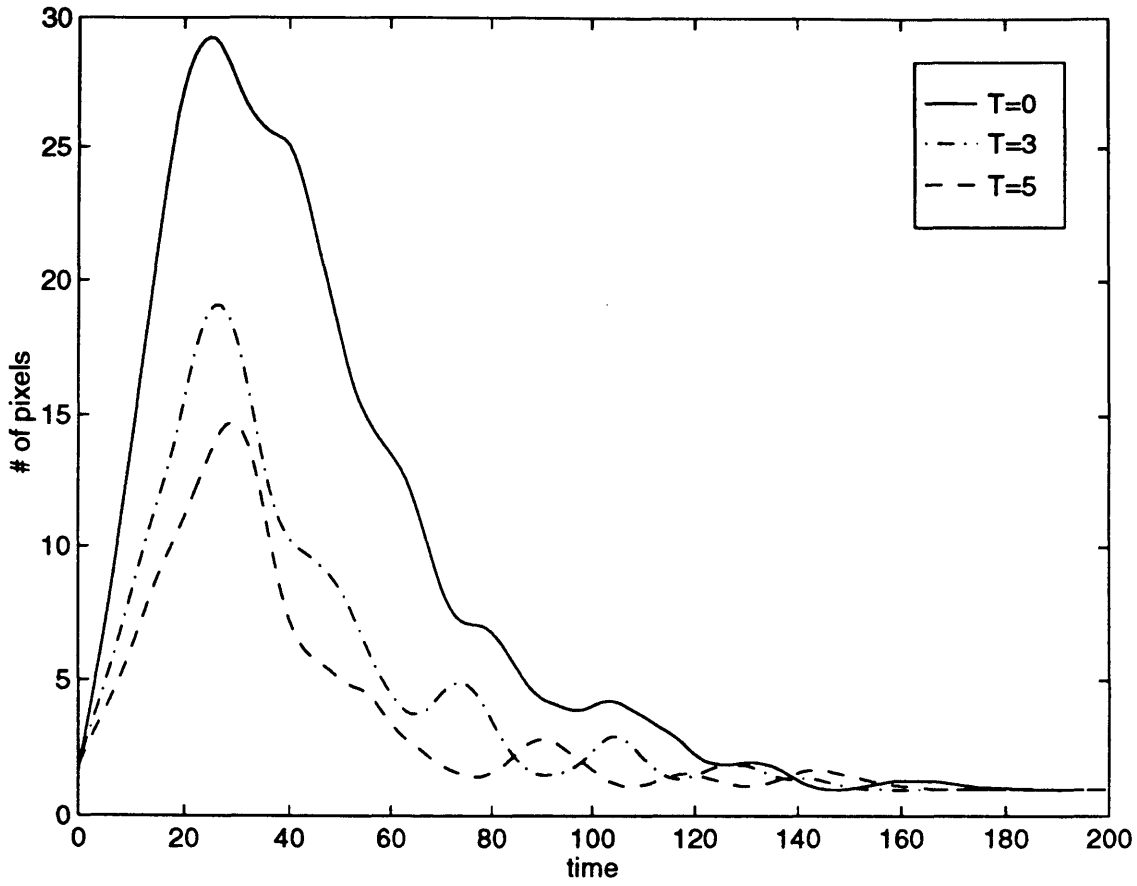

Figure 9-10: Hydrographs for heterogeneous (α = 2.0) system at three different saturation thresholds.

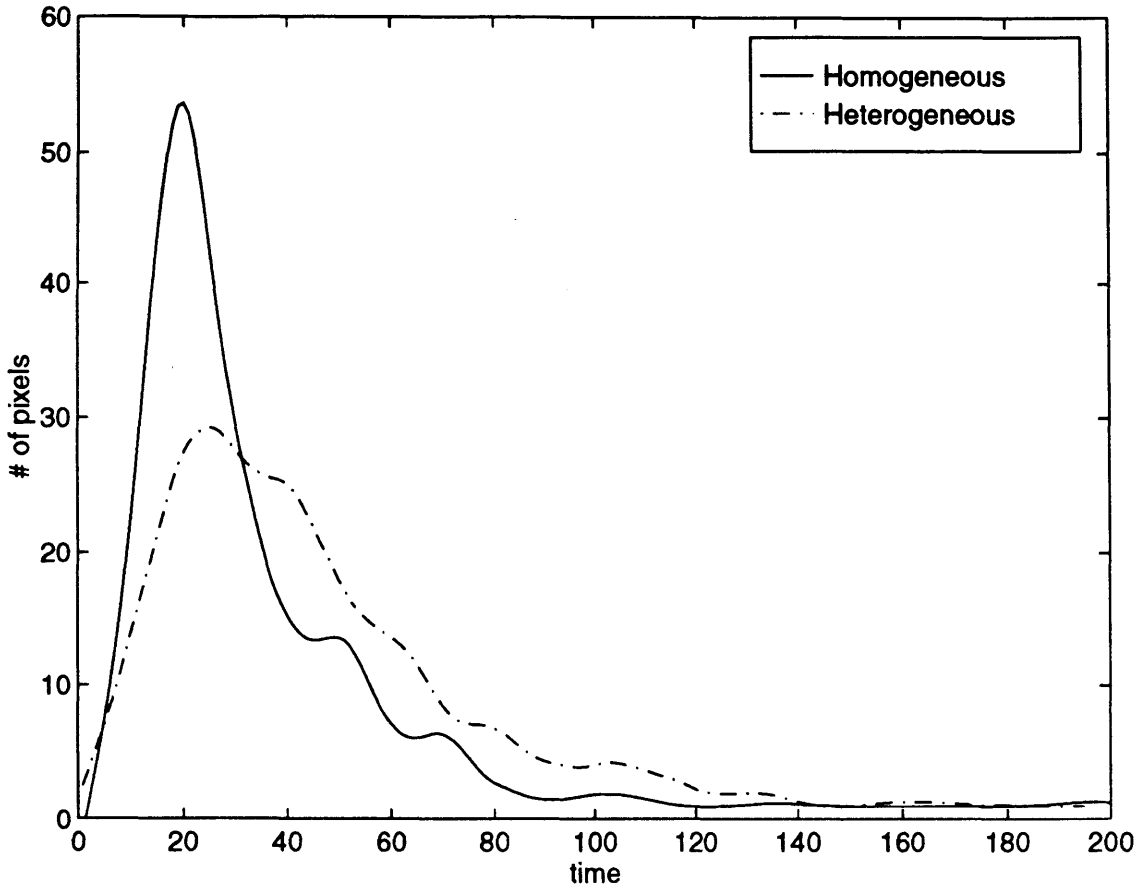

Figure 9-11: Simulated hydrographs for systems with equivalent model parameters: one with homogeneous erosivity and one with heterogeneous erosivity. (All pixels assumed contributing.)

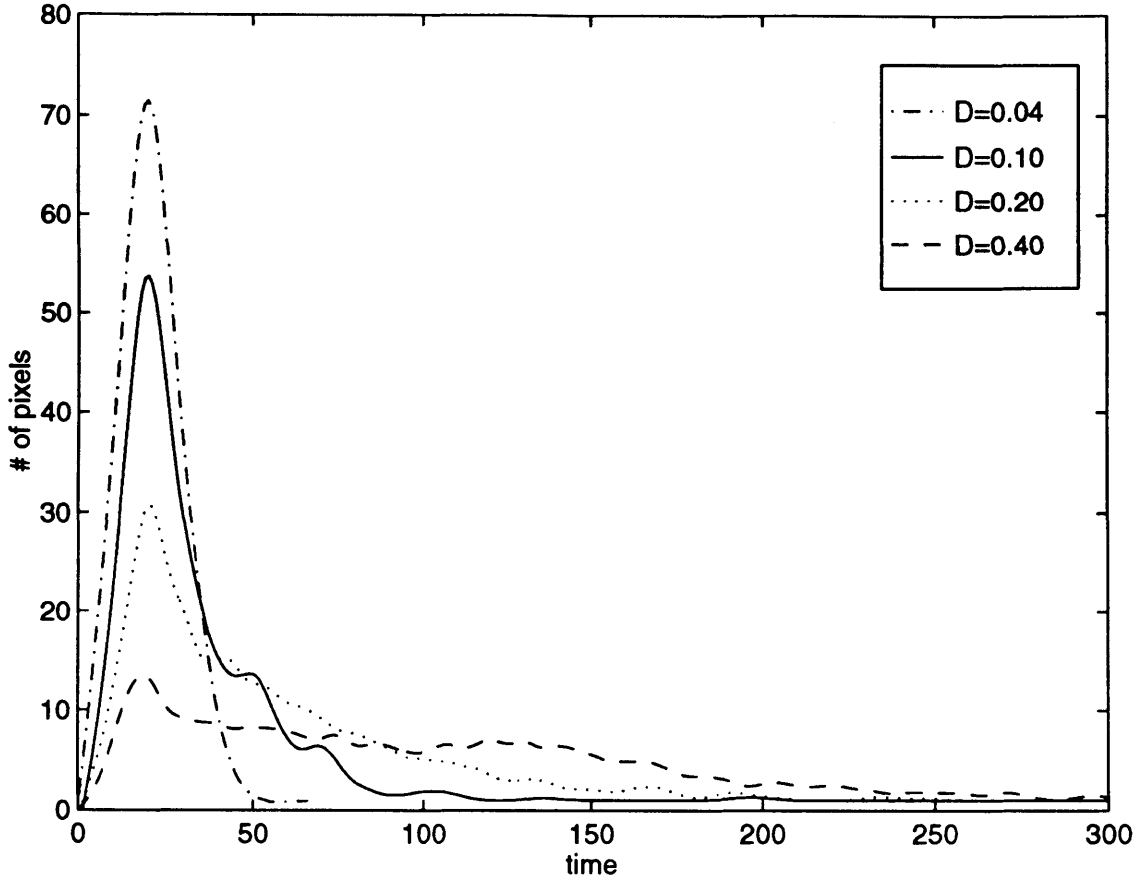

Figure 9-12: Hydrographs for basins with four different hillslope scales. (All pixels assumed contributing.)

9.3.2 Effect of Hillslope Scale on Hydrologic Response

We have previously stated that hillslope scale is the fundamental quantity when quantifying the hydrologic behavior of a basin. This section will examine this issue in greater detail.

Four simulations were performed with $\beta = 0.01$, $\alpha = 0.0$, and $D = 0.04$, 0.1, 0.2, and 0.4. The resulting basins have (from equation 9.3) hillslope scales, A_* of 2.15, 3.97, 6.30, and 10.0, respectively. The hydrographs corresponding to these basins are illustrated in Figure 9-12.

This figure illustrates that as the hillslope scale decreases (i.e. D becomes smaller or β becomes larger) the peak of the hydrograph becomes larger and the overall time base of the hydrograph is diminished. Although this particular figure shows the effect of varying the value of the diffusion coefficient, D, the same effect (in the opposite direction) would result by varying β, since it is the changing hillslope scale that is causing the effect as indicated by equation 9.3.

Figures 9-13 and 9-14 illustrate two homogeneous basins in which the only differ-

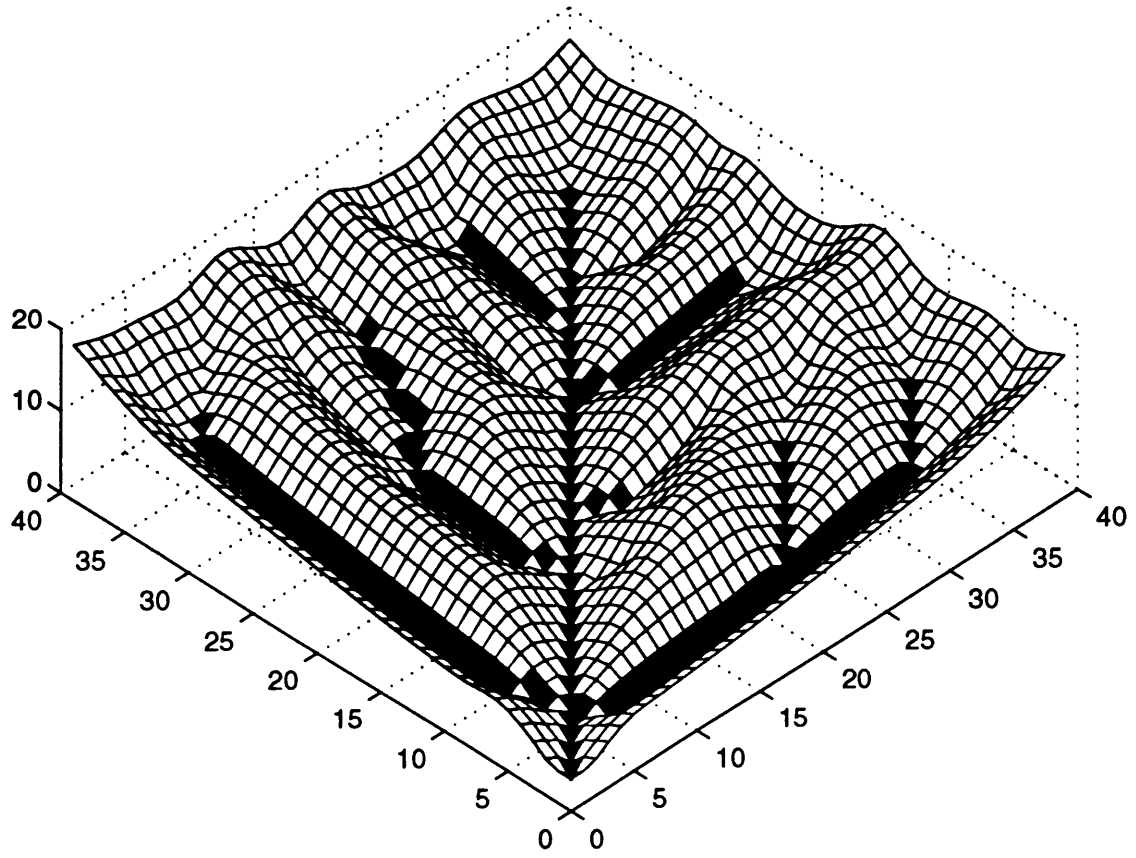

Figure 9-13: 3-D perspective of homogeneous basin with $D = 0.04$ and $A_* = 2.15$.

ence is the value of the diffusion coefficient (and the ensuing value of A_*). Figure 9-13 corresponds to $D = 0.04$ and $A_* = 2.15$ while Figure 9-14 corresponds to $D = 0.4$ and $A_* = 10.0$. The rapid and large peak of the hydrograph corresponding to Figure 9-13 is caused by the close proximity of a channel pixel to any hillslope pixel as compared to a hillslope pixel in Figure 9-14 in which a significant distance may be traveled (at low velocity) before reaching a channel pixel. This causes a more delayed and smaller hydrograph peak, and an overall longer hydrograph duration, since runoff from the more remotely located pixels in the diffusion-dominated basin will take a much longer period of time to reach the basin outlet.

9.4 Conclusions

This chapter discussed the influence that geomorphology has on the hydrology of a basin. The hydrology was characterized primarily by a saturation mechanism sensitive to slope and cumulative area and a topography sensitive, simulated hydrograph. The presence of heterogeneity in erosivity and the representative hillslope scale were shown

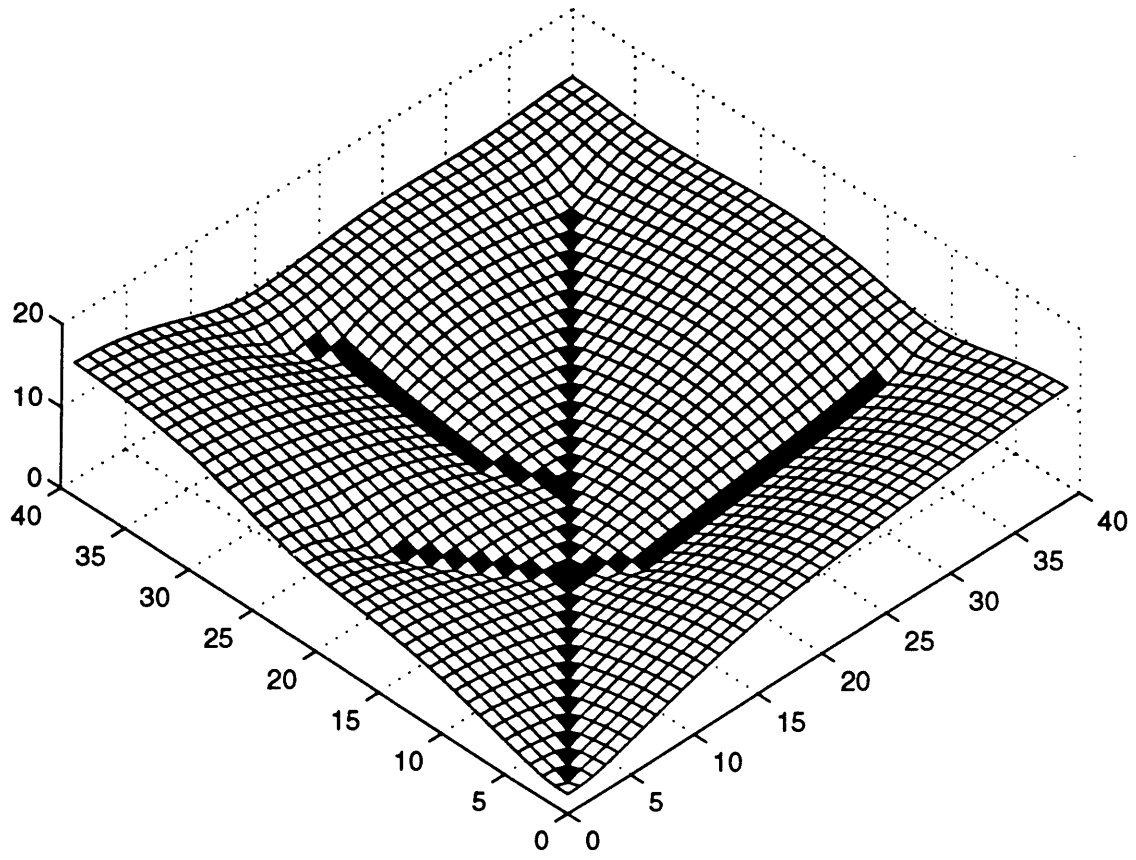

Figure 9-14: 3-D perspective of homogeneous basin with $D = 0.4$ and $A_* = 10.0$.

to have strong influences on the hydrologic response of a basin.

The topographic index, A/S was used to characterize the propensity of a pixel to saturate. The distribution of all topographic indices (analogous to the distribution of cumulative areas) was shown to be strongly affected by heterogeneity. In a homogeneous system the degree of saturation of a basin was shown to be extremely sensitive to the saturation threshold. Small changes in the threshold close to the hillslope scale of the basin result in large changes in the hydrologic response. In contrast, a heterogeneous system exhibits a more even distribution of topographic indices and is thus much less sensitive to the saturation threshold.

The average hillslope scale, governed by the relative magnitudes of D and β also has a controlling effect on the degree of basin saturation. The greater the hillslope scale, the more likely it is to exhibit saturated conditions at a given threshold since larger hillslope scales are characterized by larger cumulative areas before aggregating to a channel and smaller overall slopes. Both quantities serve to increase the topographic index and increase the likelihood of saturation.

Hydrologic response was ultimate quantified by simulated hydrographs considering, in some instances, only those pixels that would be saturated at a given threshold. These width functions further illustrated the greater sensitivity of the homogeneous systems to saturation threshold than the heterogeneous systems. This analysis also illustrated how heterogeneity tends to delay the time to peak and diminish the magnitude of the hydrograph peak. The magnitude and overall shape of the simulated hydrographs were shown to be a function of the hillslope scale, A_*. As hillslope scale decreased, the hydrograph peak was shown to increase and the overall hydrograph duration decreased, resulting in a more peaked and short-lived hydrograph.

Chapter 10

Conclusions

This chapter will summarize the content and findings of each of the chapters and appendices contained in this work. Next, an itemized list of the primary innovations and discoveries will be presented. And finally, since research often generates more questions than it answers, some possible future directions for research will be identified.

10.1 Summary of Contents and Findings

Chapters 2 and 3 of this thesis introduced the reader to some measures which are useful in quantifying observed and simulated landscapes, and to the basin evolution model. Chapter 4 served as a large-scale case study illustrating the sensitivity of simulated topography to the structure of initial conditions. By applying a series of measures to these simulations we were able to illustrate the qualities that they measured, and to discern the merits of each of these measures in discriminating between different systems. The measures which were found to be most meaningful from our analyses were the slope-area relationship, the cumulative area relationship, the hypsometric distribution, and the width function. Chapter 5 contrasted the mathematical consequences of using two different flow algorithms and of the interrelationships among model parameters. Ultimately, this chapter argued for fixing one model parameter, $n = 2$ and for the strict utilization of the multiple flow direction algorithm.

Chapter 6 introduced an important contribution of this work: the implementation of heterogeneities into the evolution model. Spatial heterogeneity was shown to have a strong influence on simulated output. The degree of this influence was controlled by the model parameter, α, which quantified the variance of the heterogeneities. We illustrated how the shape of the cumulative area distribution shifted as a function of the magnitude of α. Visual inspection of simulated landscapes and determination of the cumulative area distribution illustrated both qualitatively and quantitatively how heterogeneities affected the simulated topography. The simulated basins with heterogeneities had cumulative area distributions more closely resembling observed distributions. Also, the channel head was shown to be effectively choosing between three potential growth sites during the channel growth stage of landscape evolution.

This had a systematic effect of shifting the fluvial portion of the slope-area relationship towards smaller slopes.

Chapter 7 addressed the issue of spatial structure in the heterogeneities. We examined both vertical stratification and horizontally correlated heterogeneities. The hypsometric curve was found to vary considerably depending on the structure of these heterogeneities. The mean relative elevation of the entire basin was shown to shift upwards when a basin was carving into increasingly harder stratified material and to shift downwards when the opposite was true. Additionally, the quantity θ, of the slope-area relationship was shown to be influenced by these heterogeneities. If material softness increases as one traces upstream from the outlet, the resulting value of θ will be smaller than if the material was homogeneous. The opposite is true if the material becomes harder as one traces upstream from the outlet.

Chapter 8 dealt with the primary objective of this work which was to produce a systematic methodology for estimating model parameters to reproduce an observed basin. First, an off-line version of the evolution model was developed. This model estimated the cumulative area distribution that would result from a simulation of the actual evolution model for a particular combination of β, D, θ, and α. This model was preferable to using the actual evolution model because of its speed and simplicity. It was readily put into a non-linear optimization package and used to estimate appropriate values of D and α, with θ and β previously determined from the slope-area relationship. A series of five case studies were performed for basins from throughout the United States. Each observed basin was reproduced and favorable comparisons with the slope-area, cumulative area, and hypsometric curve measures were made.

Chapter 9 discussed the influence of geomorphology on basin response. First, the issue of saturation induced runoff was addressed using Beven and Kirkby's (1979) topographic index. It was shown the the distribution of topographic indices varied dramatically as a function of the presence of spatial heterogeneities in erosivity. Basins where heterogeneities were present had a much broader range over which saturation would take place when compared to homogeneous systems. Basin response was quantified in terms of Manning's equation based hydrograph, that was sensitive to topography and the distinguished between channels and hillslopes. Coupling the saturated areas and the hydrograph produced runoff hydrographs which were dependent on the degree of heterogeneity and also the assumed saturation threshold. Basin response was shown to be strongly influenced by heterogeneities in erosivity. The shape of the simulated hydrographs were shown to depend on the hillslope scale. As hillslope scale decreased, hydrograph peaks increased and overall hydrograph duration decreased.

The structure of the heterogeneities used everywhere else in this work was of uniformly distributed noise. Appendix A discussed the consequences of employing normally distributed noise instead. It was shown that model behavior was predictable and consistent with behavior observed for uniform noise, although differences were observed because of the variance structures of the two distributions.

Appendix B provided a detailed account of the parameter estimation and adjustment process applied to a particular observed basin. This appendix could serve as

a tutorial for anyone interested in using this model to reproduce an observed landscape. In this appendix we illustrate a preliminary calibration attempt and measure its quality of agreement to the observed basin. Based on measured shortcomings we demonstrate how parameter values are updated and an improved simulation follows.

Appendix C addressed the issue of grid resolution and its relationship to model parameters. Relationships between β and D at different grid resolutions were derived. A small case study was performed to illustrate the production of equivalent topography at three different resolutions.

10.2 Innovations and Discoveries

The following is an itemized list of the primary innovations and discoveries that were developed during the execution of this work.

- **Multiple flow direction algorithm implemented:** Chapters 2 and 3 described the reasoning behind the multiple flow direction algorithm and illustrated its implementation into the basin evolution model. In Chapter 5 it was shown how the use of multiple flow directions allocated area (or discharge) more evenly, especially on diverging surfaces. This was in contrast to the single flow direction algorithm which suffers from discretization effects.

- **Sensitivity to initial elevation structure demonstrated:** Chapter 4 examined and illustrated the effect that initial structure in the elevation field has on the ultimate drainage pattern. In particular, starting conditions that were characterized as a sagging membrane "stretched" around the basin boundaries (like a drum) yielded a drainage network with a centered main channel. Flat initial conditions produced no such channel. The presence of small perturbations in elevation produced small scale irregularities in the drainage network that were not present in the absence of such perturbations.

- **Heterogeneity in erosivity introduced:** A formulation was presented which introduced the concept of variable erosivity at each point in the basin. Previously, all material was assumed to be homogeneous in its resistance to erosional processes.

  - **White noise heterogeneity:** This most arbitrary form of heterogeneity involved erosivity that was distributed as a white noise process in space. It was shown that as the variance of the heterogeneities increased, the degree of irregularity in both the channel network and the hillslope surface increased. The cumulative area distribution, in particular, is affected by these heterogeneities in a way which is much more consistent with actual observed distributions than when homogeneous material is assumed.
  - **Vertical stratification:** The presence of vertically stratified material was simulated and was shown to have a predictable effect on the hypsometric distribution. It was shown that mean elevations could be reduced or enhanced depending on the assumed trend in stratification.

- **Horizontal correlation:** Similar to the case of vertical stratification, horizontal correlation was shown to affect the hypsometric distribution. Reductions in mean elevation were shown to be dependent on the correlation scale of the heterogeneities.
- **Channel selectivity:** Channels were shown to be selectively choosing relatively soft material in which to grow. It was demonstrated that, on average, the growing channel is choosing the softest among three potential growth sites, and that this leads to a systematic reduction in slope associated with the fluvially dominated portion of the slope-area relationship.

- **Calibration methodology developed:** An off-line version of the basin evolution model was developed and coupled with a non-linear optimization package to estimate initial values for the diffusion coefficient and heterogeneity amplitude parameters. Additionally, a systematic means of updating all model parameters was provided towards the end goal of calibrating the model to reproduce observed topography.

- **Relationship between geomorphology and hydrology shown:** One of the initial objectives of studying basin geomorphology was to predict the hydrologic response that could be anticipated given a particular topography. A simple parameterization was presented for converting topography into a hydrograph. This parameterization considered issues of saturation potential, surface roughness, depth of flow, and surface gradient.

  - **Effect of heterogeneities:** Simulated topography corresponding to heterogeneous material produced hydrographs with smaller peaks and longer durations than those corresponding to homogeneous material.
  - **Saturation behavior:** The sensitivity to saturation threshold was much greater for a homogeneous system than a heterogeneous one. This implies that the precise estimation of saturation conditions becomes less crucial as heterogeneities (indicated by irregularities in the hillslope topography and drainage network organization) increase.
  - **Effect of Hillslope Scale:** As hillslope scale decreased (as a function of the relative strength of diffusive and fluvial sediment transport) the peak discharge increased and hydrograph duration decreased. This suggests that we can infer the relative shape and timing of the hydrographs from two different drainage basins from a knowledge of the relative strengths of different sediment transport processes acting in each basin.

10.3 Future Directions

10.3.1 Effect of Land Cover Change

One of the most obvious potential uses of the model is as a predictive tool to forecast changes in topography resulting from drastic changes in land cover. Such events as

deforestation, strip mining, urbanization, and forest fires would all have the effect of reducing the vegetative cover of an area and rendering it more prone to enhanced erosion. The modeling procedure would be straightforward:

- **Step 1:** Follow the procedure illustrated in Chapter 8 and Appendix B for calibrating the evolution model to the pre-existing (before land cover change) basin condition. Note the parameters: θ, β, D, α, and ξ. These are the parameter values which produce a topography which best approximates the observed terrain.

- **Step 2:** Obtain the actual terrain (from a DEM) and place these elevations in the basin evolution model as the initial condition.

- **Step 3:** Adjust the material softness value, η for all pixels in the region which is to undergo a change. The larger η is, the more readily eroded the material will be.

- **Step 4:** Using the information collected in Steps 1 through 3, begin the simulation. Simulation may proceed for a desired duration or until a new equilibrium condition is obtained.

The simulation should approximate the actual evolution of the basin since the initial condition is the observed topography and the parameter values are calibrated to the basin. Taken together, in the absence of land use change, these data should produce no further evolution. However, since the new η values reflect the land cover change, further evolution can be expected wherever the material has become more susceptible to erosion.

10.3.2 Structure of Heterogeneities

The work presented in this thesis made the most simple assumptions that heterogeneities are uncorrelated in space (except in Chapter 7) and stratification is a log-linearly increasing or decreasing property in depth. These assumptions are not the general case in most areas. The actual structure is likely to be quite complex.

Consider the issue of vertical stratification and its influence on the hypsometric curve. We have shown previously that linearly increasing material hardness tended to shift the hypsometric distribution towards higher mean elevation, and that linearly decreasing hardness had the opposite effect. By controlling the rate of this increase/decrease in material hardness we were able to simulate a fair approximation of the observed hypsometric distribution. Consider Figures 8-9, 8-14, 8-19, 8-24, and B-9. These all show good approximations of the observed hypsometric distributions, however the observed distributions show irregularities that do not appear in the smoother, simulated distributions. It is plausible that irregularities in the stratification pattern are responsible. In other words, the stratification pattern is not linearly increasing/decreasing in hardness with depth, but rather that there is distinct layering over which material properties do not change. It seems possible to examine the

deviations of observed distributions from the simulated ones and prescribe a layering scheme that will produce a closer match to observation.

A more extensive examination of correlation structures in the horizontal plane also is merited. This is a more complex question to address because simulations are profoundly influenced by the relative hardness of the material in the immediate neighborhood of the outlet. Drainage outlets should naturally occur in relatively soft material, therefore a methodology must first be developed for generating a correlated erosivity field which has a biased softness occurring at and near the outlet. Detractors would correctly argue that this is a biased initial condition. It is the nature of this analysis, however, that it leaves the investigator vulnerable to such a criticism. Nevertheless, there is still more to be learned in this area, particularly an examination between correlation scales and their influence on θ. In fact, both vertical stratification and horizontal correlation have an influence on θ as argued in Chapter 7 and illustrated in Figure 7-12.

10.3.3 Incorporating a Soil Production Function

Soil is not infinitely available to erode at all points in a drainage basin. Complex feedbacks between weathering rates and sediment transport may lead to a very large depth of soil material or to an exposed area of highly erosion resistant rock material. The introduction of a soil production mechanism in the model would allow us to study the balance between soil production and soil removal and also to model the development of exposed rock escarpments which are characteristic of some regions.

Different soil production functions have been hypothesized. A typical assumption is that soil production decays exponentially with soil depth (Ahnert, 1976 and Tucker & Slingerland, 1994) while others have assumed that soil production is an increasing function of depth up to some optimum depth and then decays thereafter. Both functions could be implemented and their results compared against observations.

In this way we can address the issue of whether a landscape is weathering or transport-limited. In actuality, it would likely be some combination of the two: weathering-limited in areas that have a zero depth soil horizon, and transport-limited where the soil depth is non-zero.

10.3.4 Thresholds in Landscape Evolution

The erosion mechanisms within this model, both fluvial and diffusive, are inherently lacking in a threshold mechanism. There are those that argue that fluvial erosion is not as we present it here:

$$Q_s = \beta A^m S^n$$

but rather that there is some threshold which must be exceeded in order for erosion to take place:

$$\begin{aligned} Q_s &= 0, & \tau < \tau_{crit} \\ Q_s &= (\tau - \tau_{crit})^r, & \tau > \tau_{crit} \end{aligned}$$

where τ_{crit} is a critical shear stress above which erosion takes place, and τ is likely to be some non-linear function of area and slope.

Diffusion processes can also exhibit threshold behavior. Sand piles (or in nature, talus slopes) exhibit a characteristic slope called the angle of repose. This is the largest slope the material can support. If more mass is added a landslide will result with the material being redistributed until all slopes are, at most, equal to the angle of repose. Landsliding, especially in arid environments, is a good example of a diffusive transport mechanism dependent on a threshold quantity.

It is a rather simple matter to modify the evolution model to incorporate thresholds of these kinds. But two questions arise:

1. How do we recognize that an observed topography is the result of threshold dominated processes?

2. Given a threshold dominated process, how do we determine what the thresholds are?

The success of the current formulation of the basin evolution model suggests that either thresholds are not needed to reproduce topography, or that the topography we have concentrated on reproducing is not threshold process dominated. The role of thresholds in future work should proceed along two lines:

1. More observed topographies should be obtained, particularly in arid regions where rock falls, landsliding, and talus slopes are common features. This would almost certainly provide a chance to incorporate different diffusion mechanisms which involve a natural threshold behavior.

2. Wherever shortcomings in an attempted reproduction of observed topography are encountered, the modeler should question whether the discrepancies may be the result of some threshold phenomena which is not currently in the model formulation.

10.3.5 Isostatic Uplift Feedback

Uplift as it has been treated in this work is a prescribed constant value. It provides the forcing mechanism which drives the system to equilibrium. It is possible to model uplift which occurs episodically (Willgoose, 1994) or to have no uplift at all. In these cases uplift is a simple force which acts irrespective of the conditions present in the eroding landscape. This is the nature of *tectonic* uplift which is in response to large scale movements and collisions of the earth's crustal plates.

Isostatic uplift is a different form of uplift which results from shifts in the mass loadings from one place to another on the earth's crust. Under isostatic uplift, a section of the earth's crust experiences an uplift because erosion has removed material from it thus reducing the load supported by the section, much as a boat will rise up in the water when some of its cargo has been removed.

Consider this example. We have a block of the earth's crust with density, ρ_c overlying a pool of the earth's mantle with density, ρ_m. Since $\rho_c < \rho_m$ the crust

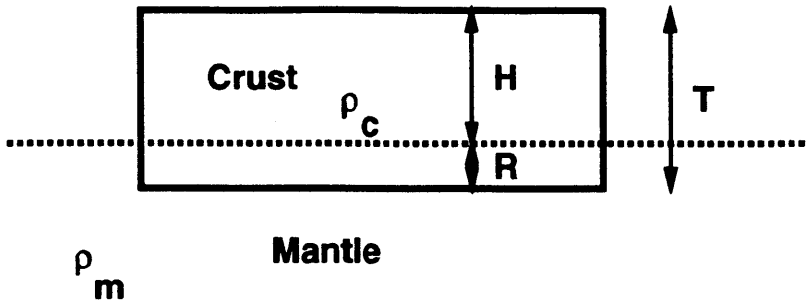

Figure 10-1: Schematic diagram of crust floating in mantle.

floats in the mantle as a boat would in water. Figure 10-1 shows the geometry of an idealized system. The block has total thickness, T of which H floats above the mantle fluid and R lies below the fluid level. By Archimedes principle, the weight of the displaced fluid is equal to the weight overlying crust:

$$R\rho_m = T\rho_c$$

and since $R = T - H$,

$$(T - H)\rho_m = T\rho_c$$

$$H = T\left(\frac{\rho_m - \rho_c}{\rho_m}\right)$$

Imagine now that a thickness, ΔT is eroded off the top of the crustal block. The block will rebound due to its lightened load by an amount, ΔH:

$$\Delta H = \Delta T\left(\frac{\rho_m - \rho_c}{\rho_m}\right)$$

In this frame of reference, the observed uplift would be the change in thickness, minus the isostatic rebound:

$$U_{iso} = \Delta T - \Delta H = \Delta T\left[1 - \left(\frac{\rho_m - \rho_c}{\rho_m}\right)\right] = \Delta T\left(\frac{\rho_c}{\rho_m}\right)$$

Some representative values used for ρ_c and ρ_m 2700 kg/m^3 and 3300 kg/m^3. Therefore,

$$U_{iso} = 0.8\Delta T$$

or in other words, erosion of 10.0 units of elevation will result in an isostatic rebound of 8 units.

If we have a system in which erosion is triggered by some initial elevation difference due to uplift at the outlet of the system of height, ΔT, then erosion will not only remove this initial elevation difference of ΔT, but all subsequent uplift due to isostasy. In the end the ultimate amount of material removed as the result of the initial uplift will be:

$$\Delta T_{tot} = \Delta T + \Delta T \left(\frac{\rho_c}{\rho_m}\right) + \Delta T \left(\frac{\rho_c}{\rho_m}\right)^2$$

so finally,

$$\Delta T_{tot} = \frac{\Delta T}{1 - \frac{\rho_c}{\rho_m}}$$

which for the quoted values of ρ_c and ρ_m gives:

$$\Delta T_{tot} = 5\Delta T$$

Meaning that an initial disturbance to a system subject to isostatic forces will produce an ultimate amount of erosion equal to approximately five times the amplitude of the initial disturbance.

In actuality, the response is likely not be this great since the earth's crust is all interconnected so the eroding block would not be free to uplift, but rather there would be bending moments imparted to the block which would cause flexural isostasy and thus spatially varied uplift (see Tucker and Slingerland, 1994). The point being made here is that uplift is potentially a much more complicated force than it has been treated in the past. Most importantly, through isostatic uplift, erosion may cause a positive feedback which would support conditions for further erosion to take place.

10.3.6 Other Open Modeling Issues

This work addressed the problem of calibrating a basin evolution model to reproduce, in a statistical sense, an observed basin. Many choices were made along the way to expedite the process of refining the calibration methodology. What effect does imposing the basin boundary of the observed system on the simulated system have on the geomorphic measures of the simulated topography, especially on the hypsometric curve? How does the assumed structure of the heterogeneities (its functional formulation, the pdf, horizontal and/or vertical correlation) influence the simulated basin? Does the issue of point-to-point transfer versus direct removal of material influence transients of the basin evolution process? Do different parameterizations of the runoff producing process lead to fundamentally different hydrographs given the same basin?

These questions remain unanswered to various degrees. We have shown (in Appendix A) how normally distributed heterogeneous erosivity produces different behavior than uniformly distributed heterogeneities. We have also shown different correlation structures. However, many other different forms or combinations could be attempted depending on the physical characteristics desired to be modeled. For example, one could imagine a mechanism where the material hardness at a point changes dependent on whether the point is a channel or hillslope. In this way, the evolution

process itself provides a feedback into the material properties. This could take on the form of the soil production function discussed earlier, or could even be as simple as making the hardness a function of the hillslope scale:

$$\begin{aligned} \eta_{i,j} &= \eta_0 \quad \text{if } A_{i,j} \leq A_* \\ \eta_{i,j} &= c\eta_0 \quad \text{if } A_{i,j} > A_* \end{aligned} \tag{10.1}$$

where c is a constant which represents the increased resistivity to erosion that might occur in a channel if bed armoring were present.

One's imagination is the only limit to possible modifications to this model.

10.3.7 Integration with GIS System

A Geographic Information Systems (GIS) is a software package which provides a means for computations and comparisons in a visual, database style format. Computations can be simple (e.g. Display all pixels whose cumulative area exceeds 50 pixels.) or can be quite complex such as involving watershed delineation. A GIS is a natural tool for the DEM analysis and model simulations described in this work. We found numerous occasions when questions like, "Where are the unstable pixels located?" or, "Is there any trend in the position of the pixels draining areas between 10 and 50 pixels?" With our current capabilities questions like these would require that a program be written and executed, followed by the output being incorporated into a graphics package and plotted. With a GIS, built in instructions would address these problems and provide visualization of the solutions directly.

An added bonus is that the GIS would provide a standard for file formats. This would halt the current proliferation of data file structures associated with different programs and investigators. It would also make our data more accessible to others and vice-versa. Finally it would provide for a more user-friendly interface than the current UNIX environment prompt.

There are numerous GISs on the market today. Of those available, GRASS seems like the logical choice since it is widely used (especially in academia) and it is an "open GIS" meaning that the code is not owned by a company, but by the community at large. Furthermore, the community is invited to contribute code which is compatible with the GRASS environment, so GRASS is always growing. It may even be possible that our basin evolution model could be modified or translated to be GRASS compatible.

All this said, a GIS is not an end in itself, but merely a tool which my make future developments come more quickly while providing easy access to data visualization. It seems to be a logical extension of what we are trying to accomplish and would broaden the audience that we are trying to reach.

Appendix A

Channel Selectivity in an Normally Distributed Erosivity Field

This appendix will address the issue of channel selectivity in a normally distributed erosivity field. In Chapter 6 it was shown that the channels tended towards a mean softness index of 0.25 in a uniformly distributed erosivity field varying between -0.5 and 0.5. It was argued there that this tendency was due to the channel selectively choosing the softest material in which to erode. If the channel is choosing from among three sites in which to erode then the expected maximum of three uniformly distributed values on [-0.5, 0.5] would be 0.25.

To check this hypothesis a small set of simulations were performed with normally, $N(0, 0.083)$, distributed white noise rather than the uniformly distributed erosivity generally used. A variance of σ^2=0.083 is used to be consistent with the variance for the uniformly distributed erosivity fields. Tables A.1 and A.2 show the expected value and variance of the maximum of n values taken from a uniform and normal distribution, respectively.

Table A.1: Maximum of ζ Uniform values on [-0.5, 0.5]. (Asterisks indicate numerically estimated quantities.)

ζ	$\mu(\zeta)$	$\sigma^2(\zeta)$
1	0.000	0.083
2	0.167	0.054*
3	0.250	0.037*
4	0.300	0.026*

Table A.2: Maximum of ζ Normal $N(0, 0.083)$ values. (Asterisks indicate numerically estimated quantities.)

ζ	$\mu(\zeta)$	$\sigma^2(\zeta)$
1	0.000	0.0830
2	0.163*	0.0564*
3	0.244*	0.0464*
4	0.297*	0.0408*

The values shown in Tables A.1 and A.2 were determined by Monte Carlo simulation. Inspection of these tables indicates that the expected values, $\mu(\zeta)$ are very comparable between the two distributions. Therefore, even before performing a simulation with normally distributed erosivity (rather than uniform erosivity), we would expect the mean channel selectivity behavior to be comparable between the two cases. Note that the variance decreases as ζ increases for both distributions. This decrease in the variance is not as rapid for the normally distributed data as for the uniformly distributed data. Because of this, we might expect that the average of the results from the normally distributed simulations would be more "noisy" than those from the uniformly distributed simulations shown in Chapter 6.

Figure A-1 shows a moving average plot (analogous to Figure 6-12) of five simulations with normally distributed white noise erosivity. The solid horizontal lines mark the expectations from equations A.2 while the other solid line indicates the average of the five simulations. Although five simulations provide only a small sample, these data show that the moving average of erosivity, for areas greater than 100 pixels, tends towards a mean value comparable to the uniform case (i.e. softness index close to 0.25) for the case where $\zeta = 3$. This suggests that the reduction in mean slope associated with channel selectivity will be comparable whether the underlying distribution is uniformly or normally distributed, provided that both distributions have the same variance. Moreover, the data support the hypothesis that on average, the growing channel head is choosing from among three potential growth sites, regardless of the probability distribution of the erosivity field.

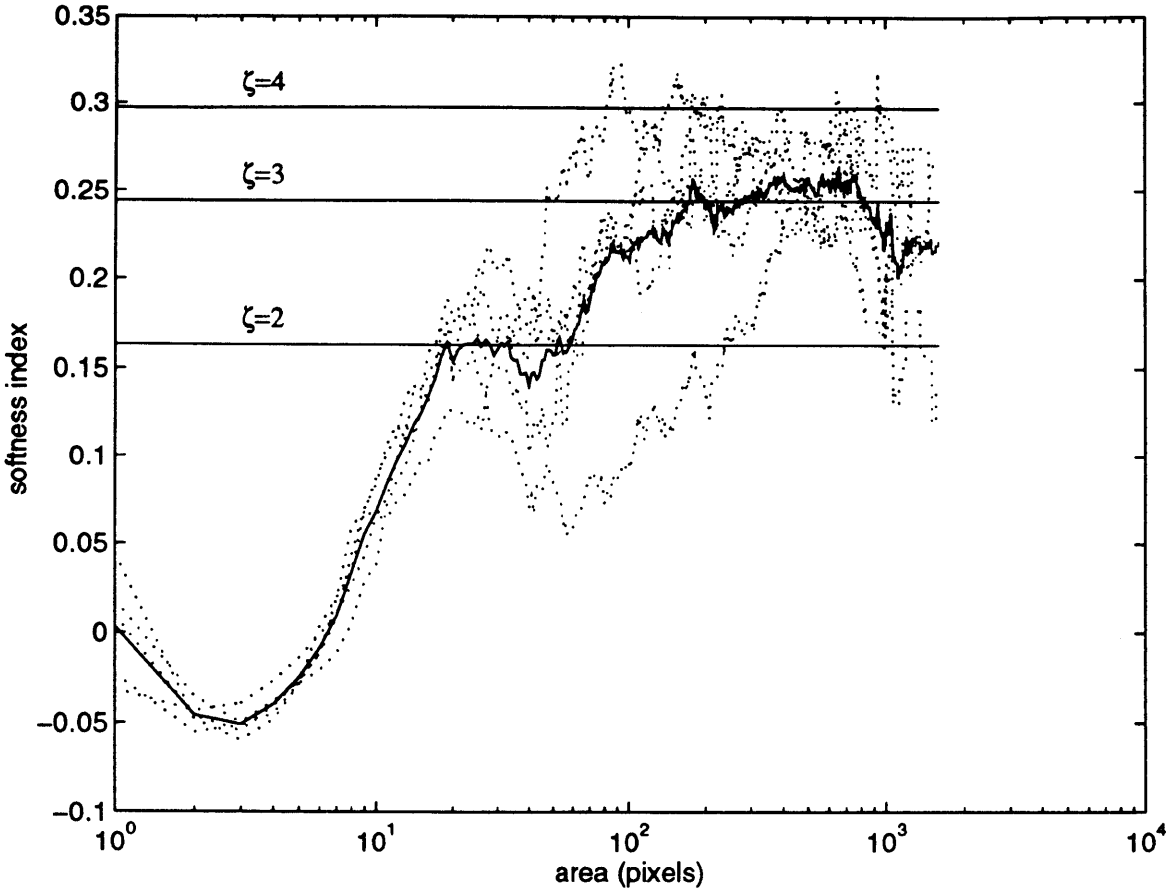

Figure A-1: Five individual simulations (dotted lines) and ensemble average (solid line) of softness index as a function of area. Horizontal lines indicate expected mean of maximum value of 2, 3, and 4 $N(0, 0.083)$ values.

Appendix B

A Sample Calibration

This appendix will illustrate the procedure for calibrating the parameters of the basin evolution model to an observed topography. The topography we are trying to calibrate to corresponds to a small drainage basin in western Pennsylvania. Figure B-1 shows the topography and channel network of this basin. This basin was selected by employing software developed by David Tarboton in his research at MIT (1989). The elevation data are provided by the U.S. Geological Survey. The data are scanned and drainage directions are assigned based on a steepest descent method. These drainage directions are then used to determine cumulative areas draining through each pixel in the basin. An outlet is selected based on an arbitrary drainage basin size of about 2000 pixels (1.8 km^2). A simple routine is used to isolate the set of points which drain to the selected outlet pixel. These points define the drainage basin we wish to reproduce. Channels pixels (pixels draining an area of more than 50 pixels) are painted in dark gray to help visualize the basin more clearly.

The first step of the calibration process is to determine θ and β from the observed slope-area relationship for this basin. These data are shown plotted in Figure B-2. The slope of the scatter for large area ($A > 10$ pixels) suggests that $\theta = 0.3$. We will fix $n = 2.0$ since this is a good central value of n from the literature. This immediately determines the value of m since θ is related to m and n by $\theta = m/n$ and we obtain that $m = 0.6$.

The determination of β is more complicated. The theoretical value of β is related to the value of slope at $A = 1$ of the projected power-law relationship which is fit through the fluvial portion of the slope-area relationship. In this case, $S_{A=1} = 7.5$. From this information we can determine β using the fact that:

$$\beta_{theoretical} = \frac{U}{S_{A=1}^n} = \frac{0.1}{7.5^2} = 1.8 \times 10^{-4} \tag{B.1}$$

The operational value of β is reduced by the presence of heterogeneity due to both channel selectivity and the fact that the the value of β cited above represents a mean value, while the operational value must be diminished to reflect that we are working with a log-uniformly distributed random variable. First, to account for channel selectivity:

$$\beta_{channel\ selectivity} = \beta_{initial}(10^{\frac{\sigma}{4n}}) \tag{B.2}$$

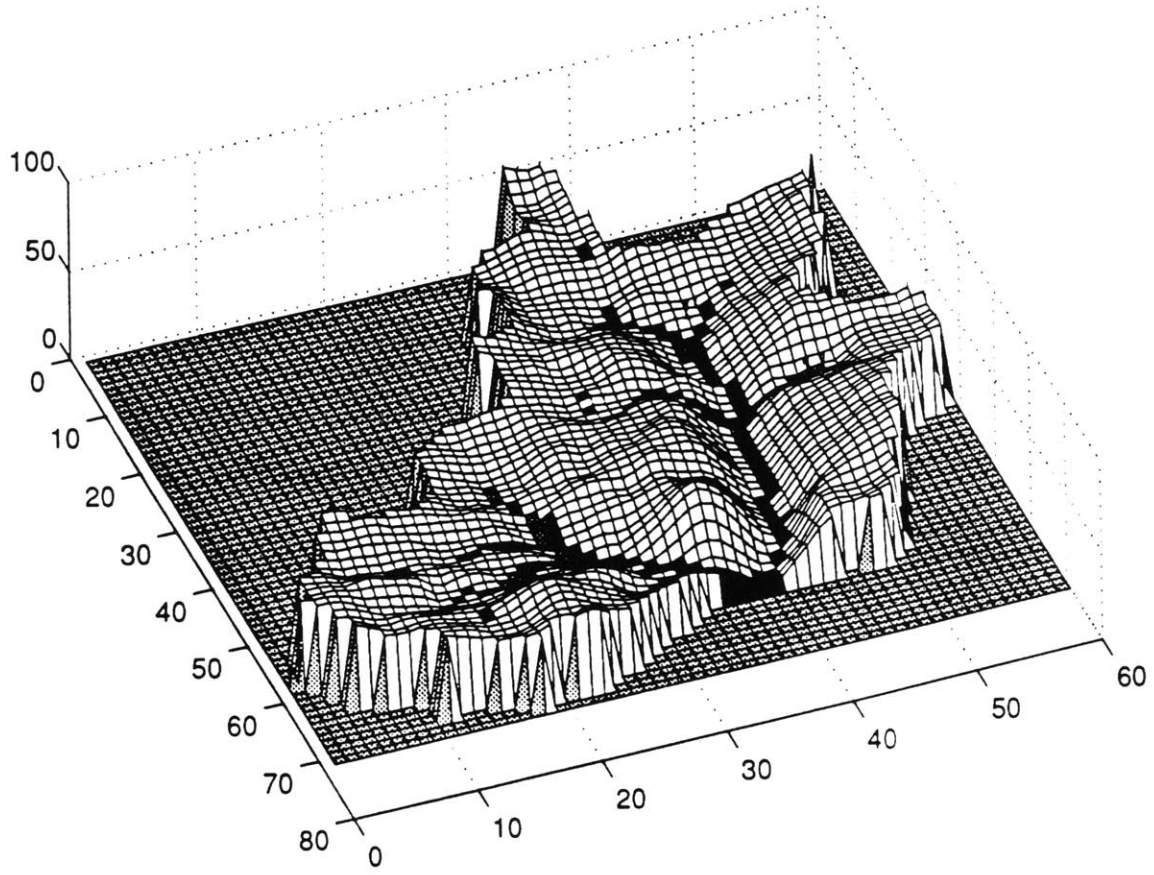

Figure B-1: 3-D perspective of observed topography for Racoon data set.

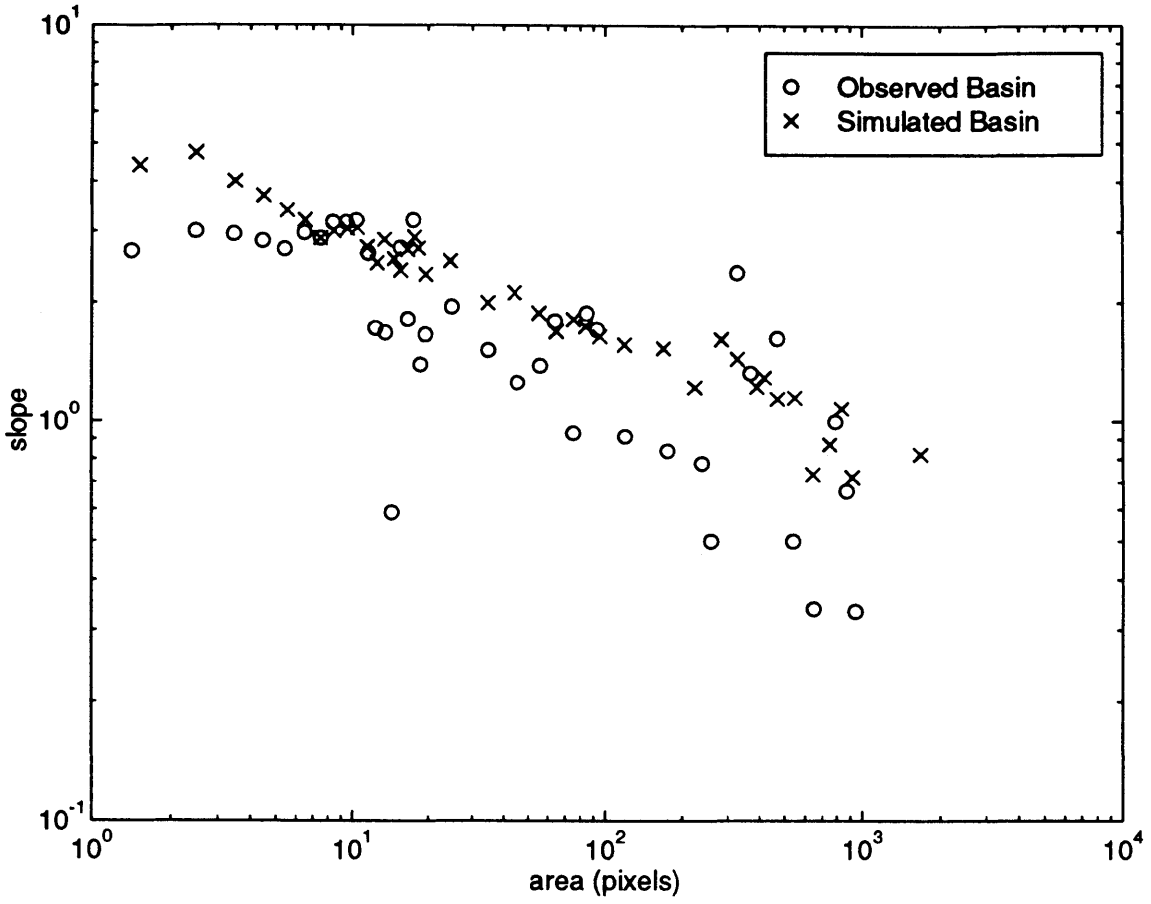

Figure B-2: Slope-area relationships for Racoon data set. (Shown are the relationships for the observed "o" and simulated basin "x".)

and second, to account for the mean of a log-uniform distribution:

$$\beta_{operational} = \beta_{channel\ selectivity} \left[\frac{10^{\alpha y}}{\alpha \ln(10)} \right]_{y=-0.5}^{y=0.5} \tag{B.3}$$

Notice that both equation B.2 and B.3 are dependent on α which we have yet to estimate. This necessitates an iterative process in which both α and the reduction of β due to α are determined. In truth, an initial estimate of $\alpha = 2.0$ is generally close for real topography and provides a good approximation for use in equations B.2 and B.3. In the case where $\alpha = 2.0$ the reduction factors associated with these two equations are 1.78 and 2.15, respectively. Thus, the operational value for β in this case, becomes:

$$\beta_{operational} = \frac{1.8 \times 10^{-4}}{(1.78)(2.15)} = 4.9 \times 10^{-4}$$

Next, the cumulative area distribution is determined for the observed basin. This provides the set of values $P_{obs}(A \geq a)$ to be used in equation 8.3. We now have all the information we need to use the off-line version of the model discussed in Chapter 9. By numerical optimization we learn that $D = 0.180$ and $\alpha = 2.0$ provide good initial estimates for the observed cumulative area distribution. This reinforces the initial estimate of $\alpha = 2$ used in the determination of β.

Using these parameter values (and assuming no stratification $\xi = 0.0$), we obtain the simulation shown in Figure B-3. The simulated slope-area relationship, cumulative area distribution, and hypsometric distribution are shown in Figures B-2 through B-5.

Analysis of this initial simulation indicates that the the parameter estimation process was reasonably successful. Several systematic errors, however, are evident. The slope-area relationship indicates that although we have successfully matched the overall observed data, the particular sub-basin we are trying to reproduce exhibits consistently smaller slopes at all values of area. This presents a dilemma in terms of the objectives in the parameter estimation process. There was the implicit assumption that the the sub-basin we were trying to reproduce was consistent with the overall basin of which it is a part. The results here suggest this is not the case, namely, the D and β would both need to be changed to obtain a simulation more closely approximating the characteristics of the smaller sub-basin. In this case both parameters would need to be increased since the objective is to produce a basin with less relief and slopes reduced at all values of cumulative area. This will be our goal in subsequent iterations of the parameter estimation process.

The cumulative area distribution shows the simulated sub-basin consistently aggregates too quickly, however the degree of heterogeneity implied by $\alpha = 2.0$ seems appropriate. Likewise, there is a clear discrepancy in the third measure, the hypsometric distribution. The observed distribution indicates that there is a greater proportion of higher elevations in the observed basin than in the simulated one. Recall from Chapter 7 that the introduction of stratification will shift the simulated hypsometric distribution towards higher or lower elevations depending on the nature

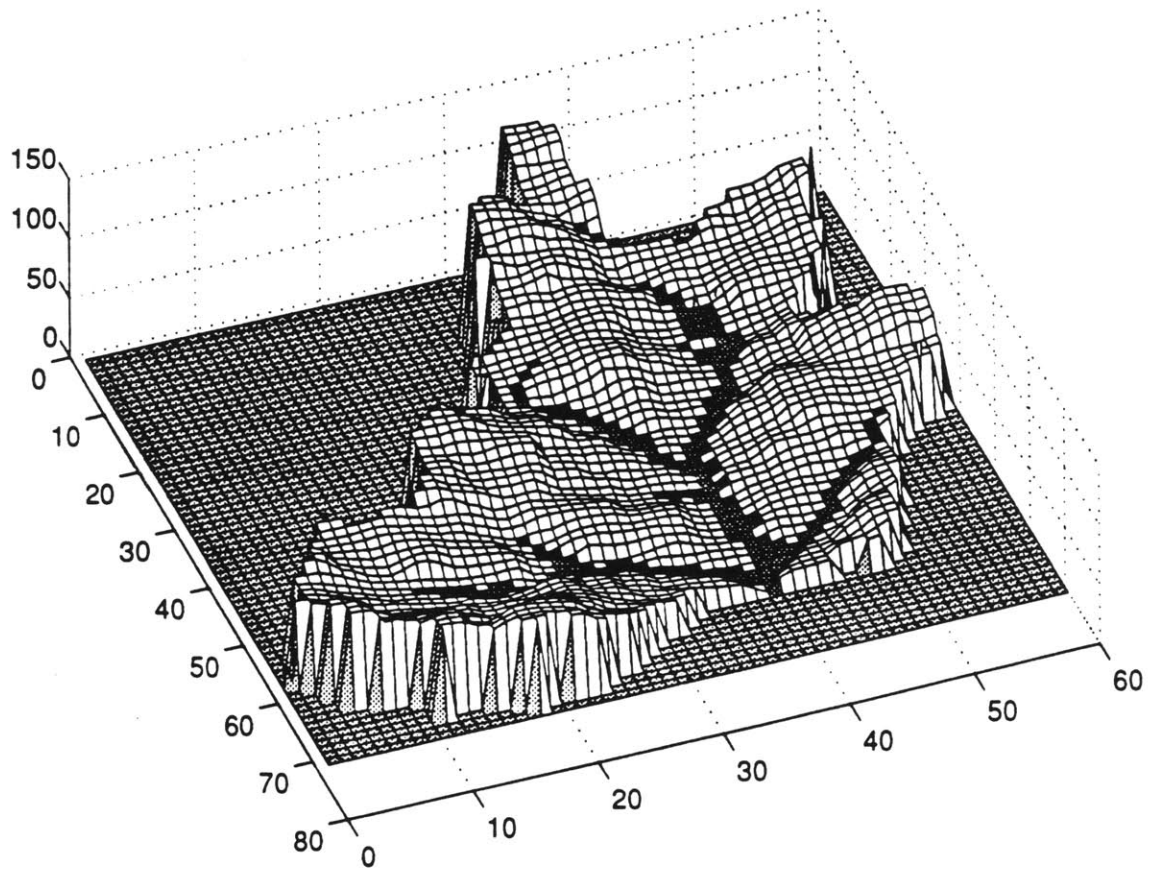

Figure B-3: 3-D perspective of initial simulated topography for Racoon domain.

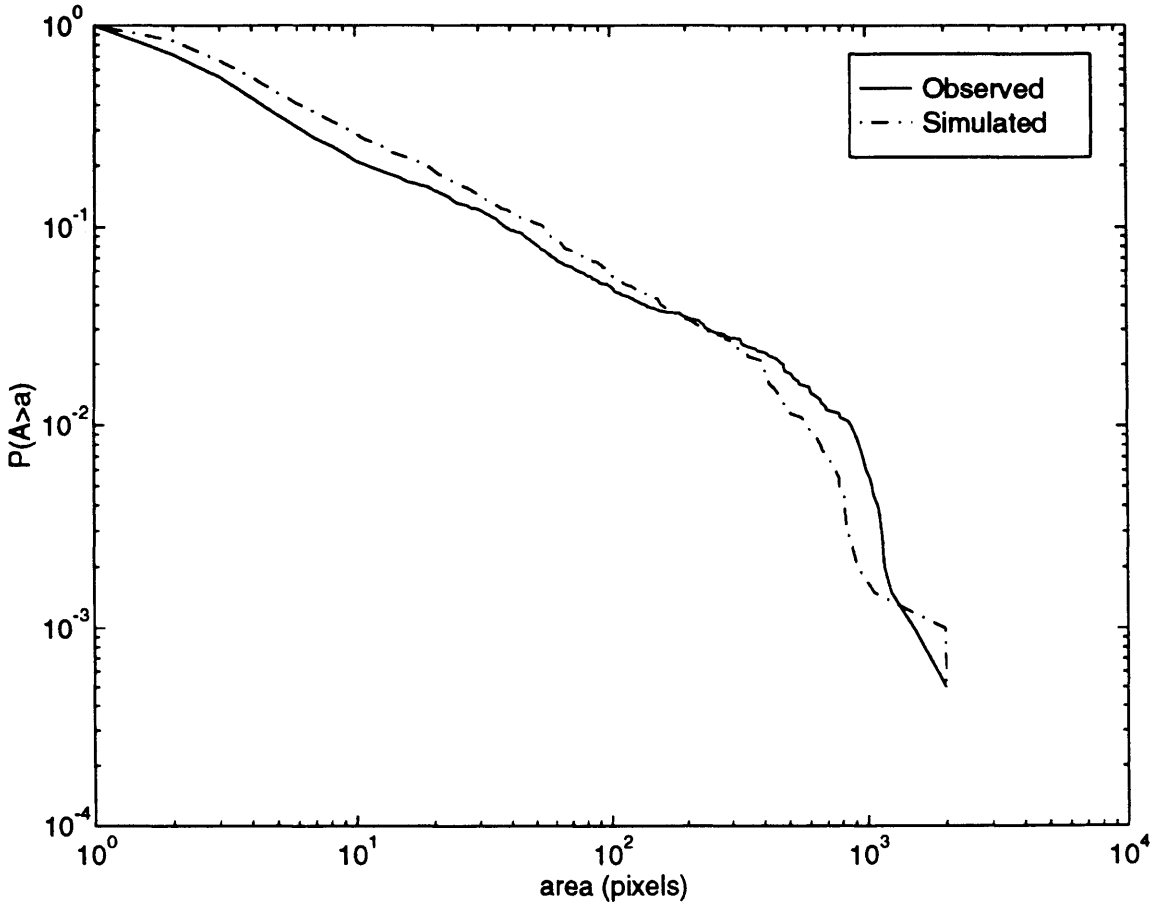

Figure B-4: Observed and initial simulated cumulative area distributions for Racoon data set.

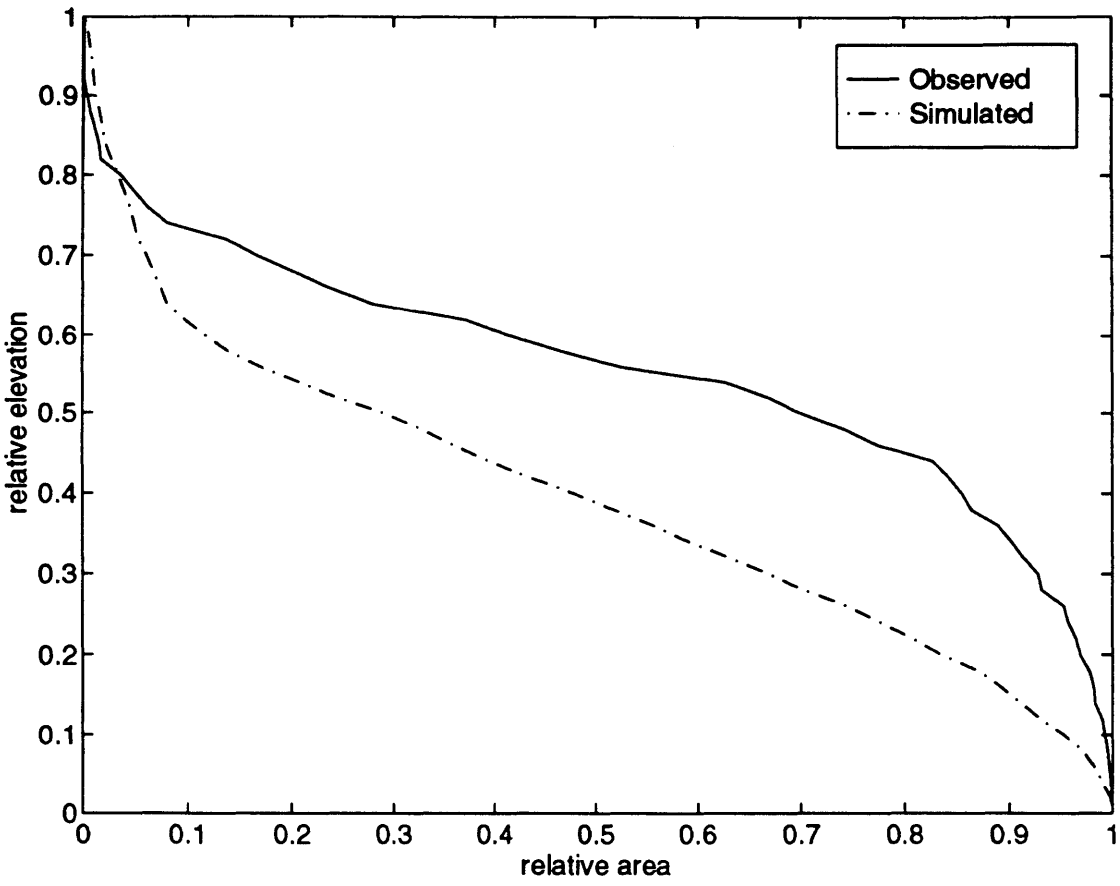

Figure B-5: Observed and initial simulated hypsometric distributions for Racoon data set.

of stratification. In this case, positive stratification (softer material overlying harder material would produce to desired effect of raising the average elevation of the basin.

From this analysis of these three measures we now know the following:

- β needs to be increased to reduce the slopes in the slope-area relationship and diminish the simulated relief.
- By the same reasoning as above, D needs to be increased. This parameter needs to be increased still further to reduce the aggregation rate as indicated by the cumulative area distribution.
- $\xi > 0$ should be used to increase the hypsometric distribution.

The question now arises of how to adjust each of the above parameters. The following is one way of doing so.

B.1 Updating m and n

In this particular example, the simulated power law scaling of slope with area seems consistent with the observed behavior and thus no change in the ratio of m to n is called for. This will always be the case provided that there is no stratification ($\xi = 0.0$) in the simulated domain. If stratification is present then m will have to be increased or decreased depending on whether the stratification is positive or negative, respectively. The degree to which m should be adjusted depends on the degree of stratification.

B.2 Updating β

The best method for updating β is to compare the relief from the previous simulation to the relief of the observed system. Relief of a basin is proportional to the average slopes within the basin raised to the power, n:

$$\beta_{new} = \beta_{old} \left(\frac{\Re_{old}}{\Re_{obs}} \right)^n \tag{B.4}$$

where $\Re_{old}$ is the relief produced in the previous simulation and $\Re_{obs}$ is the relief of the observed system.

B.3 Updating D

Recall that the relative magnitudes of β and D govern the extent of the hillslope scale. Thus any change in β necessitates a corresponding change in D even if the degree of diffusion in a given simulation is what is desired to reproduce observation.

In order to keep β and D in correct proportion, we need to preserve the size of the hillslope scale. From Chapter 3 the hillslope scale was defined as:

$$A_* = U^{\frac{1-n}{n+m}} \beta^{\frac{-1}{n+m}} (fD)^{\frac{n}{n+m}}$$

If we wish to maintain the same hillslope scale through two different pairs of β and D the following relationship must be maintained:

$$D_{new} = D_{old} \left(\frac{\beta_{new}}{\beta_{old}} \right)^{1/n} \tag{B.5}$$

If, in addition we wish to modify the strength of diffusion relative to the previous simulation, this should be done to the value of D_{new} obtained from equation B.5.

B.4 Updating α

Modification of the value of α is required whenever there is a discrepancy in the rate of aggregation of intermediate area pixels ($5 < A < 30$) as indicated by the cumulative area distribution. To reduce the aggregation rate (make the slope of the cumulative area distribution less negative), increase the value of α. If the aggregation rate is too slow, decrease α. From experimentation $1.5 < \alpha < 2.2$ produce topography and statistics which are consistent with natural landscapes.

Whenever α is changed, there are some implied changes on β and D, caused by the change in the mean behavior of a log-uniform distribution and channel selectivity.

- **Effect on β:** The new value of β is related to the old value by calculating the factors itemized in equations B.2 and B.3 and multiplying by the ratio factors associated with α_{old} and α_{new}:

$$\beta_{new} = \beta_{old} \left(\frac{\alpha_{new}}{\alpha_{old}} \right) \left(10^{\frac{\alpha_{old} - \alpha_{new}}{4n}} \right) \left(\frac{10^{\frac{\alpha_{old}}{2}} - 10^{\frac{-\alpha_{old}}{2}}}{10^{\frac{\alpha_{new}}{2}} - 10^{\frac{-\alpha_{new}}{2}}} \right) \tag{B.6}$$

- **Effect on D:** The new value of D is modified in a similar way except that there is no need to adjust for channel selectivity since diffusion is only important on the hillslopes:

$$D_{new} = D_{old} \left(\frac{\alpha_{new}}{\alpha_{old}} \right) \left(\frac{10^{\frac{\alpha_{old}}{2}} - 10^{\frac{-\alpha_{old}}{2}}}{10^{\frac{\alpha_{new}}{2}} - 10^{\frac{-\alpha_{new}}{2}}} \right) \tag{B.7}$$

B.5 Updating ξ

Stratification is introduced in this model through the parameter, ξ. This parameter represents the doubling rate of material hardness with elevation. Examination of the observed and simulated hypsometric curve (initial simulation with $\xi = 0$) will indicate whether a change in the stratification behavior is required. If a modification to

ξ is needed, then the issue of how much to change ξ must be addressed. From an operational standpoint one must judge how large a discrepancy exists between the observed and simulated hypsometric distributions. We have found that 1 to 3 doublings of material hardness over the observed system relief will adequately adjust almost any simulation to more closely agree with the observed system. A single doubling will take care of small differences (within 10% of observation), while 3 doublings will account for differences of 30%-40%. Once the number of doublings needed has been determined, ξ can be calculated from:

$$\xi = \pm \frac{\#\ of\ doublings}{\Re_{obs}} \tag{B.8}$$

where the leading sign of B.8 is positive if the simulated hypsometric curve needs to be shifted upwards, and negative if downwards.

If ξ is changed to a non-zero value then a number of parameters are affected. The values of m must be changed such that the overall value of θ remains consistent with observation. From experience, it has been found that the simulated m should be changed according to:

$$m_{new} = m_{old} + \frac{\xi \Re_{obs}}{12.5} \tag{B.9}$$

which indicates that operational value of m will increase for positive ξ and decrease for negative ξ. The value of the parameter β is also influenced since now the carving strength of a channel is a function of elevation. From experience, β should be adjusted according to:

$$\beta_{\xi \neq 0} = \beta_{\xi=0} \frac{1}{2.5 \xi \Re_{obs}} \tag{B.10}$$

which indicates that the operational value of β is reduced relative to the case of no stratification when $\xi > 0$ and the opposite is true when $\xi < 0$.

B.6 Adjustments for Racoon Simulation

From the results of the initial simulation, the need for several adjustments was indicated. First we need to adjust ξ to account for the rather large discrepancy between the simulated hypsometric distribution and the observed one. From experience the degree of this discrepancy can be accounted for by allowing material hardness to increase with depth ($\xi >$) about 2.5 times. Thus we calculate ξ to be:

$$\xi = \frac{\#\ of\ doublings}{\Re_{obs}} = \frac{2.5}{62} \approx 0.04$$

This creates the need to adjust m to reflect the presence of stratification:

$$m = 0.6 + \frac{(0.04)(62)}{12.5} \approx 0.8$$

Table B.1: Summary of Racoon Calibration Process

Quantity	Observed	Simulated (initial)	Simulated (final)
θ	0.3	0.3	0.3
m		0.6	0.8
β		4.9×10^{-4}	2.8×10^{-4}
D		1.8×10^{-2}	8.4×10^{-3}
α		2.0	2.0
ξ		0.0	0.04
Relief	62.0	122.1	65.8

Next, we need to adjust β to produce much less overall relief (at the same time this will reduce overall slopes in the fluvially dominated portion of the slope-area relationship). The reduction is given by equation B.4:

$$\beta_{new,\xi=0} = 4.9 \times 10^{-4} \left(\frac{122.1}{62}\right)^2 = 1.9 \times 10^{-3}$$

This value of β must also be adjusted for stratification. Using equation B.10 we get

$$\beta_{new,\xi\neq 0} = 1.9 \times 10^{-3} \frac{1}{(2.5)(0.04)(62)} \approx 2.8 \times 10^{-4}$$

Likewise, D must be changed just to keep pace with the change in β. Using equation B.5 we get:

$$D_{new} = 1.8 \times 10^{-2} \left(\frac{2.8 \times 10^{-4}}{4.9 \times 10^{-4}}\right)^{1/2} \approx 1.05 \times 10^{-2}$$

The value of D needs to be further reduced as reflected in the cumulative area distribution. We will choose to use about 80% of this value or $D = 8.4 \times 10^{-3}$. These parameters produce a much closer reproduction of the observed topography as shown in Figures B-6 through B-9. Each of these figures shows good with the observed system and much better agreement than that of the initial simulation. The parameters used in the calibration process are summarized in Table B.1.

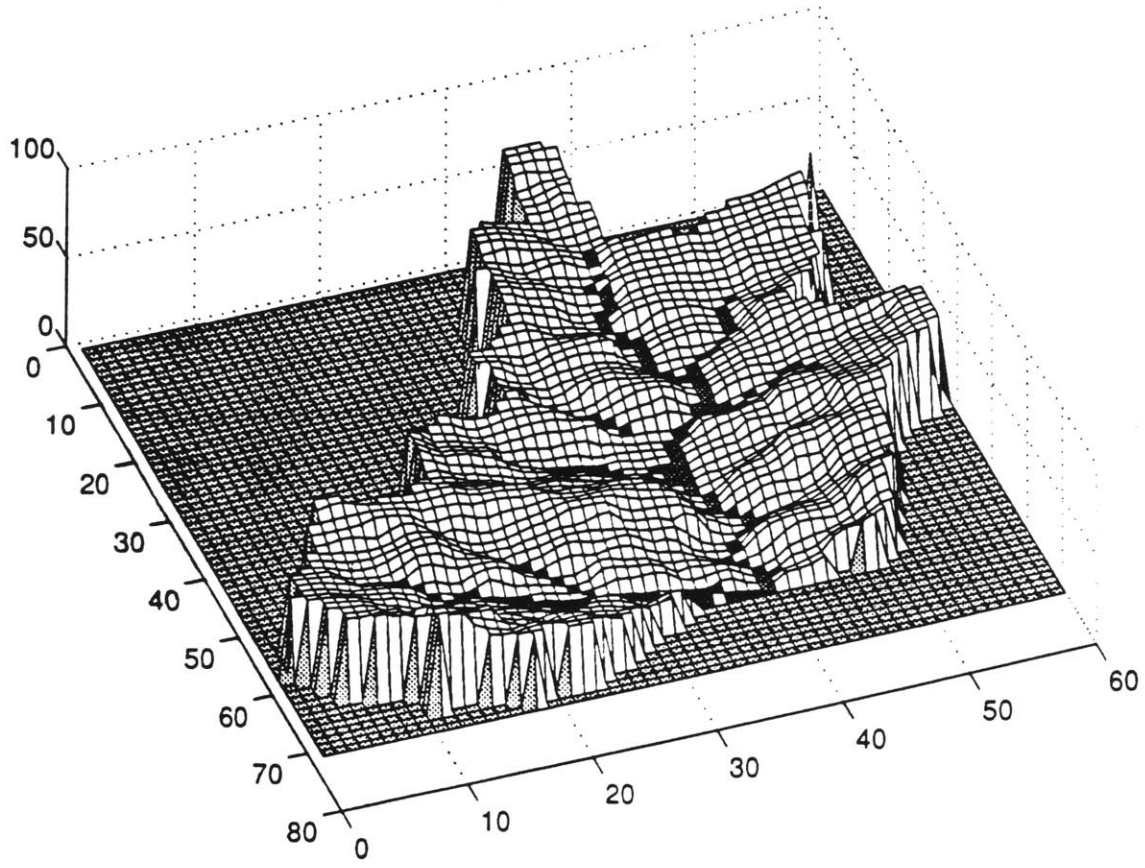

Figure B-6: 3-D perspective of final simulated topography for Racoon domain.

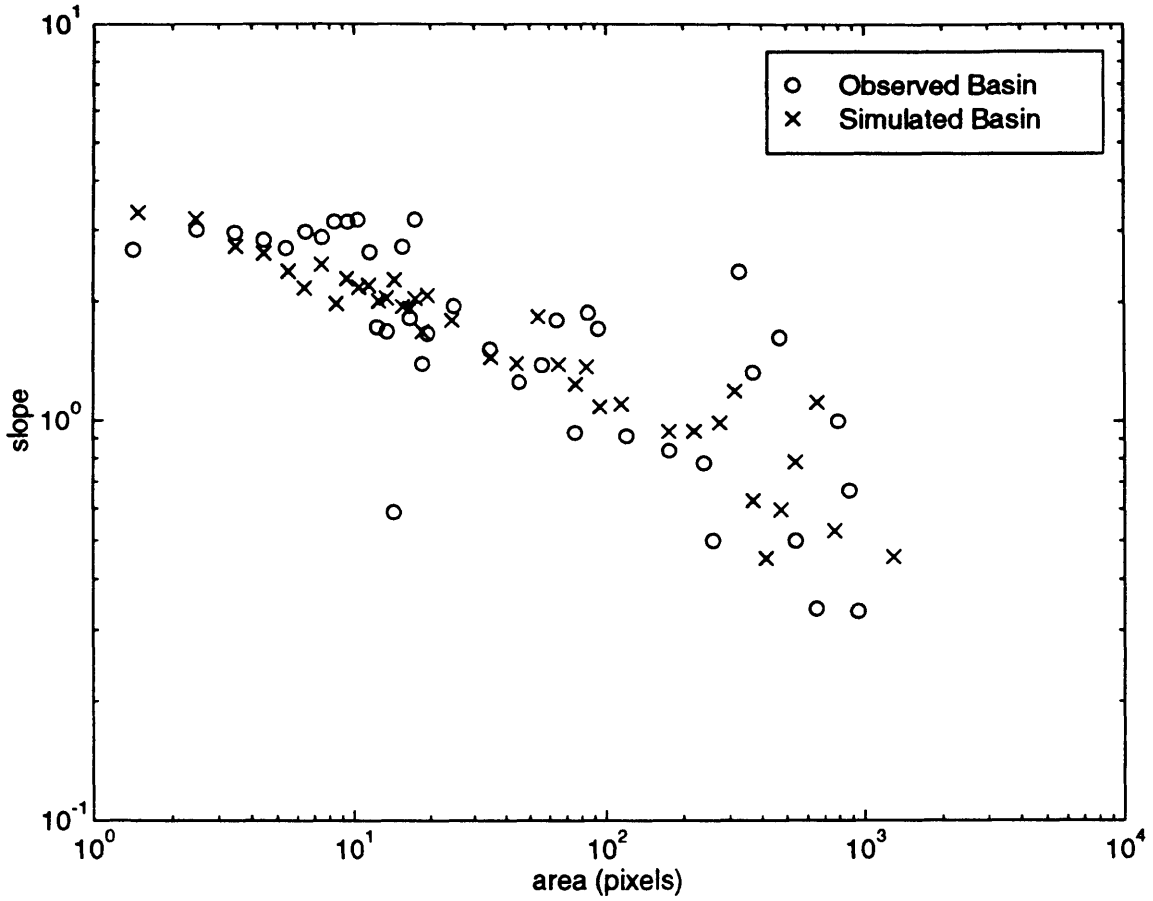

Figure B-7: Slope-area relationships for Racoon data set. (Shown are the relationships for the observed "o" and simulated basin "x".)

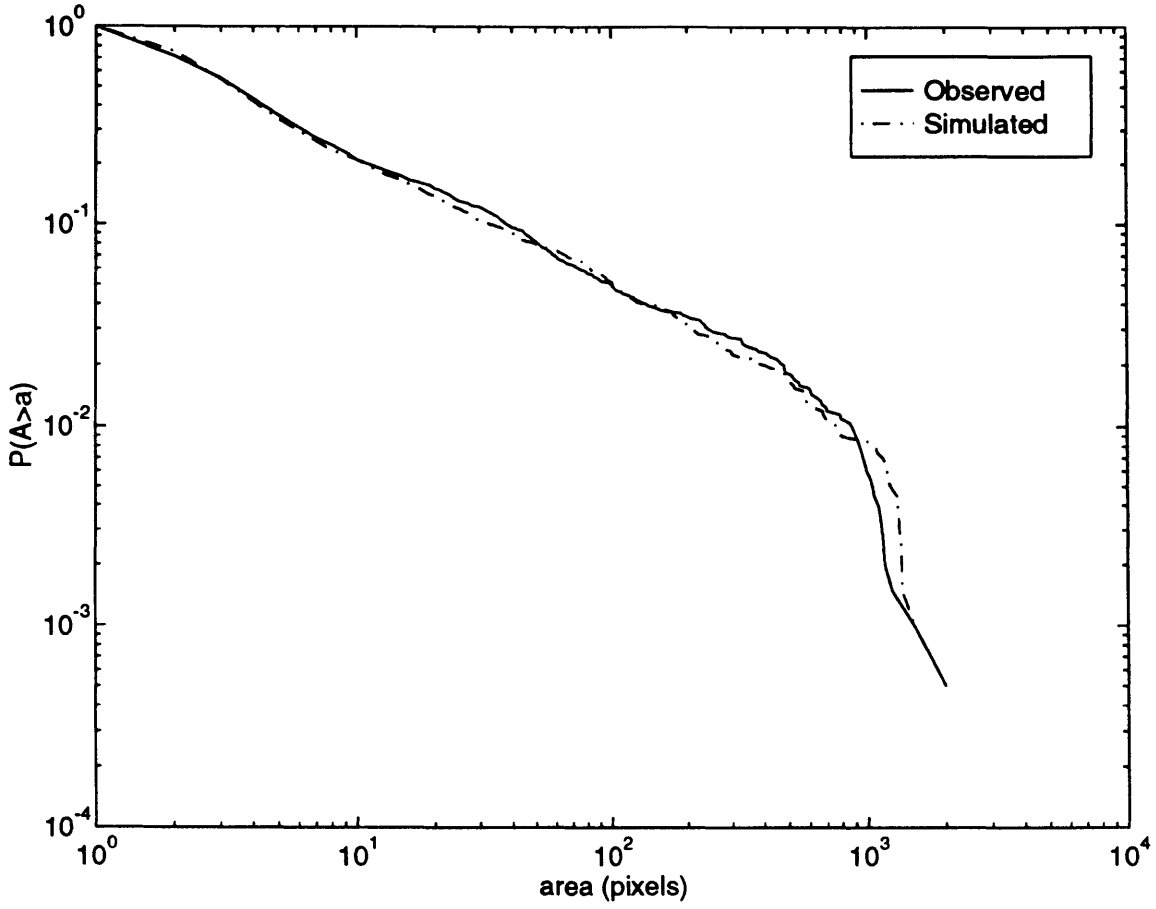

Figure B-8: Observed and final simulated cumulative area distributions for Racoon data set.

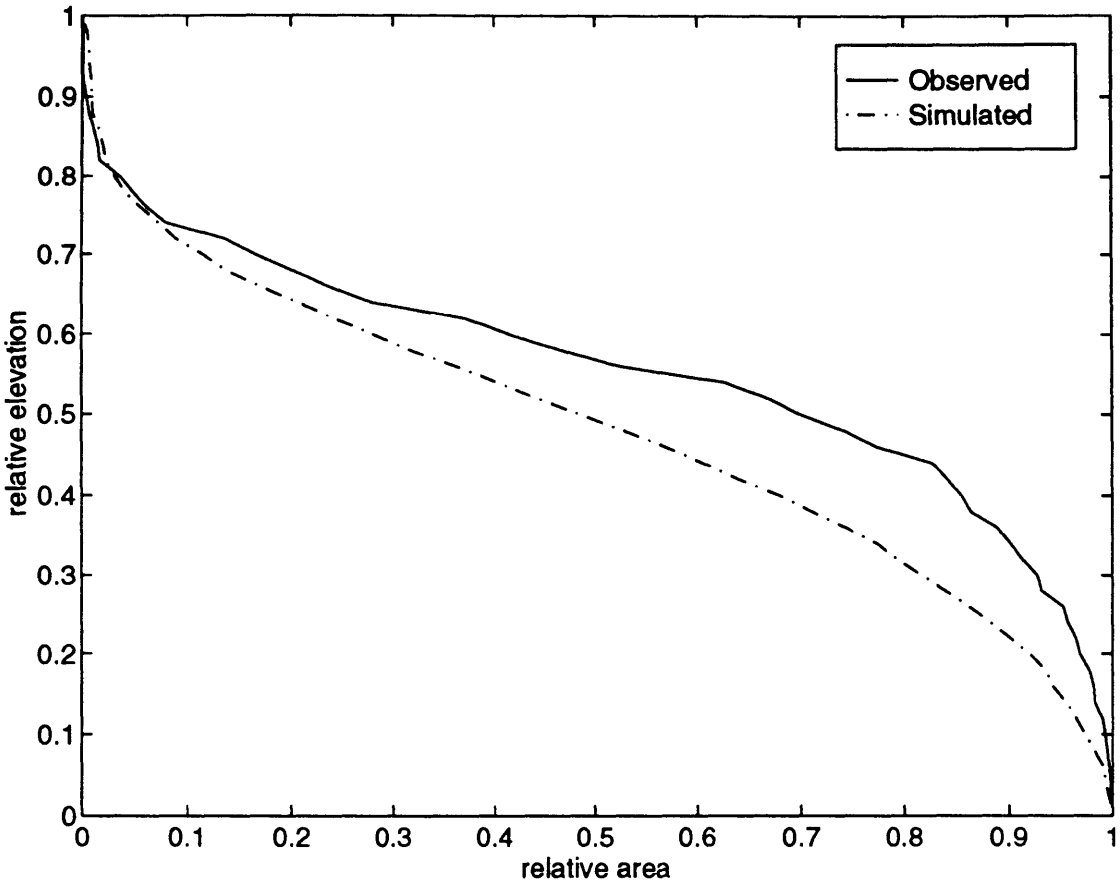

Figure B-9: Observed and final simulated hypsometric distributions for Racoon data set.

B.7 Summary

The details of the computations necessary to calibrate the parameters of the basin evolution model were presented. The calibration of the evolution model to a sub-basin of the Racoon (Pennsylvania) drainage basin was illustrated explicitly. It was shown how initial estimates can be drawn from the observed slope-area and cumulative area distributions and how subsequent refinements of the model parameters can be made based on a combination of observed and simulated data.

Appendix C

Simulations at Various Grid Resolutions

All simulations presented elsewhere in this work have had an implied grid resolution equivalent to the standard DEM resolution: 30m x 30m. This does not mean that the evolution model has an intrinsic grid scale of 30 meters. The decision to perform simulations at this resolution was made simply to be consistent with the observed data. Willgoose *et al.* (1991b) present a nondimensionalization of their basin evolution model. The results presented in this ap

An interesting question that arises is: *"How do we simulate* **equivalent** *systems at different degrees of grid resolution?"* Willgoose *et al.* (1991b) present a nondimensionalization of their basin evolution model dependent on several fundamental scales such a grid scale (referred to in their work as the "horizontal length scale"). The results presented in this appendix are essentially an application of this non-dimensionalization to the specific problem of representing equivalent systems at different grid resolutions.

C.1 Derivation of Grid Scale Relationships

Imagine that we have one drainage system sampled at two different resolutions with side lengths, Δx_1 and Δx_2. We will define r, the ratio between the grid spacings of the two systems such that:

$$\Delta x_1 = \frac{1}{r}\Delta x_2 \tag{C.1}$$

It is important to make a distinction between model output and the scales represented by the model output. The model formulation treats each pixel as having unit side length, and thus, unit area. Slopes too, are based on change in elevation per pixel or per unit length. Thus the model output must be rescaled in situations where the grid spacing differs from unity.

Given two systems related by equation C.1, the model will produce areas for the systems such that:

$$A_1 = r^2 A_2 \tag{C.2}$$

Likewise, the slopes produced by the model will differ with:

$$S_1 = \frac{1}{r} S_2 \tag{C.3}$$

For example, imagine that we have two grid resolutions covering the same domain size with system 2 having a grid twice a fine as system 1. From equation C.1, $r = 1/2$. A pixel in system 2 represents one-fourth of the area of a pixel in system 1 as stated by equation C.2 and the slopes in system 2 are twice as small as those in system 1 as given by equation C.3. If we take system 1 as the standard, then the model output corresponding to system 2 must be adjusted by dividing the system 2 areas by four and doubling the system 2 slopes.

The parameters, β and D have an intrinsic scale associated with them. These parameters must be modified to produce an equivalent simulation for a different scale of resolution. *Given the parameters for system 1 are β_1 and D_1. What parameters, β_2 and D_2, will produce an equivalent system at the new grid spacing?*

First let us determine the relationship between β_1 and β_2. From dynamic equilibrium considerations we have:

$$S_1 = \left(\frac{U}{\beta_1}\right)^{\frac{1}{n}} A_1^{\frac{-m}{n}} \tag{C.4}$$

and,

$$S_2 = \left(\frac{U}{\beta_2}\right)^{\frac{1}{n}} A_2^{\frac{-m}{n}} \tag{C.5}$$

Starting from equation C.3 and substituting from equations C.4 and C.5 we have:

$$S_1 = \frac{1}{r} S_2$$

$$\left(\frac{U}{\beta_1}\right)^{\frac{1}{n}} A_1^{\frac{-m}{n}} = \frac{1}{r} \left(\frac{U}{\beta_2}\right)^{\frac{1}{n}} A_2^{\frac{-m}{n}}$$

Substituting for A_2 from equation C.2:

$$\left(\frac{U}{\beta_1}\right)^{\frac{1}{n}} A_1^{\frac{-m}{n}} = \frac{1}{r} \left(\frac{U}{\beta_2}\right)^{\frac{1}{n}} \left(\frac{1}{r^2} A_1\right)^{\frac{-m}{n}}$$

Simplifying:

$$\frac{1}{\beta_1} = \frac{1}{r^n \beta_2} \left(\frac{1}{r^2}\right)^{-m}$$

We arrive at:

$$\beta_2 = \beta_1 r^{2m-n} \tag{C.6}$$

Likewise, we can solve for the relationship between D_1 and D_2. In Chapter 3 we

developed a relationship for the representative hillslope scale, A_*:

$$A_* = U^{\frac{1-n}{n+m}} \beta^{\frac{-1}{n+m}} (fD)^{\frac{n}{n+m}}$$

Analogous to equation C.2 we can say that,

$$A_{*,1} = r^2 A_{*,2}$$

So, substituting for the two A_* values:

$$U^{\frac{1-n}{n+m}} \beta_1^{\frac{-1}{n+m}} (fD_1)^{\frac{n}{n+m}} = r^2 U^{\frac{1-n}{n+m}} \beta_2^{\frac{-1}{n+m}} (fD_2)^{\frac{n}{n+m}}$$

Simplifying:

$$\beta_1^{\frac{-1}{n+m}} D_1^{\frac{n}{n+m}} = r^2 \beta_2^{\frac{-1}{n+m}} D_2^{\frac{n}{n+m}}$$

$$\beta_1^{-1} D_1^n = r^{2(n+m)} \beta_2^{-1} D_2^n$$

$$D_2^n = D_1^n \left(\frac{\beta_2}{\beta_1}\right) r^{-2(n+m)}$$

$$D_2 = D_1 \left(\frac{\beta_2}{\beta_1}\right)^{\frac{1}{n}} r^{\frac{-2(n+m)}{n}}$$

Substituting for β_2 from equation C.6:

$$D_2 = D_1 \left(\frac{\beta_1 r^{2m-n}}{\beta_1}\right)^{\frac{1}{n}} r^{\frac{-2(n+m)}{n}}$$

$$D_2 = D_1 r^{\frac{2m-n-2(n+m)}{n}}$$

We arrive at:

$$D_2 = D_1 r^{-3} \tag{C.7}$$

Let us consider the implications of these results. Consider first the relationship between the β values. Because the slope-area scaling exponent, θ is related to the ratio of m/n, when $\theta = 0.5$ we have the result that $\beta_2 = \beta_1$. When $\theta > 0.5$ then $\beta_2 < \beta_1$ and when $\theta < 0.5$, $\beta_2 > \beta_1$. The result for D is independent of θ. It says that D simply needs to multiplied by a factor depending on the relative sizes of the two grids. If $r < 1$ implying a finer scale of resolution then $D_2 > D_1$. In other words, diffusion becomes a more powerful agent of erosion when the area represented by a pixel is smaller.

Once can also think of changing the grid size as either magnifying or reducing the area under study. Increasing the resolution of the grid effectively magnifies each pixel. With each pixel representing a smaller real area, the apparent diffusion must be enhanced to produce an equivalent topography. The converse is also true that a coarser grid diminishes the apparent diffusion needed to produce an equivalent topography.

Table C.1: Parameters of three equivalent systems at different grid resolutions.

Quantity	Medium Grid	Fine Grid	Coarse Grid
r	1	1/2	2
grid size	40 x 40	80 x 80	20 x 20
β^*	0.01	0.01	0.01
$D^\dagger$	0.1	0.8	0.0125
channel threshold	50	200	12.5
simulated relief	15.1	14.3	14.8

*β values are equal because simulations were performed with $\theta = 0.5$.
†Channel threshold used for plotting purposes only.

C.2 Simulation of Equivalent Landscapes

To illustrate the results presented in this appendix, three simulations of equivalent systems were performed at different resolutions. The parameters of these simulations are identified in Table C.1

Figures C-1 through C-3 show 3-D perspective plots of the three equivalent landscapes, each representing the same total area. Although the basins appear different because of their resolutions, the average length from divide to channel in each of the three systems is comparable. Furthermore, all three landscapes have a similar overall total relief.

Figures C-4 and C-5 show the slope-area relationships for the three systems before and after being adjusted for equations C.2 and C.3. Figure C-4 shows how the three systems have very different representative hillslope scales, A_*, in absolute model dimensions. Notice also that the fluvial scaling line coincides for the three systems because the simulated value of $\theta = 0.5$ which results in the same β value for each system. However, when we adjust area and slope according to equations C.2 and C.3 the three slope-area relationships coincide, indicating that the systems are equivalent.

The reader may be disconcerted that although the landscapes shown in Figures C-1 through C-3 are portrayed to be "equivalent", the landscapes seem to possess different degrees of roughness. This roughness is the consequence of characterizing the landscape at different resolutions. The coarser the resolution, the rougher the apparent landscape. Additionally, the coarser the grid being used, the greater the area represented by each grid.

The actual roughness of a landscape is best characterized by the cumulative area distribution. There is a complicating factor which arises in the determination of the cumulative area distribution as a result of different grid resolutions. The cumulative area distribution is a pixel based measure which treats all pixels (regardless of grid

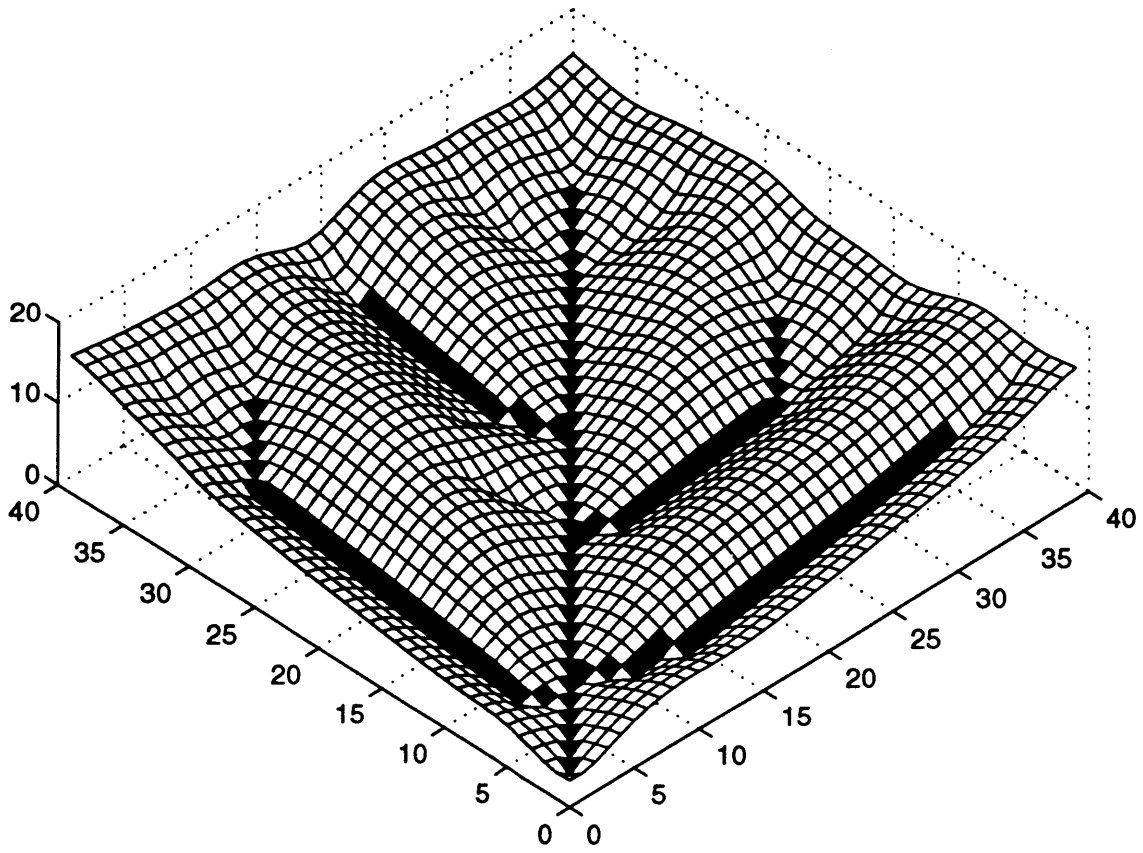

Figure C-1: 3-D perspective plot of medium resolution system. ($D = 0.1$, $\beta = 0.01$)

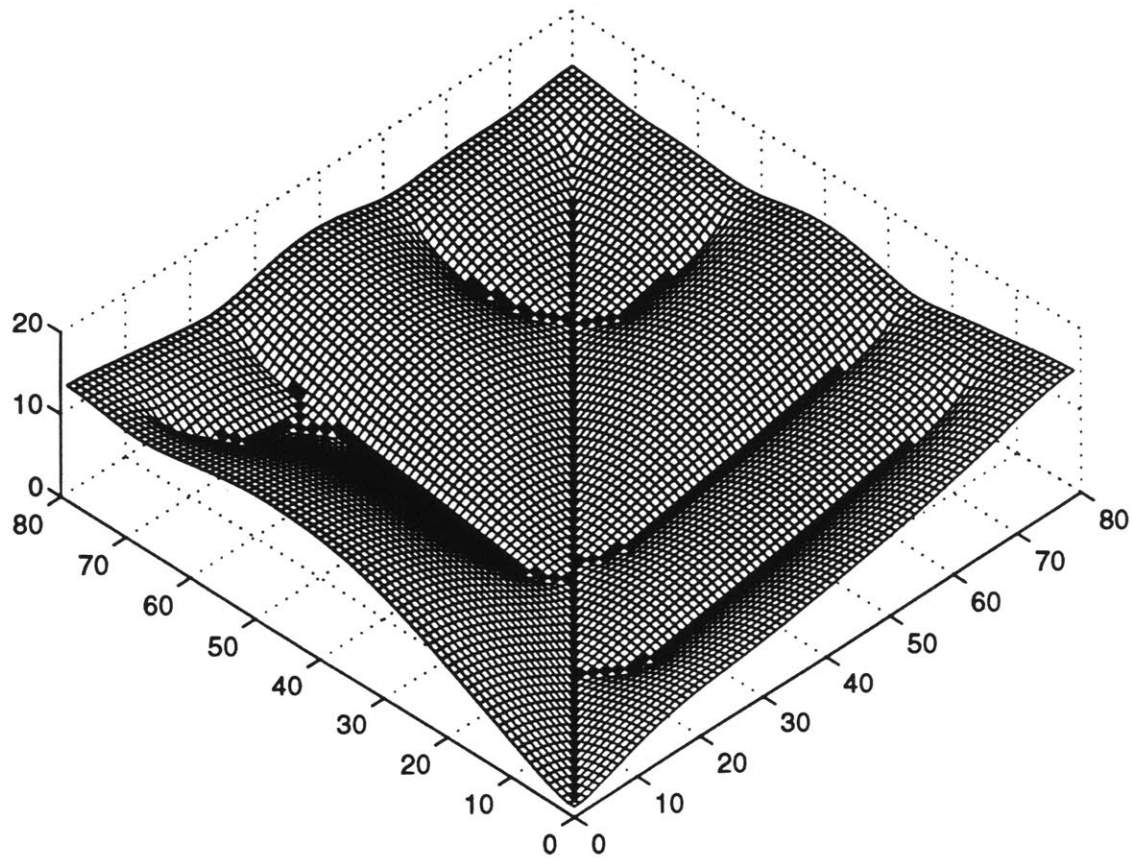

Figure C-2: 3-D perspective plot of fine resolution system. ($D = 0.8$, $\beta = 0.01$)

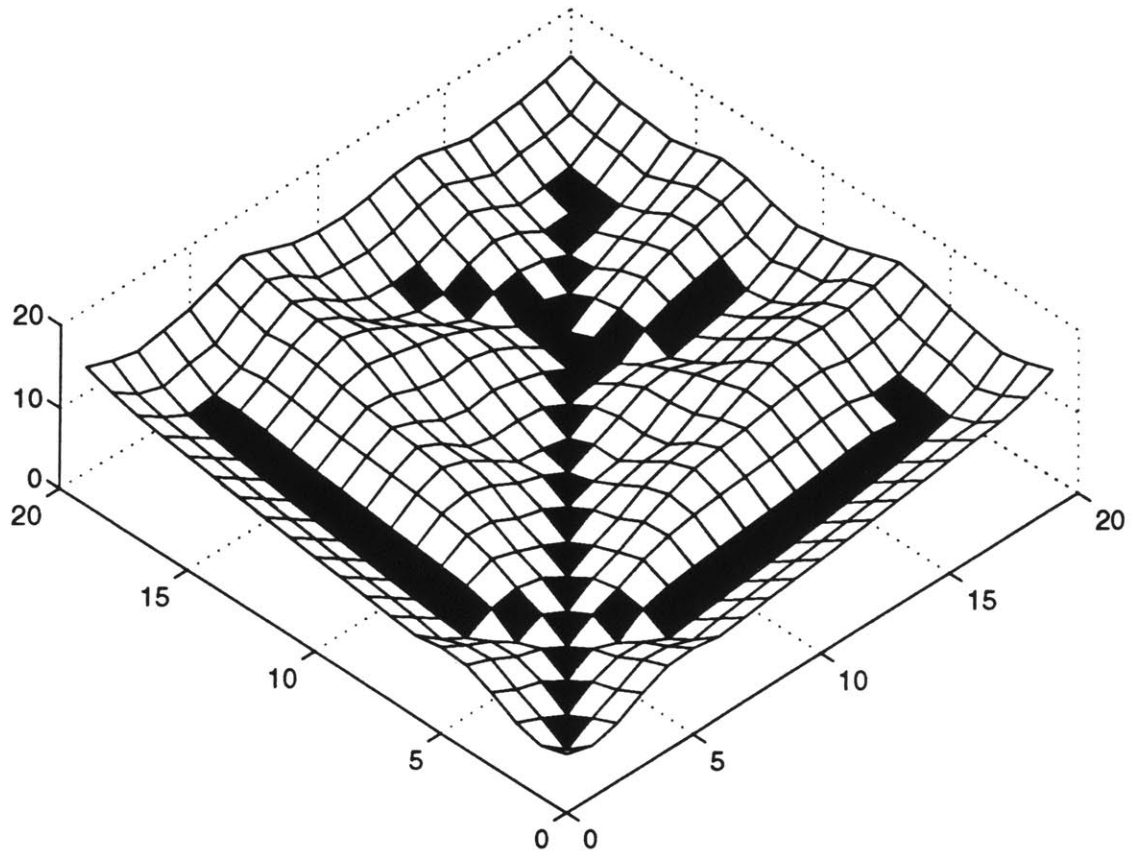

Figure C-3: 3-D perspective plot of coarse resolution system. ($D = 0.0125$, $\beta = 0.01$)

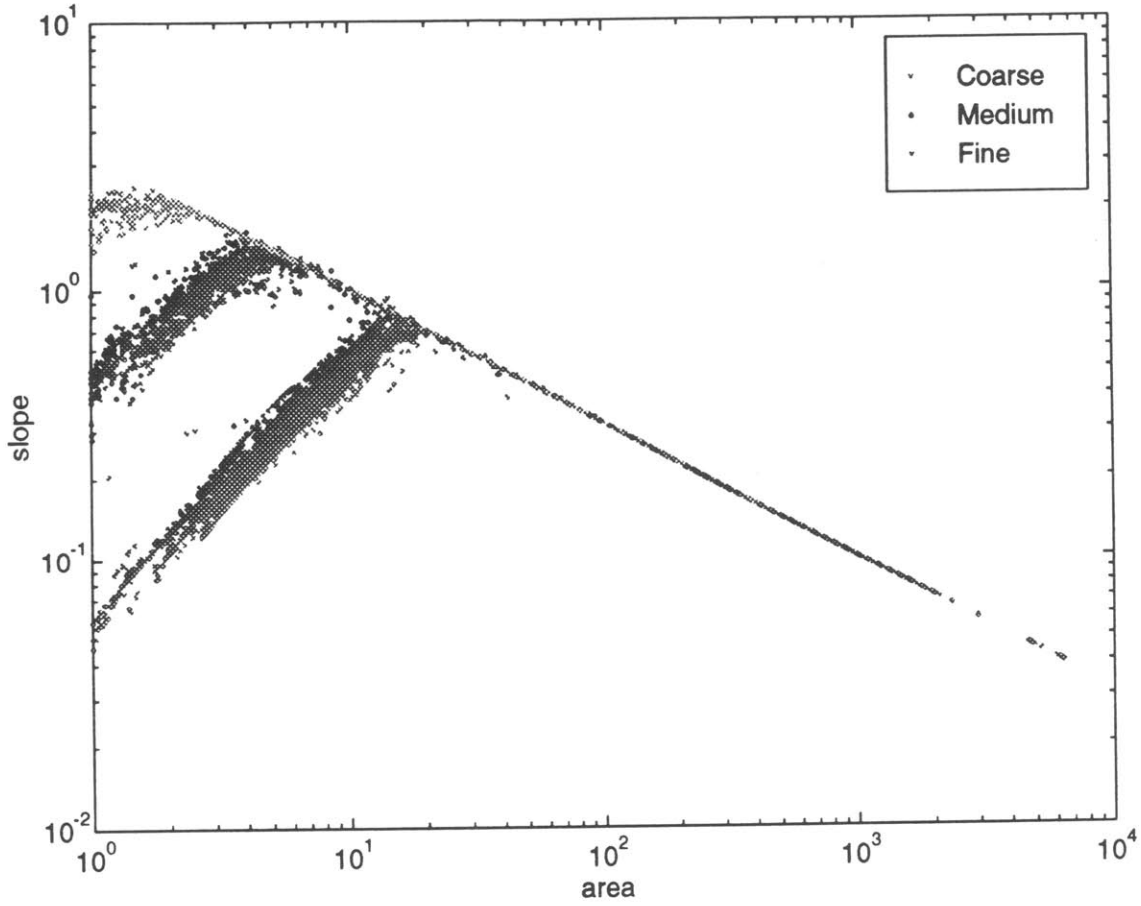

Figure C-4: Slope-area relationships for three equivalent systems before adjusting for equations C.2 and C.3.

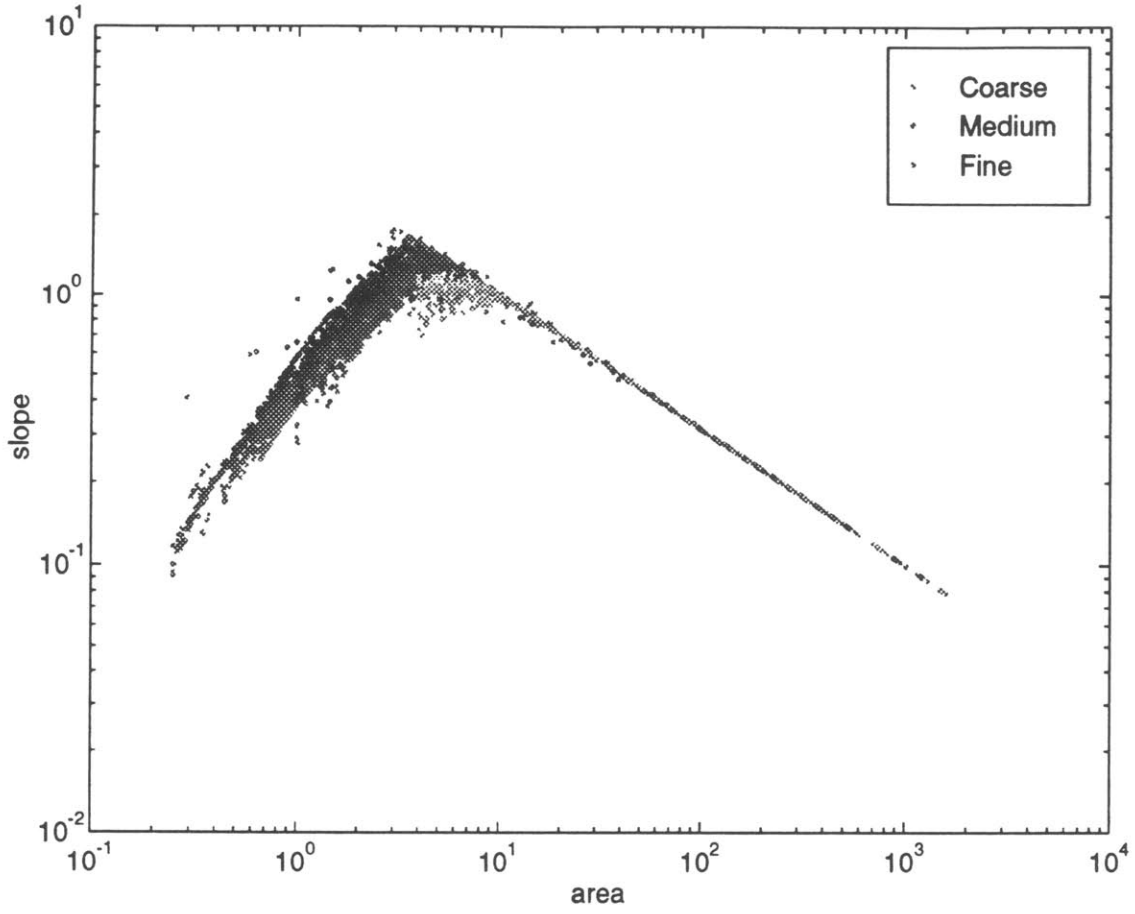

Figure C-5: Slope-area relationships for three equivalent systems after adjusting for equations C.2 and C.3.

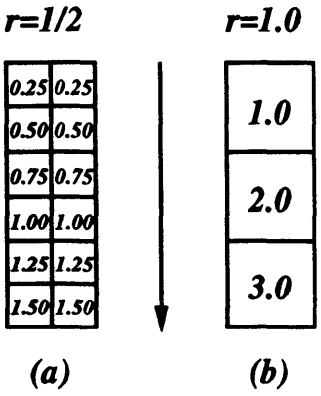

Figure C-6: Flow aggregation in two equivalent systems at resolutions: $r = 1/2$(a) and $r = 1.0(b)$. Arrow indicates direction of flow.

resolution) as if they have unit side length. The resulting problem is illustrated in Figure C-6 which shows the cumulative areas of a linearly aggregating system at two different resolutions. Although the flow patterns are equivalent there is a factor of two difference in the accumulated areas. The total flow crossing any horizontal line in either system is the same, but system (a) has unit contour lines half as long as system (b) and thus appears to have half as much flow as system (b).

Let us compare the cumulative area distributions of two systems, each with a simple aggregation pattern as illustrated in Figure C-7. In this system we have linear accumulation of area from left to right and a "channel" at far right which linearly accumulates area from top to bottom. Figure C-8(a) shows the "raw" cumulative area distributions for two different resolution systems with this drainage structure. The linear hillslope accumulation corresponds to the leftmost part of the curve for both distributions. The sharp break in the curves corresponds to the scale at which channel aggregation begins. Notice that the fine resolution cumulative area distribution has an apparently larger hillslope scale and total area. This is an artifact of the algorithm which sees all pixels as having unit area. In this comparison, $r = 1/2$ so by equation C.2, we adjust the area of the fine grid,

$$A_{coarse} = r^2 A_{fine} = \frac{A_{fine}}{4} \tag{C.8}$$

With this adjustment made the two distributions are shown in Figure C-8(b). Notice now that both distributions stop at the same total area suggesting that both drain the same size domain. However, now the fine grid distribution has an apparently much shorter hillslope scale than the coarse grid distribution. This is caused by the flow per unit contour length discrepancy discussed earlier in Figure C-6. If we now

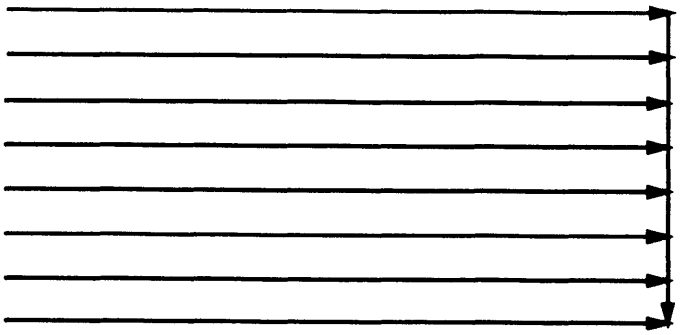

Figure C-7: Aggregation structure of simple system. Arrows indicate direction of flow.

adjust for this problem by using the transform:

$$A_{fine,trans} = \frac{A_{fine}}{r} = 2A_{fine} \tag{C.9}$$

Figure C-8(c) is generated using equation C.9 to modify the fine resolution distribution. The hillslope aggregation curves for both systems now become comparable.

By similar arguments Figures C-9(a-c) are generated for the landscapes shown in Figures C-1 through C-3. The aggregation patterns of the fine grid scale landscape compared to the medium grid scale landscape behave analogously to the simple case discussed in the previous figure. This is again true when comparing the medium grid scale to the coarse grid scale. This indicates that the aggregation patterns at the hillslope scale are comparable for all three systems which supports the assertion that the three systems are equivalent.

C.3 Summary

This appendix illustrated how the model can simulate a given topography at different resolutions. Relationships between the model parameters, β and D were derived to reflect how these parameters are related at different resolutions. A series of three simulations, each representing the same topography at different resolutions, were performed. It was shown that these simulations produced different slope-area relationships in absolute terms, but very comparable slope-area relationships when adjusted to reflect their respective grid resolutions. Additionally, the cumulative area distributions were comparable at the hillslope scale when properly transformed to reflect flow per unit contour width.

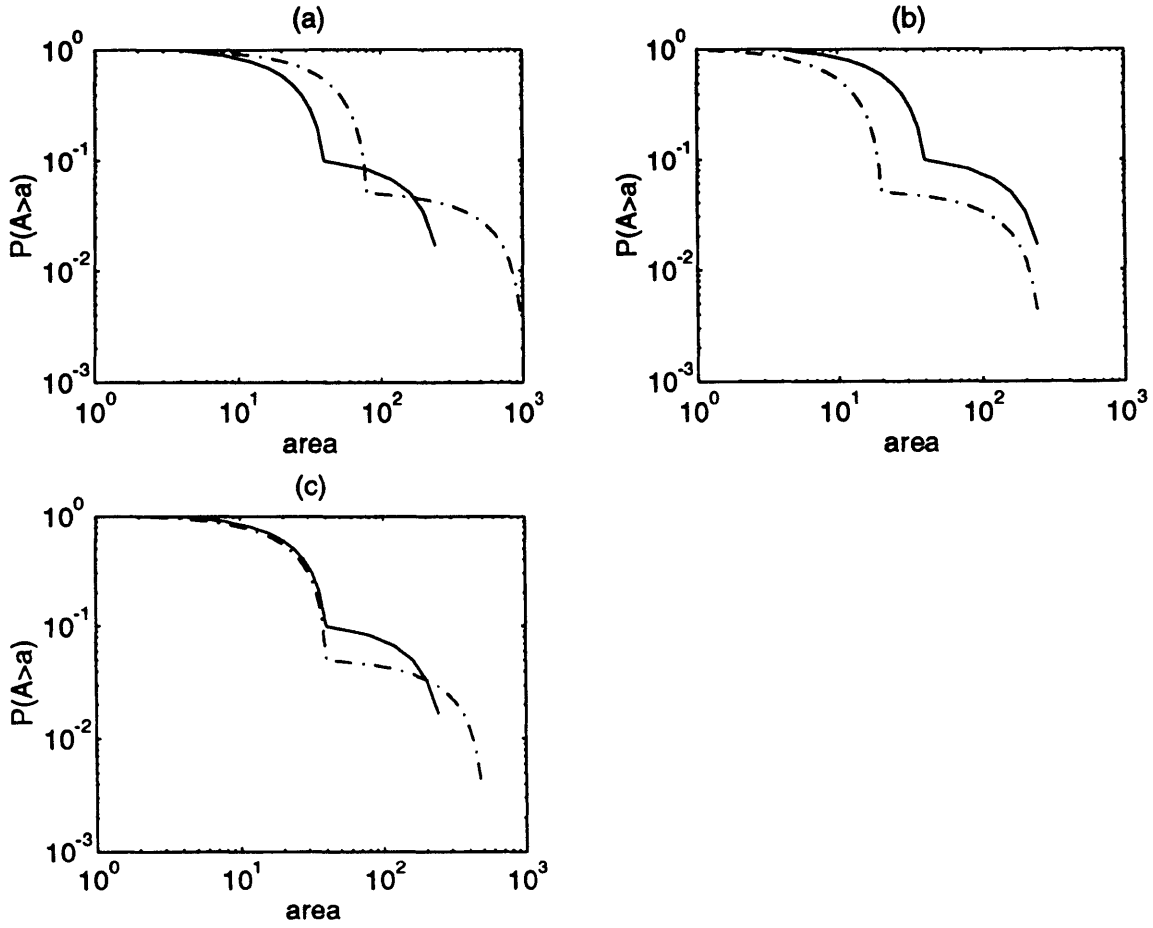

Figure C-8: Cumulative area distributions for simple system shown in Figure C.7. Solid line is coarse resolution, dot-dashed line is fine resolution. Figure (a) shows raw distributions, (b) are distributions transformed with equation C.8, and (c) are distributions transformed with equation C.9.

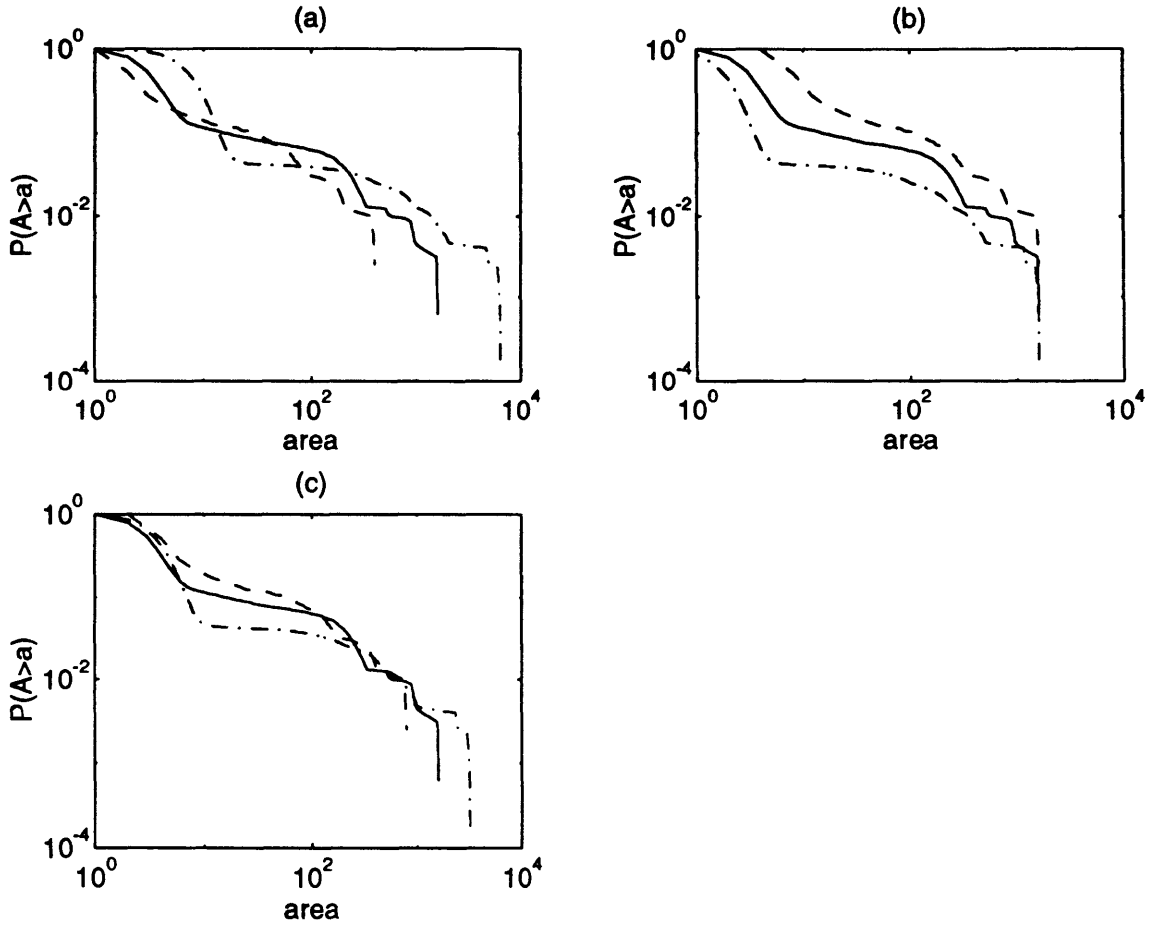

Figure C-9: Cumulative area distributions for systems shown in Figures C.1 (solid line), C.2 (dot-dashed line), and C.3 (dashed line). Figure (a) shows raw distributions, (b) are distributions transformed to match total area, and (c) are distributions transformed to match hillslope areas.

Bibliography

Ahnert, F., 1976. Brief description of a comprehensive three-dimensional process-reponse model of landform development. *Z. Geomorph, N.F. Suppl.* 25:29-49.

Ahnert, F., 1977. Some comments on the quantitative formulation of geomorphological processes in a theoretical model. *Earth Sur. Processes*, 2:191-201.

Beven, K.J., and M.J. Kirkby, 1979. A physically-based variable contributing area model of basin hydrology. *Hydrol. Sci. J.*, 24(1): 43-69.

Bierman, P.R., 1994. Using in situ produced cosmogenic isotopes to estimate rates of landscape evolution: A review from the geomorphic perpsective. *J. Geophys. Res.*, 99(B7):13,885-13,896.

Bloom, A.L. 1978. *Geomorphology - A systematic analysis of late Cenozoic landforms.* Prentice-Hall, New Jersey, 510 pp.

Burbank, D.W., 1992. Characteristic size of relief. *Nature*, 359: 483-484.

Carson, M.A., and M.J. Kirkby, 1972. *Hillslope Form and Process.* Cambridge University Press, 475 pp.

Cordova, J.R., I. Rodriquez-Iturbe, and P. Vaca, 1982. On the development of drainage networks. In: D.E. Wallings (Editor), *Recent developments in the explanation and prediction of erosion and sediment yield*, Exeter, U.K., 19-30.

Costa-Cabral, M.C., and S.J. Burges, 1994. Digital elevation model networks (DEMON): A model of flow over hillslopes for computation of contributing and dispersal areas. *Water Resour. Res.*, 30(6): 1681-1692.

Davis, W.M., 1909. *Geographical Essays.* Ginn, Boston, 777 pp.

Dietrich, W.E., C.J. Wilson, D.R. Montgomery, and J. McKean, 1993. Analysis of Erosion thresholds, channel networks, and landscape morphology using a digital terrain model. *J. Geology*, 101:259-278.

Ellison, W.D., 1947. Soil Erosion Studies. *Agric. Engng.*, 28.

Flint, J.J., 1974. Stream gradient as a function of order, magnitude and discharge. *Water Resour. Res.*, 10(5): 969-973.

Gelhar, L.W., 1993. *Stochastic Subsurface Hydrology.* Prentice-Hall, New Jersey, 390 pp.

Gilbert, G.K., 1877. *Report on the Geology of the Henry Mountains*, U.S. Geographical and Geological Survey, Washington, D.C., 160 pp.

Hack, J.T., 1957. *Studies of Longitudinal Stream Profiles.* U.S. Geological Society professional paper, 294-B. Washington, D.C., pp. 45-97.

Horton, R.E., 1945. Erosional Development of Streams and Their Drainage Basins: Hydrophysical Approach to Quantitative Geomorphology. *Bull. Geol. Soc. Am.* 56: 275-370.

Howard, A.D. 1994. A detachment-limited model of drainage basin evolution. *Water Resour. Res.*, 30(7): 2261-2285.

Ijjasz-Vasquez, R.L. Bras, and G.E. Moglen, 1992. Sensitivity of a basin evolution model to the nature of runoff production and to initial conditions. *Water Resour. Res.*, 28(10): 2733-2741.

Izumi, N and G. Parker, 1993. Channelization and Drainage Basin Formation in Cohesive Soils. *Trans. Am. Geophys. Union,* 74(16): 152.

Kirchner, J.W., 1993. Statistical inevitability of Horton's Laws and the apparent randomness of stream channel networks. *Geology,* 21: 591-594.

Kirkby, M.J., 1971. Hillslope process-response models based on the continuity equation. In: *Slopes, Forms and Processes,* Institute of British Geographers. Special Publication No. 3.

Kirkby, M.J., 1986. A two-dimensional simulation model for slope and stream evolution. In: A.D. Abrahams (Editor), *Hillslope Processes.* Binghamton Symp. Geomorph., Int. Ser., no. 16. Allen & Unwin, Boston, 205-222.

Kramer, S. and M. Marder, 1992. Evolution of river networks. *Phys. Rev. Let* 68(2): 205-208.

La Barbera, P. and G. Roth, 1993. Invariance and scaling properties in the distributions of contributing area and energy in drainage basins. *Hydrol. Proc.* 8(2):125-136.

Langbein, W.B., 1947. *Topographic characteristics of drainage basins.* U.S. Geological Society water supply paper, 968-C. Washington, D.C.

Leheny, R.L., and S.R. Nagel, 1993. Model for the evolution of river networks. *Phys. Rev. Let.* 71(9): 1470-1473.

Leopold,L.B., and T. Maddock, Jr., 1953. *The hydraulic geometry of stream channels and some physiographic implications.* U.S. Geological Survey professional paper, 282-A. Washington, D.C.

Loewenherz, D.S., 1991. Stability and the initiation of channelized surface drainage: A reassessment of the short wavelength limit. *J. Geophys. Res.*, B96, 8453-8464.

Montgomery, D.R., and W.E. Dietrich, 1988. Where do channels begin? *Nature,* 336, 232-234.

Montgomery, D.R., and W.E. Dietrich, 1994a. Landscape dissection and drainage area-slope thresholds. In: M.J. Kirkby (Editor), *Process Models and Theoretical Geomorphology,* John Wiley & Sons, New York, 221-246.

Montgomery, D.R., and W.E. Dietrich, 1994b. A physically based model for the topographic control on shallow landsliding. *Water Resour. Res.*, 30(4): 1153-1171.

Montgomery, D.R. and E. Foufoula-Georgiou, 1993. Channel network source representation using digital elevation models. *Water Resour. Res.*, 29(12): 3925-3934.

O'Callaghan, J.F., and D.M. Mark, 1994. The extraction of drainage networks from digital elevation data. *Comput. Vision Graphics Image Process.*, 28, 323-344.

O'Loughlin, E.M., 1986. Prediction of surface saturation zones in natural catchments by topographic analysis. *Water Resour. Res.*, 22(5): 794-804.

Quinn, P., K. Bevin, P. Chevallier, and O. Planchon, 1991. The prediction of hillslope flowpaths for distributed hydrological modelling using digital terrain models. In: K.J. Bevin and I.D. Moore (Editors), *Advances in Hydrological Processes, Terrain Analysis and Distributed Modelling in Hydrology.* John Wiley & Sons., New York, 63-83.

Rigon, R., A. Rinaldo, and I. Rodriguez-Iturbe, 1994. On landscape self-organization. *J. Geophys. Res.*, 99(B6):11,971-11993.

Rinaldo, A., I. Rodriguez-Iturbe, R. Rigon, E. Ijjasz-Vasquez, and R.L. Bras, 1993. Self-Organized Fractal River Networks. *Phys. Rev. Let.*, 70(6): 822-825.

Rinaldo, A., I. Rodriguez-Iturbe, R. Rigon, R.L. Bras, and E. Ijjasz -Vasquez, 1992. Minimum Energy and Fractal Structures of Drainage Networks. *Water Resour. Res.*, 28(9): 2183-2195.

Rodriguez-Iturbe, I., E.J. Ijjasz-Vasquez, R.L. Bras, and D.G. Tarboton, 1992. Power law distributions of mass and energy in river basins. *Water Resour. Res.*, 28(4): 1089-1093.

Seidl, M.A., W.E. Dietrich, M.W. Caffee, and R.C.Finkel, 1992. Evidence for the transition from transport-limited to production-limited hillslopes due to knickpoint propagation. *Trans. Am Geophys. Union,* 73(43): 212.

Shreve, R.L., 1966. Statistical law of stream numbers. *J. Geology,* 74: 17-37.

Shreve, R.L., 1967. Infinite topologically random channel networks. *J. Geology,* 75: 178-186.

Smith, T.R., and F.P. Bretherton, 1972. Stability and the conservation of mass in in drainage basin evolution. *Water Resour. Res.*, 8(6): 1506-1529.

Stark, C.P., 1991. An invasion percolation model of dranage network evolution. *Nature*, 352, 423-424.

Stark, C.P., 1994. Cluster growth modeling of plateau erosion. *J. Geophys. Res.*, 99(B7):13,957-13,969.

Strahler, A.N., 1952. Hypsometric (area-altitude) analysis of erosional topography. *Bull. Geol. soc. Am.*, 63, 1117-1142.

Strahler, A.N., 1957. Quantitative analysis of watershed geomorphology. *Trans. Am. Geophys. Union,* 38(6): 913-920.

Strahler, A.N., 1964. Quantitative analysis of drainage basins and channel networks. In: V.T. Chow (Editor), *Handbook of Applied Hydrology,* McGraw-Hill, New York, pp 4-39-4-76.

Surkan, A.J., 1968. Synthetic hydrographs: Effects of network geometry. *Water Resour. Res.*, 5(1): 112-128.

Tarboton, D.G., R.L. Bras, and I. Rodriguez-Iturbe, 1988. The fractal nature of river networks. *Water Resour. Res.*, 24(8):1317-1322.

Tarboton, D.G., R.L. Bras, and I. Rodriguez-Iturbe, 1989. The analysis of river basins and channel networks using digital terrain data. Report 326, Ralph M. Parsons Lab., Massachusetts Institute of Technology, Cambridge, MA.

Tarboton, D.G., R.L. Bras, and I. Rodriguez-Iturbe, 1991. On the extraction of channel networks from digital elevation data. *Hydrol. Proc.* 5(1):81-100.

Tucker, G.E., and R.L. Slingerland, 1994. Erosional dynamics, flexural isostasy, and long-lived escarpments: A numerical modeling study. *J. Geophys. Res.*, 99(B6):12,229-12243.

Vanmarke, E. 1983. *Random Fields: Analysis and Synthesis,* MIT Press, Cambridge, MA. 382 pp.

Willgoose, G.R., R.L. Bras, and I. Rodriguez-Iturbe, 1991a. A coupled Channel Network Growth and Hillslope Evolution Model 1. Theory. *Water Resour. Res.*, 27(7):1671-1684.

Willgoose, G.R., R.L. Bras, and I. Rodriguez-Iturbe, 1991b. A coupled Channel Network Growth and Hillslope Evolution Model 2. Nondimensionalization and Applications. *Water Resour. Res.*, 27(7):1685-1696.

Willgoose, G.R., R.L. Bras, I. Rodriguez-Iturbe, 1991c. A coupled Channel Network Growth and Hillslope Evolution Model 3. A physical explanation of an Observed Link Area-Slope Relationship. *Water Resour. Res.*, 27(7):1697-1702.

Willgoose, G.R., R.L. Bras, and I. Rodriguez-Iturbe, 1994a. Hydrogeomorphology modelling with a physically based river basin evolution model. In: M.J. Kirkby (Editor), *Process Models and Theoretical Geomorphology,* John Wiley & Sons, New York, 271-294.

Willgoose, G.R., 1994b. A physical explanation for an observed area-slope-elevation relationship for catchments with declining relief, *Water Resour. Res.*, 39(3): 151-159.

Willgoose, G.R., 1994c. A statistic for testing the elevation characteristic of landscape simulation models. *J. Geophys. Res.*, 99(B7):13,987-13,996.